A New Computational Tool to Assess the Integrated Ventilation, Thermal and Energy Performance of a Seasonal-Adaptive Double Skin Façade Retrofit for Warehouses in the UK

Thesis submitted to the University of Nottingham for the degree of Doctor of Philosophy, November 2024.

Kate Pelletier

14301728

Supervised by

Dr. Christopher Wood

Dr. John Calautit

Dr. Yupeng Wu

Abstract

The growth of the industrial logistics sector in response to e-commerce demand in the UK has led to a construction boom of increasingly large storage and distribution warehouses yet little is understood about them from a building physics and energy efficiency standpoint. These modern warehouses offer a unique opportunity for the application of façade-based technologies, such as double skin facades, on their expansive envelope.

This thesis presents a new computational tool to assess the integrated ventilation, thermal and energy performance of a seasonal-adaptive double-skin façade retrofit for UK warehouses. Double skin facades are a ventilation technology applied to the interface between indoor and external environments where the energy balance is highly influential on the building's energy consumption. The novel application of the proposed "seasonal-adaptive" opaque double skin façade to a case study warehouse comprises an aluminium outer skin and warehouse cladding inner skin, separated by a 0.2m air cavity. A level of control over its ventilation and thermal capacity is achieved through percentage closures of the DSF inlet from 25-75% in the direction of both the outer and inner skins.

The computational fluid dynamics tool required a three-step validation process including wind tunnel tests of a 1:50 scale model of the double skin façade warehouse to assess wind performance, climate chamber tests of a 1:1 prototype of the opaque double skin façade to assess buoyancy performance, and lastly, heat mat tests to simulate stratification. Together, in addition to an analytical validation of cross-ventilation in the case study warehouse, this research process ensured a level of validity and reliability. CFD-derived cavity air velocities and temperatures applied to Bernoulli-adapted equations can determine ventilation, and heat gain/removal supplied by the proposed double skin façade system to the warehouse.

The first results chapter assessed the wind-driven ventilation performance of the double skin façade on the warehouse achieving a final error of 7.8% against the experimental data with expected aerodynamic behaviour. A stable vertical cavity airflow rate was observed until it increases at the warehouse inlet height of 9m and promoted cross-ventilation with neutral pressure heights of 4-4.75m in all four seasons in the UK climate. This chapter concluded the double skin façade's capacity as a natural ventilation technology as it delivered 37ACH at an occupant level of 2m. These results suggest that a modernisation of warehouse ventilation design guidelines is required.

The second results chapter evaluated the buoyancy-driven ventilation and thermal performance of the double skin façade at prototype and full-scale dimensions. Winter conditions (300W/m^2 and -4^{o}C) produced the highest thermal gradients in the prototype cavity of 13^{o}C/m suggesting a high thermal potential in colder climates or seasons. For cavity air velocity and temperature from CFD, errors of 16% and 27% were obtained against existing literature, whilst 12% and 3.5% were achieved versus the climate chamber data. Flow rates of 1000-6100L/s and 27kW, 10kW and -5kW of pre-heating or "cooling" are produced in winter, intermediate and summer conditions. The double skin façade retrofit also reduced the U-value of the original warehouse cladding to 0.19-0.27W/m^2K from 0.31W/m^2K.

The stand-alone chapter excluded the double skin façade to instead focus on vertical heating at 1:50 and full-scale in the case study warehouse. Storage racking increased the thermal gradient of the empty small-scale warehouse by 23%, a significant impact on stratification. The analytically predicted Grashof number at full-scale from temperature data in the empty small- scale warehouse is an overestimation of $4.8x10^{11}$ compared $4.5x10^9$ obtained in CFD. Applying cross-ventilation openings reduced stratification in the presence of 40W/m^2 floor area heat gains, and storage racking presents issues for controlling internal airflow and thermal patterns.

The integrated computational tool, presented in the final chapter, assesses the double skin façade warehouse performance in combined wind and buoyancy conditions. Cross-ventilation in the warehouse was analytically validated with an error of 23%. Wind conditions representative of the four seasons applied under an irradiance of 300W/m^2 produced significant pre-heating of 12.6^{o}C (winter) and 21-23^{o}C (intermediate) with minimal summer heating of 1.8^{o}C. A total warehouse inlet opening area of 3.75m^3 provides 2-3 times the ventilation requirements, and the DSF inlet area could reduce from 7.2m^2 to 0.95-1.4m^2. Different DSF inlet configurations were optimised for the warehouse inlet openings. The fully open DSF (36m x 9m) can deliver 0.59MW, 0.50MW, 18kW and 0.45MW in winter, spring, summer and autumn at 2% of the warehouse construction cost, and a payback period of under a year.

At a minimum, this thesis closes knowledge gaps in the performance of opaque double skin façades, the viability of DSF retrofits for warehouses, and the experimental methods to validate CFD models simulating air and thermal phenomena occurring in warehouses. However, it also challenges existing regulatory, industrial and academic understanding of a largely overlooked building type in building physics research and low-energy building technology application.

Publications

Journal Paper

[1] Pelletier, Kate et al. “The Viability of Double-Skin Façade Systems in the 21st Century: A Systematic Review and Meta-Analysis of the Nexus of Factors Affecting Ventilation and Thermal Performance and Building Integration.” Building and environment 228 (2023): 109870. Web.

**the publication is based on the literature review in Chapter 2 in this thesis.*

Conference

[1] Pelletier, Kate, Calautit John, and Wood, Christopher. “Storage and Distribution Warehouses: A Neglected Building Type in Natural Ventilation Design”. 20th International Conference on Sustainable Energy Technologies.

**the publication is based on the experimental and computation results in Chapter 4 in this thesis.*

Acknowledgements

First and foremost, I would like to thank the University of Nottingham and in particular the Department of Architecture and Built Environment for providing the opportunity for me to undergo an EPSRC-funded PhD, and all the resource and training that has been a part of this. I am also extremely grateful to my supervisors, Dr. Chris Wood, and Dr. John Calautit for their endless guidance, and patience throughout my PhD. Both their insights, expertise and feedback have been invaluable and instrumental in producing this thesis. I would also like to thank Dr. Yupeng Wu for supervision in the first year of my PhD and literature review feedback.

Special thanks go to my research group, Buildings, Environment and Energy (BEE) led by Dr. Saffa Riffat which has provided me with opportunities to present my PhD work at an international conference, and work with other PhD students who had methodology overlaps with my research. I would also like to show my appreciation to other academic colleagues such as Dr. John Owen from the Department of Civil Engineering who allowed me to use the Atmospheric Boundary Layer tunnel and provided the relevant training and advice on how to best perform my wind tunnel tests. I would also like to extend thanks to Dr. Rabah Boukhanouf, Rob Shipman, Dr. Chris Wood, and Dr. Ben Jones for giving me the opportunity to be involved with teaching either through lab demonstrations, tutorials or exam marking. Additionally, the help from technicians such as Tony Gospel, Malcolm Dugdale and James Hazzledine in the planning, health and safety, and model construction for my climate chamber and wind tunnel experiments was essential to the successful completion of my experiments.

Alongside my PhD, I had the privilege to work with an education charity called the Brilliant Club as a PhD tutor. As part of my role, I delivered national curriculum mathematics sessions to pupils who face barriers to higher education to help close the learning gaps created by Covid-19. I also partnered with the charity to create a Key Stage 4 programme titled “The Future of Our Built Environment” based off my education as an engineer and PhD researcher and was delivered by myself as a STEM programme in several schools to GCSE students.

Finally, I would like to express my deepest gratitude to everybody in my personal life, both friends and family, but especially Rhys Hill, Thea, Sam and Joanne Pelletier who have been endlessly supportive, positively encouraging and an integral part of my PhD journey.

Contents

1. Introduction 1
1.1 Storage and Distribution Warehouses – A Neglected Building Type 2
1.1.1 The Energy Consumption of Warehouses 2
1.1.2 The Internal Environment and Conditions of Warehouses 4
1.1.3 Challenges Facing Roof-Top PV Installation for Warehouses 5
1.2 Façade Technologies – Maximizing Building Envelope Potential 7
1.2.1 Review of Solar-Assisted Façade Technology 8
1.2.2 The Limitations of Transpired Solar Collectors for Warehouses 11
1.2.3 Is Natural Ventilation Achievable in Warehouses? 12
1.3 A Building-First approach to Designing Double Skin Facades 13
1.3.1 Treating the DSF as a Duct (Ventilation Performance) 14
1.3.2 Treating the DSF as a Wall Retrofit (Thermal Performance) 15
1.3.3 Determining the Energy Performance of a DSF Retrofit 15
1.4 Methods of Natural Ventilation Modelling 15
1.5 Research Scope, Novelty and Process 18
1.5.1 A "Seasonal-Adaptive" Opaque Aluminium DSF for Warehouses 19
1.5.2 A Computational Fluids Dynamics tool to Assess Ventilation, Thermal and Energy Performance of a DSF Warehouse 20
1.5.3 Research Process 20
2. Literature Review 22
2.1Chapter Introduction 23
2.1.1 Motive and Context 23
2.1.2 Classification of Double Skin Facades 25
2.1.3 Mechanism of Double Skin Facades 26
2.1.4 Novelty of Review Methodology and Concept 27
2.2 Factors Affecting the Ventilation and Thermal Performance of Double Skin Facades 29
2.2.1 Climate Type and Location 30
2.2.2 Building Application 36
2.2.3 Double Skin Façade Cavity Geometry and Layout 45
2.2.4 Double Skin Façade Construction Layers 49
2.3 Factors Affecting Building Integration of Double Skin Facades 60
2.3.1 Energy Performance 60
2.3.2 Occupancy Comfort and Safety 69
2.3.3 Life Cycle Analyses of Double Skin Facades 74
2.4 Methodology Trends in Double Skin Façade Research 78
2.5 Chapter Summary 79
2.5.1 Research Gaps 80
3. Methodology 81
3.1Chapter Introduction 82
3.1.1 Case Study Warehouse and Cross-Ventilation Scenario 82
3.1.2 Case Study Climate and Meteorological Data 85
3.2Atmospheric Boundary Layer Wind Tunnel Experiment 88
3.2.1 Experimental Theory 89
3.2.2 Model Build and Pressure Tap Locations 90
3.2.3 Experimental Set-Up, Measurement Variables and Equipment 92
3.2.4 Design Conditions and Reference Point Measurements 93
3.3 Climate Chamber Experiment 95
3.3.1 Experimental Theory 96

3.3.2 Rationale for an Opaque Outer Skin in the Double Skin Facade 98
3.3.3 DSF Prototype Construction and Laboratory Set-Up 99
3.3.4 Measurement Variables, Equipment and Design Conditions 100
3.4 Heat Mat Tests for Simulated Stratification 101
3.4.1 Experimental Theory 101
3.4.2 Experimental Set-Up, Measurement Variables and Equipment 102
3.5 Experimental Error Analysis Theory 103
3.5.1 Fractional Error Analysis 103
3.5.2 Standard Deviation Error Analysis 105
3.6 Computational Fluid Dynamics 106
3.6.1 Reynolds-Averaged Navier Stokes (RANS) Modelling 106
3.6.2 Geometry, Computational Domain and Boundary Conditions 107
3.6.3 Mesh Generation and Model Set-Up 109
3.6.4 Boussinesq Approximation and Heat Generation 111
3.6.5 User-Defined Wind Velocity Profiles 112
3.7 Chapter Summary 113
4. Wind-Driven Ventilation Performance of the Double Skin Facade 115
4.1 Chapter Introduction 116
4.2 Experimental Results 117
4.2.1 ABL Experimental Wind Profile 117
4.2.2 Pressure Differential Data for Different Wind Speeds and Angles 118
4.2.3 Error Analysis 121
4.3 Experimental Validation of Computational Models 122
4.3.1 Initial Model Comparison with Experimental Data 122
4.3.2 Grid Independence Tests 124
4.3.3 Turbulence Model Sensitivity Analysis 126
4.3.4 Wind Shear Exponent Sensitivity Analysis 127
4.4 Computational Modelling of A Full-Scale Warehouse (Wind-Only) 129
4.4.1 Dynamic Similarity Test 129
4.4.2 Seasonal Wind Performance of the Double Skin Façade Warehouse 132
4.4.3 Neutral Pressure Height in the Double Skin Façade Warehouse 135
4.4.4 Ventilation Assessment 137
4.5 Ventilation Performance of the Full-Scale Double Skin Façade Warehouse (Wind-Only) 140
4.5.1 Treating the Double Skin Façade as a Ventilation Duct 140
4.6 Chapter Summary 141
5. Buoyancy-driven Ventilation and Thermal Performance of the Double Skin Facade 143
5.1 Chapter Introduction 144
5.2 Experimental Results 145
5.2.1 Simulated Solar Irradiance Tests 146
5.2.2 Cavity Velocity and Temperature Profiles 148
5.2.3 Thermal Gradients 150
5.2.4 Error Analysis 151

5.3 Experimental Validation of Computational Model 152
5.3.1 Preliminary Validation against Literature 152
5.3.2 Validation against Original Experimental Data 156
5.3.3 Grid Independence Analysis 157
5.3.4 Turbulence Model Sensitivity Analysis 159
5.3.5 Pre-Heating and Ventilation Analyses of DSF Prototype 160
5.4 Computational Modelling of a Full-Scale Double Skin Façade (Buoyancy-Only) 164
5.4.1 Cavity Velocity and Ventilation Performance 165
5.4.2 Cavity Temperature and Thermal Performance 167
5.5 Energy Savings from a Full-Scale Double Skin Façade (Buoyancy-Only) 169
5.5.1 Treating the Double Skin Façade as a Thermal Chimney 169
5.5.2 Treating the Double Skin Façade as a New Wall 170
5.6 Chapter Summary 171
6. Stratification in Warehouses 174
6.1 Chapter Introduction 175
6.2 Experimental Results 176
6.2.1 Empty Warehouse (no DSF) 176
6.2.2 Warehouse with Storage Racking (no DSF) 179
6.2.3 Error Analysis 181
6.3 Validation of Computational Model 182
6.3.1 Small-Scale Empty Warehouse Model 182
6.3.2 Small-Scale Warehouse with Storage Racking 183
6.4 Stratification Modelling of a Full-Scale Warehouse 185
6.4.1 Challenges with Thermal Scaling 185
6.4.2 Empty versus Storage Racking 186
6.5 Chapter Summary 189
7. Combined Wind- and Buoyancy-Driven Ventilation, Thermal and Energy Performance of a Double Skin Façade Warehouse 191
7.1Chapter Introduction 192
7.2Analytical Validation of Cross-Ventilation in Warehouses 193
7.2.1 Cross-Ventilation and Climate Scenario 193
7.2.2 Analytical Results 194
7.2.3 Validation of Computational Model 195
7.3Wind and Buoyancy Modelling of a DSF Warehouse 197
7.3.1 Thermal Performance of a Fully Open DSF Warehouse 198
7.3.2 Ventilation Performance of a Fully Open DSF Warehouse 201
7.4Optimisation of the Seasonal-Adaptive and Inlet Openings 205
7.4.1 The Inverse Relationship Between Airflow Rate and Heating 206
7.4.2 Airflow and Temperature Distribution Within The Cavity 207
7.4.3 Using the Continuity Equation to Optimise the DSF Inlet Dimensions 208
7.5Combined Wind and Buoyancy Analytical Tool 210
7.5.1 Using CFD-Derived Values to Calculate Heat Gain/Removal 211
7.6Energy Performance Assessment of the DSF Warehouse 212

7.6.1 Energy Benchmarks for the Case Study Warehouse 213
7.6.2 Normalised Annual Energy Performance of the DSF 213
7.6.3 Embodied Energy and Payback Period 214
7.7Chapter Summary 216
8. Conclusions 219
8.1 Summary of Key Findings 220
8.2 Contribution to Knowledge and Research Impact 222
8.3 Future Research and Closing Remarks 223
References 224
Appendix 238
A.1 Contextual Warehouse Benchmark Calculations 238
A.2 Vertical Solar Irradiance Calculations 239
A.3 Wind-Only Scenario Data Collection and Calculations 240
A.4 Buoyancy-Only Scenario Data Collection and Calculations 250
A.5 Stratification Data Collection and Calculations 253
A.6 Combined Wind and Buoyancy Data Collection and Calculations 254
A.7 Appendix References 261

List of Equations

Chapter 1
Equation 1.1 *Outside Surface Heat Balance* *7*
Equation 1.2 *Inside Surface Heat Balance* *7*
Equation 1.3 *Bernoulli's Principle* *13*
Equation 1.4 *Volume Flow Rate* *14*
Equation 1.5 *Wind Pressure Drop for a Double Skin Facade* *14*
Equation 1.6 *Buoyancy Pressure Drop for a Double Skin Facade* *14*
Equation 1.7 *Combined Wind and Buoyancy Pressure Drop for a Double Skin Facade* *14*
Equation 1.8 *Dynamic U-value for a Double Skin Facade* *15*
Equation 1.9 *Heat Generation in a Double Skin Façade Cavity* *15*
Chapter 3
Equation 3.1 *Local Wind Speed* *86*
Equation 3.2 *Vertical Solar Irradiance* *87*
Equation 3.3 *Building Reynolds Number* *89*
Equation 3.4 *Pressure Coefficient* *90*
Equation 3.5 *Frictional Pressure Loss* *90*
Equation 3.6 *Buoyancy Pressure for a Double Skin Facade* *96*
Equation 3.7 *Buoyancy Velocity for a Double Skin Facade* *96*
Equation 3.8 *Buoyancy Volumetric Flow Rate for a Double Skin Facade* *96*
Equation 3.9 *Buoyancy Mass Flow Rate for a Double Skin Facade* *96*
Equation 3.10 *Buoyancy Heat Gain for a Double Skin Facade* *96*
Equation 3.11 *Thermal Resistance of Inner Skin (Cladding)* *97*
Equation 3.12 *Thermal Resistance of Outer Skin (Aluminium)* *97*
Equation 3.13 *Reynolds Number for DSF Cavity* *97*
Equation 3.14 *Nusselt Number for DSF Cavity* *97*
Equation 3.15 *Convective Heat Transfer Coefficient* *97*
Equation 3.16 *Thermal Resistance of Air* *97*
Equation 3.17 *Total Thermal Resistance of DSF Cavity* *98*
Equation 3.18 *U-Value of DSF System* *98*
Equation 3.19 *Fractional Error from Measured Value* *103*
Equation 3.20 *Fractional Error from Full Scale Value* *103*
Equation 3.21 *Absolute Error of Anemometers* *104*
Equation 3.22 *Absolute Error of Heat Flux Meters* *104*
Equation 3.23 *Absolute Error of Pyranometer* *104*
Equation 3.24 *Combined Absolute Error* *104*
Equation 3.25 *Final Absolute Error* *105*
Equation 3.26 *Compounded Fractional Error* *105*

Equation 3.27	*Standard Deviation*	*105*
Equation 3.28	*The Continuity Equation (Mass Conservation)*	*106*
Equation 3.29	*The Motion Equation (Momentum Conservation)*	*106*
Equation 3.30	*Turbulent Kinetic Energy*	*106*
Equation 3.31	*Energy Dissipation Rate*	*106*
Equation 3.32	*Boussinesq Model*	*111*
Equation 3.33	*Boussinesq Approximation*	*111*
Equation 3.34	*Validity of Boussinesq Approximation*	*111*
Equation 3.35	*Heat Generation Rate*	*112*
Chapter 4		
Equation 4.1	*Small Scale Model Reynolds Number*	*129*
Equation 4.2	*Wind Pressure for a Double Skin Facade*	*140*
Equation 4.3	*Volumetric Flow Rate for a Double Skin Façade (Wind-Only)*	*140*
Equation 4.4	*Outdoor Air Ventilation (Wind-Only)*	*140*
Chapter 5		
Equation 5.1	*Thermal Gradient*	*150*
Chapter 6		
Equation 6.1	*Grashof Number*	*178*
Chapter 7		
Equation 7.1	*Pressure Difference across Inlet and Outlet*	*194*
Equation 7.2	*Wind velocity Pressure for Cross-Ventilation*	*194*
Equation 7.3	*Density Changes in Buoyancy Pressure*	*195*
Equation 7.4	*Buoyancy Pressure for Cross-Ventilation*	*195*
Equation 7.5	*Combined Wind and Buoyancy Pressure for Cross-Ventilation*	*195*
Equation 7.6	*Volumetric Flow Rate for Cross-Ventilation*	*195*
Equation 7.7	*Volumetric Flow Rate from CFD Model*	*196*
Equation 7.8	*Continuity Equation*	*209*
Equation 7.9	*Calculated Volumetric Flow Rate (Continuity)*	*209*
Equation 7.10	*Calculated Air Velocity at Inlet Opening to Warehouse*	*209*
Equation 7.11	*Combined Wind and Buoyancy Pressure for DSF*	*210*
Equation 7.12	*Payback Period*	*216*

List of Tables

Chapter 1		
Table 1.1	*Review of Solar-assisted Façade Technology*	*9*
Table 1.2	*Benefits and Limitations of Natural Ventilation Models*	*17*
Chapter 2		
Table 2.1	*Recreated Double Skin Façade Typology*	*25*
Table 2.2	*Climate Classification and Location of DSF Systems*	*32*
Table 2.3	*Building Type, DSF Typology and Ventilation Mode*	*41*
Table 2.4	*Impact of DSF Cavity Geometry on Airflow Rate and Cavity Air Temperature*	*49*
Table 2.5	*Impact of Material Layers and Blinds on DSF Ventilation and Thermal Performance*	*56*
Table 2.6	*Energy Performance of BIPV-DSF Systems*	*67*
Table 2.7	*Impact of DSF integration with HVAC systems or passive heating or cooling techniques on building energy savings*	*68*
Table 2.8	*Impact of DSF Systems on Occupancy Comfort*	*76*
Table 2.9	*LCA Results for DSF Typology, Climate and Building Application*	*80*
Chapter 3		
Table 3.1	*Case Study Warehouse Information*	*83*
Table 3.2	*Terrain-dependent Values for Wind Profiles*	*87*
Table 3.3	*Seasonal Vertical Irradiance for All Seasons*	*88*
Table 3.4	*Wind Tunnel Model Details*	*91*
Table 3.5	*Wind Tunnel Measurement Variables and Equipment*	*93*
Table 3.6	*Climate Chamber Experiment Equipment*	*101*
Table 3.7	*Dimensions of Storage Racking and Heat Mats*	*103*
Table 3.8	*Combined Absolute Errors for Different Measurement Types*	*104*
Table 3.9	*Final Absolute Errors for Different Measurement Types*	*105*
Table 3.10	*Mesh Generation for Wind and Buoyancy Models*	*110*
Table 3.11	*Boussinesq Parameters for Each Season*	*112*
Chapter 4		
Table 4.1	*Average Façade Differential Pressure for Wind Angles 0 and 180 Degrees*	*119*
Table 4.2	*CFD Comparison of Average Façade Cp for Wind Angles 0 and 180 Degrees*	*123*
Table 4.3	*Error Between CFD and Experimental Data for Different Wind Shear Exponents*	*128*
Table 4.4	*Error Between Cp for Small-scale and Full-scale Dynamic Similarity Test*	*131*

Table 4.5	*Pressure Coefficients for DSF Outer and Inner Skins in Different Seasons*	*133*
Table 4.6	*Neutral Pressure Heights for Different Seasons*	*136*
Table 4.7	*Average Velocity at Inlet and Occupant Heights for Warehouse Only*	*139*
Table 4.8	*Average Velocity at Inlet and Occupant Heights for Fully Open DSF*	*139*
Table 4.9	*Outdoor Air (Wind-Only) Delivered from the DSF in Different Seasons*	*140*
Chapter 5		
Table 5.1	*Lighting Array Combinations and Resulting Heat Flux Values*	*147*
Table 5.2	*Impact of DSF Inlet Area on Cavity Velocity*	*149*
Table 5.3	*Fractional Errors for Climate Chamber Test Equipment*	*151*
Table 5.4	*Mesh Quality for CFD Model of DSF Prototype*	*157*
Table 5.5	*Error Between Original Experimental Data and CFD Mesh Tests*	*159*
Table 5.6	*Pre-Heating Capacity of DSF Prototype in Winter and Intermediate Seasons*	*161*
Table 5.7	*Ventilation Capacity of DSF Prototype in Winter and Intermediate Seasons*	*164*
Table 5.8	*Ventilation Capacity of Full-Scale DSF Prototype in All Seasons*	*165*
Table 5.9	*Pre-Heating/Cooling Capacity of Full-Scale DSF Prototype in All Seasons*	*167*
Table 5.10	*Values Required to Calculate DSF Energy Savings in All Seasons*	*169*
Table 5.11	*Cavity Velocity, Mass Flow and Volumetric Flow Rate (Analytical and CFD)*	*169*
Table 5.12	*Values Required to Calculate DSF Retrofit Dynamic U-Value in All Seasons*	*170*
Table 5.13	*Reynolds, Nusselt, CHTC, Thermal Resistances and New U-Values for All Seasons*	*170*
Chapter 6		
Table 6.1	*Temperature Data for Three Different Measurement Points (7W Heat Mat)*	*177*
Table 6.2	*Temperature Gradients for 1:50 Scale Warehouse Model*	*177*
Table 6.3	*Parameters Required to Calculate Gr Number (7W Heat Mat)*	*178*
Table 6.4	*Temperature Data for the Empty and Storage Racking Model (20W Heat Mat)*	*179*
Table 6.5	*Temperature Gradients for 1:50 Scale Warehouse Model With and Without Storage Racking*	*180*
Table 6.6	*Parameters Required to Calculate Gr Number (20W Heat Mat)*	*180*
Table 6.7	*Air Velocity at Different Heights for an Empty Warehouse and With Storage Racking*	*188*
Chapter 7		
Table 7.1	*Coldest Month Meteorological Scenario*	*194*
Table 7.2	*Pressure Difference across Inlet and Outlet*	*194*
Table 7.3	*Wind Velocity Pressure for Cross-Ventilation*	*194*
Table 7.4	*Buoyancy Pressure for Cross-Ventilation*	*195*
Table 7.5	*Combined Pressure Drops and Volumetric Flow Rate for Cross-Ventilation*	*195*
Table 7.6	*Comparison of Volumetric Flow Rates from Analytical and CFD Models*	*196*
Table 7.7	*Cavity Temperature at Height of Inlet to Warehouse*	*201*
Table 7.8	*Outdoor Air Delivery at Height of Inlet to Warehouse*	*203*
Table 7.9	*Comparison of Cp with CIBSE Data [8]*	*205*
Table 7.10	*Optimal DSF Heat Mode and Inlet Opening*	*208*
Table 7.11	*Optimised Area of Inlet Opening to Warehouse*	*209*
Table 7.12	*Combined Pressure for all DSF Seasonal Configurations*	*210*
Table 7.13	*Heat Gain/Removal for all DSF Seasonal Configurations*	*211*
Table 7.14	*Case Study Warehouse Energy and Carbon Consumption*	*213*
Table 7.15	*Annual Energy, Financial, and Carbon Savings of the DSF Retrofit*	*213*
Table 7.16	*Typical Carbon Costs of DSF Materials*	*215*
Table 7.17	*Cost Breakdown of Proposed DSF Retrofit*	*215*

List of Figures

Chapter 1		
Figure 1.1	*Warehouse Occupancy by Savills Research*	*3*
Figure 1.2	*Monthly Covid-19 Case Rate per 100,000 by Occupational Sector*	*4*
Figure 1.3	*Difference in Rooflight Regulations on Available Roof Space*	6
Figure 1.4	*Outside and Inside Surface Heat Balance*	*7*
Figure 1.5	*Heating and Cooling Operation of SolarWall*	*11*
Figure 1.6	*Schematic of Proposed Double Skin Façade System*	*13*
Figure 1.7	*Overview of Natural Ventilation Modelling Techniques*	*16*
Figure 1.8	*(a)LHS and (b)RHS "Seasonal-Adaptive" Openings Concept for the Double Skin Façade*	*19*
Figure 1.9	*Parallel Research Process*	*20*
Chapter 2		
Figure 2.1	*(a) DSF Cavity Partitioning Configurations and (b) Ventilation Modes*	*26*
Figure 2.2	*Heat Transfer in Outdoor Air Curtain Box-Window DSF*	*27*
Figure 2.3	*PRISMA Process*	*28*
Figure 2.4	*Factors affecting the Viability of a DSF System*	*29*
Figure 2.5	*Trend Analysis of (a) Climate and (b) Seasons*	*31*
Figure 2.6	*Trend Analysis of (a) Building Type and (b) DSF Orientation*	*39*
Figure 2.7	*Trend Analysis of DSF Type and Ventilation Mode*	*40*

Figure 2.8	*Trends in Focus of DSF Construction*	*54*
Figure 2.9	*(a) HVAC and Heat Recovery Capability and (b) Energy Generation or Savings*	*66*
Figure 2.10	*Trend Analysis of Emerging Topics in DSF Research*	*72*
Figure 2.11	*Trend Analysis of LCA Subject Focus*	*76*
Figure 2.12	*(a) DSF Research Methodology Breakdown and (b) Validation Methods*	*78*
Chapter 3		
Figure 3.1	*Case Study Warehouse*	*83*
Figure 3.2	*Pedestrian Walkways Between Storage Racking*	*84*
Figure 3.3	*Proposed Cross Ventilation Flow Path in Double Skin Façade Warehouse*	*85*
Figure 3.4	*Nottingham Wind Rose*	*86*
Figure 3.5	*(a)DSF Warehouse and (b) DSF Orthographic Views*	*90*
Figure 3.6	*(a)DSF Warehouse in ABL Wind Tunnel and (b)Pressure Tap Locations*	*92*
Figure 3.7	*ABL Wind Tunnel at University of Nottingham*	*92*
Figure 3.8	*Semi-urban Spires and Blocks (a) Dimensions and (b) Real Set-Up*	*93*
Figure 3.9	*Pitot Tube and Reference Measurement Location*	*94*
Figure 3.10	*Energy Flows of Opaque and Transparent Insulated Walls*	*98*
Figure 3.11	*Experimental Prototype of the Opaque Aluminium Double Skin Facade*	*99*
Figure 3.12	*Environmental Chamber at University of Nottingham*	*100*
Figure 3.13	*Set-Up of (a)Heat Mats and (b)Storage Racking for Stratification Tests*	*102*
Figure 3.14	*CFD Geometry for (a)1:50 and (b)Full-Scale DSF Warehouse and Domain*	*107*
Figure 3.15	*CFD Geometry for (a)3D Front and (b)2D Side View of DSF Prototype*	*108*
Figure 3.16	*CFD Geometry for (a)3D Front and (b)2D Side View of Full-Scale DSF*	*108*
Figure 3.17	*CFD Geometry for (a)Heat Mats and (b)Storage Racking for Stratification*	*109*
Chapter 4		
Figure 4.1	*Heat Recovery and Removal Operation of a DSF*	*116*
Figure 4.2	*Preliminary Wind Profile with Wind Shear Exponent of 0.18*	*117*
Figure 4.3	*Differential Pressure Distribution on DSF for Changing (a) Wind Speeds and (b) Angles*	*118*
Figure 4.4	*Differential Pressure Distribution on Warehouse Roof for Changing Wind Angles*	*120*
Figure 4.5	*Uncertainty in Average Differential Pressure Measurements for 5m/s at 0 degrees*	*121*
Figure 4.6	*Comparison of Experimental and CFD Cp for All Facades (a) 0 and (b) 180 degrees*	*122*
Figure 4.7	*Comparison of Experimental and CFD Cp for DSF Outer Skin (a) 0 and (b) 180 degrees*	*124*
Figure 4.8	*Grid Independence Test Results*	*125*
Figure 4.9	*Sensitivity Analysis of Turbulence Models*	*126*
Figure 4.10	*Wind Profiles with Different Wind Shear Exponents*	*127*
Figure 4.11	*Visual of Model Wind Blockage*	*128*
Figure 4.12	*Velocity Vector Contours for (a) 1:50 and (b) Full-Scale Models*	*130*
Figure 4.13	*Pressure Contours for (a) 1:50 and (b) Full-Scale Models*	*131*
Figure 4.14	*Wind Profile for Full-Scale Models (a=0.22)*	*132*
Figure 4.15	*Schematic of Windward DSF Facades*	*133*
Figure 4.16	*Schematic of Vertical Data Collection Points across DSF Cavity Length*	*133*
Figure 4.17	*DSF Velocity Profiles for (a) January (7.22m/s), (b) April (4.72m/s), (c), July (7.78m/s) and (d) October (3.6m/s).*	*134*
Figure 4.18	*Position of External and Internal Pressure Measurements*	*135*
Figure 4.19	*Vertical External and Internal Pressures for (a) January, (b) April, (c) July and (d) October*	*136*
Figure 4.20	*Outdoor Air Rates for the Warehouse, Fully Open DSF and Different Openings per Season*	*137*
Figure 4.21	*Schematic of Inlet Opening Height versus Occupant Level*	*138*
Chapter 5		
Figure 5.1	*Schematic of (a) LHS and (b) RHS "Seasonal-Adaptive" Openings in the Double Skin Facade*	*144*
Figure 5.2	*(a) Experimental Lamp Array and (b) Heat Flux Measurement Locations*	*146*
Figure 5.3	*Distribution of Irradiance on Experimental DSF Prototype*	*147*
Figure 5.4	*Average Cavity Velocity for Different DSF Inlet Configurations and Seasons*	*148*
Figure 5.5	*Relationship Between External Design Temperature and DSF Cavity Temperature*	*149*
Figure 5.6	*Average Cavity Temperature for Different DSF Inlet Configurations and Seasons*	*150*
Figure 5.7	*Thermal Gradients for Different DSF Inlet Configurations and Seasons*	*151*
Figure 5.8	*Standard Deviation for (a) Anemometers, (b) Heat Flux Meters and (c) PT100 RTDs*	*152*
Figure 5.9	*Adapted Geometry for Preliminary CFD Validation from Mei. et al.*	*153*
Figure 5.10	*Comparison of Mei. et al. to CFD Model for (a) Velocity and (b) Temperature*	*154*
Figure 5.11	*Contours of (a) Velocity, (b) Temperature, and (c) Velocity Vector*	*155*
Figure 5.12	*Location of Experimental Measurements of Temperature and Velocity*	*156*
Figure 5.13	*Comparison of Original Experimental Data with CFD model for (a) Velocity and (b) Temperature*	*156*
Figure 5.14	*Grid Sensitivity Analysis of CFD Model versus Experimental Data for (a) Velocity and (b) Temperature*	*158*
Figure 5.15	*Turbulence Model Sensitivity Analysis versus Experimental Data*	*159*
Figure 5.16	*Diagram of CFD Measurement Points in (a) Cavity and (b) Outlet*	*160*
Figure 5.17	*Vertical Cavity Temperature Profiles for (a) Winter and (b) Intermediate Seasons*	*161*
Figure 5.18	*Vertical Cavity Temperature Contours for (a) Winter and (b) Intermediate Seasons*	*162*

Figure 5.19	*Vertical Cavity Velocity Profiles for (a) Winter and (b) Intermediate Seasons*	*162*
Figure 5.20	*Vertical Cavity Velocity Contours for (a) Winter and (b) Intermediate Seasons*	*163*
Figure 5.21	*Position of 21 Measurements Points for Full-Scale DSF Outlet*	*164*
Figure 5.22	*Velocity Distribution at DSF Outlet Across 21 points for All Seasons*	*165*
Figure 5.23	*Velocity Contours of Full-Scale DSF for (a) Winter, (b) Intermediate and (c) Summer Seasons*	*165*
Figure 5.24	*Temperature Distribution Across 21 Measurement Points at DSF Outlet for All Seasons*	*168*
Figure 5.25	*Temperature Contours of Full-Scale DSF for (a) Winter, (b) Intermediate and (c) Summer Seasons*	*168*
Figure 5.26	*Comparison of Heat Loss through Warehouse Façade and DSF Retrofit*	*171*
Chapter 6		
Figure 6.1	*Cross-Ventilation Openings in the Case Study Warehouse (a) Empty and (b) Storage Racking*	*176*
Figure 6.2	*Vertical Temperature Distribution in 1:50 Scale Warehouse Model*	*177*
Figure 6.3	*Vertical Temperature Distribution in 1:50 Scale Warehouse Model With and Without storage racking*	*179*
Figure 6.4	*Standard Deviation Analysis of PT-100 RTDs in Stratification Tests*	*181*
Figure 6.5	*Comparison of Experimental to CFD Temperature Data in 1:50 Scale Warehouse*	*182*
Figure 6.6	*Contours of (a) Temperature and (b) Velocity Vectors of 1:50 Scale Empty Warehouse*	*183*
Figure 6.7	*Comparison of Experimental to CFD Temperature Data in 1:50 Scale Warehouse With Storage Racking*	*184*
Figure 6.8	*Contours of (a) Temperature and (b) Velocity Vectors of 1:50 Scale Warehouse With Storage Racking*	*184*
Figure 6.9	*Temperature Mid-Section Contour of Full-Scale Warehouse (20W Heat Mat)*	*186*
Figure 6.10	*Vertical Temperature Profiles for (a) Empty and (b) Storage Racking Full-Scale Warehouse Models*	*186*
Figure 6.11	*Pressure Contours for (a) Empty and (b) Storage Racking Full-Scale Warehouse Models*	*187*
Figure 6.11	*Velocity Vector Contours for (a) Empty and (b) Storage Racking Full-Scale Warehouse Models*	*188*
Chapter 7		
Figure 7.1	*Diagram of Cross-Ventilation Scenario*	*193*
Figure 7.2	*Location of Nine Measurement Points in CFD Cross-Ventilation Model*	*196*
Figure 7.3	*Contours of (a) Velocity Vector and (b) Temperature for the Cross-Ventilated Warehouse*	*197*
Figure 7.4	*DSF Warehouse Measurement Point Locations with (a) Heating and (b) Cooling Configurations*	*198*
Figure 7.5	*DSF Vertical Cavity Profiles of Temperature for (a) Winter, (b) Spring, (c) Summer, and (d) Autumn*	*199*
Figure 7.6	*Temperature Contours of the DSF Cavity for (a) Winter, (b) Spring, (c) Summer, and (d) Autumn*	*200*
Figure 7.7	*DSF Vertical Cavity Profiles of Velocity for (a) Winter, (b) Spring, (c) Summer, and (d) Autumn*	*202*
Figure 7.8	*Velocity Vectors of the DSF Cavity for (a) Winter, (b) Spring, (c) Summer, and (d) Autumn*	*203*
Figure 7.9	*Wind Direction with Labelled Facades of DSF and Warehouse*	*204*
Figure 7.10	*Key for DSF Inlet Configurations and Warehouse Inlet Openings*	*206*
Figure 7.11	*Relationship Between Airflow Rate and Heating for (a) Winter, (b) Spring, (c) Summer, and (d) Autumn*	*206*
Figure 7.12	*Average Velocity and Temperature for Different Openings in (a) Winter, (b) Spring, (c) Summer, and (d) Autumn*	*207*
Figure 7.13	*Magnitude of Heat Gain/Removal in DSF Cavity for different Seasonal-Adaptive Openings*	*212*
Figure 7.14	*Annual Energy Savings from the Fully Open Double Skin Facade*	*214*

Nomenclature and Abbreviations

Symbols	
U	U-value
h	Convective heat transfer coefficient
A	Area
d	Thickness
k	Thermal conductance
T	temperature
$\dot{m}$	Mass flow rate
ρ	Density
V/U/v	Velocity
Q	Volumetric flow rate
Cd	Discharge coefficient
ΔP	Pressure drops
g	Gravitational accelerations
z	Height
Cp	Pressure coefficient
h_L	Darcy's friction loss
f	Friction factor

L	Length
D	Hydraulic diameter
$\in/D$	Relative roughness
Re	Reynolds number
μ	Viscosity
∂_{met}	Layer thickness
a	Wind shear exponent
$S_{vertical}$	Vertical solar irradiance
GHI	Global horizontal irradiance
$alpha$	Sun elevation angle
$beta$	Wall tilt angle
psi	Wall azimuth
$theta$	Sun azimuth
P_s	Static pressure
P_R	Reference pressure
K_L	Length scale ratio
Nu	Nusselt number
R	Thermal resistance
x_i	Individual measurements
N	Number of measurements
$\frac{\partial \rho}{\partial t}$	Rate of change of density with respect to time
(ρu)	Mass flux
$\frac{\partial (\rho u)}{\partial t}$	Rate of change of momentum with respect to time
$(\rho u u)$	Momentum
$-\nabla p$	Pressure gradient
ρg	Body force
$(\mu \nabla u)$	Diffusion of momentum
τ_t	Divergence of turbulence stress
$\frac{\partial (\rho k)}{\partial t}$	Rate of change of turbulent kinetic energy with respect to time
$(\rho k u)$	Convective transport of turbulent kinetic energy
α_k	Coefficient related to Prandtl number
$\mu_{eff} \nabla k$	Effective viscosity
G_k	Source of turbulent kinetic energy due to average velocity gradient
G_b	Source of turbulent kinetic energy due to buoyancy force
$\frac{\partial (\rho \varepsilon)}{\partial t}$	Rate of change of energy dissipation with time
$\nabla(\rho \varepsilon u)$	Convective transport of energy dissipation
$C_{1\varepsilon}, C_{2\varepsilon}, C_{3\varepsilon}$	Empirical constants used in turbulence modelling
$\frac{\varepsilon}{k}$	Term relating dissipation to production
$\rho \frac{\varepsilon^2}{k}$	Rate at which energy is dissipated
∇T	Thermal gradient
Gr	Grashof number
β	Expansion coefficient of air

Abbreviations

UK	United Kingdom
UKWA	United Kingdom Warehouse Association
CIBSE	Chartered Institute of Building Services Engineers
IAQ	Indoor air quality
EMG	Environmental Modelling Group
NV	Natural ventilation
NREL	National Renewable Energy Laboratory
IEA	International Energy Agency
HVAC	Heating, ventilation and air-conditioning
TSC	Transpired Solar Collector
SC	Solar Chimney
TW	Trombe Wall
DSF	Double skin facade
US	United States
BSRIA	Building Services Research and Information Association
EEBPP	Energy Efficiency Best Practice Programme
RANS	Reynolds-Averaged Navier Stokes
AFN	Airflow Network

CFD	Computational Fluid Dynamics
RIBA	Royal Institute of British Architects
PRISMA	Preferred Reporting Items for Systematic Reviews and Meta-analyses
IBM	International Business Machines
SBS	Sick Building Syndrome
AHU	Air Handling Unit
BBRI	Belgian Building Research Institute
WWR	Window-to-wall ratio
SHGC	Solar Heat Gain Coefficient
MV	Mechanical ventilation
CO_2	Carbon dioxide
VO_2	Vanadium dioxide
NVDSF	Naturally ventilated double skin facade
UAE	United Arab Emirates
CRFS	Climate Responsive Façade System
SSF	Single Skin Facade
ATF	Active Transparent Façade
SC	Shading Coefficient
ETTV	Envelope Thermal Transfer Value
DSPF	Double-skin Perforated Façade
MVDSF	Mechanically Ventilated Double Skin Façade
HSCW	Hot Summer Cold Winter
PV	Photovoltaic
PVB-DSF	Photovoltaic Blind Double Skin Facade
PCM	Phase Change Material
SFDU	Smart Façade Demo Unit
ANN	Artificial Neural Network
BIPV	Building Integrated Photovoltaics
STPV DSF	Semi-Transparent Photovoltaic Double Skin Facade
CdTe	Cadmium Telluride
PV-IGU	Photovoltaic Insulating Glass Units
CHTC	Convective Heat Transfer Coefficient
PDSF	Pipe-embedded Double Skin Façade
PMV	Predicted Mean Value
VOC	Volatile Organic Compounds
BTEX	Benzene, Toluene, Ethylbenzene and Xylene
STL	Sound Transmission Loss
BMS	Building Management System
NPV	Net Profit Value
IRR	Internal Rate of Return
ECC	Energy Carbon Cost
LCA	Life Cycle Analysis
GHG	Greenhouse Gases
BES	Building Energy Simulation
GIA	Gross Internal Area
GEA	Gross External Area
ASHRAE	American Society of Heating, Refrigerating and Air-conditioning Engineers
ABL	Atmospheric Boundary Layer
UoN	University of Nottingham
RTD	Resistance Temperature Detector
RNG	Renormalization Group
NPH	Neutral Pressure Height
LHS	Left-hand side
RHS	Right-hand side
EWT	Enhanced Wall Treatment

Units	
Sq. ft	Square feet
TWh	Terra Watt hours
kWh	Kilo Watt hours
L/s/person	Litres per second per person
ACH	Air changes per hour
m^3	Metres cubed
kWh/m^2	Kilo Watt hours per metre squared
MWh	Mega Watt hours
m	metre
^oC	Degrees Celsius

kW	Kilowatts
m^3/h	Metres cubed per hour
W/m^2	Watts per metre squared
cm	Centimetres
mm	Millimetres
m/s	Metres per second
º	Degree
Wh/m^2day	Watt-hours per metres squared per day
$kWhth/m^2/day$	Kilowatt hours (thermal) per metres square per day
K	Degrees Kelvin
tCO_2	Tonnes of Carbon Dioxide
CO_2eq	Carbon Dioxide equivalent
gCO_2	Grams of carbon dioxide
V	Volts
mV	Millivolts
kg/m^3	Kilograms per metres cubed
W/m^3	Watts per metres cubed
Pa	Pascals
L/s	Litres per second
m^3/s	Metres cubed per second
£	Great British pounds
kgCO2	Kilograms of carbon dioxide

Chapter 1

Introduction

1.1 Storage and Distribution Warehouses – A Neglected Building Type

Over the past couple of decades, there have been continuous efforts to improve the energy consumption of the built environment. This has translated to government-backed outcomes such as improved insulation and double-glazing in residential properties, or the widespread application of renewable technologies such as photovoltaics and wind turbines. The focus of these measures is generally for buildings where occupants spend most of their daily lives – work, school, and home. However, following global events such as the Covid-19 pandemic and Brexit, the landscape of the UK built environment is changing rapidly in response to an ever-expanding industrial logistics sector to facilitate the modern demand for e-commerce. With buildings expected to consume 30% more energy relative to today's level by 2060, building engineers must look to the future of the built environment rather than the past [1].

This thesis details the development of a new computational fluid dynamics (CFD) tool capable of assessing the integrated ventilation, thermal and energy performance of a seasonal-adaptive double skin façade retrofit for storage and distribution warehouses in the UK. Several key research gaps in existing literature are addressed and the proposed double skin facade and computational tool are developed tool through a three-stage experimental validation. The building technology developed in this thesis highlights a potential low-energy solution for providing passive pre-heating, cooling and ventilation to the large singular thermal zones in warehouses. The ventilation and thermal results of the building physics modelling suggest that regulation and design guidelines regarding the internal environments of warehouses require an update.

In the following sections, the background of warehouses and façade technologies will be discussed, along with the theory behind the CFD energy performance tool and novelty highlights of the opaque aluminium double skin façade. This chapter is concluded by an overview of the research scope and objectives, and the parallel research process.

1.1.1 The Energy Consumption of Warehouses

One distinct example of a somewhat neglected building type in both engineering research and industrial building regulations is the rapidly evolving commercial warehouse sector which has seen an exponential growth of building square footage in the past decade, accelerated even further by recent events.

The 2021 United Kingdom Warehouse Association (UKWA) report highlighted that both Brexit and the global pandemic have contributed to a boom in e-commerce and home delivery [2]. To facilitate this, research conducted by Prologis as part of this report indicates that for every extra £1 billion spent online, a further 775,000 square feet of warehouse space is needed to meet the new demand [3]. Since 2015, there has been a 32% overall rise in the number of warehousing units, and online retailers have increased warehouse occupancy by a massive 614%. Figure 1.1 illustrates these trends.

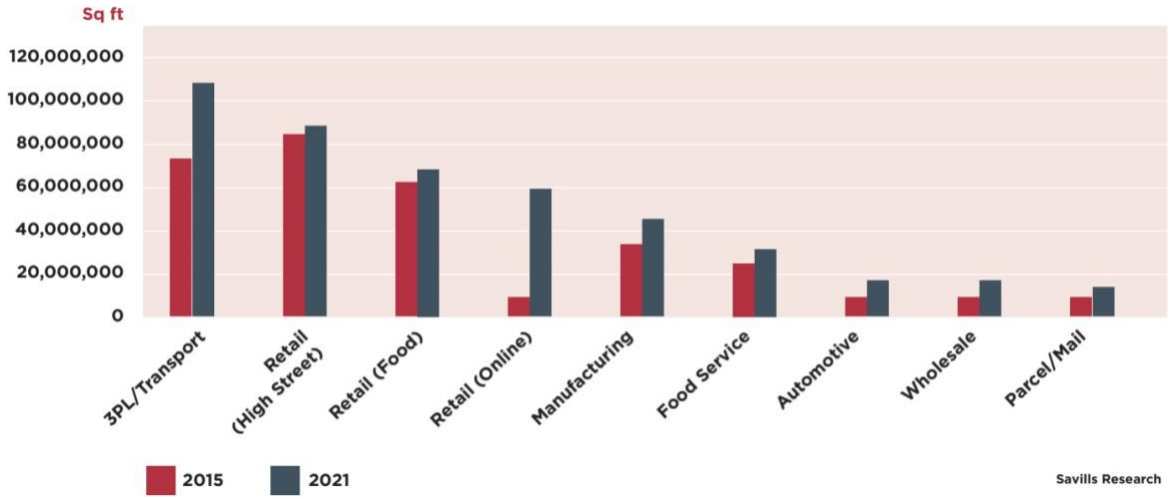


Figure 1.1 Warehouse occupants and size by Savills Research [3]

To highlight the importance of shifting research, focus from traditional building applications to those in demand, the average sized warehouse unit in 2020 was just under 32,000sq.m. which in terms of total annual electricity consumption is just under 1.6 Terra-Watt hours (TWh) based on a benchmark provided by the Chartered Institute of Building Services Engineers (CIBSE) [4]. If the average UK home uses 3,940 kilo-Watt hours (kWh) of electricity per year, then one averaged-size warehouse unit has the same electrical energy consumption as 400 British households [5]. Whilst the annual electricity consumption of warehouses might only represent 1% of the total annual electricity consumption in the UK as of 2021 (293 TWh), on a local and regional level this has important ramifications in the light of increased residential energy bills, and cost of living crisis. It should also be noted that the benchmark energy consumption for a storage and distribution warehouse from CIBSE is likely outdated as it classifies the size of the building to be 7.5m which is a lot smaller than the average-size unit today of 11m, so it is likely that the value used here is an underestimation [6].

Research conducted by Cushman estimates that the U.K. has warehouses covering a total of around 53 million sq. m., and that there may already be less than 5 million sq. m. of available warehouse space left because of the current demand [7]. Regarding losses, air

infiltration contributes as much as 30% of heat loss in industrial buildings, including warehouses [8]. This highlights that with larger warehouses, there will not only be greater consumption but also greater losses. These findings indicate that the Class B8 storage and distribution classification of warehouses is perhaps the fastest growing building type within the UK built environment, and as a result, there needs to be a new focus on how warehouses consume and utilise energy.

1.1.2 The Internal Environment and Conditions of Warehouses

Another important aspect to consider with warehouses is the present lack of building regulations surrounding the control of indoor environments from both a thermal comfort and indoor air quality (IAQ) perspective. For example, the Chartered Institute of Building Services Engineers (CIBSE) has very little detail on design criteria for warehouses in Guide A, with no recommended ventilation requirements per person, and no real design set point conditions for heating and cooling [8]. Whilst it can be argued that a warehouse might not need ventilation, or a distinct heating or cooling system, recent studies that have come from examining the spread of the coronavirus found that outbreaks were more common in open-plan spaces, with high occupancy density in certain areas [9]. A 2021 study by the Environmental Modelling Group (EMG) on the Covid-19 transmission risk by occupation and workplace reinforces this need for new building regulations as it identified that warehouses were the only sector not to see a decline in case rates after the November lockdown in the UK, and instead showed an increase over time [10], as illustrated in Figure 1.2. The occupational case rate is defined by a calculation using workplace data reporting cases of Covid-19 and taking denominators from Office for National Statistics (ONS) data.

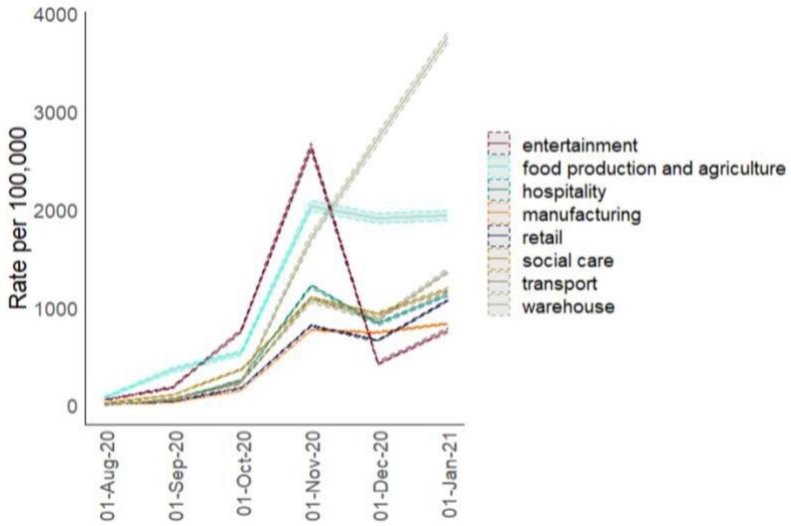


Figure 1.2 Monthly Covid-19 Case Rate per 100,000 by Occupational Sector [10]

Airborne disease is not the only motive for sufficient ventilation in warehouses as there could be other contamination sources such as exhaust fumes from lorries at loading bay doors, or chemicals and particulates in the stored goods which could range from perishable food and drink to electronics, clothes, and many more.

The difficulty surrounding natural ventilation building regulations for warehouses is the varied recommendations. For example, whilst there are no specific ventilation requirements for occupants in a warehouse, CIBSE Guide A and Approved Document F recommend 10L/s/person, which is dependent on the number of occupants [8], [11]. However, CIBSE AM10 states that if natural ventilation (NV) is to be adopted, then the system must be able to provide controllable ventilation rates across a wide range, from say 0.5 to 5ACH [12]. Air changes per hour is dependent on the volume of the space. For example, if there are 20 workers in a warehouse of volume 10,000m^3, then the minimum outdoor air requirement is 200L/s. In terms of ACH, this is 0.072ACH which does not meet the minimum requirements for an effective natural ventilation system. For perspective, to achieve 0.5ACH and 5ACH, this is equivalent to outdoor air requirements for 139 people, and 1389 people at 10L/s/person, respectively (calculations in the Appendix, Section A.1.1). Furthermore, ACH might not be the best metric for designing ventilation systems in warehouses specifically as it determines how often air is exchanged in a space but is not necessarily the best indicator that ventilation demands are met. Volumetric flow rates, on the other hand, might be more applicable to large and tall ceiling spaces as they are better suited to assess the capacity of the ventilation system and that the right volume of air is provided to ensure outdoor air is circulating the entire space.

Overall, this presents a snapshot of the state of the warehouse sector which indicates that changes need to be implemented to regulate energy consumption of the fastest growing building type in the UK. New ventilation strategies and regulations are needed to ensure warehouse occupant wellbeing is maintained. The next section 1.1.3 explores limitations in an existing energy efficiency strategy for warehouses.

1.1.3 Challenges Facing Roof-Top PV installation for Warehouses

Following changes to building regulations in Approved Document L by the UK government, rooflights on industrial and storage building must make up a minimum of 20% of the area of the roof [13]. At first glance, this would leave 80% of the total roof area for roof-top technologies such as solar panels. However, this does not consider the spacing and pattern

between the rooflights to achieve the internal design daylighting regulations of a 10-15% rooflight area for effective daylighting, outside of offsetting artificial lighting demand [14]. To illustrate the potential impact of these new regulations, the architectural plans from an example warehouse have been amended where Figure 1.3 (a) shows only 10% of the roof area comprising rooflights, and (b) shows 20%. The main assumption is that the size of the skylights would stay the same therefore there is a linear relationship between percentage of area of the roof and number of skylights. The purpose of this diagram is to visualise that a 20% roof lighting requirement can end up covering most usable space on the roof, thus severely reducing the surface area application of solar panels on warehouse rooftops.

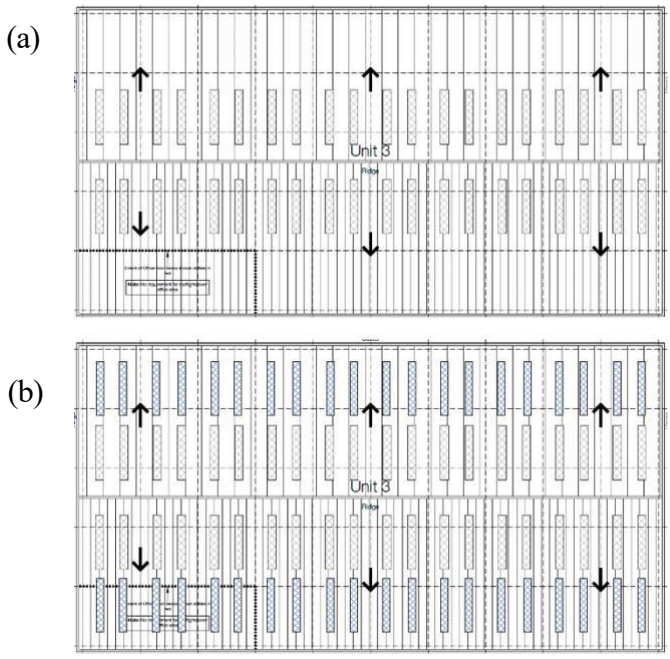


Figure 1.3 Difference in Rooflight Regulations on Available Roof Space

An additional point to make about the limitation of roof-top solar panels for warehouses is the added embodied energy. A report from the National Renewable Energy Laboratory (NREL) in the United States found that the embodied energy of silicon-based PV panels falls within the range of 200-400kWh/m^2 [15]. Furthermore, there is a mounting controversy surrounding the obstacles to recycling decommissioned solar panels exemplified by a study from the International Renewable Energy Agency (IRENA) that estimates the cumulative waste from solar panels could reach 60-78 million tonnes by 2050 [16]. As a result, it is up to researchers and engineers to devise new energy-efficient solutions for warehouses whilst keeping in mind modern regulations and minimising embodied energy. If these new regulations limit the potential for roof-top PV installation on warehouses, then other building technologies applicable elsewhere on the building envelope should be explored.

1.2 Façade Technologies – Maximizing Building Envelope Potential

Warehouses are a unique building type in that the sheer size of the building envelope does not serve any functional purpose, other than structural as compared to other building types where daylighting through glazing is essential. As warehouses are largely unglazed, relying on roof skylights or artificial lighting, the under-utilised facades of a warehouse present an opportunity to optimise, or even control the energy balance across its façade. Figure 1.4 illustrates the outside and inside surface heat balance across a building's envelope.

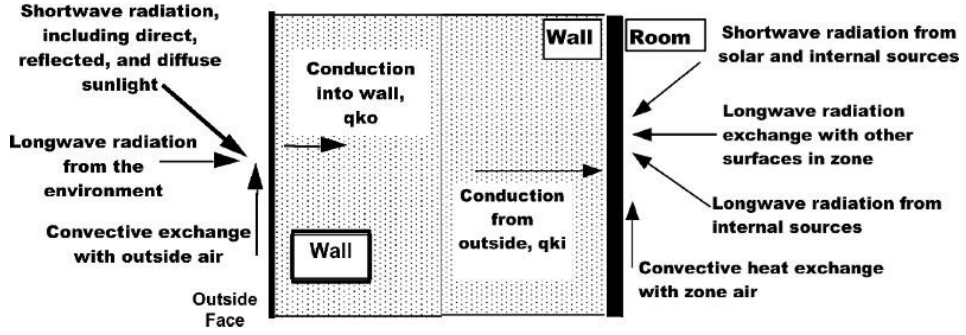


Figure 1.4 Outside and Inside Surface Heat Balance [17]

Equations 1.1 and 1.2 show the outside and inside surface heat balance, respectively. All symbols are in the nomenclature.

Equation 1.1 Outside Surface Heat Balance

$$q"_{asol} + q"_{LWR} + q"_{conv} - q"_{ko} = 0$$

Equation 1.2 Inside Surface Heat Balance

$$q"_{LWX} + q"_{SW} + q"_{LWS} + q"_{ki} + q"_{sol} + q"_{conv} = 0$$

What can be inferred from the energy balance across a building envelope is that any building application situated at this interface needs to be carefully designed concerning the changing external environment, and ventilation and thermal requirements of the internal conditions. As the research in this thesis is in response to developments in the UK construction sector, the suitability of a northern-hemisphere, temperate climate for a façade-based technology must be considered. This is explored in detail in Section 3.1.2 of Chapter 3. The UK climate can pose many challenges to designing any passive solution, including façade technologies, because of temperature variability, sunlight availability, wind exposure and more. However, an area of building application that considers how to balance passive design against external design conditions is solar-assisted façade technology.

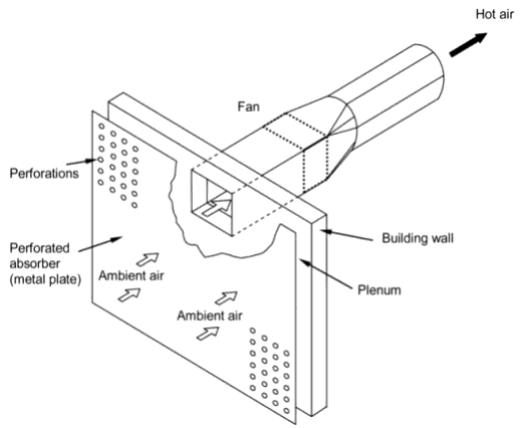
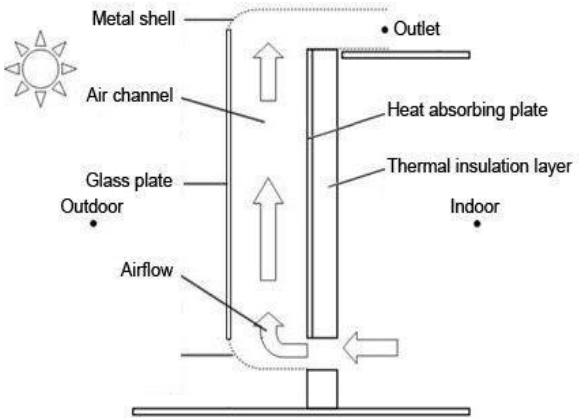
1.2.1 Review of Solar-Assisted Façade Technology

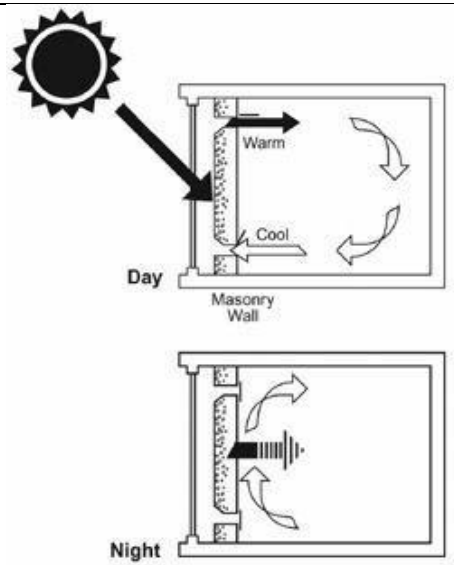
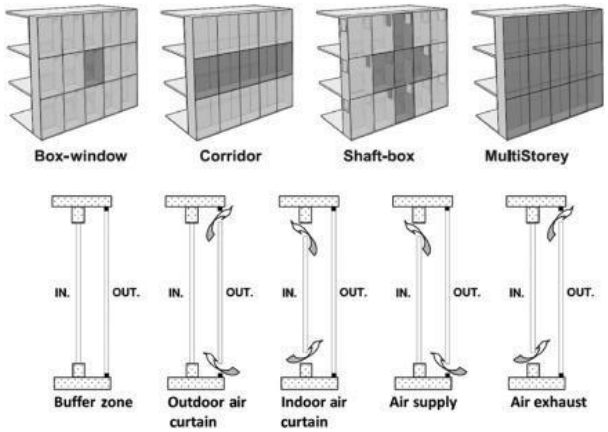
This summary is confined to the following four related, but distinctly different solar-assisted façade technologies: Transpired Solar Collectors (TSC), Solar Chimneys (SC), Trombe Walls (TW) and Double Skin Facades (DSF). What all these technologies have in common is that they are typically situated on the sunshine-oriented walls of a building envelope to enhance solar gain, as they utilise solar energy. However, the ways in which they harness solar energy and ventilation capabilities are different. In terms of applicability to a temperate climate typical of the UK, these solar-assisted façade technologies benefit from favourable conditions for the stack effect (the driving force of airflow in a cavity) to arise as well as good levels of solar irradiance annually [18-22].

Table 1.1 overleaf provides a summary of each of these solar-assisted façade technologies, as well as some benefits and limitations whereby the information has been obtained from [18-22]. Highlighted in red is the important distinctions between these different concepts: primarily is it glazed or unglazed, is it perforated or non-perforated and does it have an absorber material. What is immediately apparent is that the transpired solar collector and Trombe wall are predominantly heating technologies, whilst solar chimneys and double skin facades (DSF) utilise the stack effect to also achieve cooling [18-22]. The most flexible application is the DSF as it has multiple configurations, can be naturally or mechanically ventilated, and can provide a means of heating, cooling, or ventilation. However, despite this potential, DSFs are usually applied to office buildings because they are commonly glazed, whereas the unglazed transpired solar collectors have been widely used with warehouses in Canada and United States of America [18,22].

The primary difference between transpired solar collectors and double skin facades are that TSCs are typically sealed opaque perforated cladding, whereas DSFs are non-perforated, glazed, or unglazed double-layered façade duct capable of being fully open, partially open or closed. In terms of integration with buildings, TSCs require a fan however DSFs do not, and are typically naturally ventilated when applied to temperate climates in Europe and the UK [23]. The next section looks at a specific example of limitations in employing TSCs for warehouses, and why there is a gap for alternative façade technologies.

Table 1.1 Review of Solar-assisted Façade Technology [18-22]

	What is it?	How does it work?	Does it have an absorber?	Diagram	Benefits	Limitations
Transpired solar collectors	Unglazed solar-space heating technology.	Works with a fan to draw solar-heated air into the building through perforated metal façade.	Yes, the perforated outer metal plate is the absorber.		Fast capital payback of approx. 3-7 years. High conversion efficiency of under 75% of solar energy to usable heat energy. Savings of up to 50% in annual heating bills.	Not typically used for cooling. Relies on a fan to ventilate the space.
Solar chimneys	Partially glazed chimney to generate stack-driven ventilation.	Air in chimney needs to be warmer than ambient air to maintain temperature differential, no fan.	Yes, non-perforated absorbing plate on inner layer of chimney.		When placed on sunny side of building, it encourages cooler air from opposite shaded side.	In winter if conduction loss is greater than solar gain, which may cause down draughts. Only provide ventilation.

Trombe walls	Glazed solar-space heating technology.	Comprises a glazed outer layer and thick thermal mass wall to utilise Wien's displacement law so solar radiation is trapped in cavity.	Yes, non-perforated, thick high thermal mass inner masonry wall acts as an absorber.		No moving parts and almost no maintenance. Simple and inexpensive construction, made of masonry and glass. Significantly reduce heating bills.	Can be source of heat loss during extended overcast days.
Double skin facade	Special form of solar chimney where the whole façade acts as an air duct, either glazed or unglazed.	Multiple operations. Can operate with or without a fan, uses stack effect to remove heat gain at surface or recover heat and ventilate the space.	No, does not have an explicit absorber but glazed DSFs usually have opaque blinds in the cavity to absorb solar gain.		Reduces both heating and cooling demand. Can be used on a variety of building types. Allows natural ventilation to create a better indoor environment.	High initial cost of construction. Reliant on meteorological conditions (wind and temp) – climate specific.

1.2.2 The Limitations of Transpired Solar Collectors for Warehouses

Transpired solar collectors were first developed in the 1970s through extensive testing conducted by the US Department of Energy and had been in commercial production in Canada for over 15 years before entering the UK market [24]. In 2007, a leading British industrial and commercial metal roofing, cladding and gutter manufacturers, CA Group rolled out their brand of transpired solar collectors, SolarWall. Figure 1.5 below demonstrates the operations of the SolarWall integrated with a warehouse for space heating and cooling.

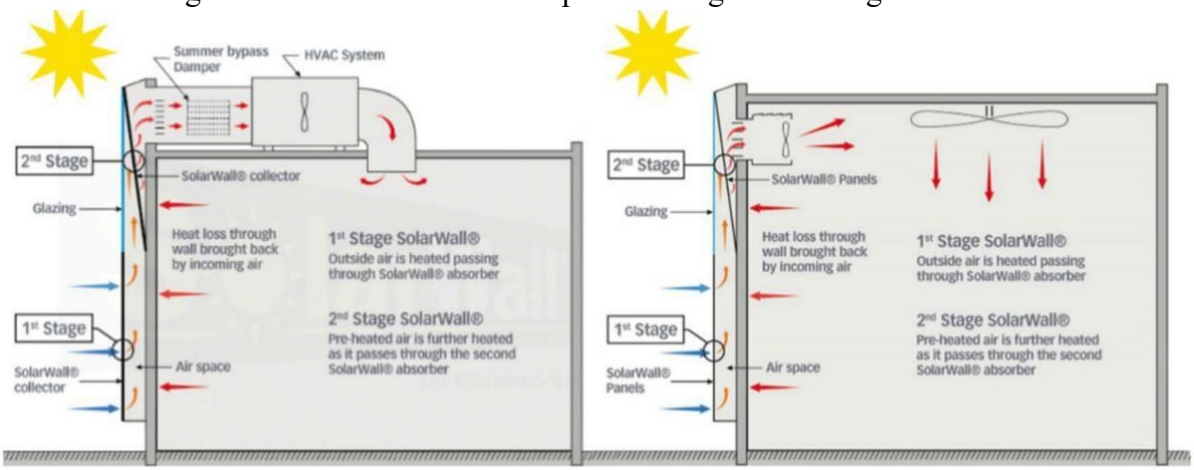


Figure 1.5 Heating and Cooling Operation of SolarWall [24]

The SolarWall comprises a cladding made from either aluminium or Colorcoat precoated steel from Corus, and the panels typically incorporate 2500 small perforations per square meter and creates a cavity depth of typically 100 to 300mm. The mechanism behind this technology involves solar-heated air being drawn through the perforations and fed into the air cavity before being delivered to the space via an existing or new fan. In terms of efficiency of the SolarWall, it can be up to 50%, and the temperature of the incoming ambient air can be increased by as much as 22K [24]. For the closely monitored installation of CA Group's roll mill in County Durham, the Building Services Research and Information Association (BSRIA) conducted an independent testing for 12 months with instrumentation including 32 thermocouples, a pyranometer, room temperature and humidity sensors and monitoring of air temperature stratification. The notable benefits seen in this review was that SolarWall was able to deliver 21% of total heating energy used which was about 79 MWh of a total heating use 375MWh and reducing CO_2 emissions by nearly 59 tonnes [25],[26].

Whilst this is a promising commercial example of a solar-assisted façade technology for warehouses, it is worth noting a comment made by consulting engineers Battle McCarthy who also carried out a study on the SolarWall for the CA group. It was stated that destratification

from the fans contributes to the reduction of heat demand even when the SolarWall is not supplying heat, as well as positive pressurisation of the building by preventing cold air blowing through open doors. This is highly notable given that temperature stratification occurs naturally in warehouses due to the high ceilings, allowing the hot, less dense air to rise and the cooler, dense air to sink to the occupied space [27]. As a result, if there are fans situated in the upper limits of the building, such as those used in integration with SolarWall, then those fans will encourage destratification regardless of SolarWall, which in turn combats air infiltration losses through open bay doors. What has not been clarified in these independent testing of SolarWall is the proportion to which the energy benefits can be attributed to the high-ceiling fans, and there is also not an extensive independent monitoring of how SolarWall performs in a fully naturally ventilated (no fans) warehouse. This leads to the following question.

1.2.3 Is Natural Ventilation Achievable in Warehouses?

Building standard 5925:1991 Code of Practice for ventilation principles and designing for natural ventilation defines natural ventilation as "*the movement of air through openings in the building fabric, due to wind or to static pressures created by differences in temperature between the interior and exterior of the building (generally known as the "stack effect"), or to a combination of these*" [28].

The Energy Efficiency Best Practice Programme (EEBPP) energy consumption guide ECG18 states that storage and distribution warehouses (of typical height 7.5m) are naturally ventilated to 16ºC for single shift operation during the day and condensation protection at night [29]. The issue here is not that natural ventilation is not achievable in a warehouse, but rather the existing building regulations and design guidelines are lacking. For example, CIBSE AM10 simply states that "*NV is generally applicable in many building types of up to 15m depth or greater if designed appropriately… [however] few data exist for buildings with floor-to-ceiling heights greater than 3.5m"* [12].

In conclusion, existing energy efficiency solutions for warehouses such as roof-top PV and façade-based TSCs are limited either by new regulation or technical deficit and therefore, both have created a gap for new or improved passive building technologies. The review of solar-assisted façade technologies highlighted the potential of naturally ventilated double skin facades for warehouse application, but also why they might not have been explored, until now.

1.3 A Building-First Approach to Designing Double-Skin Facades

The design approach to DSFs in this thesis is built upon the natural ventilation (NV) models described in [30] and [31]. It covers wind-only, buoyancy-only and wind and buoyancy driven flow, an adaptation of Bernoulli's principle and the Bernoulli equation which describes the conservation of energy appropriate for flowing fluids, accounting for major losses through the Darcy-Weisbach equation term and elbow bend component losses represented by a pressure loss factor, K. This can be simplified for double skin façade application on buildings by setting pressure at points, P_1 and P_2 as 0Pa as the system is exposed to atmospheric pressure that is unlikely to change.

Equation 1.3 Bernoulli's Principle

$$P_1 + \frac{1}{2}\rho v_1^2 + \rho g h_1 = P_2 + \frac{1}{2}\rho v_2^2 + \rho g h_2 + f\frac{L}{D}\frac{\rho v^2}{2} + K\frac{\rho v^2}{2}$$

The added novelty is to adapt this for a double skin façade whilst incorporating the horizontal thermal energy balance across a building's envelope and vertical cavity heating from the stack effect. It aims to standardise the means of assessing ventilation, thermal and energy performance of double skin facades (DSF) as, at present, most DSF research focuses on the DSF as a standalone building technology rather than explicitly as a building retrofit. In this thesis, DSF performance is measured as a function of the building to which it is applied (warehouses) and involves a three-step process: treating the DSF as a natural ventilation duct, treating the DSF as thermal wall retrofit and assessing the heat gain/removal (energy performance) in the cavity. Figure 1.6 shows schematic of ventilation and thermal operation for the proposed double skin façade for reference in the following sections.

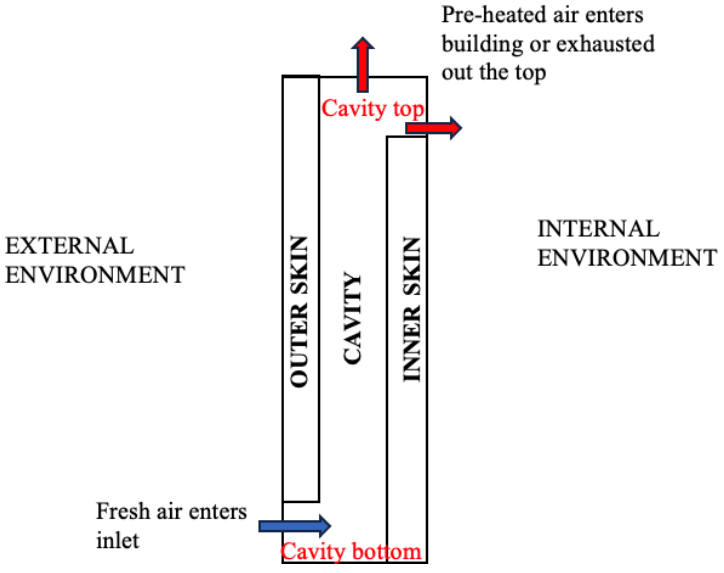


Figure 1.6 Schematic of Proposed Double Skin Façade System

1.3.1 Treating the DSF as a Duct (Ventilation Performance)

The BSRIA Illustrated Guide to Ventilation defines a ductwork system as the network to supply and extract air from around the building [32]. In terms of a naturally ventilated building, it is possible to treat an air cavity as a duct and in doing this the DSF is a function of the pressure drop across its own cavity. By determining relevant air velocity and pressure data, pressure drops from a wind-only, buoyancy-only, or combined wind and buoyancy conditions can be used to determine volume flow rate. For either wind-driven, buoyancy-driven or combined wind and buoyancy ventilation, the following equation is used to determine volume flow rate in the DSF cavity:

Equation 1.4 Volume Flow Rate [30]

$$Q = C_d A \sqrt{\frac{2\Delta P}{\rho}}$$

Three adaptations of Bernoulli's equation are required to determine the pressure drop in wind-only, buoyancy-only or combined wind and buoyancy conditions as shown below where all symbols are in the nomenclature. All equations have been reinterpreted in the context of double skin facades from key natural ventilation through openings principles and Bernoulli theory [12,28,30,31]. Examples of similar application are covered in the literature review in Chapter 2.

Equation 1.5 Wind Pressure Drop for a Double Skin Facade

$$\Delta P_{wind} = \frac{1}{2}\rho v_{cavity}^2 \left(C_{pouterskin} - C_{pinnerskin}\right)$$

Equation 1.6 Buoyancy Pressure Drop for a Double Skin Façade

$$\Delta P_{buoyancy} = \rho_{average} g H_{cavity} \left(\frac{1}{T_{cavitytop}} - \frac{1}{T_{cavitybottom}}\right)$$

Equation 1.7 Combined Wind and Buoyancy Pressure Drop for a Double Skin Facade

$$\Delta P_{windandbuoyancy} = \frac{1}{2}\rho v_{cavity}^2 \left(C_{pouterskin} - C_{pinnerskin}\right) + \rho_{average} g H_{cavity} \left(\frac{1}{T_{cavitytop}} - \frac{1}{T_{cavitybottom}}\right)$$

Chapter 3, Section 3.2 and Section 3.3 go into detail on how the different variables or parameters were obtained in the results section. All symbols and terms are in the nomenclature.

1.3.2 Treating the DSF as a Wall Retrofit (Thermal Performance)

A retrofit is defined by the Royal Institute of British Architects (RIBA) as *"the introduction of new materials, products and technologies into an existing building to reduce the energy needed to occupy that building"* [33]. This step of the building-first design approach to DSFs aims to determine a new dynamic U-value for the DSF retrofit with the existing building envelope.

If both thermal conductance and solar gain are proportional to the U-value of the building envelope, then a new dynamic U-value accounting for the DSF can be calculated by considering the composite thermal transmittance of the three main layers of the DSF, outer skin, cavity and inner skin.

Equation 1.8 Dynamic U-value for Double Skin Facades

$$U = \frac{1}{R_{outerskin} + R_{cavity} + R_{innerskin}}$$

1.3.3 Determining the Energy Performance of the DSF Retrofit

To estimate the overall energy performance of a DSF retrofit as a function of the heat gain in the cavity, the combined buoyancy and wind mass flow rate is calculated from the volumetric flow rate calculated from the pressure drop and applied in the heat generation equation below:

Equation 1.9 Heat Generation in a Double Skin Façade (kW)

$$Q = \dot{m} C_p (T_{cavitytop} - T_{cavitybottom})$$

All symbols are in the nomenclature. Chapter 7, Section 7.5 applies this equation to the proposed DSF to determine the energy that can be saved from pre-heating air entering the building or exhausted from the top of the cavity. The next section looks at the different available methods of assessing natural ventilation in technologies like DSFs and buildings.

1.4 Methods of Natural Ventilation Modelling

The primary methods for modelling natural ventilation are empirical, numerical, and physical models. Figure 1.7 overleaf is an overview of these methods, and the different sub-models or methodology required to employ them whilst Table 1.2 discusses the benefits and limitations.

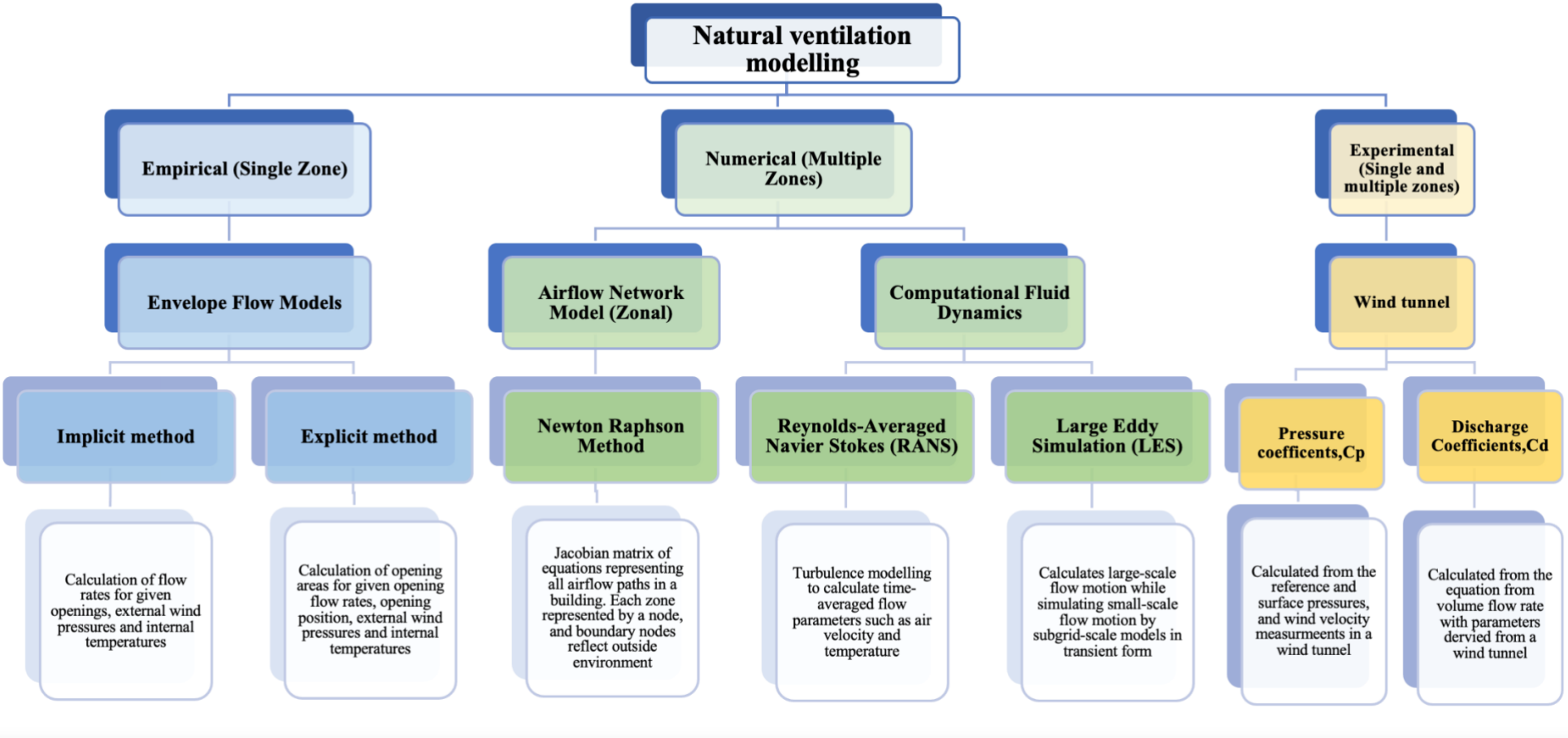


Figure 1.7 Overview of Natural Ventilation Modelling Technique

Table 1.2 Benefits and Limitations of Natural Ventilation Models

	Benefits	*Limitations*
Envelope Flow Models	• Best suited for initial sizing of openings with unidirectional flow • Explicit methods are easiest to use for openings	• Not as detailed as other tools • Relies on assumptions about the internal density (temperature distribution)
Airflow Network Model (AFN)	• Faster than CFD for certain problems, at a reduced computational cost • More detailed but still uses envelope flow models	• Power law assumption can lead to over-simplification • Inability to quickly model transient airflows caused by short term transients in pressure • Needs experimental validation • The assumption that air flows from one node to the other means it cannot predict internal air circulation, e.g., in a thermal zone
Computational Fluid Dynamics (CFD)	• Most detailed approach, can address stratification and local air movement • Can model velocity and temperature fields in both single-cell and multi-cell buildings and spaces, surface pressure distributions and discharge coefficients • CFD solves fundamental equations of motion for individual elements of fluid at all points in specified space	• Computationally intensive • Needs experimental validation • Some flows may be inherently unsteady so the use of a steady CFD solution can only provide a snapshot
Experimental model (Wind Tunnel)	• Able to assess cross ventilation, downwind or windward ventilation, changed wind angles • Can analyse elements present in the façade and their behaviour in contact with the wind	• High operating costs as fan must continually accelerate flow through tunnel • Not 100% accurate, always uncertainties in measurement equipment

The choice of NV methods applied in this thesis is the result of balancing these benefits and limitations against availability of resource, computational cost and expertise. The chosen numerical method to model natural ventilation in this thesis is Computational Fluid Dynamics (CFD) because is because of the capabilities of Reynolds-Averaged Navier Stokes (RANS) modelling over the Airflow Network (AFN) Model when it comes to large-space buildings such as warehouses, and the stack effect in a DSF cavity. In CFD, the geometry can be discretized into millions of mesh elements, at little computational cost due to the availability of powerful computing but this is limited under the Jacobian Matrix through the Newton- Raphson Method in AFN. Validating the CFD model through experimental data from an Atmospheric Boundary Layer Wind Tunnel for wind performance, and a climate chamber for buoyancy performance provides an effective means of modelling natural ventilation scenarios.

1.5 Research Scope, Novelty and Process

Overall, this research offers both academic contribution and real-world application by closing knowledge gaps in the building physics understanding of warehouses and opaque double skin facades (DSF) as a building retrofit in response to a changing built environment. The aim of this research is to develop an experimentally validated CFD energy performance tool for a novel seasonal-adaptive DSF system applied to warehouses in the UK. There are four objectives required to achieve this.

The first objective is to develop a multi-stage experimental and computational methodology to reflect gaps in DSF performance testing as identified in the systematic meta-analysis and literature review in Chapter 2. Relevant empirical methods will be employed to quantify the vertical solar irradiance incident on the DSF's outer skin and external air temperatures throughout an annual period in the UK which is essential to accurate performance prediction.

Then, the performance of the DSF will be experimentally tested under wind-only and buoyancy-only conditions as these are the two primary driving forces of ventilation in the cavity and the resulting data will form two parts of the computational tool's validation. The wind tunnel study will be conducted on a 1:50 scaled model of the DSF attached to the south-facing façade of the case study warehouse, exposed to different wind speeds and angles. The climate chamber study will comprise a 1:1 prototype of the DSF with a dark-coated aluminium outer skin and warehouse cladding inner skin, exposed to changing temperatures. The second experiment will also explore the impact of changing cavity closures on thermal and airflow phenomena at the top of the DSF cavity to introduce seasonal-adaptivity to its operation.

The third objective addresses the common issue of thermal stratification in warehouses by placing heat mats in the 1:50 scale model of the case study warehouse (excluding the DSF) from the wind tunnel study to simulate the vertical heating effect to validate the CFD tool. This step involves a comparison of scaling Grashof number empirically versus computationally to discuss accuracy and relevancy for unique large spaces like warehouses.

The final objective combines the results from the second and third objectives to present the final computational tool capable of assessing the integrated ventilation, thermal and energy performance of a seasonal-adaptive DSF for warehouses in the UK. This includes an additional

empirical validation stage of cross-ventilation in the case study warehouse (without the DSF). Additionally, there is both an empirical and computational estimation of the energy, financial and carbon savings delivered by the DSF to highlight the importance of assumptions.

The significance of this research is two-fold: firstly, it experimentally and computationally develops an opaque double skin façade for storage and distribution warehouses; secondly, it simultaneously produces a computational tool capable of assessing the energy performance of a DSF warehouses as well as ventilation and thermal analyses of the warehouse space. Both primary contributions are explained in detail in the following sections; however, chapters 2 to 7 offer their own novelty concerning method, and findings.

1.5.1 A "Seasonal-Adaptive" Opaque Aluminium DSF for Warehouses

The integration of a seasonal-adaptive, opaque double skin façade with a storage and distribution warehouse operating on a fully naturally cross-ventilated design has not previously been attempted in research, or industry. For cavity-based ventilation techniques, such as double skin facades, the design needs to account for the inverse relationship between increased airflow rate and heat recovery as well as a reliance on solar radiation to achieve a temperature differential across the cavity and outside environment. It is essential that this airflow rate is controlled to ensure that it is not too high in winter, and thus hinders the heat recovery, and that it is not low in summer, and promotes heat gain in the cavity.

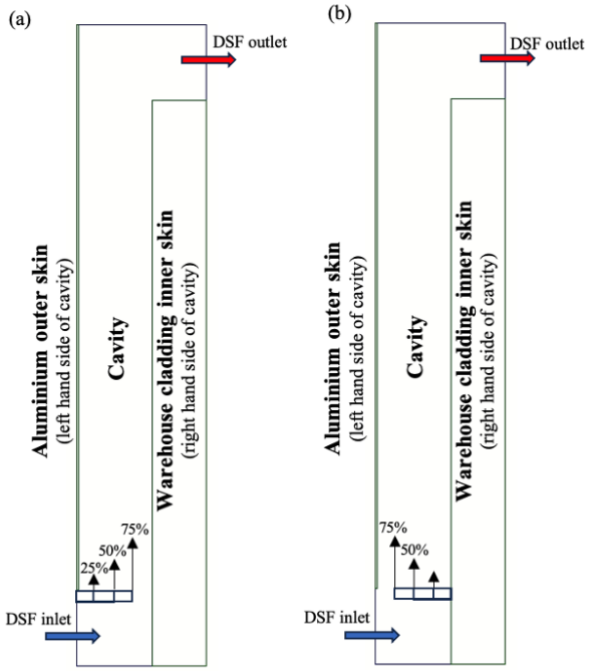


Figure 1.8 (a) LHS and (b) RHS "Seasonal-Adaptive" Openings Concept for DSF

Through developing the geometry to have "seasonal-adaptive" openings that open as a percentage of the depth of the cavity, and from either the inner skin or outer skin position, it can adapt its operation for off peak design conditions. What is not included in this thesis is a sensor or control strategy to achieve an automated responsive opening system and is limited to simulated closures instead. This concept is illustrated in Figure 1.8 above where the side-view shows where the openings are situated with respect to the aluminium outer skin (left-hand side of the cavity) or the warehouse cladding inner skin (right-hand side of the cavity). The feasibility of this technical improvement on existing double skin facades is tested at lab-scale in Chapter 5, and then computationally at full-scale in Chapter 7.

1.5.2 A Computational Fluid Dynamics Tool to Assess Ventilation, Thermal and Energy Performance of a DSF Warehouses

The computational fluid dynamics (CFD) tool gives an insight into the building physics of large space buildings such as warehouses which experience complex thermal, airflow and stratification phenomena. The novel process to develop it involves a three-stage experimental validation of the computational model, covered by Chapters 4-6 with the final tool presented in Chapter 7. CFD is commonly used in double skin façade (DSF) research to assess glazed outer and inner skins, not for two opaque layers of construction separated by an air cavity. The purpose of developing an experimentally validated CFD tool capable of assessing the ventilation, thermal and energy performance of a DSF retrofit for warehouses is to computationally derive cavity air velocity and temperature values for use in analytical calculations to estimate heat gain or removal detailed back in sections 1.3.1-1.3.3. Then, these values can be used to normalise energy savings across an annual period to calculate the viability of the opaque double skin façade as a retrofit for warehouses.

1.5.3 Research Process

The research process within this thesis is parallel and, at times, concurrent. Multiple research objectives are conducted at the same time, or with the same end-goal in mind. Figure 1.9 details how Chapters 2-7 form the bulk of this research process to deliver a novel opaque aluminium double skin façade specifically for warehouses, and the CFD performance tool to assess its energy, ventilation and thermal performance.

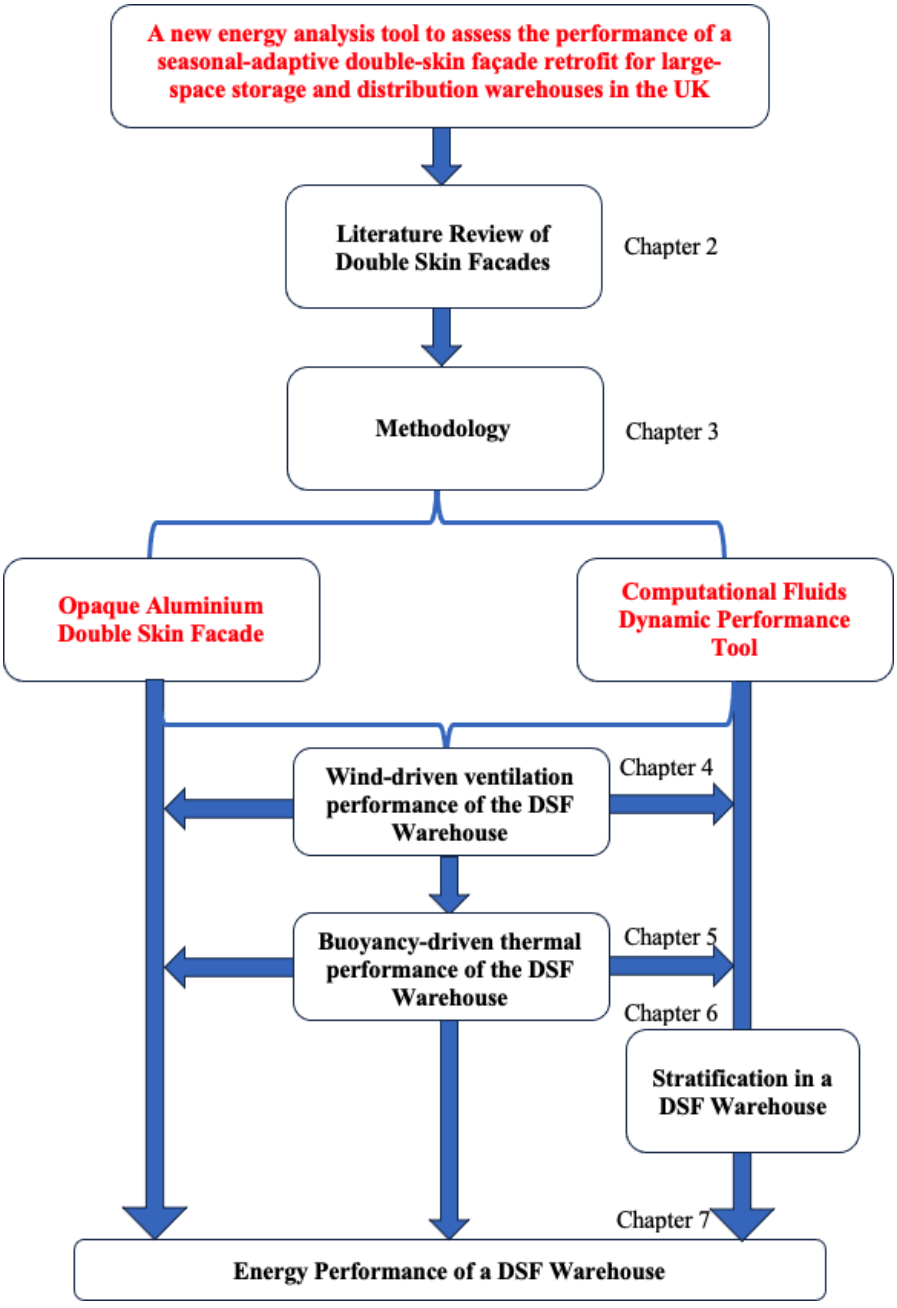


Figure 1.9 Parallel Research Process

Chapter 2

Literature Review

2.1 Chapter Introduction

With the potential to serve as an alternative to traditional heating, ventilation and air-conditioning systems, double skin facades are a popular research topic but by no means a complete one. The purpose of this chapter is to deliver a literature review that acts as a synopsis of double skin façade research as it stands in the 21st century and to highlight why perhaps research popularity and flexibility does not always yield commercial success in industry. The choice to exclude work from before the year 2000 is to ensure that the focus of the review is on modern developments in the double skin façade field.

The review in this chapter differentiates itself from existing studies by exploring the nexus of factors affecting ventilation and thermal performance and building integration of double skin facades. The scope includes a sample of over 100 papers dated between 2000 and 2024 which were selected through the identification, screening and refinement stages of the Preferred Reporting Items for Systematic Reviews and Meta-analyses (PRISMA) method. The organisation of the review comprises a systematic categorisation dependent on a range of parameters affecting double skin façade performance.

There are tabular summaries, and specially produced graphics in each sub-section under the "factors affecting ventilation and thermal performance" and "building integration", and there is an additional section which covers key trends in methodology, climate and operative conditions. In reviewing all these areas, this chapter will identify key research gaps to help guide the thesis' overall research objectives and contributions.

2.1.1 Motive and Context

Alongside diversifying the energy market by divesting from fossil fuels to mixed renewables and nuclear energy, there needs to be a global effort from countries, sectors, and companies to take accountability of their energy consumption and the associated carbon emissions. For example, the engineering and construction industry is the world's largest consumer of raw materials (3 billion tonnes) [34]. Within this sector is the built environment, primarily designed to maintain building occupants' comfort and wellbeing, consuming 30-40% of global energy demand and producing 40-50% of world carbon emissions [35-37].

People spent around 90% of their daily lives indoors even before the Covid-19 pandemic struck [38] and in advanced economies such as the United Kingdom, buildings already standing today will likely make up a considerable share of the total stock to 2050 [39]. Where buildings rely on

traditional building services such as Heating, Ventilation, and Air-Conditioning (HVAC) systems, these can account for up to 70% of a building's energy consumption, and the fans alone typically constitute 25% of the total building electricity consumption [38],[40]. Furthermore, according to International Business Machines (IBM) research [41], building energy consumption is projected to increase by 1% annually, meaning buildings will consume 30% more energy relative to today's level by 2060. Thus, there needs to be a re-design of HVAC systems to combat these projections, ideally by retrofitting or replacing existing systems with low-energy hybrid or natural ventilation (no fan) solutions, where applicable, with integrated passive heating and cooling techniques.

Additionally, in the wake of the Covid-19 pandemic, several governmental and scientific bodies have looked at how the disease may have spread more easily in open-plan, mechanically ventilated spaces such as offices, restaurants, and schools [42]. Operable windows are a solution to improving Sick Building Syndrome (SBS) [43], and governments such as the UK have adopted campaigns to encourage people to ventilate their homes by regularly opening windows during the pandemic [44],[45]. These new findings add to what is already known of the various health benefits of occupants in naturally ventilated spaces such as a stronger physiological regulation of heat shock than occupants in air-conditioned environments [46].

As well as these various health benefits, it has long been known that the energy cost of a naturally ventilated building is 40% less than that of an air-conditioned building [47],[48]. This suggests that building technologies which can deliver natural ventilation could help countries achieve the energy efficiency strategies required to meet 2030 and 2050 sustainable energy goals. However, naturally ventilated building design needs careful technical consideration, and to improve the feasibility of natural ventilation technologies, there should be some incorporation of a heat recovery technique.

The most straightforward application of natural ventilation is window openings. However, there are a range of technologies which can better enhance airflow into a space as well as providing passive heating and cooling. One unique example of an NV system applicable to predominantly temperate climates characterised by cold winters and warm summers, such as the UK, underutilised until recently in the current building industry is the double-skin façade (DSF) or ventilation façade. This type of NV application is situated on the sunshine-oriented building façade and can be directly integrated into the existing HVAC system of a building by providing a source of pre-heated air from the cavity to offset the Air Handling Unit (AHU) load, offering

flexibility as a hybrid ventilation solution. Additionally, openings on the inner façade can provide outdoor air directly into the adjacent spaces. This chapter looks to concisely organise the last two decades of double skin façade research into a novel system which examines how different parameters affect the ventilation and thermal performance of a double skin façade, as well as design factors which impact the overall viability of this building technology. Throughout the systematic review, there is also meta-analysis of the key trends in each key area of DSF research to visually highlight the current research gaps.

2.1.2 Classification of Double Skin Facades

While there are many available descriptions of double-skin facades (DSF), the following definition by the Belgian Building Research Institute (BBRI) [49] defines the technology as "*an active façade covering one or several stories constructed with multiple glazed skins... In this kind of façade, the air cavity situated between the skins is naturally or mechanically ventilated*."

A deeper classification of DSF systems is required as there are multiple geometric arrangements and ventilation modes which various researchers employ in their studies. Bonham [50] builds upon an existing classification of double skin facades proposed by researchers Oesterle et al. [51] and BBRI [49], to offer a combined typology, with a new ventilation mode addition, "closed cavity façade" as detailed below in Table 2.1.

Table 2.1 Recreated Double Skin Façade Typology [50]

Cavity Depth	Cavity Partitioning	Ventilation Type	Ventilation Mode
Thin Profile	Box Window	Natural (Passive)	Externally Ventilated (Outdoor Air Curtain)
			Internally Ventilated (Indoor Air Curtain)
	Shaft Box	Mechanical (active)	Air Supply
Thick Profile	Corridor		Air Exhaust
	Multistorey	Hybrid (interactive)	Buffer/Breathable Façade
			Closed Cavity Façade Variable

Figure 2.1 (a) demonstrates the DSF configuration in terms of cavity partitioning, and (b) shows the five main ventilation modes with possible variations with reversal of airflow direction. These illustrations are for referring to in aid of the following review.

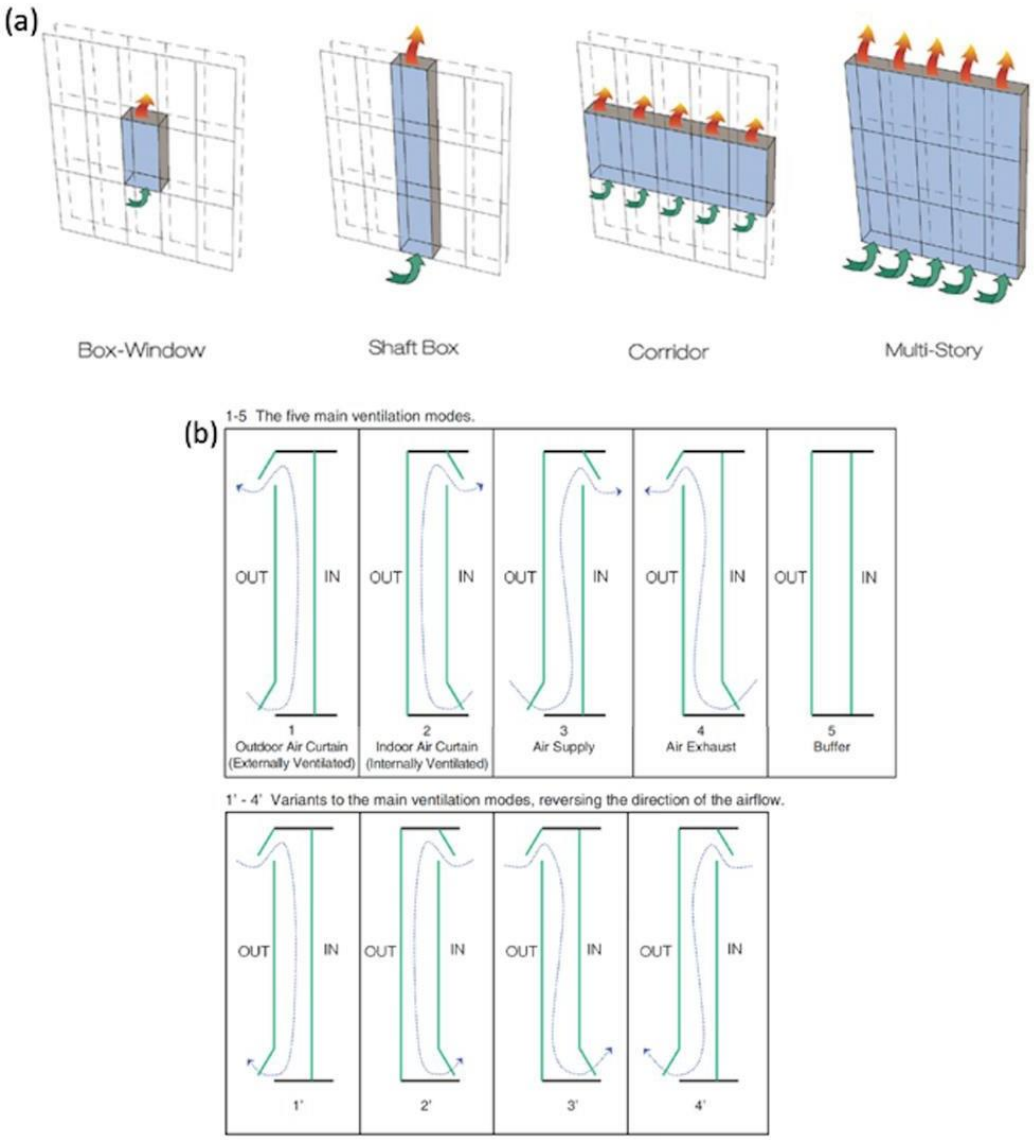


Figure 2.1 (a) DSF Cavity Partitioning Configurations [56] and (b) Ventilation Modes [49]

2.1.3 Mechanism of Double Skin Facades

Perhaps the most crucial element of a double-skin façade (DSF) system is its primary mechanism and associated energy balance. Given that a DSF is a natural ventilation building technology that utilizes the solar chimney effect, it is worth highlighting the airflow and heat transfer phenomena occurring within the system in Figure 2.2. Broadly, the areas of heat transfer that inform the thermal behaviour of a double-skin façade system are conduction, convection, and radiation. When there is a sufficient temperature differential across the external skin, the buoyancy (or stack) effect occurs, drawing air up through the DSF cavity to exhaust heat gains from solar radiation or the building out the top.

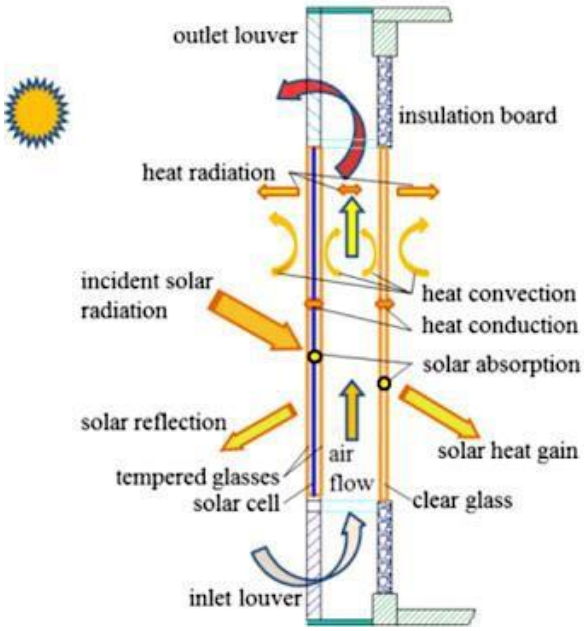


Figure 2.2 Heat Transfer in Outdoor Air Curtain Box-Window DSF [52]

The airflow rate within the cavity can also be affected by wind pressure distributions at the openings and external façade. Additionally, glazed DSFs typically employ shading devices in the cavities to reduce glare and excessive solar heat gain in warm weather [53]. Although, the effectiveness of blinds depends on their form and orientation relative to the solar altitude and azimuth for the time of day and season of the year [54].

2.1.4 Novelty of Review Methodology and Concept

What this chapter offers as a distinction to literature reviews carried out by other researchers is a novel systematic organisation of the critical design factors explored in double skin façade research in the 21st century, as well as a meta-analysis of key research trends. This review considers *both* ventilation and thermal performance, and the viability of double skin façade systems in terms of energy performance, occupancy comfort and safety, and life cycle analyses, understood not to have previously been attempted. The closest existing review by Jankovic and Goia [55] has a primary focus confined only to the structural parameters, whereas this review considers all aspects that may affect the viability of a double skin façade technology as a building application. The method for selecting the papers is an adaptation of the PRISMA transparent reporting of systematic reviews and meta-analysis, depicted in Figure 2.3 below. The key terms used for the PRISMA method search include ‘double skin facades’, ‘ventilated facades’, ‘ventilation performance of double skin facades’, ‘thermal performance of double skin facades’, ‘double skin façade buildings’, ‘fire safety in double skin facades’, and ‘occupancy comfort and double skin facades’.

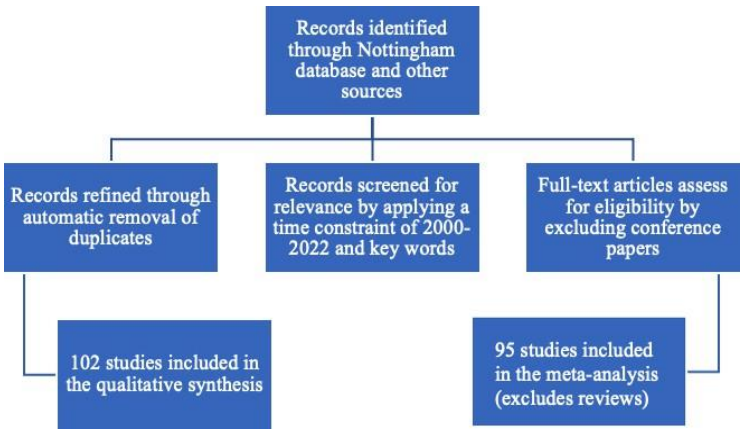


Figure 2.3 PRISMA Process

This review aims to highlight that the present nature of double skin façade research focusses primarily on phenomena within the double skin façade cavity, and how it performs within the external environment but neglects its wider application as a building technology, and how it interacts directly with the internal environment of a building. The objectives to achieve the aim of this review are below:

- Organise a sample of around 100 papers identified, screened and dated between 2000 and 2021 into a systematic categorisation dependent on parameters examined
- Provide tabular summaries of sample papers in each relevant section to provide an overview of whether the research considered either the ventilation or thermal performance of a DSF or both
- Present a new review looking distinctly at the viability of a DSF integrated with buildings from a technical, economic, and environmental perspective
- Explore methodology trends

Using an Excel spreadsheet, and the adapted PRSIMA method, this review comprises three key sections : 'Factors affecting ventilation and thermal performance of double skin facades'; 'Factors affecting building integration of double skin facades'; and 'Key trends in methodology'. Within these sections, a nexus of sub-topics is explored including: 'Climate and location'; 'Building application and orientation; 'DSF configuration and construction layers'; 'Energy performance'; 'Occupancy comfort and safety'; and 'Life Cycle Analyses'. Every paper in this sample was examined to see what section it aligns with, and the key trends were created on a similar method of categorisation. Each of these topics is concluded with a tabular summary in addition to appropriate trend analyses of a selected sample of peer-reviewed articles published in the last two decades.

Figure 2.4 below shows the interconnectedness of the research areas of double skin facades discussed and analysed in this article.

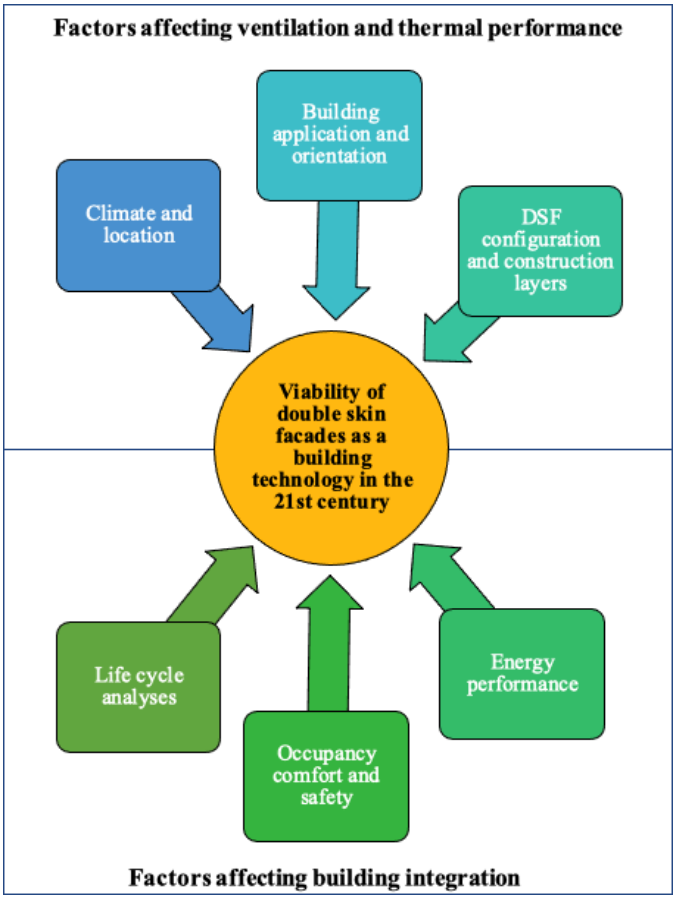


Figure 2.4 Factors affecting the Viability of a DSF System

2.2 Factors affecting Ventilation and Thermal Performance of Double Skin Facades

Broadly, the ventilation performance reflects whether the system reaches a sufficient airflow rate to aid in the heat recovery or heat removal of heat gains within the cavity and, if applicable, outdoor air to the indoor space adjacent to the double-skin façade. The thermal performance is the system's ability to respond to the ambient environment in a way that preserves the thermally designed indoor environment – essentially, reduce heat loss in heating seasons, and reduce overheating in cooling seasons. The different design factors include climate type and location, building height, type and DSF orientation, DSF typology and ventilation mode, DSF cavity geometry and layout, glazed external and inner skins, perforated ventilated facades and lastly, shading devices. It is worth noting that the behaviour of DSF technology is intermittent and will vary throughout the day, with some hours achieving no ventilation. The following sections present the critical design factors that need to be assessed to achieve optimal ventilation and thermal performance of double skin façade.

2.2.1 Climate Type and Location

Researchers generally agree that DSF systems are bespoke to individual climates. Whilst double skin facades have considerable application in hot climates, there is also the issue of overheating in the cavity due to high solar irradiance levels in warm weather. Popular solutions tend to be changing glazing properties and the ventilation mode to combat the buoyancy-driven accumulation of heat in the traditional box-window configuration. Su et al. [56] confirm the influence of such warm and high irradiance climates in their study of DSF application in regions in China for an entire cooling season, whilst Gelesz et al. [57] suggest that optical properties are more important in their assessment of Torino, Oslo and Hong Kong. A combination of these findings is reflected in the work by Aleksandrowicz and Yezioro [58] and Larsen et al. [59]. Both studies identify cavity overheating in the hot climates of Tel Aviv, Israel and Salta, Argentina during cooling periods, respectively.

Within each climate, there are also varying seasonal conditions which could dictate the performance of a DSF, in terms of the inverse relationship between airflow rate and the heating effect in the cavity. Local wind variabilities and solar irradiance levels are key to understanding performance. For example, Xu and Ojima [60] discovered that for a residential house in Kitakyushu, Japan, strong sunlight in autumn allows for NV and sun shading, but no solar radiation requires Completely Closed Cavity (CCF) as indoor air temperature can be 5-12ºC higher than outside air when it is cold. In line with these findings, Andelkovic et al. [61] concluded that the highest effectiveness for multi-story naturally ventilated DSF in Belgrade, Serbia was during transitional seasons.

Not many researchers choose to look solely at the performance of double skin facades in a wind-only scenario, excluding buoyancy conditions. However, both Kim et al. [62] and Hu et al. [63] considered only the wind-induced response of a DSF system. The former researchers employed computational fluid dynamics (CFD) to highlight that wind perpendicular to openings created the lowest ventilation rate (and therefore the highest indoor temperature), a reduction of 47.6% compared to parallel and leeward wind directions. This suggests that for DSF systems applied to tall buildings where a large wind load is to be expected, its performance in a wind-only scenario might be more important.

i. Trend Analysis and Research Gaps

Of the 50 papers over the two-decade period that examined a distinct climate, the most looked at climate is temperate, followed by continental, dry and tropical as per the Koppen Geiger classification. As previously mentioned, the primary driving force of double skin facades is the stack effect which is most effective in temperate climates and therefore, in line with these findings, however there is also great variation within this climate category.

Figure 2.5 (a) below shows that the predominant sub-climate is Oceanic temperate, followed by Humid Subtropical and Mediterranean Hot Summer. This is an important distinction as it shows that present research focusses on the warmer temperate climates. This is reflected in Figure 2.5 (b), where applying summer conditions in DSF research was as common as looking at both winter and summer (heating and cooling). This suggests that colder climates, with predominant heating requirements, may present a current research gap.

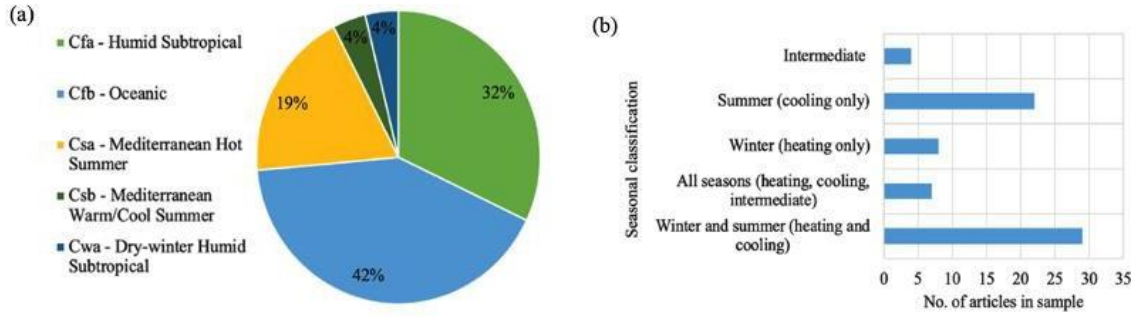


Figure 2.5 Trend Analysis of (a) Climate and (b) Seasons

Table 2.2 highlights that the most important climate factor affecting both ventilation and thermal performance is solar irradiance levels which is dependent on the hemispherical location of the application, and changeable throughout seasons. Parameters that change seasonally will affect the annual performance of a double skin façade. So, researchers have noted that while one type of DSF configuration might be effective for specific conditions in specific seasons, this might not be the case outside of this. The summary table is a chronological overview of locations, Koppen Geiger climate classification, hemisphere, seasonal and heating and cooling focus.

Table 2.2 Climate Classification and Location of DSF Systems

Author and chronology of publication	Location	Koppen Geiger Climate Classification	Hemisphere	Seasonal focus	Heating or cooling?
Balocco (2002)	Florence, Italy	Cfb, Marine West Coast	Northern	Winter and Summer	Both
Gratia and De Herde (2004)	Belgium	Cfb, Moderate Sea	Northern	Summer	Cooling
Park et al. (2004)	Atlanta, Georgia	Cfa, Warm and Temperate	Northern	Spring	Both
Stec et al. (2005)	Delft, Netherlands	Cfb, Warm and Temperate	Northern	Winter and Summer	Both
Stec and Passen (2005)	Delft, Netherlands	Cfb, Warm and Temperate	Northern	Winter and Summer	Both
Ballestini et al. (2005)	Cavaso del Tomba, Italy	Cfb, Oceanic	Northern	Winter and Summer	Both
Gratia and De Herde (2007)	Belgium	Cfb, Moderate Sea	Northern	Winter and Summer	Both
Xu and Ojama (2007)	Kitakyushu, Japan	Cfa, Humid Subtropical	Northern	Winter, Summer, and Autumn	Both
Hoseggen et al. (2008)	Trondheim, Norway	Dfc, Continental Subarctic	Northern	Winter	Heating
Pappas and Zhi (2008)	Leuven, Belgium	Cfb, Marine West Coast	Northern	All seasons	Both
Wong et al. (2008	Singapore	Af, Tropical Rainforest	Northern	Cooling	Cooling
Chan et al. (2009)	Hong Kong	Cfa, Humid Subtropical	Northern	Cooling	Cooling
Fallahi et al. (2010)	Torino, Italy & Munich, Germany	Cfb, Marine West Coast	Northern	Winter and Summer	Both
Gavan et al. (2010)	Lyon, France	Cfb, Marine West Coast	Northern	Summer	Cooling
Zeng et al. (2012)	Beijing, China	Dwa, Hot Summer Continental	Northern	Winter and Spring	Both
Kim and Park (2011)	Seoul, Korea	Dfa, Hot Humid Continental	Northern	Spring and Autumn	Both
Ghadamian et al. (2012)	Tehran, Iran	Csa, Mediterranean	Northern	Winter and Summer	Both
Valentin et al. (2013)	Barcelona, Spain	Csa, Maritime Mediterranean	Northern	Summer	Cooling
Andelkovic et al. (2015)	Serbia	Cfa, Humid Subtropical	Northern	Winter, Summer, and Transition	Both
Larsen et al. (2015)	Salta City, Argentina	Cfb, Humid Subtropical	Southern	Spring and Summer	Both

Andelkovic et al. (2016)	Belgrade, Serbia	Cfa, Humid Subtropical	Northern	Winter, Transitional and Summer	Both
Shen and Li (2016)	Urumchi, China	BSk, Tropical and Subtropical Steppe	Northern	Summer	Cooling
Blanco et al. (2016)	Bilbao, Spain and Seville, Spain	Cfb, Marine West Coast and Csa, Mediterranean	Northern	Winter and Summer	Both
Peng et al. (2016)	Hong Kong	Cfa, Humid Subtropical	Northern	Winter	Heating
Pomponi et al. (2016)	London, UK	Cfb, Marine West Coast	Northern	Winter and Summer	Both
Dama and Angeli (2016)	Aalborg, Denmark	Cfb, Warm and Temperate	Northern	Winter	Heating
Wang et al. (2016)	Changsha, China	Cfa, Humid Subtropical	Northern	Winter and Summer	Both
Elarga et al. (2016)	Venice Helsinki and Abu Dhabi	Cfb, Marine West Coast; Dfb, Warm Summer Continental and Bwh, Subtropical Desert	Northern	Winter and Summer	Both
Peng et al. (2016)	Hong Kong	Cfa, Humid Subtropical	Northern	Winter	Heating
Nastase et al. (2016)	Brasov, Romania	Dfb, Warm Summer Continental)	Northern	Winter and Summer	Both
Sanchez et al. (2016)	Spain	Csa Hot-Summer Mediterranean	Northern	Winter and Summer	Both
Vatavalis and Bikas (2017)	Athens, Greece	Csa, Mediterranean	Northern	Summer	Cooling
Su et al. (2017)	Harbin, Beijing, Shanghai and Guangzhou, China	Dwa, Monsoon-influenced Humid Continental; Dwa, Hot Summer Continental; Cfa, Humid Subtropical; Cwa, Humid Subtropical Hot Summer	Northern	Summer	Cooling
Ioannidis et al. (2017)	Montreal, Canada	Dfb, Warm Summer Continental	Northern	Annual	Both
Slakovic (2017)	Novi Pazar, Serbia	Cfb, Warm and Temperate	Northern	Winter and Summer	Both
Wang et al. (2017)	Hong Kong	Cfa, Humid Subtropical	Northern	Summer	Cooling
Bueno et al. (2017)	Villafranca di Verona, Italy	Cfa, Humid Subtropical	Northern	Winter and Summer	Both
Alberto et al. (2017)	Porto, Portugal	Csb, Mediterranean	Northern	Winter and Summer	Both
Kilaire and Stacey (2017)	Nottingham, UK	Cfb, Temperate Maritime	Northern	Winter and Summer	Both

Wen et al. (2017)	Wuhan, China	Cfa, Warm and Temperate	Northern	Summer	Cooling
Hay and Ostertage (2018)	Singapore	Af, Tropical Rainforest	Northern	Summer	Cooling
Zomorodian & Tahsildoost (2018)	Tehran, Iran	Csa, Mediterranean	Northern	Winter and Summer	Both
Aleksandrowicz and Yezioro (2018)	Tel Aviv, Israel	Csa, Dry-Summer Subtropical	Northern	Summer	Cooling
Souza et al. (2018)	Ouro Preto, Brazil	Cwa, Humid Subtropical	Southern	Summer	Cooling
Hassanli et al. (2018)	Sydney, Melbourne, Brisbane, and Adelaide, Australia	Cfa, Humid Subtropical; Cfb, Temperate Oceanic; Cfa, Humid Subtropical & Csb, Mediterranean	Southern	Winter and Summer	Both
Kim et al. (2018)	Seoul, Korea	Dfa, Hot Humid Continental	Northern	Winter and Summer	Both
Inan and Basaran (2019)	Istanbul	Csa, Mediterranean	Northern	Winter and Summer	Both
Barbosa and Alberto (2019)	Rio de Janeiro, Brazil	Aw, tropical savanna	Northern	Winter and Summer	Both
Lee et al. (2019)	Changsha, China	Cfa, Humid Subtropical	Southern	Annual	Both
Iken et al. (2019)	Meknes, Morocco	Csa, Hot-Dry Summer Subtropical	Northern	Winter and Summer	Both
Yoon et al. (2019)	Seoul, Korea	Dfa, Hot Humid Continental	Northern	Winter	Heating
Seo et al. (2019)	Miami, Florida	Am, Tropical Monsoon	Northern	Summer	Cooling
Bielek et al. (2019)	Bratislava, Slovakia	Cfb, Marine West Coast	Northern	Winter	Heating
Sung and Kim (2019)	Daejeon, South Korea	Dfa, Hot Summer Continental	Northern	Winter	Heating
Yahiaoui (2020)	Delft, Netherlands	Cfb, Warm and Temperate	Northern	Winter and summer	Both
Radmard et al. (2020)	Karaj, Iran	BSk, Cold Semi-Arid	Northern	Summer	Cooling
Shakouri et al. (2020)	Tehran, Iran	Csa, Mediterranean	Northern	Winter and Summer	Both
Yang et al. (2020)	Darwin, Canberra and Sydney, Australia	Aw, Tropical Savanna; Cfb, Oceanic & Cfa, Humid Subtropical	Southern	Winter and Summer	Both
Wang et al. (2020)	Yangtze River Area, China	Cfa, Humid Subtropical	Northern	Winter and Summer	Both

Zhu et al. (2020)	Tianjin, China	Dwa, Hot Summer Continental	Northern	Summer	Cooling
Sarglou et al. (2020)	Tel Aviv, Israel	Csa, Dry-Summer Subtropical	Northern	Winter and Summer	Both
Gelesz et al. (2020)	Torino, Italy & Oslo, Norway & Hong Kong	Cfb, Marine West Coast; Dfb, Warm Summer Continental & Cfa, Humid Subtropical	Northern	Winter and Summer	Both
Pourshab et al. (2020)	Isfahan, Iran	BSk, Tropical and Subtropical Steppe	Northern	Summer	Cooling
Ioanniddis et al. (2020)	Montreal, Canada	Dfb, Warm Summer Continental	Northern	All Seasons	Both
Yoon et al. (2020)	Seoul, Korea	Dfa, Hot Humid Continental	Northern	Winter	Heating
Preet et al. (2020)	Jaipur, India	Bsh, Mid-latitude Steppe and Desert	Northern	Summer	Cooling
Srisamranrungruang and Hiyama (2020)	Japan	Cfa, Humid Subtropical	Northern	Spring and Autumn	Both
Hou et al. (2021)	Nanjing, China	Cfa, Warm and Temperate	Northern	Summer	Cooling
Kim (2021)	Saudi Arabia	Bwh, Tropical and Subtropical Desert)	Northern	Summer	Cooling
Sotelo-Salas et al. (2021)	Mexicali, Northwest Mexico	Bwh, Tropical and Subtropical Desert	Northern	Summer	Cooling

2.2.2 Building Application

Depending on the methodology employed to evaluate double skin façade performance, if the researchers opt to include the adjacent building application, then this will have an influence on airflow rate and cavity air temperature. The critical design factors looked at include building height and type, DSF orientation, DSF typology and ventilation mode.

i. Building Height, Type and DSF Orientation

The height and type of the building that a double skin façade is applied to may impact the ventilation and thermal performance of a DSF itself. In some cases, the DSF vent is the same as the height of the building, for example with multi-storey configurations, but it is more common that the DSF vent height is equal to only one-storey. Sarglou et al. [64] and Yoon et al. [65] explored the relationship between wind speed and pressure and the height of DSF high- rise office buildings in Tel Aviv, Israel and a 25-storey apartment block in Daejeon, South Korea through EnergyPlus, respectively. Both studies concluded that both the heating and cooling loads drop across the height of the DSF building due to an increase in wind speed, even for different DSF typology of corridor-type and box-window-type.

Other researchers have considered how specific building types might influence the performance of a DSF system which has been applied as a retrofit. Ballestini et al. [66] used TRNSYS and LOOPDA models in their study of a decommissioned silk factory in a Mediterranean climate to find 12% in annual energy savings. The authors noted that pre-existing chimney stacks on the roof strongly contributed to achieving necessary airflows which suggests that if DSF are applied as retrofits, the existing building layout will determine its performance. Similarly, Slavkovic [67] modelled an east and west-facing DSF on an industrial textile factory in Serbia in EnergyPlus to find that the highest energy efficiency in summer is achieved when the DSF can provide night cooling to the building adjacent. Gratia and De Herde [68] assessed an office building with DSF in Belgium using TAS software and highlighted that the case study building had a high level of insulation with a narrow plan making it very well adapted for the cross ventilation that the DSF was able to provide.

The orientation of a DSF building and window-to-wall ratio (WWR) of the building façade are both important aspects to consider with a DSF system due to its performance being reliant on

the level of solar irradiance. Inan and Basaran [69] conducted experimental and numerical measurements of heat gains and loss values for a DSF in the heating and cooling season in Istanbul, Turkey, for all orientations. The DSF, compared to a single skin façade, saw cooling loads decrease up to 26% in all directions, although the DSF was disadvantageous in the heating season due to external airflow ventilation mode. The importance of building orientation in this study is further reflected in a study by Gratia and De Herde [70]. The south oriented DSF received the maximum solar radiation for winter in Belgium, and the cavity air temperature reaches 32.3ºC when the sky is clear. For summer, with clear sky conditions at 1 pm, minimum solar radiation occurs for the north-oriented DSF getting a cavity air temperature of 30.5ºC compared to 47.8ºC for a south-oriented DSF, 51.2ºC in east-oriented DSF, and 49.5ºC in west DSF.

Similarly, the sun path across the sky depending on the northern and southern hemisphere will affect the Solar Heat Gain Coefficient (SHGC) of the DSF building. Chou et al. [71] assessed the impact of SHGC in a DSF fenestration system through a laboratory test rig. The values observed in the East and West facing DSF resulted in significantly higher SHGC than the North and South facing façade. Vatavalis and Bikas [72] examined a corner double-skin façade facing south and west with rotating glass louvres during the cooling season in Athens, Greece. As a result of solar irradiance vector differences at midday when south-facing from a slightly different position, the west elevation does not perform well.

ii. DSF Typology, Airflow Configurations and Ventilation Modes

Researchers have looked at both naturally and mechanically ventilated double skin facades, and a range of airflow configurations detailed back in Section 2.1.2. Sanchez et al. [73] explored the different airflow configurations for a south-facing box-window DSF in Spain using a simplified CFD model in ANSYS Fluent 14. The results indicate that closed vents (thermal buffer mode) are the most efficient for winter conditions, with energy savings reaching 75% in the presence of solar radiation. However, during summer, there should be open vents to encourage the stack effect and consequent heat removal, leading to up to 4% of cooling load energy savings. Alberto et al. [74] employed EnergyPlus to assess a building with box-window and shaft models on the north and south façade while corridor and multistorey models were oriented east and west. They concluded that airflow path was the most crucial aspect affecting DSF efficiency, with the maximum performance achieved with a multi-story DSF and outdoor air curtain ventilation mode presenting 30% less HVAC-related energy demands. Furthermore, there was a difference of up to 40% in energy demand reductions between north and southern oriented

facades in the Indoor Air Curtain ventilation mode, and notably, this difference reduced to 9% for a single skin façade.

In terms of ventilation, the critical differentiating aspect in the outcomes of studies looking at the effect of cavity opening geometry on DSF performance is whether researchers have looked at wind-driven ventilation, buoyancy-driven ventilation, or both. Dama and Angeli [75] conducted experimentally validated CFD and building simulation models and found that despite a reasonable maximum deviation between the two models of 15%, both exhibited a high sensitivity to differential wind pressures depending on the pressure coefficient source used. Concerning mass flow rate, the maximum divergence between the models is found when wind differential pressure is opposite to flow direction (with buoyancy still prevalent), amounting to about 30% when wind pressure is null and reducing to 10% if wind pressure strongly promotes flow rate. The previous study's results are further confirmed by those found by Andelkovic et al. [61] in their long-term experimental analysis of a building with a multistorey naturally ventilated double-skin façade in Belgrade, Serbia, and later EnergyPlus simulations [76]. The findings concluded that in the case where the façade is open, the value of air cavity velocity markedly depends on wind speed and can be affected by solar radiation, making it directly proportional to both conditions. These results suggest coupling wind-driven and buoyancy-driven ventilation together for an assessment of DSF performance.

Various researchers have explored both mechanically and naturally ventilated DSFs. For example, Perez-Grande et al. [77] found that blowing air through the cavity at a box-window DSF at 6m/s in summer season reduces the heat load into the building by a factor larger than 1.5 when compared to the heat load corresponding to free convection case suggesting that mechanical ventilation of the DSF is better for cooling conditions. Additionally, for winter, the authors suggest that since the air is heated when flowing through the channel, regardless of free or forced convection, the mass of air could be used for heating purposes in the winter to save energy. Gavan et al. [78] and Wang et al. [79] both found that the airflow rate influences surface and air temperatures for box-window DSFs. The latter study varied the ventilation rate from 200 to 800 m^3/h (metres cubed per hour), which resulted in the maximum decrement of inner glass temperature and heat gains is 0.8ºC and 20 W/m^2 (Watts per metre squared) for a summer season in China. Smaller DSF openings are required in colder seasons and larger openings in summer for a naturally ventilated double-skin façade connected to a room in a multi-storey building [80].

iii. Trend Analysis and Research Gaps

University laboratories or buildings were the most common application for double skin facades in the research sample, followed closely by offices or commercial buildings. There are few papers looking at the performance of DSF systems in tandem with industrial or residential buildings. In terms of the orientation of double skin facades, South prevailed which reflects the research largely being undertaken in northern hemisphere conditions. Many researchers opted to assess all orientations ([57],[68],[64],[69],[74],[81-87]) rather than just sunshine-oriented as double-skin facades can offer other advantages such as wind shielding [88].

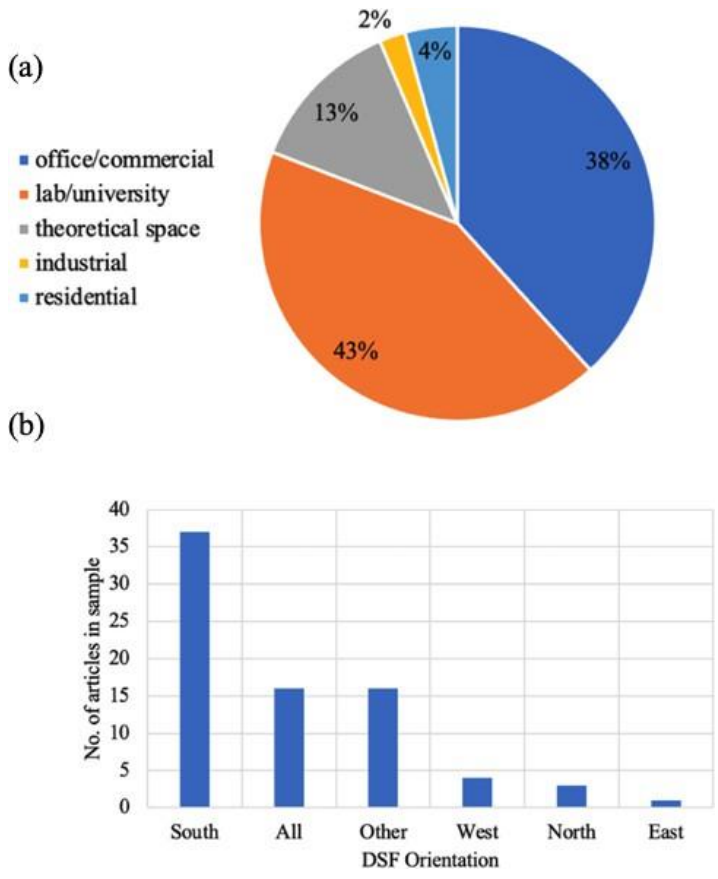


Figure 2.6 Trend Analysis of (a) Building Type and (b) DSF Orientation

The building that a DSF system is attached to might also influence its performance. The orientation of a building or the direction of the DSF building façade will have a significant effect on both its ventilation and thermal performance as it is affected by sun paths. It is interesting that from a retrofit perspective, the existing structure of a building may promote airflow through a DSF building [66-68]. Therefore, it is crucial to study the performance of a DSF and the adjacent building, especially if it is working to bring outdoor air indoors.

Figure 2.7 shows a breakdown of the type of double skin façade and ventilation modes applied in the research article sample. The preferred type of DSF is the box-window which is largely a matter of convenience for laboratory testing as well as in application where dimensions can be mirrored off typical one-storey building levels. Multi-storey double skin facades are relatively popular due to application in high-rise buildings.

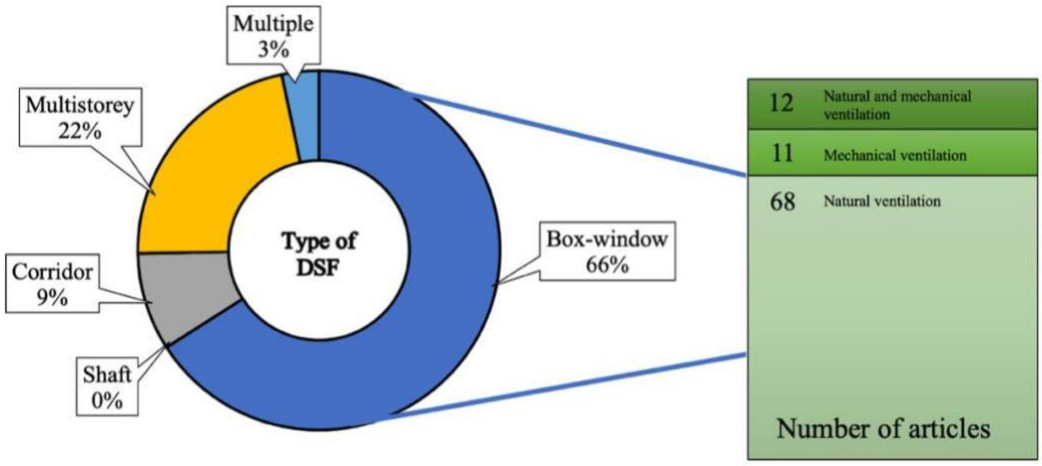


Figure 2.7 Trend Analysis of DSF Type and Ventilation Mode

While the preferred ventilation mode of double skin facades is natural ventilation, this does not necessarily mean researchers have assessed the outdoor air ventilation capacity, and rather that this is the means of removing heat from the cavity. Hybrid ventilation of the DSF cavity is as common as looking at purely mechanically ventilated cavities, which shows the awareness of the difficulty of controlling mass flow rate in the cavity, but the energy intensiveness of applying fans.

Table 2.3 Building type, DSF typology and Ventilation Mode

Author and year of publication	Type of DSF	Ventilation mode	DSF Orientation	Case study building
Balocco (2002)	Box-window	NV	South	Experimental Rig
Gratia and De Herde (2004)	Multi-storey	NV	South and North	Office
Park et al. (2004)	Box-window	NV	South	Experimental Rig
Stec et al. (2005)	Multi-storey	NV	Sunshine-oriented	Experimental Rig
Stec and Paassen (2005)	Box-window	MV & NV	South	Experimental Rig
Ballestini et al. (2005)	Multi-storey	NV	North-West, South-East	Dismissed Silk factory
Gratia and De Herde (2007)	Multi-storey	NV	All	Middle-size Office
Xu and Ojama (2007)	Multi-storey	NV	South	Two-storey Residential House
Hoseggen et al. (2008)	Multi-storey	NV	East	Office
Pappas and Zhi (2008)	Box-window	NV	Sunshine-oriented	Experimental Rig
Jiru and Haghihat (2008)	Box-window	MV	Sunshine-oriented	Experimental Rig
Wong et al. (2008)	Multi-storey	NV	All	18-storey High-rise Office
Chan et al. (2009)	Box-window	NV	South-West	Typical Office
Fallahi et al. (2010)	Box-window	NV	South	Experimental Rig
Gavan et al. (2010)	Box-window	MV	West	Experimental Rig
Zeng et al. (2012)	Box-window	NV	South	Experimental Rig
Kuznik et al. (2011)	Box-window	MV	South	Experimental Rig
Kim and Park (2011)	Box-window	NV	South	Experimental Rig
Ghadamian et al. (2012)	Box-window	NV	West/South	Experimental Rig
Pasut and De Carli (2012)	Box-window	NV	Sunshine-oriented	Single-storey Commercial Office
Valentin et al. (2013)	Corridor	MV	South	Office
Andelkovic et al. (2015)	Multi-storey	NV	North-East, South-East	Office
Larsen et al. (2015)	Corridor and Multi-storey	NV and MV	West	High-rise Office
Andelkovic et al. (2016)	Multi-storey	NV	South-East	Office
Shen and Li (2016)	Box-window	NV	All	Experimental Rig

Blanco et al. (2016)	Multi-storey	NV	South	Office
Peng et al. (2016)	Box-window	NV	South	Experimental Rig
Pomponi et al. (2016)	Multi-storey	NV	All	Typical Office
Dama and Angeli (2016)	Box-window	NV	South	Experimental Rig
Lee et al. (2016)	Box-window	NV	Sunshine-oriented	Experimental Rig
Wang et al. (2016)	Box-window	NV & MV	South	Experimental Rig
Elarga et al. (2016)	Bow-window	NV	West	Office
Peng et al. (2016)	Box-window	NV	South-West	Office
Nastase et al. (2016)	Box-window	NV	South	Experimental Rig
Barbosa and Ip (2016)	Multi-storey	NV	North	Office
Sanchez et al. (2016)	Box-window	NV	South	Experimental Rig
Dama et al. (2017)	Box-window	NV	North and South	Experimental Rig
Su et al. (2017)	Box-window	NV	Sunshine-oriented	Experimental Rig
Hassanli et al. (2017)	Corridor	NV	All	Tall Building
Hu et al. (2017)	Corridor	NV	All	Tall Building
Luo et al. (2017)	Box-window	NV & MV	South	Experimental Rig
Kim et al. (2017)	Multi-storey	NV	Sunshine-oriented	Commercial Office
Vatavalis and Bikas (2017)	Multi-storey	NV	South and West	Office
Inan et al. (2017)	Box-window	MV	Sunshine-oriented	Experimental Rig
Su et al. (2017)	Box-window	NV	South	Experimental Rig
Pomponi and D'Amico (2017)	Box-window	N/A	All	Office
Ioannidis et al. (2017)	Box-window	NV & MV	South	Three-floor Office
Slakovic (2017)	Box-window	NV	East and West	Industrial Facility
Wang et al. (2017)	Box-window	NV	South	Office
Bielek et al. (2017)	Corridor	NV	All	Laboratory Room
Bueno et al. (2017)	Box-window	NV & MV	South	Experimental Test Chamber
Alberto et al. (2017)	All four types	NV	All	Office

Kilaire and Stacey (2017)	Cascade	NV & MV	Sunshine-oriented	Office
Kimouche et al. (2017)	Box-window	NV	Sunshine-oriented	Theoretical
Wen et al. (2017)	Box-window	NV	Sunshine-oriented	Laboratory
Hassanli et al. (2018)	Corridor	NV	All	Tall Building
Zomorodian & Tahsildoost (2018)	All four types	NV & MV	South-East & North-West	Office
Aleksandrowicz and Yezioro (2018)	Box-window	MV	All	Office
Souza et al. (2018)	Box-window	NV	West	Experimental Test Cell
Luo et al. (2018)	Box-window	NV	South	Laboratory
Hassanli et al. (2018)	Corridor	NV	All	Tall Building
Kim et al. (2018)	Box-window	NV	South	Office
Yan et al. (2019)	Box-window	NV	Sunshine-oriented	Theoretical
Inan and Basaran (2019)	Box-window	MV	All	Office
Li et al. (2019)	Box-window	NV	South	University Building
Li et al. (2019)	Box-window	NV	South	University Building
Yanjin et al. (2019)	Box-window	NV	South	University Building
Barbosa and Alberto (2019)	Multi-storey	NV	South	University Building
Lee et al. (2019)	Multi-storey	NV	South	Office
Iken et al. (2019)	Box-window	NV	South	Generic Office
Yoon et al. (2019)	Box-window	MV	South	25-storey Apartment
Seo et al. (2019)	Multi-storey	NV	South	Office
Bielek et al. (2019)	Box-window	MV	Sunshine-oriented	Office
Sung and Kim (2019)	Multi-storey	NV & MV	South	University Building
Yahiaoui (2020)	Box-window	NV & MV	South-East	Experimental Test Cell
Lee and Park (2020)	Box-window	NV	South-West	Laboratory
Li et al. (2020)	Box-window	NV	South	Theoretical
Radmard et al. (2020)	Box-window	NV	South-West	Office
Shakouri et al. (2020)	Multi-storey	NV	South	Office

Yang et al. (2020)	Box-window	NV & MV	North	Office
Wang et al. (2020)	Box-window	NV	All	Experimental Test Room
Zhu et al. (2020)	Box-window	NV	Sunshine-oriented	Theoretical
Sarglou et al. (2020)	Corridor	NV & MV	All	High-rise Office
Gelesz et al. (2020)	Box-window	MV	All	Office
Pourshab et al. (2020)	Multi-storey	NV	South	Office
Ioanniddis et al. (2020)	Box-window	MV	South	Experimental Test Room
Preet et al. (2020)	Box-window	NV & MV	South	Experimental Chamber
Srisamranrungruang and Hiyama (2020)	Box-window	NV	South	Theoretical Model Room
Tao et al. (2021)	Box-window	NV	Sunshine-oriented	Experimental
Hou et al. (2021)	Box-window	NV	South and North	Office
Kim (2021)	Box-window	NV	Sunshine-oriented	Office
Sotelo-Salas et al. (2021)	Box-window	NV	Sunshine-oriented	Experimental Test Cell

2.2.3 DSF Cavity Geometry and Layout

Cavity geometry comprises the depth and height of the DSF as well as the shape of the individual construction layers, and these parameters have a direct influence over the ventilation and thermal performance of a DSF. A study [89] at the start of the 21st century determined that a wider channel was required in the summer for a sensible solar cooling effect, denoted by a reduction of 27.5% in overheating with a width of 35 centimetres (cm) compared to only 7% with a width of 7cm. Similarly, the mass flow rate in the channel increases with cavity width and stack effect increases, with a maximum impact when the cavity width is 20-30cm. Some of the more recent studies further confirm this exact relationship between cavity depth and DSF performance. Saroglou et al. [64] found that for a corridor-type DSF for high rise buildings in Tel-Aviv, Israel, increasing the cavity width from 0.2 metres (m) to 0.5m, cooling loads decrease significantly, but there are still substantial reductions with 0.5m to 1.0m and 1.0m to 2.0m. Similarly, using EnergyPlus, Alberto et al. [74] found that increasing the depth of the cavity from 25cm to 100cm resulted in a decrease in energy demand of 9.5% in Indoor Air Curtain ventilation mode.

Interestingly, these findings are not consistent across other hot climates. For example, Kim [90] found that an increase in cavity depth increases the air temperature with an average temperature ranging from 26ºC to 50ºC observed on the inner façade for a CFD analysis of 13 box-window DSF models under climatic conditions in Saudi Arabia for office buildings. Like this study, Wang et al. [91] found that for a naturally ventilated DSF in Changshin, China, an increase in cavity thickness led to a rise in the inner glazing temperature. For a smart double-skin façade integrating vanadium dioxide (VO_2) in Morocco during summer, Iken et al. [92] found through CFD analysis that increasing the air gap thickness above 50mm does not enhance the convection-radiation interaction, the indoor surface temperature stays at around 25ºC except for the 10mm air gap in which indoor surface temperature reaches 27ºC.

Besides focussing on the cavity depth, there are numerous studies which look at DSF height. For example, Wen et al. [93] conducted CFD analysis and experimental testing of a DSF building in Wuhan, China and discovered that when the DSF height is 0.3-0.45m, the air velocity of the outlet reaches the highest velocity of 4m/s for an opening height of 0.05m. However, when the height of the outlet increases further to 0.6m, the air velocity of the outlet decreases to around 2.5-3m/s. Looking at the performance of a DSF and an adjacent building for the purpose of providing indoor space ventilation, Tao et al. [94] addressed the influences of DSF and room configurations, together with buoyant-driven ventilation, through an experimentally validated

numerical model of an NVDSF to achieve an optimal vent height between inlet and outlet is around 0.2-0.3m. For a fully glazed building in the United Arab Emirates (UAE), Radhi et al. [95] used CFD to assess a Climate Responsive Façade System (CRFS) thermal performance on cooling loads. Results suggested that heat transfer coefficients increase at higher levels because flow gets warmer as it rises towards the top of the cavity, so floors at higher levels gain the most heat. This is important findings for multi-storey DSFs which span across the height of buildings.

As there is a relationship between the depth and height of a DSF cavity on both ventilation and thermal performance, some work has been carried out looking specifically at aspect ratios. For example, Lee et al. [96] found that for a box-window DSF with an air cavity length of 8 meters and depth of 1 meter, there is a higher potential of overheating than the cases with 1 meter in length to 1 meter in depth, and 2 meters in length to 1 meter in depth which both produced relatively lower mean air temperature through better heat dissipation. Similarly, Inan and Basaran [69] used experimental and CFD studies to evaluate the aspect ratio for a box-window DSF from 0.10 to 0.16 for three flow velocities. The flow was in the thermal and hydrodynamic entrance region for almost all nine experiments. The convection heat transfer coefficient values for each case were relatively higher in the entrance regions than fully developed regions regardless of dimensions. Guardo et al. [97] found that an increase in the length-to-depth ratio causes a decrease of efficiency in terms of solar load gains in Mediterranean climates.

Typically, researchers do not tend to deviate from the typical geometric layouts of a DSF as laid out in Figure 2.1(a) in Section 2.1.2. However, Kimouche et al. [98] assessed the effect of angle inclination on the heat transfer between non-tilted and tilted walls using CFD software ANSYS. Results showed the maximum heat transfer rate, as well as maximum mass flow, was found for angle alpha = 0 degrees, and for – 2 degrees suggesting vertical orientation as most appropriate but allowing for flexibility of architectural design.

The sizing and location of openings within a DSF building also affect overall building ventilation performance. For example, a reduced scale model experiment and CFD analysis was carried out by Ding et al. [99] for a prototype eight-storey office building with an atrium space in the north side with the south façade being a DSF with a solar chimney connected above. The authors recommend that the opening areas between the outside and atrium not be less than 16 metres squared (m^2), i.e., $2m^2$ per floor. Although larger openings can increase the ventilation rate, they are disadvantageous to the upper floors in terms of pressure difference, and the growth

rate of air change rate decreases sharply when areas over $2m^2$ are used. A similar study by Tao et al. [94] found similar sizing to be appropriate; windows on the back wall achieve 85-93% ventilation rates from window sizes 0.18-2.88m^2.

There is still a focus on the constructional aspect of a double skin façade on its ventilation and thermal performance. For example, Tao et al. [100] utilised computational fluid dynamics to model a naturally ventilated DSF (NVDSF) with six outlet louvres with adjustable angles between 30 and 150 degrees. The ventilation rate improves by 9.7% and 4.2% with angles of 45^o and 67.5^o, respectively. Conversely the ventilation rate can be reduced by as much as 35% with a louvre angle of 150^o. In a later study, Tao et al. [101] continued computational studies of a NVDSF where the authors looked at how changing the area, height, and aspect ratio of the cavity impacts ventilation flow rate and indoor air quality in and adjacent room for transition seasons, Autumn, and Spring. The highest natural ventilation rate is achieved with bigger air supply vent size, lower installation height and narrower aspect ratio. Yoon et al. [102] also looked at the importance of aspect ratio on DSF performance, but also parameters such as opening-to-glazing ratio and solar heat gain coefficient (SHGC) for a dynamic operating DSF on an office building in Korea. The results for summer conditions indicate that a higher SHGC increases incoming airflow rate, and a cooling effect is greater when cavity depth increases to 0.9m. For winter, when ventilation rates were kept to minimum requirements, indoor air temperatures were 2^oC warmer.

i. Trend Analysis and Research Gaps

The following summary table concludes that various researchers have explored an increasing cavity depth between 0.07m and 1.2m with there being general agreement that the optimal cavity depth for increased airflow rate being less than 0.50m. For thermal performance, an increased cavity depth will reduce overheating to an extent but can increase inner skin glazing, and an increased height of cavity sees improved stack effect, and higher heat transfer coefficients. Determining an optimal aspect ratio between cavity height and depth is therefore important.

In terms of DSF opening size, it is understood that smaller vent openings are appropriate for colder conditions, and larger vent openings for warmer conditions. In terms of airflow path, the ventilation and thermal performance of the outdoor mode is directly proportional to wind speed and solar radiation. Adding to what was identified in terms of cavity height and depth in the previous section, a multi-storey DSF seems to be most effective across various climates.

Table 2.4 Impact of DSF Cavity Geometry on Airflow Rate and Cavity Air Temperature

Author	Ventilation or thermal performance focus	Impact on airflow rate or cavity air temperature	DSF geometry
Balocco (2002)	Both	Mass flow rate increases with cavity width, 35cm achieves 27.5% in overheating	7cm, 15cm, 25cm and 35cm depth
Guardo et al. (2009)	Both	Increase of length-to-depth ratio reduces solar load efficiency due to increases in Reynolds number	DSF heights of 4m and DSF cavity depths of 0.4m and 0.8m
Mingotti et al.(2011)	Ventilation	Taller façade height increases buoyancy drive of airflow whilst smaller openings perform better in cold seasons, and larger openings perform better in warmer seasons	0 to 3m^2 effective area
Radhi et al. (2013)	Thermal	HTC increases with DSF height and decreases as cavity depth reduces	DSF cavity depth from 0.7 and 1.2m
Lee et al. (2016)	Ventilation	Smaller aspect ratio improves heat dissipation and lower mean air temperature	Aspect ratios including of length 8m, depth 1m; length 1m, depth 1m and length 2m, depth 1m
Inan et al. (2017)	Both	Temperature gradient decreases along cavity height	Aspect ratio from 0.10 to 0.16
Alberto et al. (2017)	Thermal	Increasing depth from 25cm to 100cm decreased energy demand by 9.5%	DSF cavity depth from 25cm to 100cm
Kimouche et al. (2017)	Thermal	Maximum mass flow rate and heat transfer rate found for angles of 0 and -2 degrees	wall angle inclination from $\alpha = -10°$ and $\alpha = +10°$.
Wen et al. (2017)	Ventilation	DSF height of 0.3-0.45m, air velocity reaches 5m/s. and for 0.6m, it reduces to 2.5-3m/s	DSF height between 0.1m and 0.6m and DSF opening height of 0.05m
Iken et al. (2019)	Thermal	Indoor surface temperature decreases by 2C in summer and increases by 3C during a sunny winter day, air velocity in cavity is higher in winter than summer	DSF cavity depth of 10, 25, 50 and 75mm
Wang et al. (2019)	Ventilation	Airflow rate of 0.08kg/s achieved when DSF height is 1.5m	DSF cavity depth of 0.1m to 0.4m and DSF height up to 1.5m
Sarglou et al. (2020)	Thermal	Increasing cavity widths decreases cooling loads significantly	DSF cavity depth from 0.2m to 2.0m
Tao et al. (2021)	Ventilation	Optimal cavity depth is 0.2m and optimal vent height is 0.2-0.3m with a reduction in heat transfer of 16% and 26% per 0.1m shortening in cavity depth and DSF height	DSF cavity depth and DSF height
Kim (2021)	Thermal	Airflow speed increases with opening size but airflow temp decreases, increase in cavity depth increases air temp	Cavity depths of 0.3m to 0.6m

2.2.4 DSF Construction Layers

Asides from the geometric layout of a double skin façade, the material layers that comprise the construction of a DSF system will also impact the ventilation and thermal performance. In this review, this includes glazed external and inner skins, perforated and opaque ventilated facades, and shading devices.

i. Glazed External and Inner Skins

The obvious advantage that a DSF has over existing building facades is an additional layer of construction to resist external conditions such as wind loads, direct solar radiation, and rain. Therefore, many researchers have compared the performances of DSFs and Single Skin Facades (SSF) from the perspective of differentiating optical, material, and construction properties. Hamza [103] used dynamic simulation software IESVE to assess cooling loads of DSF office buildings in Cairo, Egypt. A reflective outer skin DSF can achieve better energy savings than an SSF with reflective glazing. On the other hand, transparent DSF increases cooling loads compared to SSF with a reflective skin. The author concluded that using a lower shading coefficient and g-value than transparent glass on the external skin of a DSF offers protection from direct solar radiation without compromising visual continuity.

In a similar study [97], the optical properties of the external skin have the most significant effect on the reduction of solar load entering a building in Mediterranean climates via an Active Transparent Façade (ATF). A comparison of the heat losses of a single skin façade (SSF) and DSF for office buildings in Istanbul, Turkey, was assessed via a CFD method. The purpose of this is to show the effect of a closed cavity DSF on building energy demand in a winter period – the SSF heat loss is 40% higher than DSF.

Investigation of new materials has also started, such as the thermal and energy performance of a smart double-skin façade integrating Vanadium Dioxide (VO_2), an optically smart thin material and high absorbing aluminium nitride coating to control the greenhouse effect [92]. Using 2D CFD modelling of the new DSF applied to a south-facing wall on a building in Morocco, results found that indoor surface temperature has decreased by around 2ºC during summer and increased by about 3ºC during a sunny winter day.

Some studies have looked at both the external and internal skin properties together. For example, Chan et al. [104] used measured data from an experimental setup and an EnergyPlus model for

a typical office building in Hong Kong to assess the energy performance of a DSF depending on glazing type, positioning, and layers. Results indicate that compared to an SSF with single absorptive glazing, a DSF with single clear glazing as the inner pane and double reflective glazing as the outer pane can provide an annual saving of around 26% in building cooling energy. A decade later, Wang et al. [87] found conflicting results for the Yangtze River Area in China in that the thermal performance of an NVDSF with interior double glass is better than exterior double glass for both heating and cooling seasons.

Gratia and De Herde [81] assessed the glazing ratio of the inner skin façade in a DSF office building using thermal analysis software, TAS. In winter conditions, if the interior façade is glass, the cavity air temperature is always lower, i.e., with clear sky conditions at 1 pm, if the interior façade is glazed 39.5%, the cavity air temperature is 32.3ºC compared to 26.5ºC when 74.1% glazed.

There is some scepticism surrounding whether the performance of DSF is greater than an SSF with improved U-values, as suggested by the results in a study by Hoseggen et al. [105]. The applicability of a DSF was explored by Chou et al. [71] by optimising the relationship between window-to-wall ratio (WWR), shading coefficient (SC), and envelope thermal transfer value (ETTV) of a building. These values helped evaluate the solar radiation gain component through a glazed DSF fenestration system as a higher WWR (0.9) diminishes the potential of a DSF to reduce solar heat gain. However, a building with a lower WWR of 0.3 saw the DSF produce an ETTV reduction of up to 45%. As the shading coefficient of the inner glass increased from 0.3 to 0.7, the ETTV also increased from 18W/m^2 to 59.6W/m^2. This relationship suggests an optimal balance between SC and ETTV for a required WWR.

Integrated building energy simulations and CFD to establish boundary conditions such as outdoor conditions, cavity, and indoor environment found that applying a climate responsive façade system (CRFS) in hot-arid climates such as the UAE reduces solar gains internal spaces [95]. On a typical summer day, between 17% and 20% of cooling energy can be saved, and the parameters which impact this the most are floor level related to screening height, followed by glazing properties (SHGC) and cavity depth. Compared to an SSF, the trapped air and solar gains in the CRFS are higher, although the SSF receives a higher amount of radiation. In addition, the CRFS is more effective in orientations with high angles of incidence (closer to 90 degrees).

ii. Perforated and Opaque Ventilated Facades

As an extension of various materials integrated into DSF design, there has been an increased number of studies exploring the use of perforated and opaque facades. Perforated facades refer to the external layer of the double skin façade which has many small holes, allowing for ventilation. Researchers tend to vary the percentage of the perforation to balance ventilation and thermal performance. Opaque ventilated facades are when either the external or inner skin (or both) of a double-skin façade construction is an opaque material, rather than transparent glazing.

Barbosa and Alberto [106] studied the effect of a north-oriented multi-storey, indoor air exhaust DSF made of both glazing and perforated metal sheet on the thermal performance in Rio de Janeiro, Brazil. The building energy simulation (IESVE) results, compared to CFD simulations previously published by Barbosa and Ip [107] showed a DSF made with glazing presented a clear dependence on solar radiation incidence to induce cavity stack effect. In contrast, a DSF with perforated metallic screens showed a relatively constant airflow over the year. Blanco et al. [108] conducted a case study in Spain using EnergyPlus to assess and optimise perforated metal sheet double-skin facades. For the coldest areas, the total building load savings are around 20% of energy consumption and 45% for hottest regions. However, this did not include the impact of the shape and size of perforation holes.

Another study looked at balancing natural ventilation, daylight, and thermal effect for a building with a double-skin perforated façade (DSPF) [109]. The results from EnergyPlus and daylighting software DIVA found that a perforated percentage of 50% is the optimum rate for balancing natural ventilation and daylight in spring when the climate is NV favourable but is changeable depending on time and local weather.

In a similar study, the efficiency of an opaque NVDSF made of a cement sheet built in a test cell in Brazil, including a numerical analysis using ANSYS CFX software, was explored by Souza et al. [110]. The results included maximum temperature values of 25.6ºC on the inner façade and 23.6ºC on the inner face of the test cell obtained while the outdoor temperature is 23.1ºC, demonstrating a reduction of temperature across the cavity by inhibiting direct solar radiation.

iii. Shading Devices

Based on the sun path in temperate climates, the southern façade of a building will experience the highest solar gains making horizontal shading more applicable as the best orientation for

these is south. The southern-oriented façade sees higher solar gain in winter, whilst eastern and western facades are most critical in summer due to the differences in solar azimuth angle. Vertical shading is most applicable for north orientation. For the tropics, this is reversed. At the equator, the application is the same. Wang et al. [79] employed an improved zonal approach for the dynamic modelling of a mechanically ventilated box-window double-skin façade in China's hot summer and cold winter zone, validated by experimental data. Increasing the slat angle can decrease the inner glass temperature and heat gains by a greater range than the ventilation rate. For example, a slat angle of 60 degrees can reduce heat gains by 63% compared to 0 degrees, and the temperature decrement of the inner glass reaches 1.5ºC. These results align with a previous experimental study of a mechanically ventilated box-window double-skin façade in the CETHIL laboratory in France [78]. If the sun-shading device is closed, the outdoor air cavity and sun-shading device itself will have higher temperatures than when open. Therefore, shading devices have a significant effect on the thermal performance of a DSF ([111],[112]).

In recent years, there has been some interest in improving the thermal mass of DSF systems via the use of concrete and cement elements. For example, Fallahi et al. [113] found that for a mechanically ventilated box-window double skin façade (MVDSF), replacing the Venetian blind slats with concrete slabs can save 21-26% of energy in summer and 41-59% in winter. However, the authors did note some inefficiency in a naturally ventilated double skin facade (NVDSF) with thermal mass due to the increased stack effect and airflow rate in the air cavity.

Wang et al. [91] found that for Changsha, China (HSCW zone), increasing the slat angle decreases the temperature of the inner glazing in a box-window DSF. The airflow rate reduced when this angle was within 0-60 degrees but increased when larger than 60 degrees. This applies to a naturally ventilated cavity, but Kuznik et al. [114] changed the tilt angle of blinds between 0 and 90 degrees for three different controlled ventilation rates (200,400 and 600m^3/h). This resulted in the temperature inside the interior glass decreasing when the tilt angle increases across an increased ventilation flow rate for a box-window DSF.

There have been some studies that deviate from the typical use of horizontal Venetian blinds within the cavity, as demonstrated by Kim et al. [62] who investigated the thermal and daylighting effects of a buffer type DSF system with interior and exterior slat type blinds for a cooling period in Daejeon, South Korea using EnergyPlus and daylighting software, Daysim. While external blinds applied to a non-DSF building could lead to a high reduction of building thermal loads, interior blinds increase thermal loads compared to baseline, with the highest drop

for a middle blind in the cavity. Similarly, Pourshab et al. [115] evaluated a south-oriented multi-storey double-glazed façade with horizontal (90-degree angle) and vertical (45-degree angle) louvers to increase natural airflow in office buildings in Isfahan, Iran, using the CFD technique, ANSYS software. In the DSF with horizontal louvers, the buoyancy forces inside the cavity are more substantial, and the ventilation rate is higher than the model with vertical louvers.

In addition, due to stronger convective flow in the cavity with horizontal louvers, the heat flux on the interior glass is higher than in the cavity with vertical louvers. This phenomenon causes part of the heat inside the cavity to transmit through the interior skin to the occupied spaces while the heat flux of the internal glass in the case of vertical louvers is very low and close to zero due to the blocking of solar radiation. Other researchers have confirmed that for multi-storey DSF, the best position for louvers is closer to the outer layer to allow for sufficient airflow on either side while maintaining an adequate distance from the interior glass [81].

A more recent development in research on the shading devices within a DSF system includes the material and multi-purpose function that blinds could potentially offer, including photovoltaic blinds. Luo et al. [116] conducted experimental and comparative studies of the performance of a photovoltaic (PV)-blind embedded box-window double-skin façade in a climate chamber to simulate HSCW conditions for China. The study's results showed that the photovoltaic blinds double skin facade (PVB-DSF) could save about 12.16% and 25.57% of energy in summer compared with conventional DSF with and without shading blinds. Furthermore, the performance of the PVB-DSF is less sensitive to PV-blind angle than PV-blind spacing as the averaged SHGC at noontime for different blind spacings of 2.5cm, 3.5cm, and 4.5cm are 0.2015, 0.2596, and 0.3112, respectively. In a following study, Luo et al. [117] concluded that the box-window PVB-DSF could save about 1121 Wh/(m^2day) of heating energy in winter compared with the brick wall. The PVB-DSF can achieve better thermal performance (heat gain could be 73.74%) but lower power generation efficiency than semi- transparent PV-DSF with an electrical efficiency of less than 6% for ventilation and non- ventilation modes.

Another area of interest has been a phase change material (PCM) blind system, as developed by Li et al. [118] for a box-window DSF. This study evaluates the performance of a PCM blind system for a typical DSF building using validated numerical models. Compared to traditional aluminium blinds, the PCM system was thermally performing better with a 2.2ºC (about 5.5%) decrease in average cavity air temperature. It was able to keep the average air temperature in the DSF below 35ºC during a summer monitored period, and the temperature of the inner skin

reduced up to 2.9ºC compared to external skin surface temperature. The authors noted that a blind tilt angle of 30 degrees resulted in the lowest surface temperature of PCM layer blind, possibly because it matches the local latitude better. Another parametric study [119] conducted with CFD simulation in ANSYS Fluent 14.5 highlighted no significant difference between DSF air temperature for the two different PCM types. The authors noted needing careful selection to consider optimal energy storage capacity and melting temperature range suitable to the local environment.

Another example of alternative shading involves the concept of a green wall situated within the cavity of the DSF. Stec et al. [120] explored this idea at TU Delft by implementing plants in a box-window DSF cavity and comparing its thermal performance to traditional blinds. Generally, the temperature of each layer of the DSF was much lower with plants than blinds. For the same solar radiation, the temperature rise of the plant was about twice lower than for blinds. Additionally, the plant's temperature never exceeded the temperature of 35ºC when blinds could exceed 55ºC. Installation of plants in the DSF allows for reduced cooling capacity by almost 20%. This study did not cover the influence of plants on the heating system. However, the authors noted that plants might cause increased heat demand in buildings than a system with blinds.

iv. Trend Analysis

Figure 2.8 displays the trends in focus on aspects of a double skin façade's construction through the two decades of research examined in the sample of articles.

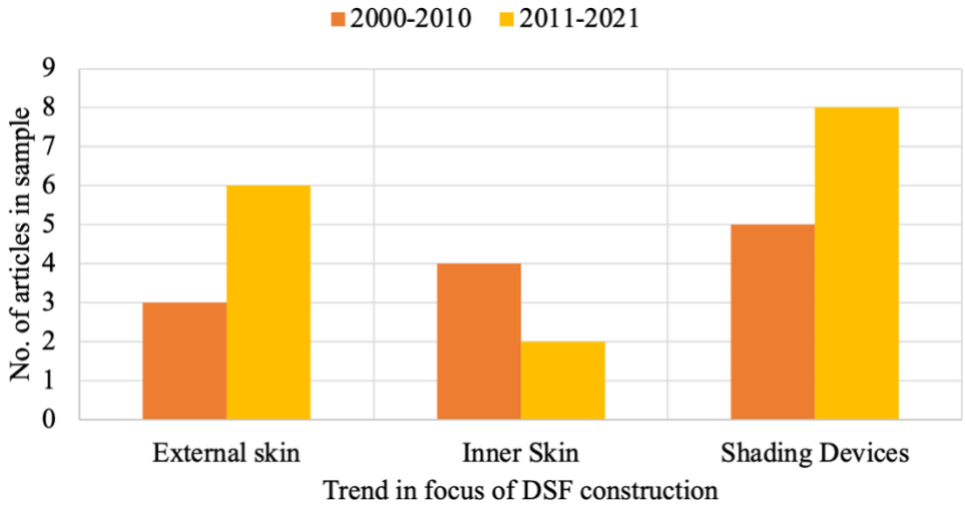


Figure 2.8 Trends in Focus of DSF Construction

Out of the papers which focussed specifically on the impact of the external skin, inner skin, or shading devices on DSF performance, it is notable that there has been a recent peak in the focus on shading devices. This is in line with the analysis conducted in Section 2.2.1 which suggested

that warmer or “sunny” climates reign dominant in current DSF research and is further confirmed by the rise of smart or photovoltaic external skins in the last decade, highly applicable in climates with high levels of solar irradiance.

The following summary table confirms that many researchers have compared the performance of a single skin façade (SSF) and DSF and found that overall, the DSF outperforms the SSF however, in some cases, an SSF with advanced glazing properties might perform equally. One of the main issues with improving the optical properties of the DSF’s external skin for the purpose of reducing solar heat gains and therefore overheating in the presence of high solar irradiance is that it will have a negative impact in winter conditions by taking away the benefit of solar heat gains for heating. Therefore, there needs to be a balance in the glazing properties in terms of transparency, shading coefficient, and solar heat gain coefficient (SHGC) to optimise performance in all ambient conditions.

Glazing type and positioning on the external and inner skin have a significant impact on the thermal performance of a DSF. There are conflicting results as to whether double glazing as the external or inner skin is better depending on the climatic conditions, and it is important that performance is assessed for different angles of incidence throughout the day in all seasons. If the inner skin of a DSF represents the building envelope, the Window-to-Wall Ratio (WWR) will have a considerable influence on a DSF’s potential to reduce solar heat gain. The properties of shading devices which are most influential on the ventilation and thermal performance of a DSF are the slat angle and spacing between them. It is largely agreed amongst researchers that increasing the slat angle decreases the inner glass temperature and decreases the airflow rate. If the shading device is closed, its own temperature will increase and in turn increase the temperature of the cavity. Some researchers have concluded that slat angle has a more significant impact on DSF performance than airflow rate so this should be considered.

Table 2.5 Impact of Material Layers and Blinds on DSF Ventilation and Thermal Performance

Author	Hemisphere	DSF typology	Construction parameters	Impact on airflow rate or cavity air temperature
Stec et al. (2005)	Northern	Multi-storey	Shading device - Plant blind system	Temp of DSF layers much lower with plants than blinds, with temp rise twice lower than blinds never exceeding 35C – reduces cooling capacity by almost 20%.
Gratia and de Herde (2007)	Northern	Multi-storey	Inner skin Glazing ratio of the inner skin façade	If interior façade is glazed 39.5%, cavity air temperature is 32.3C compared to 26.5C when 74.1 glazed.
Hoseggen et al. (2008)	Northern	Multi-storey	Inner skin SSF and DSF	Performance of DSF not much greater than SSF with improved U-values.
Hamza (2008)	Northern	Multi-storey	External glazing – reflective (R), transparent (T), shading coefficient and g-value	Reflective DSF better than reflective SSF. Transparent DSF increases cooling loads compared to reflective SSF. Lower SC and g-value than transparent glass blocks direct solar radiation.
Guardo et al. (2009)	Northern	Box-window	Glazing - DSF and SSF	The SSF heat loss is 40% higher than DSF.
Chan et al. (2009)	Northern	Box-window	Inner skin Glazing type, positioning, and layers	An SSF with single absorptive glazing, a DSF with single clear glazing as the inner pane and double reflective glazing as the outer pane can provide an annual saving of around 26% in building cooling Energy.
Chou et al. (2009)	Theoretical	Box-window	Inner skin Window-to-Wall ratio, Shading Coefficient, and Envelope Thermal Transfer Value (ETTV)	The results suggest that a higher building WWR (0.9) diminishes the potential of a DSF to reduce solar heat gain. However, a building with a lower WWR of 0.3 saw the DSF produce an EETV reduction of up to 45%. As the Shading Coefficient (SC) of the inner

				glass increased from 0.3 to 0.7, the ETTV also increased from 18W/m2 to 59.6W/m2.
Fallahi et al. (2010)	Northern	Box-window	Shading device - Thermal mass, concrete slabs	Concrete slabs for blinds and outer skin increase airflow rate which is beneficial in summer but not winter. An MVDSF, replacing the Venetian blind slats with concrete slabs can save 21-26% of energy in summer and 41-59% in winter.
Gavan et al. (2010)	Northern	Box-window	Shading device - Slat angle and open/closed position	Airflow rate follows sun-shading angle in impact on thermal performance. If the sun-shading device is closed, the outdoor air cavity and sun-shading device itself will have higher temperatures than when open.
Kuznik et al. (2011)	Theoretical	Box-window	Shading device - Tilt angle	This is the same across controlled ventilation rates of 200,400 and 600m3/h. Tilt of blind angle between 0 and 90 degrees decreases interior glass temperature.
Radhi et al. (2013)	Northern	Multi-storey	Inner skin Screening height, followed by glazing properties (SHGC) and cavity depth.	N/A – only thermal performance. In summer, 17-20% of cooling energy can be saved. Compared to SSF heat gains in CRFS are higher but SSF receives higher amount of radiation. CRFS more effective in orientations with high angles of incidence.
Barbosa and Ip (2016)	Southern	Multi-storey	DSF with glazing and perforated metal sheet comparison	Perforated DSF has a relatively constant airflow over the year. Wind pressures on the building surface significantly impact cavity ventilation in both cases. Glazing DSF has a clear dependence on solar radiation incidence to induce cavity stack effect.

Blanco et al. (2016)	Northern	Multi-storey	Perforated metal sheet DSF	Did not include the impact of the shape and size of perforation holes. Perforated metal sheet outer skin results in total building load savings around 20% for coldest areas, and 45% for hottest regions.
Wang et al. (2016)	Northern	Box-window	Shading device - Slat angle	Ventilation rate not as effective as increasing slat angle. Increasing slat angle can decrease inner glass temp and heat gains by greater range than ventilation rate for MVDSF. Angle of 60 degrees can reduce heat gains by 63% compared to 0 degrees.
Luo et al. (2017)	Northern	Box-window	Shading device - PV-blind spacing and angle	N/A – only thermal performance. PVB-DSF could save about 12.16% and 25.57% of energy in summer compared to conventional DSF with and without shading blinds. PV-blind angle has lower impact than PV-blind spacing on SHGC.
Kim et al. (2018)	Northern	Multi-storey	Shading device - Exterior and interior slat positioning	N/A – only thermal performance. While external blinds applied to a non-DSF building could lead to a high reduction of building thermal loads, interior blinds increase thermal loads compared to baseline, with the highest drop for a middle blind, i.e., DSF cavity with blinds fixed horizontally at 90 degrees.
Luo et al. (2018)	Northern	Box-window	Shading device - PV-blind spacing and angle	Perform betters than conventional DSF in both ventilation and non-ventilation modes. PVB-DSF could save about 1121 Wh/(m^2day) of heating energy compared to brick wall. Heat gain could be 73.74% higher than conventional DSF.

Barbosa and Alberto (2019)	Northern	Multi-storey	North-oriented multi-storey, indoor air exhaust DSF made of both glazing and perforated metal sheet	NV rates and increased solar heat transmitted towards user space. Increasing the outer layer perforation rate from 20-40% showed little or no improvements thermally, explained by slightly increased.
Wang et al. (2019)	Northern	Box-window	Shading device -Slat angle	Airflow rate reduced when slat angle was within 0-60 degrees but increased when larger than 60 degrees. Increased slat angle decreases the temp of the inner glazing for Changsha, China (HCSW).
Li et al. (2019)	Northern	Box-window	Shading device PCM blinds	N/A – only thermal performance. No significant difference between DSF air temp for two different PCM types.
Pourshab et al. (2020)	Northern	Multi-storey	Shading device - horizontal (90-degree angle) and vertical (45-degree angle) louvers	Horizontal louvers cause higher heat flux on interior glass than vertical. Due to stronger convective flow in the cavity. Vertical louvers block more solar radiation.
Wang et al. (2020)	Northern	Box-window	Inner skin Glazing type, positioning, and layers	N/A – only thermal performance. The thermal performance of an NVDSF with interior double glass is better than exterior double glass for both heating and cooling seasons.
Srisamranrungruang and Hiyama (2020)	Northern	Box-window	Perforated DSF	50% perforated percentage is optimum rate for balancing natural ventilation and daylight in spring – when NV favourable 60% in spring, 10% in autumn and 30% through a year. When sky is clear, optimum percentage is 30% in spring and 10% in autumn, 60% for overcast.

2.3 Factors affecting Building Integration of Double Skin Facades

The literature did not have many reviews concerning the true viability of a double skin façade system in the last two decades, and where there are research contributions, the reporting is inconsistent in the case of energy performance, economic feasibility, and environmental impact due to changing assessment methods, climates, and measurement variables. There also very few studies that consider factors such as occupancy wellbeing, including thermal comfort and indoor air quality, which is a side-effect of a lack of research into the application of a double skin façade and the adjacent building working together.

2.3.1 Energy Performance

Broadly, the overall system performance is a balance between the energy performance and environmental and economic impact, as well as occupancy comfort. For this review, the energy performance of a DSF comprises HVAC integration, energy generation and passive heating and cooling.

i. *Advanced Adaptive Façades and HVAC Integration*

Throughout this review, embedding the operation of a DSF into a more comprehensive control system and allowing for flexibility in modality is highlighted as the key to both improved occupancy comfort and reduced energy consumption (heating & cooling efficiency). The first study by Park et al. [121] concerned the calibration of a simulation model of DSF with controlled rotating louvers and ventilation openings based on a parameter estimation technique and in situ monitoring of a full-scale experiment of a south-facing unit at Georgia Institute of Technology in Atlanta. They furthered this investigation of a Smart Façade Demo Unit (SFDU) in a second paper and the performance comparison of the SFDU to a manually controlled façade system and a conventional window system, smart façade systems more advantageous in terms of energy, visual comfort, and thermal comfort [122]. Indoor Air Quality (IAQ) and how double skin facades can impact ventilation levels in an adjacent building are discussed in the later section 2.3.2 (ii).

Regarding the energy assessment of integrating a double skin façade into the HVAC system of a building, most researchers have opted to employ EnergyPlus as the primary methodology. For example, Hong, et al. [123] used DesignBuilder and EnergyPlus to determine that for winter conditions, a shaft box DSF with static cavity air was optimal with an energy-saving rate of

4.13% and for summer conditions, a multi-storey DSF with natural ventilation was optimal with an energy saving rate of 12.67%. Similarly, Slavkovic [67] utilised EnergyPlus and found the most energy-efficient scenario for a double layer skin on the east and west facades of an industrial facility of Raska textile factory in Novi Pazar, Serbia, is the DSF with fixed blinds and night ventilation during summer. Yoon et al. [124] used EnergyPlus to evaluate a floor radiant heating system (typical gas boiler) in tandem with the advanced DSF for an apartment. The DSF retrofit saves 38.8% on the annual heating energy compared to the base case and primary heat loss areas are windows, walls, and infiltration.

In a study carried out by Stec and van Passen [125], measurements in a test cell at TU Delft validated Simulink models for a multi-storey DSF office building which calculated simple night cooling mode by MV may save around 40% of the cooling capacity and energy. Application of NV by operable windows and simple algorithms for weather prediction allows for further reductions that can reach even 70%. The simulation results developed by Bueno et al. [126] for a south-facing façade with ventilated window and compact fan coil unit, validated by experimental data, only saw energy savings below 5%. Radmard et al. [127] also combined numerical modelling and experimental test cell data to assess energy efficiency. For a typical sunshine-oriented office room in Karaj, Iran, there are savings of 0.27-0.42kWh/m^2/day by decreasing room inlet temperature between 4ºC and 6ºC on peak solar gain summer days in July when integrating a DSF into a southwest-facing double-glazed window.

More recently, this area of research has considered the application of an artificial neural network (ANN) for the optimum control of HVAC systems in double-skinned office buildings conducted by Seo et al. [128]. The results indicate that the ANN model developed using EnergyPlus and Python could achieve a 10.5% cooling energy reduction from the DSF building than the non-DSF building with the same HVAC control.

ii. *Energy Generation – Building Integrated Photovoltaics (BIPV)*

A relatively new and emerging area of DSF research revolves around integrating a form of energy generation within a DSF system, with a focus on Building-Integrated Photovoltaics (BIPV). Various researchers have evaluated the performance of a Semi-Transparent Photovoltaic Double Skin Façade (STPV DSF). Two separate studies by Peng et al. [129], [130] assessed the performance of an STPV DSF in terms of ventilation mode, and material properties. For a cool-summer Mediterranean climate zone, a ventilated PV-DSF was able to

generate about 65 kilowatt hours (kWh) of electricity yearly per unit area, and if high-efficiency Cadmium Telluride (CdTe) semi-transparent PV modules are adopted, annual energy output could even be doubled. Compared to non-ventilation PV-DSF, the NV PV-DSF saves about 35% of electricity use per year. In a similar study by Preet et al. [131], the performance of a naturally ventilated semi-transparent (30%) CdTe PV DSF is assessed by experimental tests in summer in Jaipur, India. For a mechanically ventilated mode, there was a 19.24% reduction in SHGC for a 200mm air cavity depth at an air velocity of 5m/s, leading to up to 36% less SHGC than NV mode for the same cavity. Power generation from PV panel in MV mode is better due to better heat removal, 28.38% higher than NV.

Given that the transparency of the PV module has a direct impact on performance, researchers such Ioannidis et al. [132] have made comparisons between opaque and semi-transparent PV DSFs. During winter in Canada, the DSF-PV system can supply approximately 120kWh/façade area/year, covering the yearly electricity demand of adjacent offices if the floor area is around less than three times larger than the floor area. Solar radiation is almost blocked during the summer months by opaque PV at exterior skin, preventing overheating effects. Integrated PV panels can supply 26.3kWh/m^2/year of solar electricity. For the investigated building parameter zone, the use of semi-transparent PV (transmittance 70%) allows reaching the nearly zero-energy goal for an indoor space area up to 27m^2.

Similarly, Wang et al. [133] assessed the overall energy performance of a PV-DSF and a PV insulating glass unit through comparative experiments on a test rig in Hong Kong to validate simulation models for five different climates in China. Average solar heat gain coefficients (SHGCs) of the PV-DSF and the photovoltaic insulating glass units (PV-IGU) are 0.152 and 0.238, while the U-values are 2.535W/m^2K and 2.281 W/m^2K. These results indicate that the PV-DSF has better performance than PV-IGU in reducing solar heat gains, while it has worse performance regarding thermal insulation. The annual energy saving potential of the PV-DSF and the PV-IGU are 28.4% and 30%, respectively, compared to commonly used insulating glass windows in five different climates.

Zhu et al. [134] analyse the heat transfer performance of DSF integrated with high concentration photovoltaic (CPV-DSF) by establishing an energy balance equation and thermal resistance model as the calculation model. Under optimal conditions in Tianjin, China the Convective Heat Transfer Coefficient (CHTC) is 1.179 W/m^2K, exhaust heat is 143.70W, and the average temperature of concentrating cell is 59.81ºC, 15.07ºC lower than that without ventilation. The

solar radiation transmittance of CPV-DSF with 0.5m channel width is 31.2%. Lee et al. [135] used statistical methods and building simulation software ESP-r to obtain monthly optimal operating angles of a PV vent window as part of a PVDSF system. It was concluded that the same operating angles to minimise heating and cooling energy demand also maximise power generation. The difference between the DSF and outdoor temperatures was 12ºC in winter, and 0.5ºC and 2ºC for decreased air and wall temperatures in summer, respectively. The optimal operating angle of the PV is 10-20 degrees in winter and 30 degrees in summer and intermediate seasons. When it was open in the intermediate season, the temperature difference between the PV-DSF and the outdoor temperature was 3ºC or less, and the temperature of the PV-DSF was the same as the outdoor temperature in summer. Cooling energy consumption was reduced by at least 10% on average.

As previously mentioned in Section 2.2.4 (iii), PCM is beneficial, if appropriately selected, to tackle overheating in the cavity. Therefore, some researchers, such as Elarga et al. [136] have developed a DSF system integrating both a PV and PCM layer. This study assesses the thermal and electrical performance by using a physical-mathematical model and numerical simulations for different climates (Venice, Helsinki, and Abu Dhabi). The system results in a reduction in monthly cooling energy demand in the 20-30% range, although improvements in heating load in more cold-dominated locations are limited. This configuration has shown the possibility of reducing PV module temperature by up to 20ºC.

A paper by Yang et al. [137] presented numerical solutions for the performance prediction of a building-integrated photovoltaic/thermal DSF (BIPV/T-DSF) as exterior cladding of a north-facing façade of an office building for Darwin, Sydney, and Canberra, Australia. By comparing the different operational modes and BIPV technologies, an NVDSF integrating the Perovskite-based solar cell is the optimal configuration achieving the highest savings. Total annual energy savings of 34.1%, 86%, and 106% annual were reached respectively in Darwin, Sydney, and Canberra compared to conventional technologies. In a similar study, Shakouri et al. [138] present an energy analysis by simulating a building integrated photovoltaic thermal DSF (BIPVT-DSF) in Middle Eastern climate condition. DesignBuilder and PVsyst software were employed to calculate that the system can reduce annual cooling and thermal loads by 251,623kWh and 17,811 kWh, respectively for chimney mode.

iii. *Passive Heating and Cooling*

Most passive cooling techniques integrated with a DSF system revolve around evaporative

cooling or heat pipes. For example, Sotelo-Salas et al. [139] used CFD simulations, validated by an experimental test cell, to assess evaporative spray cooling in opaque double skin façade for cooling load reduction in hot arid Mexicali, Mexico. The best arrangement was an air cavity width of 0.4m, a droplet size of 25 micrometres, and a separation of 0.6m between each nozzle, achieving a cooling efficiency of 33.5% with one spray with a mean surface temperature drop of 9.52ºC in the inner wall and 12.1ºC on the external wall.

Yan et al. [140] developed a method to describe the thermal property of pipe-embedded double skin façade (PDSF), comparable to a conventional DSF through the heat transfer analysis at different cooling water temperatures. On sunny days, relatively warm water can reduce the solar heat gain since the solar heat gain is dominant in total heat gain, i.e., 301.135K water, the equivalent ambient temperature is only 302.65K when the outdoor temperature is 308.15K. Cool water is recommended for cloudy days to decrease conductive heat gain, controllable with an embedded pipe. Shen and Li [141] also explored the thermal performance of a double-skin façade with built-in pipes utilizing evaporative cooling water for a cooling season in China. They suggested that the cavity be closed because the cavity air temperature is less than the ambient air temperature. The effectiveness is more than 20% in all selected cities in China, going as high as 80% in Urumchi due to sizeable solar radiation and efficient evaporative cooling. The cooling pipes are adequate for reducing the heat gain in the West, South, and East orientations but are not effective on the north side.

Heat recovery has consistently been suggested as a possible solution to improve energy savings in winter conditions. However, there has been a relatively low focus on this area compared to cooling strategies. There have been various ways that researchers have harnessed heat gain, such as using a solar chimney, as explored in a study by Ding et al. [99] whereby a solar chimney was attached to the top of a south facing DSF. Reduced scale model experiments and CFD analysis found that increasing the height of the solar chimney increases ventilation rate, offering favourable pressure difference distribution (if higher than two stories), and influences the quantity of solar radiation absorbed by the thermal storage wall, improving the stack effect. Bielek et al. [142] investigated integrating a double skin façade with a heat recovery unit (Lunos Nexxt) in Bratislava, Slovakia, using CFD software ANSYS Fluent R1. Due to the relatively small airflows of the heat recovery unit (15 to 90m^3/h), a one-storey high, H=3000mm or H=1500mm with a narrow cavity of 250mm, was chosen. Solar radiation varies from 150W/m^2 to 600W/m^2. The authors found potential in combining these two systems, especially at lower airflows (15m^3/h and 50m^3/h) where the increase in temperature is significant (up to 15.9ºC).

The inverse relationship between airflow rate and heat recovery efficiency demonstrated in this study highlights the importance of solar irradiance in influencing the heating efficiency of a DSF system in cold climates.

In a similar study, Sung and Kim [143] combined a solar chimney and heat recovery into a DSF system connected to an AHU on the roof of a building in Daejeon, South Korea. They found that with the application of a solar chimney with a south-facing multi-storey DSF and a rise in its height, heating energy increased to about 7.6 times higher than that of the original performance of the DSF. Agreement of these results are found in a study by Hou et al. [144] (2020) for an NVDSF during cold season in Nanjing, China. The results indicate that the air velocity is approximately proportional to the height of the curtain wall with the DSF of height 4m having the best air preheating effect.

Ioannidis et al. [145] developed a new index in terms of an average Nusselt number correlation corresponding to the recovered heat in an MVDSF integrating semi-transparent photovoltaics (STPV-DSF) in Montreal, Canada. The range of Reynolds numbers in this study was between 10,000 and 26,000, representing air velocities from 0.3-1.2m/s. The authors differentiated the heat recovery index from the typical definition as the heat recovered by the building is an energy source to the system, leading to a 13% difference in calculations. The total combined efficiency of the DSF-STPV can vary between 25 and 75%. The difference between predicted and measured temperature at the outlet of DSF-STPV does not exceed 2ºC, and for the temperature of the PV cells, the difference was in the 5ºC range except for cases with lower incident solar radiation causing this difference to increase.

iv. *Research Trend Analysis*

Figure 2.9 shows an analysis of whether the double skin facades in the research sample are (a) capable of heat recovery or integrated with a building's HVAC system, and (b) whether the DSF system has any form of energy generation in the form of photovoltaics or passive heating or cooling capabilities. Following on from the findings of the climate analysis in Section 2.2.1, it is expected that there is currently a research gap of heat recovery techniques within double skin façade research, and this is more applicable to predominantly colder climates. Additionally, whilst Figure 2.9(a) shows that a portion of the research has assessed DSF performance in conjunction with an adjacent building's HVAC system, it is expected that the majority have not as the analysis in Section 2.2.2 (i) of DSF building type shows that the application still largely applies to university laboratories. This implies a research gap of the real-time or realistic

performance of a DSF when applied to an actual building which may contribute to the inconsistency in reporting of energy performance. Figure 2.9(b) shows the popularity of integrating building-integrated photovoltaics with double skin facades because of most research taking place in sunny climates.

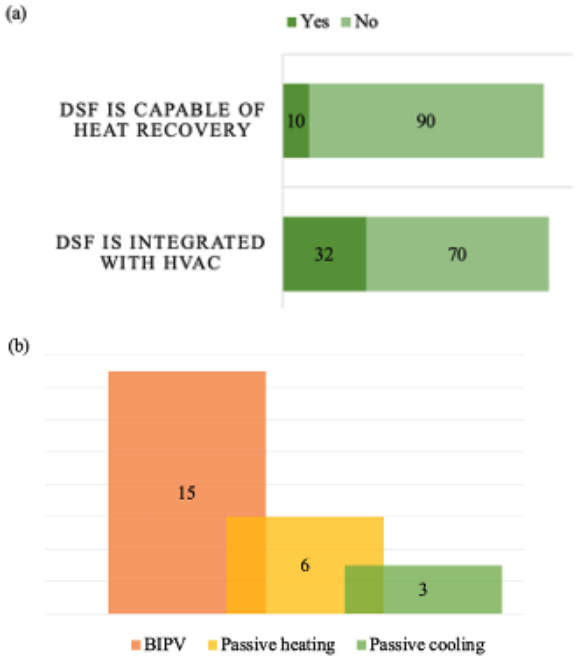


Figure 2.9 (a) HVAC and Heat Recovery Capability and (b) Energy Generation or Savings

The following table summarises the studies that looked at the impact of DSF performance on a building's HVAC system found that a DSF system capable of night ventilation in addition to its daytime operation can result in significant cooling load reductions. The combination of DSFs with a solar chimney for heat recovery is not a new concept, however direct integration with a heat recovery unit or Air Handling Unit (AHU) from the HVAC system of the adjacent building has not been explored extensively. Another notable conclusion is that the energy performance of a coupled DSF-HVAC system can be optimised by implementing sophisticated integrated control systems. This is discussed further in the next section.

A popular emerging area of DSF research currently is Building-Integrated Photovoltaics (BIPV) within the DSF system, usually placed on the external skin. The two parameters affecting the performance of a BIPV-DSF is the solar transmittance of the PV cells, and the airflow rate in the cavity. In cooling seasons, a less transparent BIPV i.e., semi-transparent, or opaque is better at reducing solar heat gains however, it will result in a higher PV module temperature and thus require a higher airflow rate to cool it and maintain its power generation efficiency without overheating. There is a similar issue when integrating Phase Change Materials (PCM), Thus, these advanced types of DSF are more reliant on mechanical ventilation in the cavity which increases cost and electricity consumption, so the system needs to outperform this consumption.

Table 2.6 Energy performance of BIPV-DSF systems

Author	Type of BIPV-DSF	Available Climate information	Building and orientation	Energy performance
Peng et al. (2016)	Amorphous-silicon PV DSF (a-Si PVDSF)	Cfa, Humid Subtropical, Hong Kong	Experimental rig, South-facing	Thermal conductivity is 0.48 +/- 0.01 (W/mK) for a temp difference of 25^{o}C.
Peng et al. (2016)	Ventilated PV-DSF	Mediterranean climate	Office, South-facing	Generates 65kWh/m^2 electricity yearly NV mode saves 35% of electricity use per year.
Elarga et al. (2016)	DSF integrating both PCM and PV	Cfb, Marine West Coast; Dfb, Warm Summer Continental and Bwh, Subtropical Desert ,Venice, Helsinki, Abu Dhabi	Office, West-facing	Monthly cooling energy demand reduction of 20-30% Smoothing of PV module increases peak values in 5-8%. Ventilation & PCM reduces PV module temp by 20C.
Ioannidis et al. (2017)	Single or multi-storey DSF with opaque or semi-transparent (70%) PV (DSF-PV)	Dfb, Warm Summer Continental, Canada	Office, South-facing	Can supply 120kWh/facade area/year and modules supply 26.3kWh/m^2/year – net zero reached for indoor areas up to 27m^2.
Wang et al. (2017)	PV-DSF and PV-IGU	Cfa, Humid Subtropical, Hong Kong	Office-South-facing	SHGCs are 0.152 and 0.238. U-values are 2.535W/m^{2}K and 2.281 W/m^{2}K. Energy conversion efficiency of PV-DSF is 1.8% better than PV-IGU with lower module temperature. Energy saving potential is 28.4% and 30%, respectively.
Lee et al. (2019)	PV-DSF	Cfa, Humid Subtropical, Changsha, China,	Office, South-facing	Winter – 12^{o}C difference between DSF and outdoor temp, optimal operating angle 10-20degrees. Summer – air and wall temps reduced by 0.5^{o}C and 2^{o}C, cooling energy consumption reduced by 10%, optimal operating angle 30. degrees. Intermediate – when open, temp difference between DSF and outside was less than 3^{o}C, optimal operating angle 30 degrees.
Preet et al. (2020)	Semi-transparent (30%) Cadmium Telluride PV module on outer skin of DSF	Bsh, Mid-latitude Steppe and Desert, Jaipur, India	Experimental rig, South-facing	NV mode – increase in cavity width from 50-250mm yields 12% reduction in SHGC. MV mode – 19.24% reduction in SHGC at an air velocity of 5m/s. NV and MV modes improved power performance by 5.63% and 8.72%, respectively.
Zhu et al. (2020)	High concentration PV DSF (CPV-DSF)	Dwa, Hot Summer Continental, Tianjin, China	Sunshine-oriented, theoretical room	CHTC is 1.179 W/m^{2}K. Exhaust heat is 143.70W. Average temp of concentrating cell is 59.81^{o}C and solar transmittance is 31.2%.
Yang et al. (2020)	(BIPV/T-DSF), Perovskite-based solar cell	Aw, Tropical Savanna; Cfb, Oceanic & Cfa, Humid Subtropical, Darwin, Sydney, and Canberra	North-facing office building	Total annual energy savings of 34.1%, 86% and 106%, but limited useful thermal energy (5% in Sydney and 20% in Canberra).
Shakouri et al. (2020)	(BIPVT-DSF)	Csa, Mediterranean, Tehran, Iran	Office, South-facing	Reducing annual cooling and thermal loads by 251,623kWh and 17,811kWh, respectively. PV system with peak power of 10.6kW can generate grid connected electricity of 18,064kWh annually, improving energy performance index of existing building by 34.3%.

Table 2.7 Impact of DSF integration with HVAC systems or passive heating or cooling techniques on building energy savings

Author	DSF integration with HVAC/passive heating/cooling	Description of DSF system	Available Climate information	Building and orientation	Building energy savings
Stec and Passen (2005)	HVAC	Box-window DSF curtain wall	Cfb, Warm and Temperate, Delft, Netherlands	Office, South-facing	Night cooling by MV mode of DSF could save 40% of cooling capacity and energy, increased to 70% with NV windows.
Ding et al. (2005)	HVAC	Solar chimney attached to DSF	Cfa, Humid and Subtropical	Office, South-facing	If height of solar chimney is more than two storeys it increases ventilation rate.
Hoseggen et al. (2008)	Passive heating	DSF with controllable windows	Dfc, Continental Subarctic, Norway	Office, East-facing	Heating demand for SSF is 20% higher than DSF.
Hong et al. (2013)	HVAC	Shaft box buffer in winter, multi-storey external airflow	Dwa, Hot Summer Continental, Seoul, South Korea	Library	Winter - energy saving rate of 4.13% and for summer - 12.67%.
Shen and Li (2016)	Passive cooling	DSF with built-in pipes	BSk, Tropical and Subtropical Steppe, Urumchi, China	Experimental rig, all orientations	Cavity should be closed, and more than 20% effective in all selected cities going as high as 80% in Urumchi.
Slakovic et al. (2017)	HVAC	DSF with fixed blinds	Cfb, Warm and Temperate, Serbia	East & west facing, industrial facility	DSF with fixed blinds and night ventilation during summer resulted in lowest heating & cooling energy, minimum CO2 emissions.
Kilaire and Stacey (2017)	HVAC	Integrated Passive and Active Double Skin Façade (IPADSF)	Cfb, Temperate Maritime, UK	Sunshine-oriented, office	Achieves better energy sustainability and spatial efficiency.
Bueno et al. (2017)	HVAC	Ventilated window and compact FCU	Cfa, Humid Subtropical, Italy	South-facing	Energy savings below 5%.
Bielek et al. (2019)	Passive heating	DSF with heat recovery unit (Lunos Nexxt)	Cfb, Marine West Coast, Slovakia	Sunshine-oriented, office	Inverse relationship between airflow rate and heat recovery efficiency.
Sung and Kim (2019)	HVAC	Solar chimney and heat recovery into a multi-storey DSF system connected to an AHU	Dfa, Hot Summer Continental, Daejeon, South Korea	South-facing	Heating energy increase to about 7.6 times higher.
Radmard et al. (2020)	HVAC	DSF integrated into window	BSk, Cold Semi-Arid, Iran	Office, South-west	Saves 0.27-0.42kWhth/m^2/day by decreasing room inlet temp between 4 and 6°C in summer.
Ioannidis et al. (2020)	Passive heating	Semi-transparent photovoltaics DSF (STPV-DSF).	Dfb, Warm Summer Continental, Montreal, Canada	Experimental rig, South	Air velocities 0.3-1.2m/s, efficiency ranges from 25-75% Measured temp at outlet does not exceed 2°C, and PV cell temp was in 5°C range.
Hou et al. (2021).	Passive heating	NV DSF, glazed	Cfa, Warm and Temperate, Nanjing, China	South facing, Office	Air velocity is proportional to height, and temp inversely proportional to DSF thickness.
Sotelo-Salas et al. (2021)	Passive cooling	Spray evaporative cooling in opaque DSF	Bwh, Tropical and Subtropical Desert, Mexicali, Mexico	Sunshine-oriented, experimental rig	Achieves a cooling efficiency of 33.5% (one spray) to 67.4% with mean surface temp. of 9.52°C in inner wall and 12.1°C on external wall, flow rate 50.64l/h.

2.3.2 Occupancy Comfort and Safety

Given that the DSF sits at the interface between the external and internal environment, it will have a direct impact on occupancy comfort, and safety in the event of a fire. This section covers thermal comfort, indoor air quality (IAQ), acoustics and daylighting and fire risk and spread.

i. Thermal Comfort

There is currently limited availability of thermal comfort studies of DSF systems with this article only considering three articles with a distinctive objective to observe thermal comfort, all of which are applied to hot climates.

Wong et al. [82] found that for an 18-storey high-rise office building in Singapore, a DSF air gap size of 300mm gives the best result in a naturally ventilated space, as does a north-facing DSF orientation - lower floors of the office space would typically generate the lowest operative temperature compared to floors near the roof level, this enhances the stack effect within the DSF configuration, providing better internal thermal comfort conditions. Barbosa and Ip [106] concluded the highest level of thermal acceptance (90%) occurred in the south and southeast climate regions for a mixed-mode ventilation strategy operating in conjunction with the mechanical air conditioning system to reduce discomfort on extremely hot days. This study was later compared to the IESVE results of Barbosa and Alberto [105], which compared the thermal performance of university building models with a north-oriented multi-storey, indoor air exhaust DSF made of glazing and perforated metal sheet under tropical climate conditions of Rio de Janeiro, Brazil. The results showed that annual thermal comfort levels reached up to 75%, indicating that actual buildings may require other means of cooling under summer conditions.

One other method of assessing the thermal comfort of occupants is the Predicted Mean Vote (PMV) which is an index of the thermal sensation. Alibaba and Ozdeniz [146] explored PMV for a box-window DSF office building in Cyprus. Compared to a single-skin façade, a double-skin façade achieves a lower PMV of around 0.5 for the whole year average, compared to 1.5.

ii. Indoor Air Quality

Despite DSFs having the potential to bring outdoor air into the adjacent building space, there are relatively few studies that consider the impact that DSFs can have on indoor air quality. Li et al. [147] developed a novel DSF integrated with TiO_2 plates (T-DSF) for decomposing Volatile Organic Compounds (VOCs). The authors estimated that a 12-story commercial building with a

south façade of 50m x 40m equipped with a T-DSF could clean about 25,666m^3/day air with 20 parts per billion (ppb) of Benzene, Toluene, Ethylbenzene and Xylene (BTEX) – the equivalent to 0.08 air changes per hour (ACH) cleaning capacity (for eight hours) for a building volume of 20m by 50m by 40m. A different study considered how controlling hybrid ventilation in a building with DSF can impact indoor air quality (IAQ). Yahiaoui [148] presented a series of experimental results of applying automated control systems in real-time hybrid ventilation (natural and mechanical ventilation) of a south-facing DSF in a test-cell building at Delft University, the Netherlands, for winter and summer conditions. During the entire occupied period, IAQ was at or between required setpoints, and the provision of outside air into the test cell could be appropriately controlled and provided during the occupied period.

iii. *Acoustics and Daylighting*

There have been various papers considering the impact that a double-skin façade system could have on the internal environment of a building, especially in urban areas. Lee et al. [96] studied the effect of positions of vertical glass fins inside a box-window double skin façade cavity as an acoustical barrier. It was found that the thicker the vertical glass fins are, the higher the Sound Transmission Loss (STL) values which in turn decreases noise transmission to indoor spaces via ventilation openings. Sarglou et al. [64] noted that a corridor type double skin façade with no interior blinds can provide more acoustic insulation than a single skin curtain wall. Kilaire and Stacey [149] designed a cascade type DSF prototype to make each unit independent to achieve minimal noise transfer. Similarly, Aleksandrowicz and Yezioro [58] looked at a box-window DSF system with the adaptation of an inward opening casement to separate each module vertically and horizontally from other modules to keep noise transmission to each individual module only. This short overview implies that incorporating modulation into the design of DSF systems across the span of a building façade is key to control noise transmission.

A similar area affecting occupancy comfort is daylighting to which DSF systems have a direct correlation as they are transparent glazing. Peng et al. [129] used a daylighting model in simulating a PVDSF with Cadmium Telluride to show that it is effective at blocking solar radiation whilst still providing considerable daylighting illuminance with a maximum monthly average of 300 lux for a cool-summer Mediterranean climate zone. Luo et al. [116] also considered daylighting control in the evaluation of a double skin façade system integrated with photovoltaic blinds. Bueno et al. [126] modelled a ventilated double-skin complex fenestration system and concluded that high glare risk in winter sun can be mitigated with interior glare protection devices if using a temperature-based control whereas a radiation-based control is

effective against glare but thermally inefficient in winter as it blocks beneficial solar gain. Kim et al.[62] explored how interior and exterior blinds in a buffer-type double skin façade system would impact daylighting and found that a blind control could reduce lighting energy consumption by around 52%.

iv. Fire Risk and Spread

Most of the research on the fire safety of double skin facades has been conducted by Chow, C.L. [150-152]. The main findings conclude that the natural airflow pattern in a DSF cavity will dictate fire spread, and narrow cavity depths present the highest risk of reaching extremely high temperatures. Thus, if there is no standard configuration of DSF, then a fire safety assessment needs to be completed for each bespoke system to anticipate fire risk. It is also worth noting that double skin façade systems which can be compartmentalized into individual modules may help reduce spread of fire and smoke.

v. Research Trend Analysis

The impact that a DSF system might have on occupancy comfort is an area of research which is lacking. There have been a few papers within the respective areas of thermal comfort, indoor air quality and acoustics and daylighting, however these are not extensive across all climates and DSF configurations.

As expected, thermal comfort acceptance is largely correlated to the local climate that a DSF is designed for, and how well it manages the changing conditions. Regarding the indoor air quality of the space adjacent to the DSF system, there is little study on this, but the most recent papers have explored localised air scrubbing in the air cavity or how to achieve hybrid ventilation through real-time control of passive and active actuators. Both the thermal comfort and indoor air quality considerations tie in with the integration of the controls of a DSF system with the Building Management System (BMS) to balance the changing ambient conditions with the setpoint requirements of the internal space. Similarly, smart blind control has been examined by several researchers in the assessment of whether a double skin façade can help or hinder daylighting of the adjacent internal space. Figure 2.10 below highlights that acoustics, and daylighting is a more popular research topic within the occupancy comfort sphere and suggests the large research gap which exists for thermal comfort and IAQ.

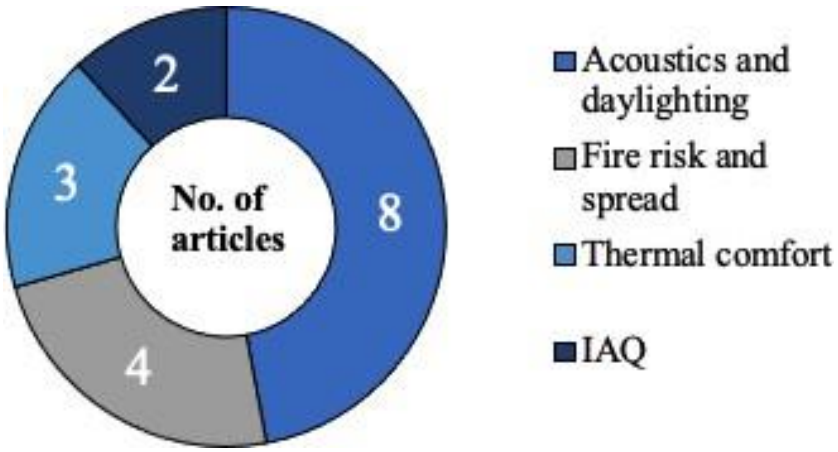


Figure 2.10 Trend Analysis of Emerging Topics in DSF Research

Table 2.8 below summarises the notable impact on occupancy comfort from the studies reviewed in this section in chronological order of publication to demonstrate that IAQ is the emerging topic in this area, whereas the other three have been considered throughout the last two decades.

Table 2.8 Impact of DSF Systems on Occupancy Comfort

Author	Research focus	DSF type	Climate	Building and orientation	Impact on occupancy comfort
Wong et al. (2008)	Thermal comfort	NVDSF	Af, Tropical Rainforest, Singapore	All orientations, office	Air gap size 300mm gives best NV in space. Height across building enhances stack effect leading to better thermal comfort.
Barbosa and Ip (2016)	Thermal comfort	NVDSF	Brazil	North-facing, office	90% thermal comfort in south & southeast. 65% in centre-west, north-west & coastal areas 20% in north-east.
Peng et al. (2016)	Daylighting	PV-DSF	Cool-summer Mediterranean climate zone	South-facing, office	Can effectively block solar radiation whilst still providing daylighting illuminance levels of 300 lux.
Lee et al. (2016)	Acoustics	Box-window	Theoretical	Sunshine-oriented, experimental rig	Airborne noise is transmitted both horizontally and vertically. Thicker vertical glass fins in cavity increase sound. Transmission loss values, decreasing noise transmission to indoor spaces.
Kilaire and Stacey (2017)	Acoustics	Integrated Passive and Active Double Skin Façade (IPADSF)	Cfb, Temperate Maritime, Urban area, UK	Medium to high rise, medium-depth office	Cascade DSF with individual modules reduces noise transmission.
Luo et al. (2017)	Daylighting	NV and MV PVB-DSF	HSCW, China	South-facing, experimental rig	Standard DSF with no blinds had high solar penetration (60-75W/m^2) whereas PVB-DSF with blinds had lower values of 33-35W/m^2.
Bueno et al.(2017)	Daylighting	Box-window MVDSF	Cfa, Humid Subtropical, Italy	South-facing, experimental rig	Temperature-based control of blinds risks high glare, whereas radiation-based control is effective against glare.
Kim et al. (2018)	Daylighting	Buffer-type NVDSF	Dfa, Hot Humid Continental, Seoul, Korea,	South-facing, office	Blind control could reduce lighting energy consumption by around 52%.
Aleksandrowicz and Yezioro (2018)	Daylighting	MV box-window DSF system	Csa, Dry-Summer Subtropical, Israel	All orientations, office	When blinds are closed (0º), diffuse solar radiation still penetrates so can still provide lighting.
Barbosa and Alberto (2019)	Thermal comfort	DSF (glazing & perforated metal sheet)	Aw, tropical savanna , Rio de Janeiro, Brazil	South-facing, university building	Annual levels of thermal comfort reached up to 75% Increasing perforation from 20 to 40% showed little improvement.
Li et al. (2020)	IAQ	DSF integrated with TiO2 plates (T-DSF) for decomposing VOCs	Bsk, Tropical and subtropical Steppe, Boulder, Colorado	South-facing, theoretical	Can clean about 77m^3/day of ambient air with 20ppb BTEX (annual average).
Yahioui (2020)	IAQ	Hybrid ventilated DSF	Cfb, Warm and Temperate, Delft, Netherlands	South-facing, experimental rig	Maintained IAQ at or between setpoints and outdoor air was properly controlled and provided – controlling passive & active actuators reduce energy consumption.
Sarglou et al. (2020)	Acoustics	Corridor	Csa, Dry-Summer Subtropical , Tel-Aviv, Israel	High-rise office building, all orientations	Provides more acoustic insulation compared to SSF.

2.3.3 Life Cycle Analysis of Double Skin Facades

As double skin facades are a solar technology that can be integrated with buildings, it is imperative that the economic feasibility and environmental impact of its construction, operation and maintenance is understood. The Life Cycle Analyses (LCA) of DSFs is an emerging research topic and this section provides a snapshot of what has been conducted thus far in the 21st century.

i. *Economic Feasibility*

One of the predominant issues with developing double-skin façade technology is the high initial investment cost associated with the material, manufacturing, and construction costs. Various researchers have attempted small economic analyses in conjunction with their assessment of DSF performance and predominantly found the technology as it currently stands to be economically infeasible. Part of the issue is also surrounding the different costing estimations used and a lack of standardised design with various researchers employing varying materials or other systems into DSF technology.

For example, Chan et al. [104] concluded a long payback period of 81 years despite a promising 26% reduction in cooling energy for a typical office building with a DSF facing south-west in Hong Kong. However, in a techno-economic feasibility study by Ghadamian et al. [153], the simple payback period for a DSF application was estimated at three years and five months with a total Net Profit Value (NPV) equal to $657,883.94 and Internal Rate of Return (IRR) is approximately equal to 29.87%. In later studies by Valentin et al. [154], the feasibility of replacing conventional fans with Coanda nozzles for forced ventilation in a Double-Glazed Ventilation System for Barcelona, Spain, is assessed. The DSF system with Coanda Nozzles had an estimated 3–5-year payback period, and in a 25-year horizon, a 300-700% return on investment.

A different study by Blanco et al. [108] for a perforated metal sheet DSF in Spain concluded economic infeasibility although total building load savings in energy consumption were around 20% for coldest areas and 45% for hottest ones. Zomorodian and Tahsildoost [155] assessed the overall carbon emissions and costs during a DSF building's life cycle, proposing a new index, Energy Carbon Cost (ECC), to help define the best DSF design scenario. Results indicate that a multi-story DSF with shadings has the lowest ECC for Tehran office buildings. However, the simple payback period is more than the building's lifetime (50 years) under current energy

prices in Iran and is therefore economically infeasible. Hay and Ostertage [85] found that the additional embodied energy and cost of a special double skin façade system with fibre-reinforced concrete could be recovered in the first 2 years and 8.2 years of operation, respectively. Yoon et al. [124] found that retrofitting old apartments with DSFs in a cold climate would incur a cost of $24,500 and a payback period of 30 years.

An example of emerging research trends is in the study by Shakouri et al. [138] which includes an energy, exergy, economic and environmental analysis of a building-integrated photovoltaic thermal double skin façade system in Tehran, Iran using MATLAB and Microsoft Excel. The key results are that the configuration with the highest PV module surface area had a payback period of 1.58 years and a life cycle revenue of $55,157 making it a feasible retrofit.

ii. *Environmental Impact*

As aforementioned, the estimated environmental impact will be highly subjective to the chosen climate and DSF configuration, materials, and construction and the methods used by researchers to assess this. The DSF system with Coanda Nozzles proposed by Valentin et al.[154] and previously mentioned in Section 2.3.3 (i) found that 5% of energy consumption occurs in the production and manufacturing of machinery, and it emits more pollutants at this stage compared to a conventional system but sees a reduction of 0.6 to 3 tonnes of carbon dioxide (tCO_2) in pollutant emissions associated with energy generation.

Pomponi et al. [84] investigate the greenhouse gases (GHG), and non-GHG life cycle impacts of several DSF configurations for office refurbishments through a parametric comparative LCA (attributional and consequential) against up-to-standard SSF refurbishment solutions. Results show that while most DSF configurations reduced GHG emissions compared to SSFs over their life cycle, they also have non-negligible ecological and environmental impacts regarding materials and final deposits. In a later study by Pomponi and D'Amico [156], the results of LCA and dynamic energy modelling of an innovative timber DSF compared to traditional steel or aluminium show that operational savings outweigh the embodied impacts, and therefore the proposed DSF is a viable and effective solution for net carbon-negative refurbishments. The increase in embodied carbon that the DSF incurs is quickly recovered in the first few years of operation of the façade by its increased thermal performance. The LCA assessment involving The Energy Carbon Cost (ECC) index proposed by Zomorodian and Tahsildoost [155] found that the energy consumption of a building with DSF in Tehran, Iran is reduced from 7.9% to

14.8%. Although the operational carbon emission reduced by 14-17%, the embodied carbon increases by 23.3-47%. Hay and Ostertage [85] proposed a new DSF system achievable with a new concrete composite called high-performance green hybrid fibre- reinforced concrete (HP-G-HyFRC) with comparison to an existing solid façade system as generally adopted in public housing in Singapore. LCA analysis found that it could reduce annual operational energy and carbon dioxide equivalent (CO_2eq) emissions by 9.2%. Radmard et al. [127] found that a solar-oriented double skin façade applied to an office could achieve a reduction of 159gCO_2 emissions per square meter per day because of electricity savings.

iii. *Research Trend Analysis*

Due to the bespoke nature of DSF systems to external design conditions, and the variability in DSF design factors, there is not a standardised assessment of feasibility in terms of economic viability and environmental impact. As a result, there are varied estimations highly dependent on individual parameters although there does need to be more Life Cycle Assessments (LCA). There is general agreement however that there is a high initial investment cost and increased embodied energy attached to DSF systems currently. A relatively new area of research is trying to address this by designing DSFs with different low energy, low carbon materials. Figure 2.11 illustrates a trend of emerging topics within the sample of articles for the last 5-6 years with an increase in papers looking at the two main objectives of LCA: environmental impact and economic feasibility. The broadening of the research scope of double skin facades reflects that more researchers are asking the question of the extent to which DSF systems are viable as a building technology.

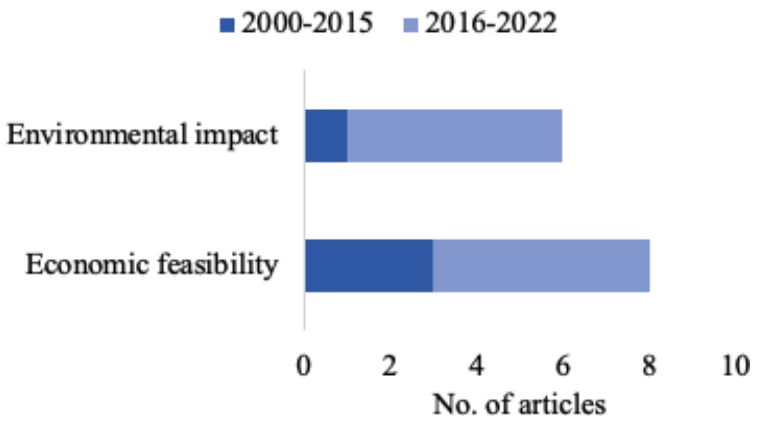


Figure 2.11 Trend Analysis of LCA Subject Focus

Table 2.9 LCA Results for DSF Typology, Climate and Building Application

	Author	DSF Type	Available climate, orientation, building application information	LCA results
Economic feasibility	Chan et al. (2009)	Box-window	South-west facing, office building Hong Kong	A long payback period of 81 years makes DSF system economically infeasible without significant government subsidies.
	Ghadamian et al. (2012)	Box-window	Tehran, Iran	Simple payback period estimated at 3 years and 5 months with a total Net Profit Value (NPV) equal to $657,883.94 and Internal Rate of Return (IRR) is approximately equal to 29.87%.
	Valentin et al. (2013)	MVDSF with Coanda nozzles	Barcelona, Mediterranean	3–5-year payback period, & in a 25-year horizon, a 300-700% return on investment.
	Blanco et al. (2016)	Perforated metal sheet DSF	Spain	Economic infeasibility although total building energy consumption was around 20% for coldest areas, and 45% for hottest ones.
	Zomoridian and Tahsildoost (2018)	Multi-storey DSF	Tehran, Iran	Simple payback period is more than 50 years.
	Hay and Ostertage (2018)	DSF system with high performance green hybrid fibre-reinforced concrete (HP-G-HyFRC)	Public housing, Singapore	Additional embodied energy and cost could be recovered in first 2 years and 8.2 years of operation respectively.
	Yoon et al.(2020)	Advanced DSF system to replace existing balcony windows	Apartments, Seoul, South Korea	Cost is about $24,500, and payback period is more than 30 years. This estimation only considers energy savings costs.
	Shakouri et al. (2022)	BIPVT-DSF	Tehran, Middle Eastern climate, office building	Highest PV module surface area had a payback period of 1.58 years and a life cycle revenue of $55,157 making it a feasible retrofit.
Environmental impact	Valentin et al. (2013)	MVDSF with Coanda nozzles	Barcelona, Mediterranean	5% energy consumption in production and manufacturing of machinery & emits most.
	Pomponi et al. (2016)	Multi-storey DSF	High-rise office, England	2 to 9 MWh can be saved in cooling load; 0.6 to 3tCO_2 reduction in pollutants.
	Pomponi and D'Amico (2017)	384 different configurations of timber made DSF	UK	Timber is better than steel and aluminium. Operational savings outweigh embodied impacts which are recovered quickly in first few years by increased thermal performance.
	Zomorodian and Tahsildoost (2018)	Multi-storey DSF	Office, Tehran, Iran	Operational carbon emission is reduced by 14-17%, embodied carbon increased by 23.3-47%.
	Hay and Ostertage (2018)	DSF system with high performance green hybrid fibre-reinforced concrete (HP-G-HyFRC)	Public housing, Singapore	Reduces annual operational energy and CO_2eq emissions by 9.2% but higher embodied energy and material costs (recovered in 2 and 8.2 years of operation).
	Radmard et al. (2020)	Box-window DSF	Sunshine-oriented office, Karaj, Iran	Reducing cooling energy consumption by over 0.27kWh per square meter per day which might contribute to a reduction of 159 g-CO_2 emission per square meter per day.

2.4 Methodology Trends in Double Skin Façade Research

Figure 2.12 shows the (a) breakdown of methodology chosen by double skin façade researchers in the last two decades, and (b) validation method.

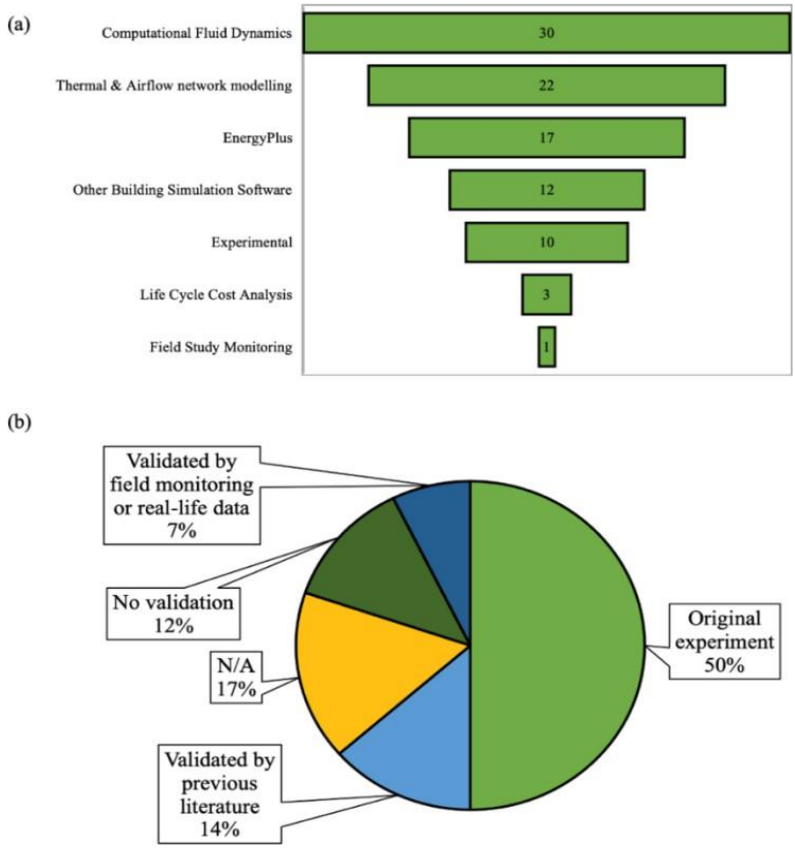


Figure 2.12 (a) DSF Research Methodology Breakdown and (b) Validation Methods

Out of the applicable papers in the sample, the preferred methodology was Computational Fluid Dynamics software which is largely due to the vast improvements in both computer processing power and software development. However, analytical methods of determining thermal and airflow networks are still widely popular demonstrated by 22 papers in this review selection, with CFD methodology in the lead with 30 papers. An emerging methodology in double skin façade research is EnergyPlus, a building energy simulation (BES) tool , as the scope broadens to consider the energy performance of a DSF building to help monitor viability. A good recent study of different building energy simulation programs including EnergyPlus, TRNSYS, IDA ICA and IES-VE by Lucchino et al. [157] demonstrates this point. It was found that for both winter and summer conditions, TRNSYS was the better performance tool with the lowest error of 14% and 6% for the no shading configuration whilst the in-built "Airflow Window" in EnergyPlus outperformed the other tools when shading was included. This suggests that perhaps the landscape of methodology to assess performance of double skin facades is evolving from thermal

and airflow network modelling to a combination of CFD and BES tools. Figure 2.12 (b) shows that the traditional means of validation is through original experiments, followed by validation with previous literature. Due to the complicated nature of the convection-conduction-radiation phenomena within the DSF cavity, it is imperative to validate any numerical solving of DSF physics with experimental data, especially due to the system's bespoke design to climate and building purpose or type.

2.5 Conclusion

The primary purpose of this literature review was to explore the nexus between ventilation and thermal performance, and the viability of double skin façade systems. It examines how the predominant focus of DSF research in the last two decades has been the technical feasibility of the technology in terms of phenomena within the cavity, and only more recently are there considerations of life cycle analyses and integration with adjacent buildings. Using an adapted PRISMA method, over 100 peer-reviewed papers from the past two decades have been selected and organised into a new categorisation of DSF research to consider specifically how different design factors affect both ventilation and thermal performance, resulting in five tabular summaries. In addition, a thorough meta-analysis of the different areas of DSF research has provided new insight into how the research scope is expanding and where the current research gaps lie. The key results are:

- Almost half of the papers in this sample look at both ventilation and thermal performance, with a preference towards thermal and a lack of outdoor air ventilation studies
- Most DSF cavities are naturally ventilated, but this does not cover both the mass flow rate required for heat removal as well as providing outdoor air to an adjacent space
- Oceanic temperate climates are predominant, followed by humid subtropical showing a shift towards the warmer temperate climates
- Winter and summer conditions are most popular, with summer/cooling in close second, which is in line with the shift to warmer climate studies
- DSF buildings are largely limited to laboratories or office/commercial, and south-oriented DSFs reflect most of the research taking place in the northern hemisphere
- The box-window DSF configuration is most common, with multi-storey DSFs becoming more widely used in numerical studies
- In line with warmer temperate climate focus, there is a rise of focus on shading devices

due to the issue of overheating in DSF cavities in summer conditions, as well as "smart" external skins incorporating photovoltaics or phase-change materials

- Some researchers have assessed how a DSF impacts a building's performance through integration with an HVAC system, however there is little study on passive heat recovery in colder temperate climates
- Emerging trends in recent DSF research include Life Cycle Cost and Environmental analyses, as well as building side parameters including thermal comfort and IAQ
- The preferred methodology used by researchers in this sample was CFD, followed by analytical modelling and validation through original experimental data

2.5.1 Research Gaps

Despite the popularity of double skin façade research, it is by no means completed from the viewpoint of building technology development. The research in this thesis aims to close the gap between double skin façade research and practical application in industry by attempting to standardise DSF performance for a specific building application by embedding the concept of the nexus between ventilation and thermal performance, and the viability of double skin façade systems. The specific research gaps that this thesis address is below:

- Develop a multi-stage experimental and computational methodology to assess both ventilation and thermal performance of the double skin façade
- Conduct wind-only and buoyancy-only experiments to evaluate the primary driving forces of the double skin façade applied specifically to warehouses using small-scale and prototype models
- Evaluate the seasonal-adaptivity of the DSF design and assess performance in intermediate seasons such as Spring and Autumn, as well as worst-case heating and cooling
- Validate the computational assessment of thermal stratification in warehouses through a small-scale heat mat test and highlight empirical limitations for such spaces
- Develop and validate the integrated computational performance tool which can predict the cross-ventilation, thermal and energy performance of a seasonal-adaptive DSF for warehouses
- Quantify the DSF's energy savings against the case study warehouse through simplified economic analysis including payback period

The next chapter presents the methodology required to address these research gaps.

Chapter 3

Methodology

3.1 Chapter Introduction

This chapter details the various methodology utilised in this thesis to conduct the research objectives as well as the case study building application and climate. The methodology is an important aspect of the research process as it lays out detailed descriptions of all necessary research methods which in this case includes three different experimental campaigns, and numerical modelling using computational fluid dynamics.

The research in this thesis was achieved through mixed methods comprising thermal and wind testing of small-scale prototypes of the seasonal-adaptive, opaque double skin façade and case-study warehouse. The reason for this was to collect original experimental data that is used to validate numerical models obtained from computational fluid dynamics modelling software. Due to the constraints and inaccessibility of performing building retrofits on full-scale warehouses, the feasible option was to develop experimental campaigns at small scale and use CFD modelling to evaluate performance at full-scale.

There are a range of limitations that can impact the effectiveness of both experimental and computational methods, and these are considered in the subsequent sections including the case study building and climate, atmospheric boundary layer wind tunnel tests, climate chamber tests, stratification heat mat tests, and computational fluids dynamics.

3.1.1 Case Study Warehouse and Cross-Ventilation Scenario

This section details the chosen case study building and climate for this research, including vertical solar irradiance calculations, and the hypothesis of why cross-ventilation could work in a warehouse space. It also justifies why an opaque double skin façade can yield competitive performance with its glazed counterparts. The chosen case study building is a type B6 Storage and Distribution classification of warehouse built in 2022 where all relevant documents, such as architectural plans, are available to the public as part of the planning procedure with Rotherham County Council. The reason behind this choice is twofold: the availability of construction data, and a direct example of the growing square footage of storage and distribution warehouses in the UK midlands, known as the “the golden triangle of logistics” [158].

Figure 3.1 shows the architect’s vision of the proposed warehouse.



Figure 3.1 Case Study Warehouse [159]

Whilst the original building does have a second-floor office, a stairwell, and toilets, for simplification this research is considering the warehouse to be confined to only a single, ground-floor thermal zone. More simplifications include excluding the surrounding buildings and orienting the building such that the south-facing façade is not obstructed by other buildings, and foliage. Table 3.1 provides some technical data available for the building, as well as generic operating conditions for a warehouse that will be used in energy demand calculations.

Table 3.1 Case Study Warehouse Information [159], [8], [12]

Warehouse floor area dimensions (m)	36.25 by 70.25
Gross Internal Area (GIA) (m^2)	2514.4
Gross External Area (GEA) (m^2)	2639.5
Shed Thickness (m)*	0.59
Haunch height (m)	10
Building materials	Haunch -Metal trim flashing slate grey RAL 7012
	Roof – RWPs slate grey RAL 7012
	Space between haunch and roof apex – Euroclad built up ‘elite plus system 55’, 32/1000 R profile with colour coat Prisma solid finish, oyster RAL 7035
	Walls – Euroclad built up ‘elite plus system55’ 32/1000 R profile with colour coat Prisma solid finish silver metallic RAL 9006, Quattro bars at typical 1.167m centres, sheeting rails/quattro brackets at 1.5m
No. and size of docks	1 High Bay
No. and size of level access doors	2 level access doors
No. and size of personnel doors	6 personnel doors
No. and size of skylights	40 skylights, 10% of roof area
Occupancy schedule	Warehouse
People/100m^2	1.5
People Sensible Heat Gain (W/person)	73.3
People Latent Heat Gain (W/person)	58.6
Lighting Load Density (W/m^2)	7.1
Equipment Load Density (W/m^2)	2.2
Infiltration Flow (ACH)	0.4
Outside Air (Ventilation air) Flow Per Person (L/s)	NULL
Outside Air (ventilation air) Flow Per Area (m^3/h/m^2)	1.1
Unoccupied Cooling Set Point (°C)	29.4

*Some of this data is used in supplementary calculations including total heat gains provided in Appendix A.1 and A.6

This section explains why the case study building is designed as part of the double skin façade retrofit as a cross-ventilation scenario. Warehouses are a deep space, which is only suited to cross-ventilation, and wind-induced pressure differences on the windward side drive the air across the building, to openings on the leeward side of the building. The height of this type of shed structure usually spans above the working zones and clearance widths for walkways between pallet racks are sufficiently wide. Thus, even if the pallet storage racks are tall, there is still direct and unobstructed flow paths across the length of a warehouse, as shown in Figure 3.2, or in the clearance above the racking.



Figure 3.2 Pedestrian walkways between storage racking [160]

In the case of the DSF retrofit for this case study warehouse, the solar technology is situated on the southern-facing façade to harness maximum solar gain in the northern hemisphere, and the dominant wind direction is also largely southerly. This means that a cross-ventilation strategy can also benefit by utilising the north-facing façade for drawing in cooler air from the shaded side [4]. This works with the outlet being positioned on the north façade as it is a negative pressure zone, whereas the DSF (and ventilation inlet) is placed in a positive pressure zone which will help to induce flow into the space. A novelty explored in Chapter 6 is the simulation of warehouse internal space with and without storage racking from a thermal stratification perspective as this phenomenon is encouraged by the tall height of these structures.

Because wind develops a pressure difference across the width of a building, the normal approach to wind driven ventilation is to design flow paths that are largely horizontal, with air entering and leaving at the same vertical level. This has informed the cross-ventilation flow path detailed in Figure 3.3 which shows a side profile of a warehouse with air entering the double skin façade on the windward side and exiting on the leeward façade across its length. CIBSE AM10 states a rule of thumb for the applicability of cross-ventilation: the distance between two facades is five times the floor-to-ceiling height. In the case study warehouse, the height is 12m and the

length between the south and north façade is 72m. This is slightly over the current guidance, but it should be noted that the limitation of the rule-of-thumb is that it does not include data for buildings with floor-to-ceiling heights greater than 3.5m [12].

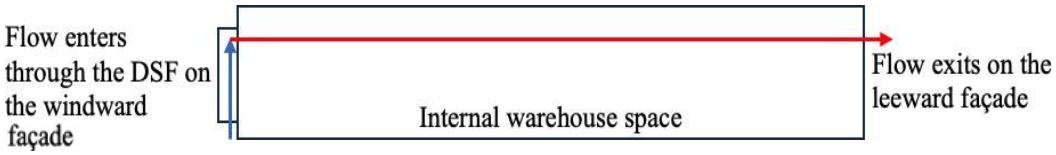


Figure 3.3 Proposed Cross-Ventilation Flow Path in the DSF Warehouse

There are some limitations to consider with naturally ventilated buildings, and these are explored in the next section where the case study climate and meteorological data are considered in detail.

3.1.2 Case Study Climate and Meteorological Data

The potential for the cross-ventilation scenario applied to case study warehouse is dependent on the presence of wind for good ventilation, but analysis of the data given in CIBSE Guide A, Tables 2.18-2.19 shows that the wind speed coincident with the temperature that is not exceeded for 99.6% of the time is more than 3.5m/s for all UK locations [8]. Another area to consider is indoor climate control, whereby NV strategies cannot offer control of space humidity, although CIBSE Guide B states that the relative humidity in non-air-conditioned buildings will not exceed 70% unless there is a very high level of internal moisture generation [4]. As the UK is a temperate climate, this should not be an issue in warehouses. However, it is still important to monitor internal humidity as too low a value can be caused by excessive infiltration or ventilation in very cold weather.

The chosen case study climate for this research is Nottingham, UK which is characterised as warm and temperate and a Koppen-Geiger classification of Cfb. The primary driving force of a double skin façade is the stack effect which is best suited to temperate climates where highest rates of airflow rates are observed [161]. This is further evidenced by a sample analysis of climates used in 100 DSF articles from the literature review in Chapter 2.

Another advantage of Nottingham as the case study climate is the four distinct weather seasons. Whilst building energy consumption traditionally focuses on the extreme case scenarios in winter and summer, there are energy savings possible in the intermediate months of spring and autumn. Additionally, a sample analysis of environmental conditions used in DSF research was conducted to highlight that few researchers were considering this despite most simulations taking place in temperate climates.

i. *Wind data*

For meteorological data, Nottingham, UK, is represented by the East Midlands Airport weather station. Nottingham is a temperate climate defined by four seasons and predominantly heating intensive. Figure 3.4 is a wind rose for the last 49 years for East Midlands Airport, showing a dominant south-south westerly wind direction the Iowa Environmental Mesonet, Iowa University.

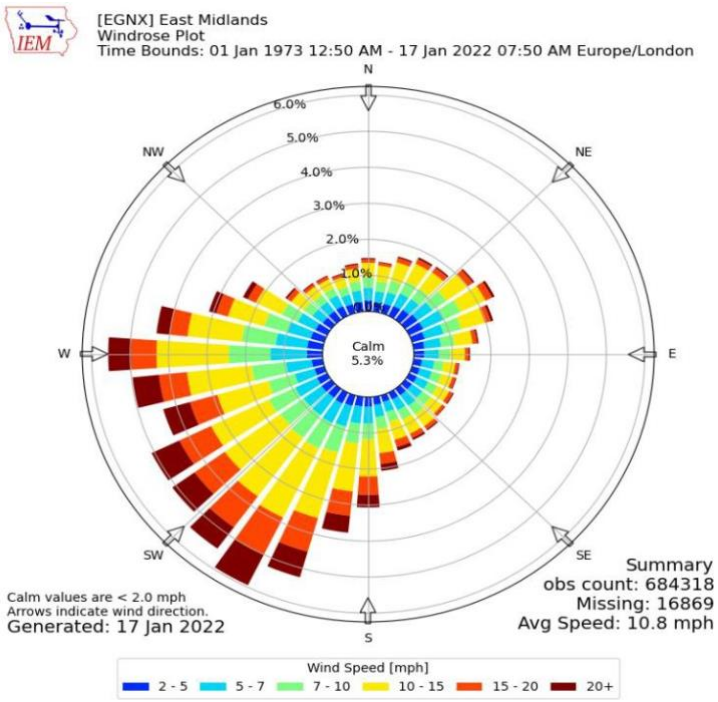


Figure 3.4 Nottingham Wind Rose [162]

This demonstrates further potential of the application of natural ventilated solar-assisted technology situated on south-facing facades of warehouses in Nottingham. The other important wind data to complete the case study climate picture is wind speed. The method to take the wind speed measured at a meteorological station, such as East Midlands Airport, and adjust it for a specific urban landscape and building height is to use the following equation from the American Society of Heating, Refrigerating and Air-Conditioning Engineers (ASHRAE) 2001 guide [163]. An assumption made is that the meteorological wind speed is measured in an open field at a height of 10m, the wind speed is modified by:

Equation 3.1 Local Wind Speed

$$U_{\infty} = V_{met}\left(\frac{\partial_{met}}{z_{met}}\right)^{a_{met}}\left(\frac{z}{\partial}\right)^{a}$$

Where z is the height of the centroid of the system, z_{met} is the height of the standard meteorological wind speed measurement, and a and ∂, are terrain-dependent coefficients. Table 3.1 details a recreation of the terrain-dependent coefficients from ASHRAE 2001 (Table 4.1).

Table 3.2 Recreated Terrain-dependent values from [163]

Terrain	Description	Exponent, a	Layer thickness, ∂ (m)
1	Flat, open country	0.14	270
2	Rough, wooded country	0.22	370
3	Towns and cities	0.33	460
4	Ocean	0.10	210
5	Urban, industrial, forest	0.22	370

For this research and given that warehouses are largely situated in areas comprising other warehouses, the description of the terrain for the purpose of building a wind profile will be semi-urban or industrial. It should be noted that the effects of other buildings, trees and other obstructions are neglected in the wind tunnel testing to reduce the computational resource of the numerical simulations the wind tunnel data is used to validate.

The other important aspect of a climate when determining potential for double skin façade application is solar irradiance levels which is covered in the following section 3.1.3.

ii. *Solar Irradiance Data*

The source for solar irradiance data in this thesis is SolCast [164] due to the level of detailed information it can provide historically for the designated weather station, East Midlands Airport. By obtaining the highest and lowest direct irradiance values for the last five years (2017-2021) for every solar noon in the months of January, July, April, and October, this data represents the best- and worst-case solar scenarios for the four seasons in a temperate climate. The reason for neglecting diffuse radiation values is because the thermal experiment detailed in the later Section 3.3 uses an artificial solar simulator that is only capable of direct irradiance. Additionally, as the double skin façade is a vertical façade technology, the value of solar vertical irradiance needs to be determined to achieve realistic simulation. The equation required to calculate solar vertical irradiance is:

Equation 3.2 Vertical Solar Irradiance

$$S_{vertical} = GHI \cdot \cos(alpha) \cdot \sin(beta) \cdot \cos(psi - theta) + \sin(alpha) \cdot \cos(beta)$$

Where alpha, beta, psi, and theta represent the sun elevation angle, wall tilt angle, wall azimuth and sun azimuth, respectively. All angles are in radians. The results tables for this are in Appendix, Section A.2, but Table 3.3 below details the average highest and lowest vertical irradiance values for each of the four months. It should be noted that the lowest vertical irradiance values concern the next lowest value that is not zero for the purpose of identifying a range of values. From this table, solar irradiance values up to 800W/m^2 would be sufficient if considering a best-case solar scenario however a more appropriate simulation is to take an

annual average which in this case is 311W/m^2 as this can account for cloud cover and low sun days.

Table 3.3 Seasonal Average, Highest and Lowest Vertical Irradiance [164]

Seasonal month	Average Highest Vertical Irradiance (W/m^2)	Average Lowest Vertical Irradiance (W/m^2)	Average solar scenario (W/m^2)
January	735	42	389
April	592	18	305
July	403	4	204
October	664	30	347
Annual average solar irradiance (W/m^2)			311

This analysis shows that there are reasonable levels of solar irradiance throughout the seasons for the chosen climate, indicating that the double skin façade is applicable in the presence of natural driving forces such as wind and temperature differentials. The next section explores the first experimental methodology to test the double skin façade warehouse under wind-only conditions.

3.2 Atmospheric Boundary Layer Wind Tunnel

An atmospheric boundary layer (ABL) wind tunnel is necessary to test a scale model of the proposed double skin facade warehouse in conditions which can be replicated in a CFD model and therefore used as a means of validation for the wind-only aspect of the performance tool. Measuring and collecting original differential pressure readings across the double skin façade and warehouse in the ABL wind tunnel and calculating pressure coefficients to compare against the CFD model instils a level of reliability in the CFD performance tool when assessing ventilation performance of the proposed double skin façade for warehouses.

Studies by [165] were essential indications that wind tunnel studies could be used to directly measure ventilation rates in scale model buildings. There are some uncertainties when measuring wind pressures, however this can be compensated by determining the pressure coefficient, Cp at key points on a building. This is because Cp does not vary greatly with wind speed as the sharp edges on the building, and purpose-provided openings fix the positions of flow separation. Thus, for a given building shape and surrounding environment, the Cp distribution depends only on wind direction and the proportion of the point where wind speed is measured [12].

The overall aim of the wind tunnel experiment is to simulate wind conditions close to the case study climate of Nottingham, UK to obtain wind pressure information from a scale model of the double skin façade warehouse which can be used to validate the numerical model version in computational fluid dynamics. The main objectives include:

- Run the ABL wind tunnel at 5m/s with a semi-urban boundary layer
- Collect differential pressure readings over 60 measurement points
- Calculate pressure coefficients from experimental readings

Comparing the experimentally derived Cp values with those obtained from numerical CFD modelling of the scale model in the wind tunnel test section is a common means of validation. Additionally, pressure coefficient values are also required for pressure drop and ventilation calculations across the DSF cavity. The following sections look at the theory behind the experimental outcomes, model construction, experimental set-up, measurement variables and more.

3.2.1 Experimental Theory

The theory covers free stream dynamic pressure, Reynolds number, wind pressure coefficient, and frictional pressure loss to building a picture of why certain measurements and calculations are being used. Boundary conditions include relative velocities, physical boundaries, and turbulence characteristics of the flow systems.

i. Dynamic pressure

The free stream reference dynamic pressure (or time averaged wind velocity pressure derived from Bernoulli) $\frac{1}{2}\rho U_R^2$ should be measured upstream of the model where turbulence effects due to the production of the atmospheric boundary layer and model form do not affect measurements, i.e., roof height of model or at a height equivalent to the 10m prototype building [166].

ii. Reynolds number

The Reynolds number is a dimensionless number used in fluid mechanics to indicate whether the fluid flow past a body or in a duct is steady or turbulent. The critical value at which turbulent flow is assumed to exist and thus flow becomes independent is typically quoted as $Re>10^4$. Buildings Reynold number, based on forced flow separation at sharp edges of buildings, H becomes d for openings, and U becomes u as in local wind speed (q/A):

Equation 3.3 Building Reynolds Number

$$Re_b \equiv \frac{UH}{\nu}$$

iii. Wind pressure coefficient

Air Information and Ventilation Centre (AIVC) defines the wind pressure coefficient, Cp as *"the basic driving force of wind-induced natural ventilation*" [167]. Cp measurement is a particularly effective method of analysis as for dynamically similar flows the pressure coefficient at full scale is equal to that at model scale. The pressure on the building surface (Ps) is also proportional to the free stream wind pressure and the surface pressure coefficient:

Equation 3.4 Pressure coefficient

$$C_p = \frac{P_s - P_R}{\frac{1}{2}\rho U_R^2}$$

iv. Frictional pressure loss

Frictional pressure loss is defined as the energy lost in a fluid transportation through a pipe due to friction between the fluid and the pipe wall, represented by Equation 3.5 below where f_D is the Darcy friction factor which can be obtained from a Moody Chart for a known $\in/D$.

Equation 3.5 Frictional pressure loss

$$\Delta h = f_D \frac{L}{D} \frac{v^2}{2g}$$

3.2.2 Model Build and Pressure Tap Locations

When using case study buildings on an experimental level, a scale model is required. In this thesis, a 1:50 scale has been applied to allow for construction of a double skin façade in addition to the warehouse. Figure 3.5 below shows a schematic for the (a) double skin façade attached to the warehouse and (b) the front, back, and bottom view of the double skin façade.

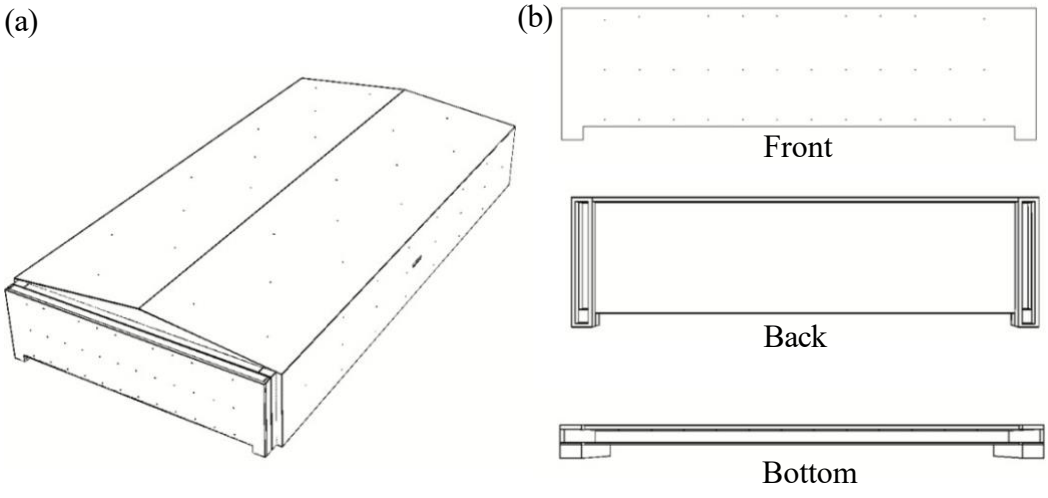


Figure 3.5 Schematic of 1:50 (a) DSF Warehouse Model and (b) DSF Orthographic Views

The scale model should be both geometrically and dynamically like the full-scale prototype building by making the size and shape of the model consistent with the prototype according to the length scale ratio K_L. Another consideration is the wind blockage ratio. British Standard BS6399 Annex A [168] note that it is good practice for wind tunnel models to have a windward façade visible area of less than 5% of the overall wind tunnel cross sectional area to ensure that the air flow around the model is not affected, and the model should not be greater than 50% of the height of the wind tunnel working section to ensure boundary layer conditions are not affected by the roof of the wind tunnel. The relevant construction details are in Table 3.4.

Table 3.4 Wind Tunnel Model Construction Details

Length (m)	Width (m)	Height (m)	Roof Slope (degrees)	Cavity depth (m)	Wind blockage ratio (%)
1.41	0.73	0.20	6	0.18	3.4

The chosen scale of the model at 1:50 is based on the wind blockage ratio and the area of the inlet to the double skin façade attachment to the warehouse. The calculated wind blockage ratio of the windward façade is 3.4%, and less than 12% of the height of the cross-sectional area. This scale also means that the width of the DSF cavity is large enough to facilitate pressure taps on the outer and inner skins.

The most important non-dimensional parameters with respect to ventilation and scale modelling of ventilation air flows is the Reynolds number (Re).The issue with Re scaling is it is not practical – for example the model would need to be exceptionally small requiring a high scale factor or the wind tunnel would have to be very large and powerful to achieve high wind velocities required to achieve full scaled Re numbers. Therefore, in this study, the scale model is based on wind blockage ratio and Holmes [169] notes this is not a major concern when dealing with flow around sharp edges of buildings.

Figure 3.6 (a) shows the 1:50 scale model that where the warehouse is made from MDF of 12mm thickness, and the DSF is made from MDF of 1mm thickness whilst (b) shows the pressure tap locations on all facades (exact CFD coordinates are in the Appendix, Section A.3.7). There are openings on the front, back and sides and shown in (b) where some are for pressure tap connections to go through.

(a)



(b)

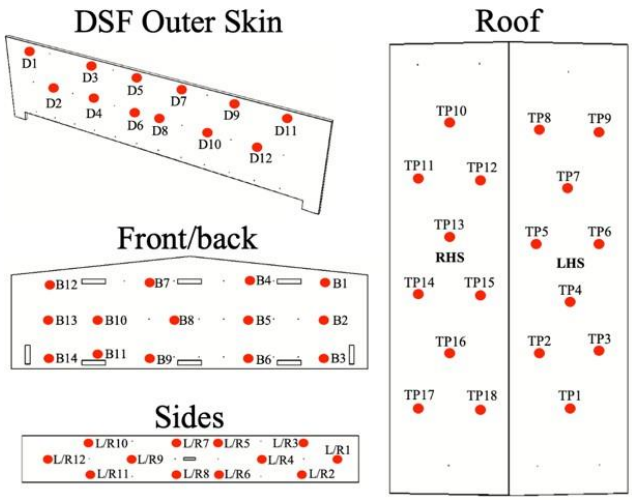


Figure 3.6 (a) DSF Warehouse Model in ABL Wind Tunnel and (b) Pressure Tap Locations

3.2.3 Experimental Set-Up, Measurement Variables and Equipment

The wind tunnel experiment took place in the ABL wind tunnel facility at the University of Nottingham (UoN) which is equipped with an open-circuit low wind-speed wind tunnel, shown in Figure 3.7. It has a test section length of 14.0m and a cross-sectional area of 2.4m width by 1.80m height. Within the test section is a turntable of diameter 2.0m, located 12.5m from the start of the test section. The ABL Wind tunnel operates by varying the fan speed controller frequency to change the speed or rotate the turntable for different wind angles.

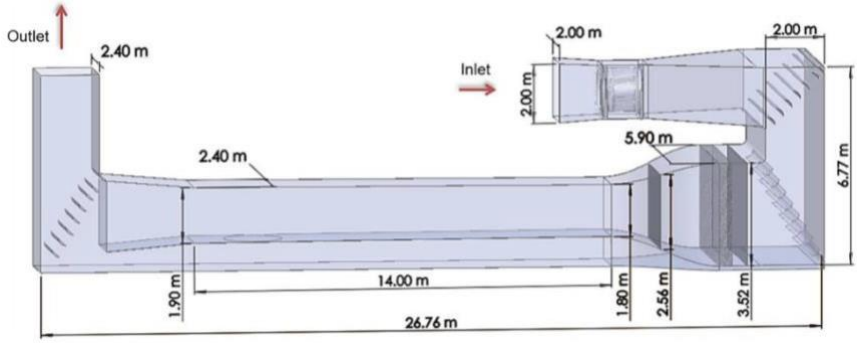


Figure 3.7 ABL Wind tunnel at University of Nottingham [170]

Regarding the atmospheric boundary layer (ABL), the UoN facility is designed for the generation of a suburban terrain, at a scale of 1:400, which results to a power law exponent (α) equal to 0.28 and a target boundary layer depth (δ) equal to 400 m in full scale or 1 m in wind tunnel scale [171]. This is achieved using spires and roughness blocks shown in Figure 3.8.

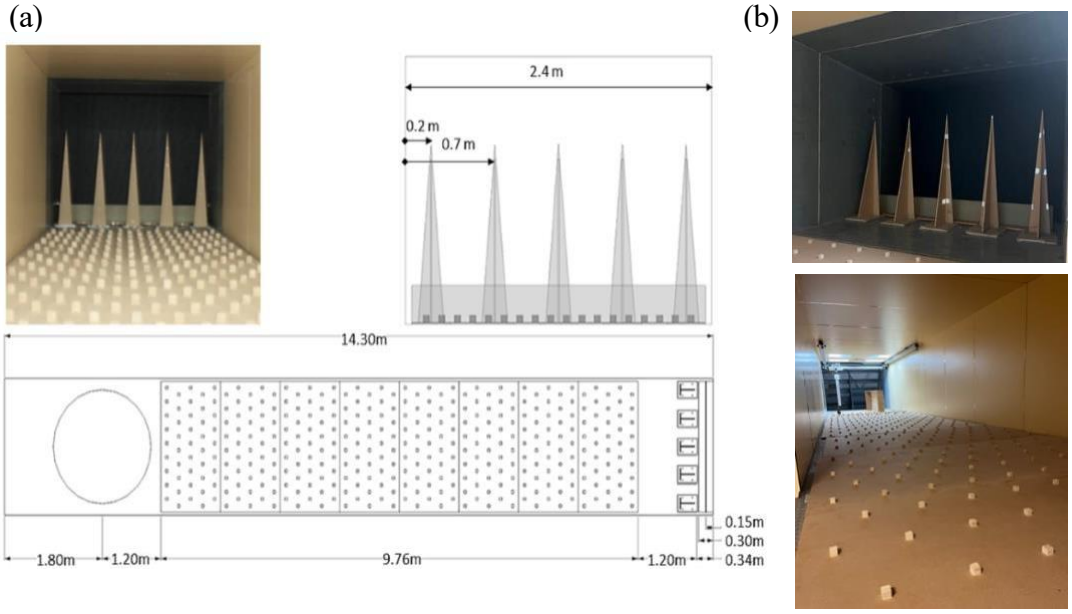


Figure 3.8 Semi-urban Spires and Blocks (a) Dimensions from [170]and (b) Real Lab Set-Up

The table below highlights the measurement variables and equipment for this experiment.

Table 3.5Wind Tunnel Measurement Variables and Equipment

Measurement variable	**How is it obtained?**
Free stream wind velocity, Uref	Measured by FC65 Furness Small Single Point Pitot tube
Free stream dynamic pressure, Pref	Measured by Pitot tube/Obtained from CFD
Building surface differential pressure, Pdiff	Measured by Scanivalve MPS4264 pressure transducer
Wind pressure coefficient, Cp	Calculated

3.2.4 Design Conditions and Reference Point Measurements

Experimentally, a range of wind speeds and angles were tested, namely 1,3 and 5m/s and 0, 90, 180 and 270 degrees. However, for the purpose of validating data against a CFD model, only a wind speed of 5m/s and wind angles of 0 and 180 degrees were used. Reasons for this are explained in the following sections in more detail.

i. Chosen wind speed for CFD validation – 5m/s

Selecting this wind speed was based off wind tunnel aerodynamics theory and applicability to the chosen climate. For example, as a 1:50 scale model was used, it is important to increase chances of achieving aerodynamic similarity, represented by Reynolds number (Re). The issue with wind speeds below 5m/s is that the flow behaviour might not behave as expected causing the Re number to drop outside of the turbulent regime [172]. A turbulent boundary layer is more

representative of the semi-urban environment being replicated in the wind tunnel and low wind speeds are more likely to yield laminar regions [173]. There are many other reasons to not use low wind speeds such as reduced measurement accuracy of equipment, flow quality, and scaling issues and therefore 5m/s was selected as the wind speed for CFD validation. This value also sits within the average of wind speeds recorded for each season in the case-study climate used to create the full-scale wind profiles. The measured velocity at the reference point for this is 2.22m/s.

ii. Chosen wind profile (semi-urban) and wind angles

The computational results were obtained utilising a preliminary wind profile with a wind-shear exponent to represent a semi-urban boundary layer, computed from the reference velocity discussed in the previous section. Table 1, Section 16.3 in ASHRAE fundamentals guide [163] provides a summary of wind-shear exponents related to different environment domains, and the initial value of 0.18 was chosen as it lies between open-country and urban, indicating a semi-urban setting. However, a sensitivity analysis is completed later to determine which exponent produces the best match with the experimental data. The computational modelling only looks at wind angles of 0 and 180 degrees for validation as when the length of the scale model is windward (at 90 and 270 degrees), the blockage ratio exceeds the limit discussed previously to 7%. Therefore, more accurate results can be obtained from the dominant windward and leeward directions.

iii. Reference Point Velocity and Pressure

Before conducting the wind tunnel experiment, a reference velocity and pressure are required. The methods for this include experimental and numerical. Based on wind tunnel theory, the maximum wind speed occurs at the centre of the cross-section, in this case 5m/s at a height of 0.9m. This along with a near-ground velocity of 2.22m/s at a height of 0.01m were used to build the wind profile. Figure 3.9 shows the position of the pitot tube and therefore the reference velocity and pressure.

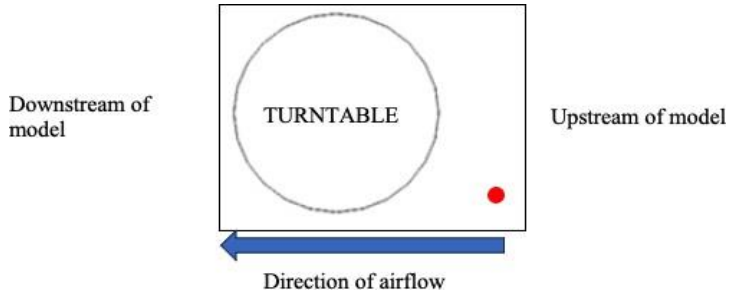


Figure 3.9 Pitot tube and reference location

Reference pressure measurements were attempted (Appendix Section A.3.2) however this thesis uses a value computed in the CFD model for calculating Cp as the pressure transducer accounts for reference pressure already in its readings of differential pressure. The pitot tube was positioned 0.38m from the right-hand side viewing window and, 0.40m from the front of the model. The measured velocity at the pitot tube inlet is used to calculate the dynamic pressure to be used in the pressure coefficient formula later in Section 4.3.1. The Scanivalve pressure transducer internally calculates the reference pressure based on the position of the pitot tube to deliver a final differential pressure result. As a result, the reference pressure was obtained numerically using computational fluid dynamics when replicating the experimental wind profile. The computed reference pressure for a wind profile equivalent to the wind tunnel speed of 5m/s is 0.25Pa. There are other means of obtaining the reference velocity and pressure measurements, and this could be explored in future work.

3.3 Climate Chamber Experiment

This section outlines a detailed experimental plan for the thermal testing required for developing the first segment to the DSF building performance tool, 'Treating the DSF as a wall retrofit'. This includes the experimental aim, objectives, theory, methodology and expected results. An advantage to conducting a buoyancy only scenario is because it is easier to treat than wind because temperatures are subject to much less uncertainty than determining wind pressures in both a wind only, and combined wind and buoyancy scenarios [12].

The primary mechanism behind double skin façade operation is the stack effect, resulting from buoyancy-driven air movement in the cavity between the two façade layers. The aim of this experiment is to assess the thermal performance of a DSF with flexible openings allowing for different heating and cooling operation for a range of design conditions, simulating both inside and outdoor environments. By treating the DSF as a wall retrofit, the purpose of this aim is to calculate the new thermal conductance of a DSF building in terms of convective, conductive, and radiative heat transfer. The objectives to achieve this are outlined below:

- Develop velocity and temperature profiles in the DSF cavity under a range of design conditions for every type of "seasonal-adaptive" opening
- Calculate the overall heat transfer coefficient for a range of design conditions
- Calculate mass flow rate for cavity in changing operation and type of opening
- Calculate heat recovered/removed at exhaust of DSF

3.3.1 Experimental Theory

As the climate chamber experiment is primarily a test of heat transfer through the opaque double skin façade, conduction, convection and radiation will occur simultaneously [174]. Other researchers such as [175] have utilised this same environmental chamber for the similar purpose of calculating U-values through windows, and other heat transmittance studies. The following sections explain how to treat the DSF as a thermal duct, as well as a new wall retrofit to determine heat gain and thermal transmittance values.

i. *Treating the DSF as a thermal duct*

The heat gain within the cavity is determined from mass flow rate, calculated by a buoyancy- only pressure drop. To do this, the air temperature at the top and bottom of the cavity are obtained either experimentally or from the validated computational model for a full-scale DSF and put into the equation below to find the pressure due to buoyancy.

Equation 3.6 Buoyancy Pressure for a Double Skin Façade

$$p_{buoyancy} = \rho_{average} g H_{cavity} \left(\frac{1}{T_{cavitytop}} - \frac{1}{T_{cavitybottom}} \right)$$

Then, the velocity due to buoyancy can be calculated in the next equation:

Equation 3.7 Buoyancy Velocity for a Double Skin Facade

$$V_{cavity} = \sqrt{\frac{2 \cdot p_{buoyancy}}{\rho_{average}}}$$

From this, the volumetric flow rate and mass flow rate can be evaluated:

Equation 3.8 Buoyancy volumetric flow rate for a double skin façade

$$Q_{flowrate} = A_{cavity} \cdot V_{cavity}$$

Equation 3.9 Buoyancy mass flow rate for a double skin façade

$$\dot{m} = \rho_{average} \cdot Q_{flowrate}$$

Finally, the heat gain in the cavity can be calculated:

Equation 3.10 Buoyancy heat gain for a double skin façade

$$Q_{heatgain} = \dot{m} \cdot c_p \cdot (T_{cavitytop} - T_{cavitybottom})$$

ii. *Treating the DSF as a new wall retrofit*

By treating the DSF as a new wall, in addition to the existing building façade, a new u-value can be determined which is helpful when calculating thermal conductance. This is achieved by determining the thermal resistance of each layer which in this case involves the warehouse cladding, a 0.2m air cavity exposed to the environment, and a 3mm aluminium outer skin. The equations for finding the thermal resistance of the warehouse cladding and aluminium outer skin are below. The u-value of the cladding is known at 0.31W/m^{2}K [176], and the thickness, d, and thermal conductivity, k, of aluminium are 3mm and 235W/mK, respectively.

Equation 3.11 Thermal Resistance of Inner Skin (Cladding)

$$R_{cladding} = \frac{1}{U_{cladding}}$$

Equation 3.12 Thermal Resistance of Outer Skin (Aluminium)

$$R_{aluminium} = \frac{d}{k}$$

As the cavity is ventilated, except for when in the fully closed mode in winter conditions, the calculation of the thermal resistance requires more steps to firstly determine the convective heat transfer coefficient. Initially, the Reynolds and Nusselt numbers should be calculated as follows where the Prandtl number for air is 0.71:

Equation 3.13 Reynolds Number for DSF Cavity

$$Re = \frac{\rho_{average} \cdot v_{average} \cdot L}{\mu_{average}}$$

Equation 3.14 Nusselt Number for DSF Cavity

$$Nu = 0.023 \cdot Re^{0.8} \cdot Pr^{0.4}$$

These are then used to find the convective heat transfer coefficient where the thermal conductivity of air changes dependent on the average cavity temperature, and the inverse of this is the thermal resistance of the cavity air:

Equation 3.15 Convective Heat Transfer Coefficient

$$h = \frac{Nu \cdot k_{average}}{L}$$

Equation 3.16 Thermal Resistance of Air

$$R_{cavity} = \frac{1}{h}$$

The total thermal resistance of the DSF, and new retrofit u-value are therefore:

Equation 3.17 Total Thermal Resistance of DSF System

$$R_{total} = R_{outer} + R_{cavity} + R_{inner}$$

Equation 3.18 U-value of DSF System

$$U = \frac{1}{R_{total}}$$

The following sections look at the choice behind an opaque double skin façade, and how it was constructed into a climate chamber laboratory setting to be tested on.

3.3.2 Rationale for an Opaque Outer Skin in the Double Skin Façade

Given that warehouses have a limited amount of glazing respective to its floor area compared to other building types such as offices or retail spaces, if a warehouse is to incorporate a double skin façade retrofit, it is more economical to use an opaque outer layer if daylighting is primarily delivered by roof skylights. The following figure compares the energy flows across both opaque and transparently insulated walls to demonstrate any differences in performance that should be considered.

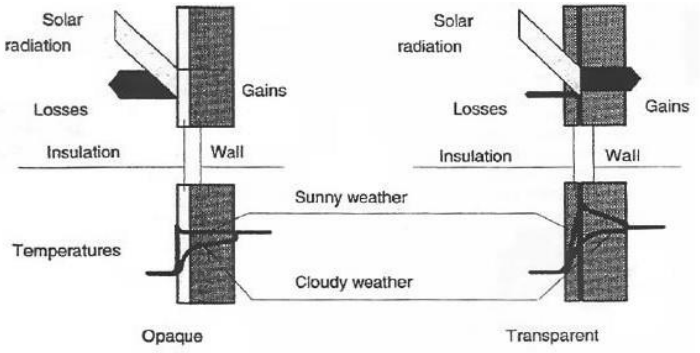


Figure 3.10 Energy flows of opaque and transparent insulated walls [177]

Whilst both material types will reduce energy losses from the building via conduction through building surfaces, the transparent insulation will allow solar radiation to penetrate deeper into surface construction. This causes an increase in construction internal temperature and can result in heat being conducted into the building under proper weather conditions. As a result, transparent insulation can offer heating during sunny winter days however this same effect can be detrimental in summer as the solar gains will add to the cooling load. Most systems, including the typical glazed double skin façade counteract this with a shading device or sophisticated insulation system, however this does not always reduce issues with heat gain as it can promote overheating in the cavity [178], [179].Therefore, the double skin façade applied to the case study

warehouse in this section will have an opaque outer skin layer as glass facades on large buildings are expensive, especially when not required for daylighting and therefore offsetting lighting loads. There are few studies of the performance of opaque double skin facades, compared to the commonly glazed version, however the specific application of opaque transpired solar collectors for warehouses mentioned in Section 2.2.4 (i) suggests that this should not be an issue.

In terms of irradiance modelling of opaque materials, this can be done without a complex solar model by applying an assumption that only direct irradiance is applied as a heat generation term for solar flux and is covered later in Section 3.6.4 (ii). The limitation of not including diffuse radiation is an underestimation of solar gain which can have an impact on the overall thermal performance of the proposed double skin façade. However, with an opaque material absorption is dominant, and scattered light from diffuse radiation will either be absorbed or reflected and is unlikely to have a significant impact on the air cavity and inner skin.

3.3.3 DSF Prototype Construction and Laboratory Set-Up

Figure 3.11 shows both a front and side view of the DSF prototype construction to display the outer aluminium skin (painted in slate grey RAL 7015), and inner skin of warehouse cladding comprising two thin layers of steel liners and insulation. The structure is made from timber, and the outer and inner skins of the double skin facades are a dark-grey-coated aluminium sheet and a bespoke warehouse cladding section, respectively. Section 3.3.2 has explained the reasoning behind testing an opaque DSF, but the decision to use aluminium is based off it being a commonly used architectural cladding material. Benefits of aluminium include not easily corroding, which is essential for the case study climate of Nottingham which experiences downpours throughout the year, and it is usually an alloy to increase its strength.



Figure 3.11 Experimental Prototype of Opaque Double Skin Facade

The purpose behind applying a slate grey paint coating to the aluminium sheet is to create a dark, matte finish to improve absorptance as the original sheet is silvery and reflective and is in accordance with the case study warehouse's cladding finish. An experimental rig was set up at the University of Nottingham by setting up the DSF prototype in the doorway of a WIR36-55 environmental chamber (SSJ System Services Ltd, Rhymney, UK) where the inner skin (warehouse cladding) is at the entrance with the cavity extending 0.2m into the chamber, as shown in Figure 3.12. The chamber was modified to integrate the DSF structure on a wooden frame with insulation boards to seal the space around it.

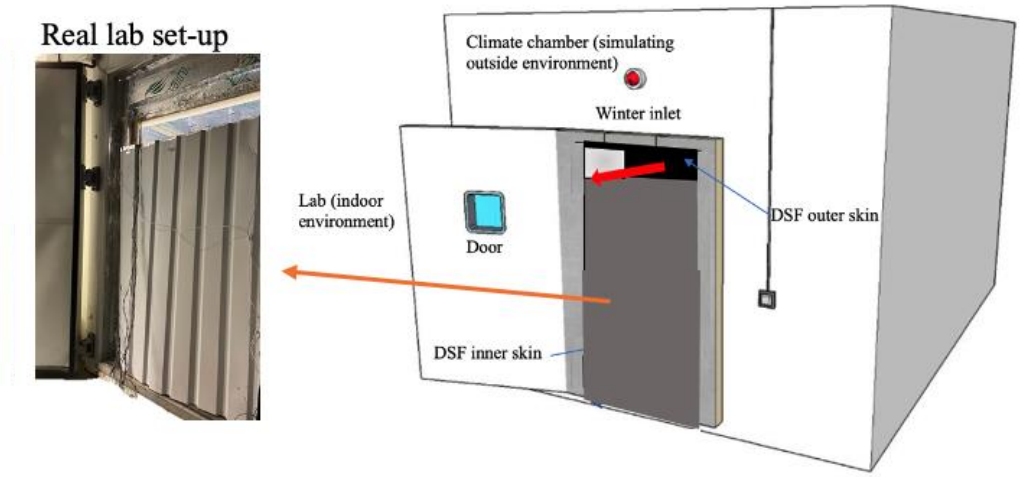


Figure 3.12 Environmental Chamber at University of Nottingham [175]

The height of the DSF comprises 1.5m for the outer and inner skins with 0.20m inlet and outlet openings, constrained by the doorframe to the chamber. The climate chamber represented the external environment as the capacity to deliver a temperature range of -4°C to 50°C. The lab air temperature was monitored to ensure it remained at around 18°C to simulate a constant indoor environment. The make-up air is coming from a mixture of infiltration and through gap which represents the DSF outlet when the lamp array is turned on and inducing buoyancy heating within the cavity but is otherwise an open airflow pathway into the climate chamber.

3.3.4 Measurement Variables, Equipment and Design Conditions

The simulated solar irradiance was constant at 300W/m^2 following the solar data analysis in the previous Section 3.1.2 (ii) and the measurement variables included surface and air temperature, air velocity, and surface heat flux. The experimentally obtained values were required to derive convective heat transfer coefficients, dynamic u-values as well as comprehensive velocity and temperature profiles in the cavity for different operating conditions. Table 3.6 has the details for the selected measurement equipment where the accuracy specifications are outlined later in Section 3.5 under experimental error theory.

Table 3.6 Climate Chamber Experiment Equipment

Equipment	Purpose/measurement	Model
Lamps	Simulate solar flux	500W Halogen -15
Hot wire anemometers	Air velocity profile in cavity	Omega FMA902R-V1 (0-5m/s) and FMA901R-V1(0-2.5m/s) series air velocity transmitters
Thermocouple	Temperature profile in cavity and surface temperatures	PT-100 4 wire RTDs exposed element
Pyranometer	Radiation at outer skin – nominal and measured irradiance	Kipp & Zonen CMP series
Data acquisition/logger	Data collation from equipment	Datataker DT85

The cavity depth of the DSF is 0.2m and is blocked off in percentage intervals of 25%-75% on either side of the cavity, i.e. at the outer skin side of the inlet or inner skin side as depicted previously in Figure 1.8, Chapter 1. The prototype DSF was tested under a constant irradiance of 300W/m^2, external temperatures of -4^{o}C, 10^{o}C and 25^{o}C to represent winter, spring/autumn and summer in the UK. The laboratory side of the DSF was maintained at a constant 18^{o}C.

3.4 Heat Mat Tests for Simulated Stratification

As the casual heat gains within a building space are typically normalised against the floor area in m^2 [8], heat mats can be placed at the floor of a small-scale warehouse to assess vertical thermal stratification across the height of the building. This section explains the theory, aim and objectives, and experimental set-up required to facilitate the heat mat tests.

The primary aim of the experiment is to visualise whether vertical thermal stratification takes place within the scale model of the case-study warehouse, and to use the data collected to validate a computational model of stratification within a warehouse. The objectives that need to be met are:

- Position heat mat centrally, and set up a vertical guide to attach RTDs
- Allow the heat mat sufficient "heating up" time by pre-measuring the temperature of the lab and monitoring the temperature inside of the scale warehouse model
- Take temperature measurement points at three locations
- Install a model of 100% storage capacity racking and repeat the previous objectives

3.4.1 Experimental Theory

The experimental theory behind using heat mats is like that of heat plate theory in that it involves the heat transfer from a flat surface to its surroundings [174], but in this case the heat mat is confined to the internal space of the building model. The heat mats used in this experiment are electrically powered uniform heating mats made from polyethylene terephthalate (PET), and an

embedded nichrome heating element wire so the heat conduction that occurs across the surface should results in a consistent temperature distribution, allowing for replicating in later computational models.

Following usual understanding of natural convection, the air in contact with the mat will warm, experience less density and rise. However, when considering this in terms of actual temperature measurement, depending where in the internal building space it is measured from will yield different results [180]. For example, directly above the heat mat, the temperature reading will start high and decrease with vertical height due to the dissipation of heat from the mat, however, if temperature readings are taken at a distance from the heat mat, the opposite should take place and readings synonymous with thermal stratification will occur. As the experimental data is temperature readings and these can be obtained directly with PT-100 Resistance Temperature Detectors (RTD) connected to a datalogger, no formulae are required.

3.4.2 Experimental Set-Up, Measurement Variables and Equipment

The experimental set-up involves taking the 1:50 scale model of the warehouse created for the wind tunnel, and utilising 7W and 20W heat mats and three different positions where vertical temperature is measured as shown in Figure 3.13. The temperature was measured using PT- 100 RTDs and a DT85 series 3 DataTaker. The measurements positions were taken centrally at 0.36m from either side of the warehouse, where position 1 is at 0.3m across the length of the warehouse, followed by 0.7m and 1.0m for positions 2 and 3, respectively. To more accurately portray the internal layout of a warehouse, polystyrene blocks were cut and placed to simulate rows of storage racking based on industry guidelines in [181].

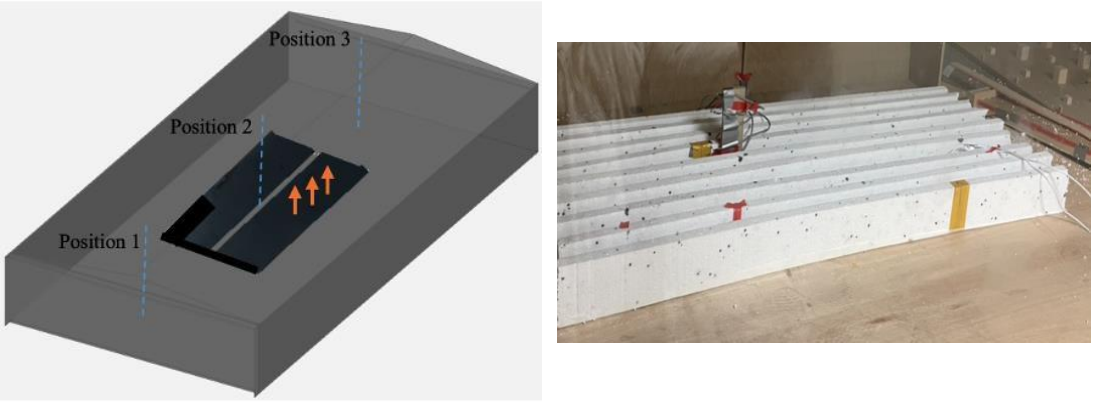


Figure 3.13 Set-up of (a) Heat Mats and (b) Storage Racking in 1:50 DSF Warehouse

Table 3.7 details the dimensions that have been selected for the storage racking rows and the aisles that separate them as well as dimensions of the heat mats used a heat source.

Table 3.7 Dimensions of Storage Racking and Heat Mats

	Dimensions (m)
Width of singular storage racking [181]	0.8
Height of singular storage racking [181]	4.8
Widths of aisles between storage racking [181]	2.5
Width of clearance at front and back [181]	5.67
7W Heat mat	0.14 by 0.28
20W Heat mat	0.28 by 0.42

3.5 Experimental Error Analysis Theory

The errors explored in the experimental data are fractional errors and standard deviation. These methods were chosen as the provide insight into different aspects of the precision and uncertainty in readings obtained through experimental equipment [182]. The theory and specifications included in this section are to be referred to in the experimental results sections in the following chapters 4, 5 and 6. The chosen equipment of anemometers, heat flux meters and RTDs produce visually normal data for the wind and thermal tests. The precision is high with all the equipment and steady state was monitored to show little variation at the end of the tests. Additionally, all experimental tests in the following chapters produced 3-4,000 readings.

3.5.1 Fractional Error Analysis

The fractional error, also known as the relative error, is a measure of the uncertainty of experimental measurements relative to the size of the measurement itself [183]. It is dimensionless and provides a means to compare the precision of different experimental measurements. For the equipment used to take measurements in this thesis, there are two different equations for the fractional error dependent on the uncertainty specifications of the equipment, as shown in Equations 3.19 and 3.20 below:

Equation 3.19 Fractional Error from Measured Value

$$fractional\ error = \frac{absolute\ error}{measured\ value}$$

Equation 3.20 Fractional Error from Full Scale Reading

$$fractional\ error = \frac{absolute\ error}{full\ scale\ reading}$$

i. Absolute errors

To calculate the fractional error, the absolute error of the measurement equipment needs to be determined, and this is different dependent on specifications [183]. The absolute error provides the worst-case error at a full-scale reading of the measurement equipment. For example, the anemometers used have an accuracy based on a 2% percentage of full-scale readings of 5V

therefore the absolute error can be found from Equation 3.21.

Equation 3.21 Absolute Error of Anemometers

$$absolute\ error_{anemometers} = 5V \cdot 0.02 = 0.1V = 100mV$$

Similarly, the heat flux meters have an accuracy of 3% of full-scale readings of 25mV so the absolute error is found from Equation 3.25.

Equation 3.22 Absolute Error of Heat Flux Meters

$$absolute\ error_{heatfluxmeters} = 25mV \cdot 0.03 = 0.75mV$$

Another measurement equipment is the RTDs which have an accuracy of 0.15°C and a full- scale reading of 51°C. The absolute error in this case is taken as the accuracy of 0.15°C. The pyranometer used to measure solar irradiance has a 5% of full-scale accuracy where the maximum voltage reading would be 50mV, so the absolute error is found from Equation 3.23.

Equation 3.23 Absolute Error of Pyranometer

$$absolute\ error_{pyranometer} = 50mV \cdot 0.05 = 2.5mV$$

The datalogger used was the DT85 series 3 which for a temperature range of -20°C to 70°C has different % of full-scale accuracies and offset errors for different measurement types. The experimental measurements were mostly in mV except for the RTDS which are in °C. The equation for combined absolute error of the data taker is below and Table 3.8 shows a summary:

Equation 3.24 Combined Absolute Error

$$combined\ absolute\ error = \sqrt{(Absolute\ error)^2 + (Offset\ error)^2}$$

Table 3.8 Combined Absolute Errors for Different Measurement Types

Measurement type	Full scale	% of full scale	offset	Absolute error	Combined absolute error
mV	30	0.16	5.7	4.8	7.45
°C	51	0.17	0.07	8.7	8.8

ii. Compounded fractional errors

As most of the measurement equipment are connected to datalogger to extract the data, the final fractional error for these tests will need to be compounded to consider both the measurement equipment and the datalogger [183]. The equations required to do this is below and the compounded fractional errors are calculated in the experimental result sections of each of the following chapters using the final absolute errors in Table 3.9.

Equation 3.25 Final Absolute Error

$$Final\ Absolute\ Error = \sqrt{\left(Absolute\ error_{equipment}\right)^2 + \left(Absolute\ error_{datalogger}\right)^2}$$

Equation 3.26 Compounded Fractional Error

$$Compounded\ Fractional\ Error = \frac{Combined\ Absolute\ Error}{Measured\ Value}$$

Table 3.9 Final Absolute Errors for Different Measurement Types

Measurement equipment + DataTaker	Final Absolute Error
Hot wire anemometers (mV)	7.5
Heat flux meters (mV)	7.5
Pyranometer (mV)	7.9
RTDs (ºC)	8.7

3.5.2 Standard Deviation Analysis

The standard deviation is a measure of the spread of a set of values around the mean and is a command that can be conducted using Microsoft Excel [184]. This analysis is more applicable to the raw experimental data obtained compared to the previous section which was focused on the accuracy specifications of the equipment used to obtain data. The equation for standard deviation is:

Equation 3.27 Standard Deviation

$$\sigma = \sqrt{\frac{\sum(x_i - \mu)^2}{N}}$$

Where x_i are the individual measurements, μ is the mean of the measurements and N is the number of measurements. The inclusion of a standard deviation analysis is useful for understanding the repeatability, reliability, and therefore rigor of the experimental data [184].

Depending on applicability, the results for fractional error and standard deviation analysis are in the relevant results chapters 4, 5 and 6. This concludes the methodology for all experimental methods covered in this thesis. The next and final section of this chapter concerns the overarching computational model that spans across all results chapters and discusses the theory and mathematics behind computational fluid dynamics and how they have been adapted or applied to build models which replicate each of the experimental conditions.

3.6 Computational Fluid Dynamics

In this section, the commercial software, ANSYS Fluent is introduced as the computational fluid dynamics tool used in this research. An explanation of the fundamental mathematical theory it is built upon is covered as well as geometry, computational domain, boundary conditions, mesh-generation and model set-up. The Boussinesq approximation, heat generation rate and use-defined wind velocity inlet profiles are also introduced.

3.6.1 Reynolds-Averaged Navier Stokes (RANS) Modelling

The numerical method for producing results in this research is from the commercial software ANSYS Fluent 18.1 with a Semi-Implicit Method for Pressure-Linked Equations (SIMPLE) for steady state analysis [185-189]. The advantages and limitations of using CFD over an Airflow Network Model (AFN) to simulate heat transfer and fluid flow have been discussed previously in Section 1.4, Chapter 1. It was concluded that when dealing with complex thermal modelling such as temperature stratification in combination with natural ventilation, the mathematical foundation of computational fluid dynamics, the Reynolds-Averaged Navier Stokes (RANS), have superior capabilities over the other primary numerical method, Airflow Network Model (AFN). Computational Fluid Dynamics is built upon the Navier-Stokes equations, which are the basic governing equations for a viscous, heat conducting fluid, applies Newton's Law of Motion to a fluid element (momentum equation), and supplemented by the mass conservation equation (continuity equation), and the energy equation [190,191]. The equations for or compressible fluids, the continuity, momentum, turbulent and energy equations are provided below where all terms and symbols are in the nomenclature.

Equation 3.28 The Continuity Equation (Mass Conservation)

$$\frac{\partial \rho}{\partial t} + \nabla\, x\, (\rho u) = 0$$

Equation 3.29 The Motion Equation (Momentum Conservation)

$$\frac{\partial (\rho u)}{\partial t} + \nabla\, x\, (\rho u u) = \, -\nabla p + \rho g + \nabla\, x\, (\mu \nabla u) - \nabla\, x\, \tau_t$$

Equation 3.30 Turbulent Kinetic Energy, k

$$\frac{\partial (\rho k)}{\partial t} + \nabla\, x\, (\rho k u) = \nabla\, x\, [\alpha_k \mu_{eff} \nabla k] + G_k + G_b - \rho_\varepsilon$$

Equation 3.31 Energy Dissipation Rate, ε

$$\frac{\partial (\rho \varepsilon)}{\partial t} + \nabla\, x\, (\rho \varepsilon u) = \nabla\, x\, \left[\alpha_\varepsilon \mu_{eff} \nabla \varepsilon\right] + C_{1\varepsilon} \frac{\varepsilon}{k} (G_k + C_{3\varepsilon} G_b) - C_{2\varepsilon} \rho \frac{\varepsilon^2}{k}$$

3.6.2 Geometry, Computational Domain and Boundary Conditions

There are several different geometries, computational domains (where relevant) and boundary conditions developed in this thesis, and they can be organised per the different stages of building the final computational tool. All geometry is 3-dimensional and was built in ANSYS Fluent's own SpaceClaim builder.

i. Small- and full-scale double skin façade warehouse in wind-only conditions

The model build details in this section are to be used in reference to Chapter 4. For the validation of the computational model, a 1:50 scale model of the double skin façade warehouse was built along with a 1:1 domain reflective of the wind tunnel test section. The full-scale modelling uses the 1:1 dimensions of the case study warehouse with a domain that follows the best-practice 5H, 5H, 15H rule from literature [192] applied to the front, back, sides and height of the building model where H is the longest dimension which in this case is the warehouse's length, 72m. Figure 3.14 shows the dimensions of the geometry with the main boundary conditions for (a) small-scale and (b) full-scale DSF warehouse used in the wind-only modelling.

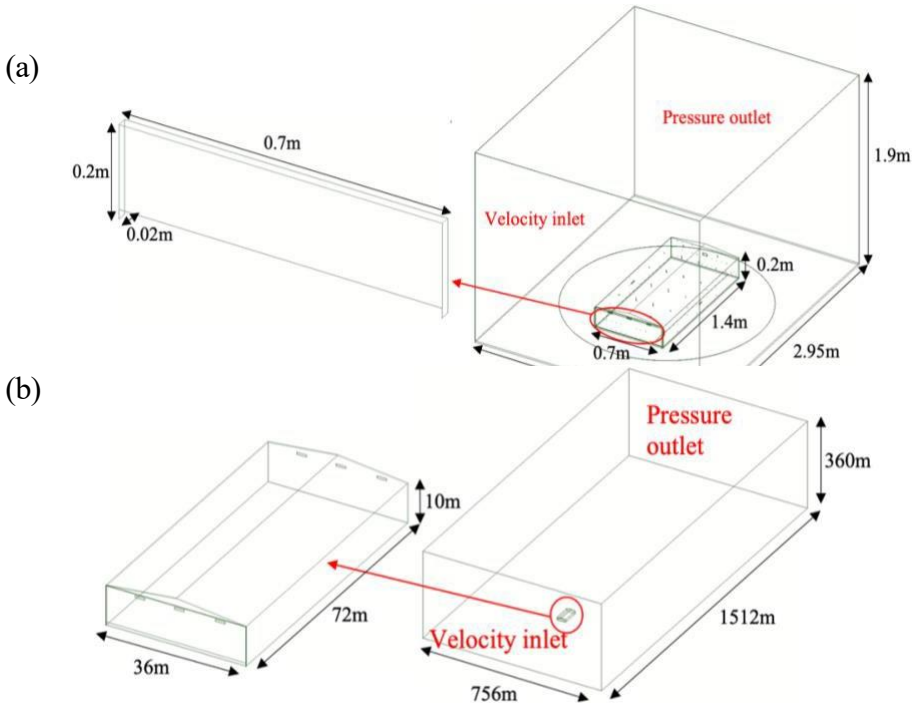


Figure 3.14 CFD Geometry for (a) 1:50 and (b) Full-scale DSF Warehouse and Computational Domain

Other boundary conditions include labelling each façade of the DSF, at both scales. The thickness of the walls for the small-scale model are the same as the plywood and MDF used in construction of the experimental model, and the thicknesses of the walls for the full-scale model are that of the case-study warehouse.

ii. Prototype and full-scale double skin façade in buoyancy-only conditions

The model build details in this section are to be used in reference to Chapter 5. These models focus only on the DSF, and the warehouse is excluded. For the validation of the computational model, a 1:1 scale model of the prototype double skin façade was built along with a 1:1 full-scale dimension to span across the front façade of the case study warehouse. Figure 3.15 shows the dimensions of the geometry with the main boundary conditions for the (a) front-view and (b) side view of the 1:1 DSF prototype. The pressure inlet is the bottom opening, and the pressure outlet is at the top, representing an inlet to the adjacent warehouse. The main boundary conditions concern the different surfaces of the outer and inner skins as depicted in Figure 3.15 (b) and the remaining surfaces encasing the cavity are assumed adiabatic. The openings have a height equal to the depth of the cavity.

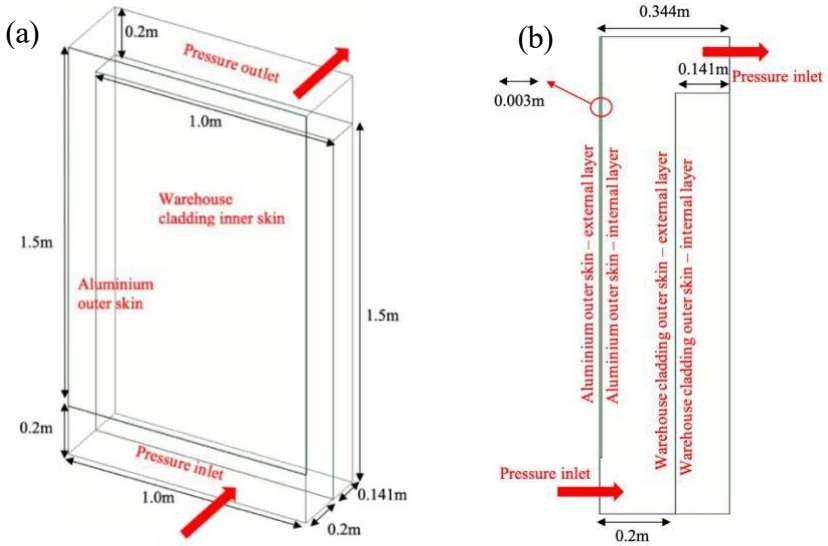


Figure 3.15 CFD Geometry for (a) 3D Front View and (b) 2D Side View of DSF Prototype

The thickness of the aluminium outer skin and warehouse cladding inner skin remain the same in the full-scale DSF geometry at 0.03m, and 0.141m respectively as does the depth of the cavity at 0.2m. The only dimensions which change are the height and width as shown in Figure 3.16 (a) front-view and (b) side-view. The boundary conditions remain the same as the 1:1 DSF prototype.

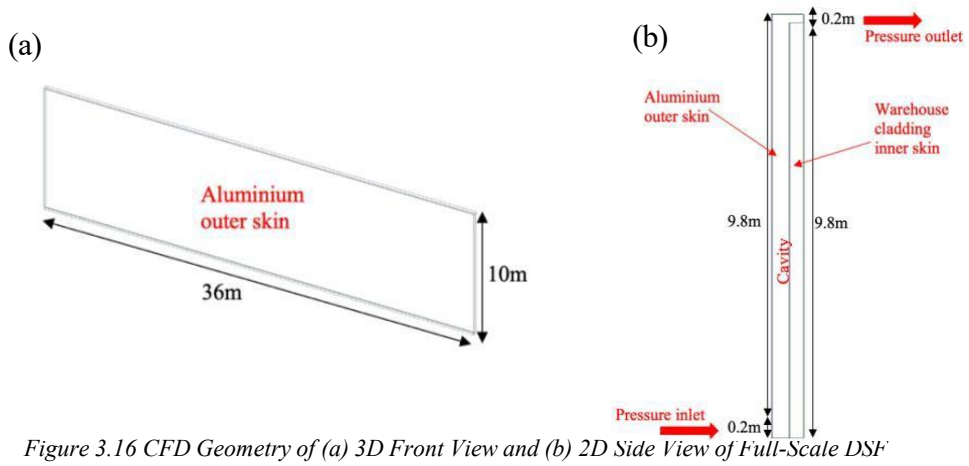


Figure 3.16 CFD Geometry of (a) 3D Front View and (b) 2D Side View of Full-Scale DSF

iii. Small- and full-scale warehouse under simulated stratification

For the laboratory simulation of stratification in the 1:50 scale warehouse (excluding DSF), any openings were sealed off to create a closed internal space. Figure 3.17 shows the dimensions and boundary conditions for the (a) 7W and 20W heat mats, and (b) storage racking where There are 8 rows of storage racking of length 1.4m, separated by aisles of 0.05m width.

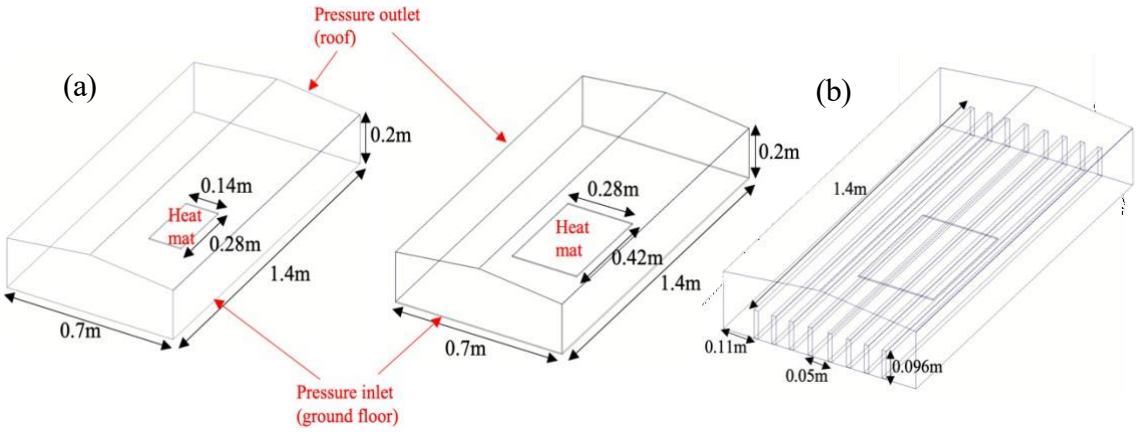


Figure 3.17 CFD Geometry for Stratification Model of (a) Heat Mats and (b) Storage Racking

iv. Full-scale double skin façade warehouse in wind and buoyancy conditions

The final geometry model is a combination of Figure 3.14 (b) and Figure 3.16 whereby the full-scale DSF warehouse is in a 5H, 5H, 15H computational domain, but taking the relevant thermal boundary conditions from part (ii). The next section looks at the meshing process of these geometries as well as the set-up for performance grid independence analyses.

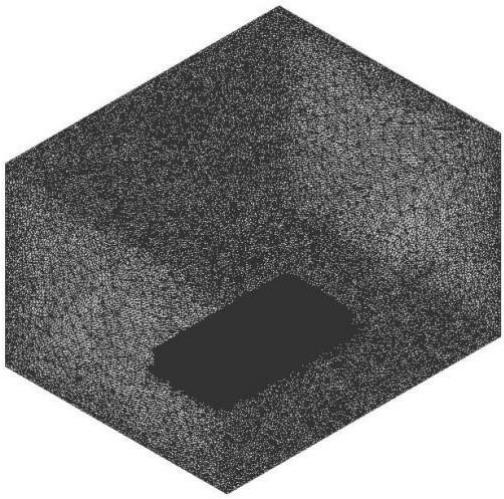
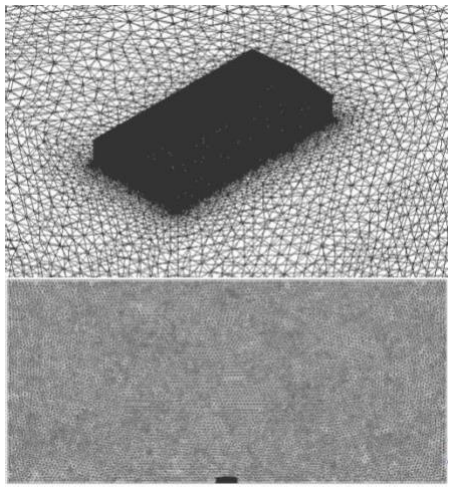
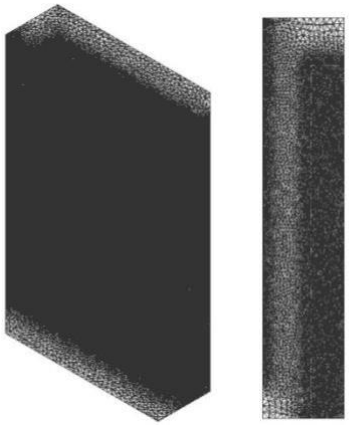
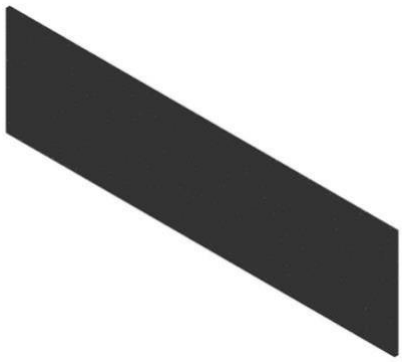
3.6.3 Mesh Generation and Model Set-Up

Table 3.10 provides an overview of the four key meshes generated. They comprise a tetrahedral mesh which is best suited to complex geometries involving sharp edges such as the inlet and outlet of the DSF cavity [187],[188]. Specific details of the mesh are included in the grid independence analyses in Sections 4.3.2 and 5.3.3 in the following chapters as a new test was completed for each change to the geometry or computational domain. The final mesh developed for the validated CFD tool in Chapter 7 is a combination of those in the above table where the number of elements is around 5 million.

All the CFD models are based off a pressure-based solver with absolute velocity formulation under steady time. When considering buoyancy and thermal conditions, gravity is turned on with a value of -9.81m/s^2 as well as energy. There are a range of viscous models applied and

any sensitivity analyses of this are explored in the individual results chapters, however all start with the standard k-epsilon model where enhanced wall treatment and full buoyancy effects are added when looking at thermal conditions. In the thermal modelling where material properties are important, Appendix Section A.4.3, Table A.19 provides details of the DSF material layers. The specifics of value inputs at the changing boundary conditions for different models is also laid out in Appendix Sections A.4.3, A.3 and A.5. Final details include the SIMPLE pressure-velocity coupling scheme, a least square cell-based gradient, body force weighted pressure (thermal) and second order upwind for momentum, turbulent kinetic energy, turbulent dissipation rate and energy. For wind only modelling, 2500 iterations were sufficient and for buoyancy/thermal only modelling, 4000 iterations were calculated.

Table 3.10 Mesh Generation for Wind and Buoyancy Models

1:50 Scale Model of DSF Warehouse and Wind Tunnel Test Domain 	Full-scale Model of DSF Warehouse and 5H,5H, 15H Domain 
1:1 Scale Model of DSF Prototype (No Domain) 	Full-scale Model of DSF for Warehouse (No Domain) 

3.6.4 Boussinesq Approximation and Heat Generation Rate

The thermal modelling in this thesis comprises application of the Boussinesq model to simulate buoyancy, and the heat generation rate to simulate solar radiation.

i. *Boussinesq Model*

When a heat source, such as solar gain, is added to a fluid, such as cavity air, the air density varies with temperature and flow can be induced due to the force of gravity acting on these density variations. This phenomenon is called buoyancy-driven flows, or natural convection and can be modelled by ANSYS Fluent and there is the option to use the Boussinesq Model [193] which treats density as a constant value in all solved equations, except for the buoyancy terms in the momentum equation:

Equation 3.32 Boussinesq Model

$$(\rho - \rho_0)g \approx -\rho_0\beta(T - T_0)g$$

Where ρ_0 is the constant density of the flow, T_0 is the operating temperature, and β is the thermal expansion coefficient. The momentum equation is solved by using the Boussinesq approximation, which eliminates ρ from the buoyancy term:

Equation 3.33 Boussinesq Approximation

$$\rho = \rho_0(1 - \beta\Delta T)$$

The Boussinesq approximation is valid when:

Equation 3.34 Validity of Boussinesq Approximation

$$\beta(T - T_0) \ll 1$$

Therefore, the approximation is limited in that it should not be used if the temperature differences in the domain are large, and it also cannot be used with species calculations, combustion or reacting flows [193]. Given that the temperature differences that will be obtained in this research are related to air and surface temperatures calculated from a maximum solar gain of 300W/m^2 and thus will likely stay below a temperature differential of 100K, the Boussinesq approximation is justified, and appropriate [194].

As the openings are on opposite sides of the cavity and exposed to different external temperatures in all three seasons, the Boussinesq operative conditions must reflect the average temperature in the cavity which is simply the average of the two external temperatures. Table 3.11 provides the Boussinesq parameters for winter, intermediate and summer conditions.

Table 3.11 Boussinesq Parameters for Each Season [195]

	Winter (7°C)	Intermediate (14°C)	Summer (21.5°C)
Temperature (K)	280.15	287.15	294.65
Density (kg/m^3)	1.259	1.229	1.198
Viscosity (kg/ms)	1.750	1.784	1.820
Specific heat capacity (J/kgK)	1005	1006	1006
Thermal expansion coefficient (1/K)	0.00341	0.00341	0.00341
Thermal conductivity (W/mK)	0.02489	0.02542	0.02598

The boundary conditions are outer aluminium, inner aluminium, outer cladding, inner cladding, pressure inlet, pressure outlet, adiabatic top, adiabatic left, adiabatic right, and adiabatic bottom. The difference with these results is that when the external temperature is colder than the internal temperature, the pressure inlet and outlet need to be reversed, i.e., the top opening becomes the inlet, and the bottom becomes the outlet as the air will move from hot to cold.

ii. Solar Irradiance and Heat Generation Modelling

There are multiple ways to model solar irradiance in computational fluid dynamics, but the method chosen in this study is to apply a heat generation rate to the outer skin, rather than a heat flux. This is a common approach to model solar gain as it can simulate the internal heat generation results from the solar radiation absorption, [196], [197]. It is relatively straightforward to calculate from the heat flux and thickness of the material, as shown in Equation 3.37 below. The heat generation rate applied to the aluminium outer skin of the double skin façade in this study is 100,000W/m^3 where the heat flux is 300W/m^2 and thickness is 3mm.

Equation 3.35 Heat Generation Rate

$$Heat\ generation\ rate\ \ (W/m^3) = \frac{Heat\ flux\ (W/m^2)}{Thickness\ (m)}$$

3.6.5 User-Defined Wind Velocity Profiles

When modelling wind conditions, a user-defined wind profile is applied to the velocity inlet boundary condition of the computational domain. There are quite a few of these involved in Chapter 4 and 7, as different wind profiles were needed for different models as detailed here:

- CFD model of the wind tunnel test section
- Dynamic similarity of small-and-full scale models
- Full-scale modelling under meteorological scenarios for winter, spring, summer and autumn

The text files for these have been included in the appendix under section A.3.4 and A.3.5 where the velocity has been calculated using the power law in Equation 3.1, in Section 3.1.2. These were imported into ANSYS Fluent via the 'profiles' option in boundary conditions.

3.7 Chapter Summary

The mixed research methods employed in this thesis include an atmospheric boundary layer wind tunnel, a climate chamber, heat mats, and computational fluid dynamics. Individually, the experimental methods serve to focus on three different phenomena occurring within or around a warehouse with a double skin façade retrofit including wind pressure, buoyancy heating in a cavity, and thermal stratification across the height of the space. The outcome of obtaining original data from each of these experimental methods is to validate models created in CFD software, ANSYS that are required to deliver the final energy performance tool of the DSF retrofit for storage and distribution warehouses at full-scale in the absence of testing on a real warehouse.

3.7.1 Limitations and Assumptions of Chosen Methodologies

There are some limitations of conducting more than one experiment such as time and budget constraints within the scope of this research and having to obtain vast amounts of data using different equipment which each have their own uncertainty. The ABL wind tunnel is limited by the cross-sectional area of its test section in terms of wind blockage ratio which means that buildings such as warehouse which have large-width spans must be a certain scale if trying to apply a façade building technology to the model. The climate chamber was limited to only comprising one controlled chamber instead of two which means that the ambient temperature of the laboratory side used to reflect internal warehouse conditions might not be uniform. The limitation of using the same scale model of the warehouse from the wind tunnel tests in the heat mat tests for stratification is that it was made from MDF which is not reflective of the typical warehouse materials like the cladding used in the prototype tested in the climate chamber. Lastly, the limitations of the CFD models are that assumptions were made so that they could be steady state, rather than transient to beat computational and time costs, and a lack of literature

surrounding the building physics development of a model to combine local wind, “solar” heat flux, and stratification presents intellectual obstacles.

3.7.2 Closing Remarks

Despite the limitations of the various research methods, the validity of the CFD model is the primary outcome of this thesis so successfully collating data from the individual experiments and finding good agreement between them and the computational model ensures a level of scientific rigor. The experimental objectives are not necessarily complex in that they have existing literature which uses the same methods, but the combination of all these methods to deliver the outcome of a CFD model validated in different wind and thermal conditions is a challenge whilst also offering the primary novelty of this research.

The next chapter comprises the results from the first experimental method, the ABL wind tunnel, to develop and validate the wind-only stage of the computational model of the double skin façade warehouse.

Chapter 4

Wind-Driven Ventilation Performance of a Double-Skin Façade Warehouse

4.1 Chapter Introduction

Where buildings rely on traditional building services such as Heating, Ventilation, and Air-Conditioning (HVAC) systems, these can account for up to 70% of a building's energy consumption, and the fans alone typically constitute 25% of the total building electricity consumption [37], [40]. Wind forces at a building façade can significantly affect both the ventilation and thermal performance of a double skin façade (DSF) system, but the focus of this chapter will look at ventilation alone. The BSRIA Illustrated Guide to Ventilation defines a ductwork system as the network to supply and extract air from around the building [32]. In terms of a naturally ventilated building, it is possible to have ducts sized to overcome the pressure drop of the duct and the same can be applied to a DSF system. Wind-driven ventilation arises when wind enters the building on the windward side where the surface pressure is high, and the air then passes through to the leeward side, exiting at openings where the pressure is lower [42]. Therefore, determining the external pressure coefficients at building surfaces is crucial to understand ventilation capacity.

This chapter looks at treating the DSF as a 'ventilation duct' and using experimentally derived pressure coefficients to calculate a pressure drop which is used to determine volume flow rate in a wind-only scenario. The double skin façade retrofit for warehouses developed in this research is designed to deliver ventilation.

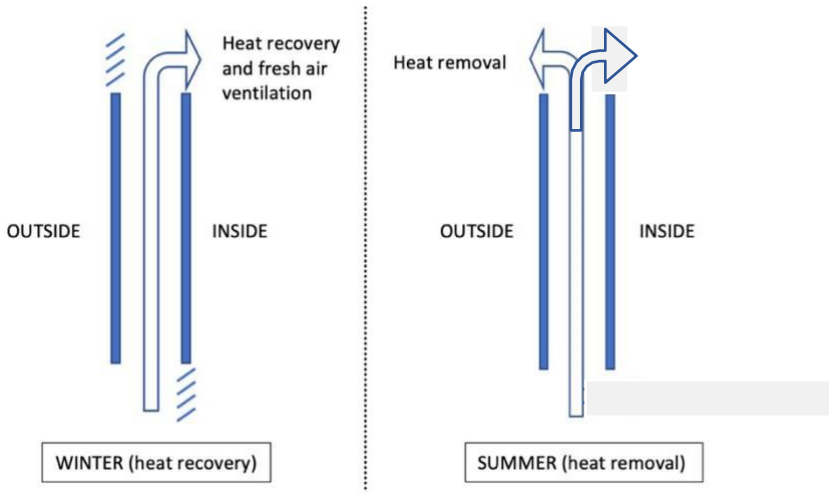


Figure 4.1 Heat Recovery and Removal Operation of a DSF

Therefore, the research in this chapter aims to assess the influence of a DSF on the cross-ventilation capacity for storage and distribution warehouses in the UK. The objectives required to achieve this include:

- Conduct a wind tunnel experiment of a scaled DSF warehouse model
- Obtain pressure coefficients from the experiment to verify a numerical model
- Assess capacity for cross-ventilation
- Complete pressure drops calculations and ventilation analyses

The novelty of this study is in two prongs: firstly, the method of conducting scale atmospheric boundary layer wind studies of a double skin façade system applied to a warehouse; and, secondly, the simulation of outdoor air delivery to large spaces via a double skin façade system.

4.2 Experimental Results

Experimental results from the wind tunnel were obtained for the 1:50 small scale double skin façade warehouse. The initial results include calculated wind profiles for the atmospheric boundary layer at the test wind speed of 5m/s, and the measured differential pressures along with calculations of pressure coefficient using a preliminary dynamic pressure from measured velocity in the wind tunnel. In terms of error analysis of the experimental data, standard deviation analyses were conducted to evaluate the accuracy in measurement from the pitot tube and scanivalve pressure transducer.

4.2.1 ABL Experimental Wind Profile

The preliminary wind profile was estimated by taking a 5m/s reading at the centre of the test section at height 0.9m, and a semi-urban wind shear exponent of 0.18, shown in Figure 4.2. The calculated data for this wind profile can be found in the Appendix, Section A.3.4.

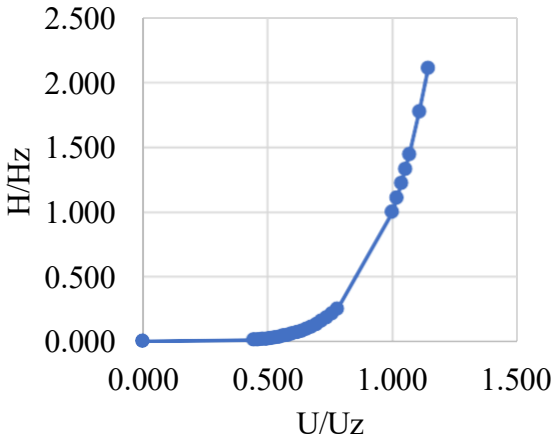


Figure 4.2 Preliminary Wind Profile with Wind Shear Exponent of 0.18

4.2.2 Pressure Differential Data for Different Wind Speeds and Angles

This section includes the experimental pressure data obtained for both the double skin façade and the warehouse for a range wind speeds and angles where Figure 3.6 (b) in Section 3.2.2 of the methodology shows the location of the differential pressure measurements. This was done to ensure that there was some consistency in the pressure transducer's ability to measure differential pressure and respond to changing conditions. Figure 4.3 below shows the distribution of differential pressure across the double skin façade's outer skin for (a) wind velocities of 1, 3 and 5 m/s, and (b) wind angles of 0, 90, 180 and 270 degrees under a constant wind speed of 5m/s. The distribution of measurement points d1-d13 are displayed in Chapter 3, Section 3.2.2, Figure 3.6 (b).

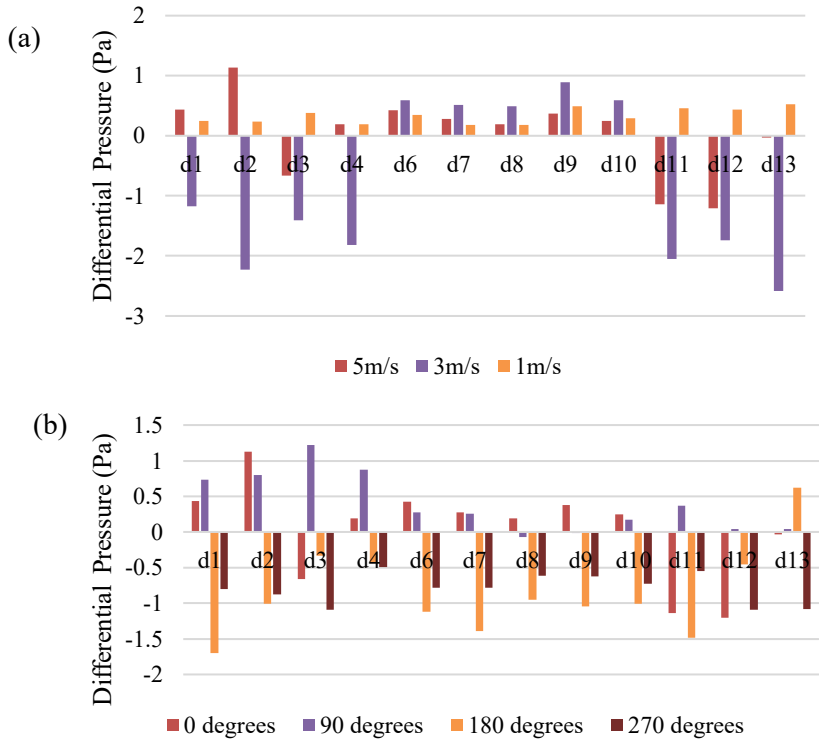


Figure 4.3 Differential Pressure Distribution on DSF for Changing (a) Wind Speeds and (b) Wind Angles

The benefit of assessing the raw differential pressure data obtained from the Scanivalve pressure transducer before calculating pressure coefficients, Cp is to evaluate if the 1:50 scale model of the DSF warehouse is behaving as expected aerodynamically. For example, in Figure 4.3 (a), rather than there being clear relationship between the increase in wind tunnel speed and magnitude of differential pressure, there are deviations where the differential pressure becomes negative for 3m/s for data points near the edges of the DSF marked by points d1-d4, and d11-d13. As the DSF outer skin is windward, it is expected that the differential pressure (and therefore the Cp) should be positive which is the case for 1 and 5m/s, but not for 3m/s. These results highlight the complexity

of interpreting this type of data as on one hand, the deviations could be explained by airflow phenomena such as vortex shedding or flow separation, especially as they occur towards the edges but on the other hand, it could indicate issues with the pressure transducer readings. This is why the DSF outer skin was tested under different wind angles, under a constant wind speed of 5m/s, to ensure that the differential pressure data was responding to these changing conditions as shown in Figure 4.3 (b). The result which is indicative of correct aerodynamic performance is that a wind angle of 180 degrees yields all negative differential pressures confirming that the DSF outer skin is leeward in this position, compared to 0 degrees when they are positive as expected for a windward surface. However, there are still some deviations such that a wind angle of 90 degrees results in positive differential pressure, whilst 270 degrees results in negative differential pressure despite the DSF outer skin being positioned on the same axis away from the upstream flow. Again, as with (a), this could be explained by intricacies within the flow distribution around the model. For example, perhaps there were higher levels of suction occurring at the DSF outer skin at 270 degrees due to the surrounding turntable or test section than was the case at a 90-degree angle. Overall, there are findings that are generally consistent with expectations of flow around a building model in an atmospheric boundary layer wind tunnel, but these results also highlight the challenges with conducting this type of experiment.

One way to solidify confidence in the findings from an ABL wind tunnel is to examine the measurements on other surfaces of the model. Average pressure coefficients for each façade under a wind speed of 5m/s and changing wind angle of the DSF outer skin from windward (0 degrees) to leeward (180 degrees) are given in Table 4.1 where the raw differential pressure data for each measurement point on the different facades is given in the Appendix Section A.3.

Table 4.1 Average Measured Façade Differential Pressure for Warehouse at 0- and 180-degrees Wind Angles

	Average Differential Pressure (Pa)	
	0 degrees	180 degrees
DSF Outer Skin	0.779	-0.859
Back Façade	-0.720	-0.664
RHS Façade	-0.662	-0.572
LHS Façade	-0.779	-1.289
LHS Roof	-0.300	-0.341
RHS Roof	-0.389	-0.367
*Taken from six central points where differential pressure is positive		

In the first column of Table 4.1 where the wind angle is 0 degrees meaning the DSF outer skin is windward, there is an expected pattern where the differential pressure is positive here and negative on the remaining surfaces which are leeward.

When the model is rotated 180 degrees so that the DSF outer skin is now leeward with the back façade facing the upstream flow, the DSF outer skin performs correctly by changing sign to a negative differential pressure whereas the back façade (now windward) does not. All other surfaces behave as expected. As previously said, this could be explained by the complex aerodynamics that occur around this warehouse model which has a length to width aspect ratio of 2:1 that could perhaps lead to more frequent flow separation at corners. Additionally, due to the limited number of pressure ports on the transducer (62), when testing all facades of a relatively large model, this meant that only 9-14 points could be measured at one time. This could present an issue of not fully capturing the airflow phenomenon taking place on the surface, especially in this case where the pressure transducer experienced overheating and fluctuating results.

The final step taken in this thesis to explore the validity of the differential pressure data obtained in the ABL wind tunnel is to assess the performance of the roof panels of 6-degree slope when exposed to different wind angles. Figure 4.4 shows the results.

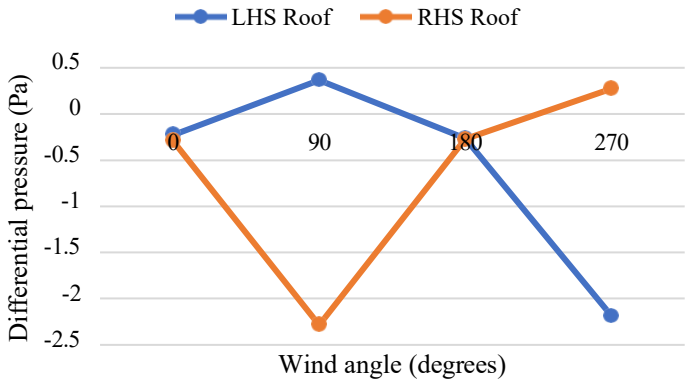


Figure 4.4 Differential Pressure Distribution on Warehouse Roof for Changing Wind Angles

Roof panels, when sloping in different directions from the apex, present a unique opportunity to assess aerodynamic performance as when one side (RHS) is faced 90 degrees away from the direction of the flow, the other (LHS) is windward and vice versa at 270 degrees. This is exemplified by a positive differential pressure, and negative differential pressure on the same roof. When the DSF outer skin is facing upstream or downstream, (0 and 180 degrees), both roof panels experience a negative differential pressure of similar magnitudes.

The final step is to conduct error analysis of the instrumentation to determine its accuracy in obtaining differential pressure readings, and this is explored in the next section.

4.2.3 Error Analysis

The theory behind the standard deviation analysis conducted for the original pressure differential data collected in the wind tunnel test is detailed in Section 3.5 of the methodology chapter, and supplementary data is in the Appendix, Section A.3.1. The pressure transducer had a sampling frequency of 500Hz, and a total of 5000 readings so an average reading was taken after every sample period. The STDDEV function in Microsoft Excel was utilised to determine the standard deviation which was used to find the positive and negative error bars. Figure 4.5 shows the results of the error analysis for the 1:50 scale DSF different pressure readings for a wind angle of 0 degrees and wind speed of 5m/s which is the experimental benchmark for validating the computational model against in the following sections.

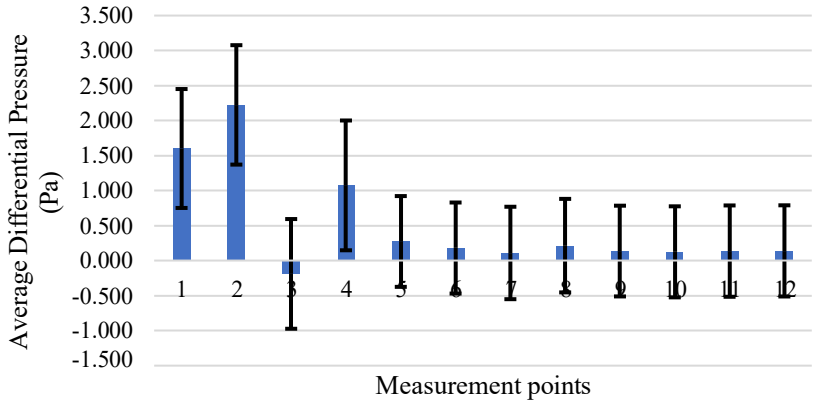


Figure 4.5 Standard Deviation Uncertainty in Average Differential Pressure Measurements for 5m/s at 0 degrees

The largest error bars occur where the readings are larger at points 1, 2 and 4 all of which are towards the left-hand side of the DSF outer skin suggesting a complex airflow phenomenon caused by flow separation and reattachment at the edges and corners. The remainder of points are generally consistent, and positive. The average standard deviation across all points is 0.50Pa, and the stated accuracy of the Scanivalve pressure transducer at +/- 2.0Pa indicates that this is well within the specification and much smaller than the maximum possible error, showing that the data is reliable. Additionally, the range of pressure values is 2.414Pa and this can be overcome when taking an average of the 12 points as best practice for comparison with the data obtained from the computational fluid dynamics in the later Section 4.3.1.

Whilst the experimental readings fall within the Scanivalve pressure transducer's stated range of readings between -995Pa to 995Pa, the manufacturer's accuracy is for tests with much higher pressure than the one in this thesis. This could explain the large fluctuation in results, and a smaller range transducer would be more applicable.

4.3 Experimental Validation of Numerical Models

The computational fluids dynamic model of the DSF warehouse includes a 3-dimensional geometry, meshes of extracted volume of air through the geometry and wind tunnel test section macro-environment and a detailed set-up of boundary conditions and velocity profiles detailed previously in Section 3.6 of Chapter 3. Specifically, the experimental verification of the numerical models comprises grid independence tests, and turbulence model sensitivity analyses to deliver a best match between the experimentally- and numerically derived pressure coefficients.

4.3.1 Initial Model Comparison with Experimental Data

Before the optimisation of the model to obtain a best-fit match to the experimental data is conducted, there needs to be a base-case reference. This initial model was built using a medium mesh and the wind profile has a wind shear exponent of 0.18. Figure 4.6 shows the comparison of pressure coefficients between the experimental and CFD data for a wind angle of (a) 0 degrees and (b) 180 degrees.

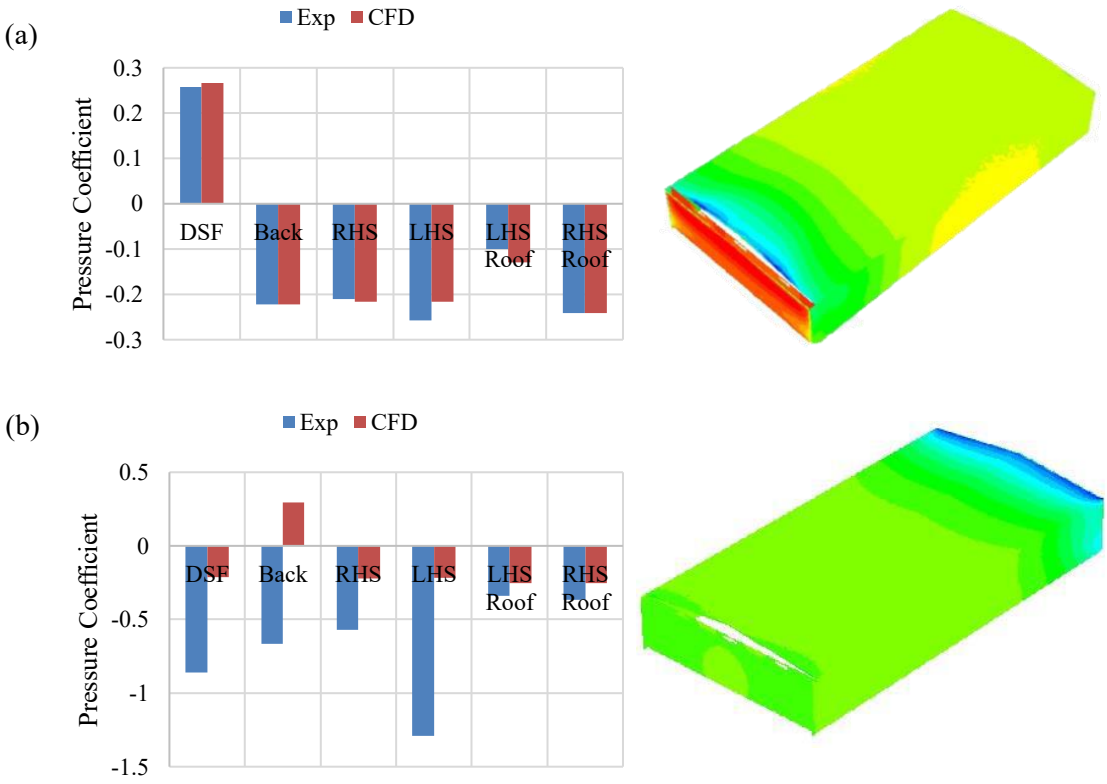


Figure 4.6 Comparison of Pressure Coefficients between Exp. And CFD Data for (a) 0 and (b) 180 degrees

There is a high level of similarity between the experimental and CFD pressure coefficient, Cp data for a wind angle of 0 degrees for all facades except for a slight deviation on the LHS and LHS roof panel.

Conversely, there are larger discrepancies between the two sets of data when the DSF warehouse is oriented at 180 degrees (leeward) with only the LHS and RHS roof showing closeness in magnitude. The main reason for this is that the experimental data produced a negative Cp for the back façade when it is now windward and should be positive. In addition, the magnitude of Cp for the DSF outer skin, and LHS façade are greater than those obtained in CFD. From an experimental perspective, this could be explained by the possibility that leeward facades are harder to obtain accurate readings for as there is higher complexity of suction and flow reattachment than that of the windward façade. It is also worth highlighting that this comparison is between 9-14 experimental measurement points (depending on location) against the average of each entire façade on the CFD model, and this can cause differences. However, from these initial results, the CFD model does seem to behave correctly from an aerodynamic perspective as the Cp of each façade changes when the model is rotated to reflect windward and leeward responses. Table 4.2 below shows the magnitude of error between the experimental and CFD Cp values for each façade.

Table 4.2 CFD Comparison of Average Facade Cp for Warehouse at 0- and 180-degrees wind angles

	% Error between Experimental and CFD Pressure Coefficients	
	0 degrees	180 degrees
DSF Outer Skin	3	75
Back Façade	0	144
RHS Façade	2.3	62
LHS Façade	16	83
LHS Roof	141	26
RHS Roof	85	31

The results in the above table show a range of discrepancy between the experimental and CFD pressure coefficient data and highlights further that the windward orientation results in the closest comparison, apart from the roof panels. The main difference between the DSF, back, RHS and LHS facades which have good similarity with the CFD model, and the roof panels is that they are vertical and perpendicular to airflow, whereas the roof panels are parallel to the flow stream. This could make obtaining pressure data more difficult. However, the roof panels have the closest similarity to the CFD model when the warehouse is oriented at 180 degrees, whilst the other facades do not. In terms of validation, this initial CFD model is a starting estimate and there could be inaccuracies in some of the experimental data rather than the CFD model itself, especially for the wind angle of 180 degrees, so the next step is to compare the specific pressure tap locations rather than the average façade.

The DSF outer skin is the façade of most interest in this study which is why it is the focus of the comparison of exact pressure tap locations between experimental and CFD Cp data as show in Figure 4.7 for a wind angle of (a) 0 degrees, and (b) 180 degrees.

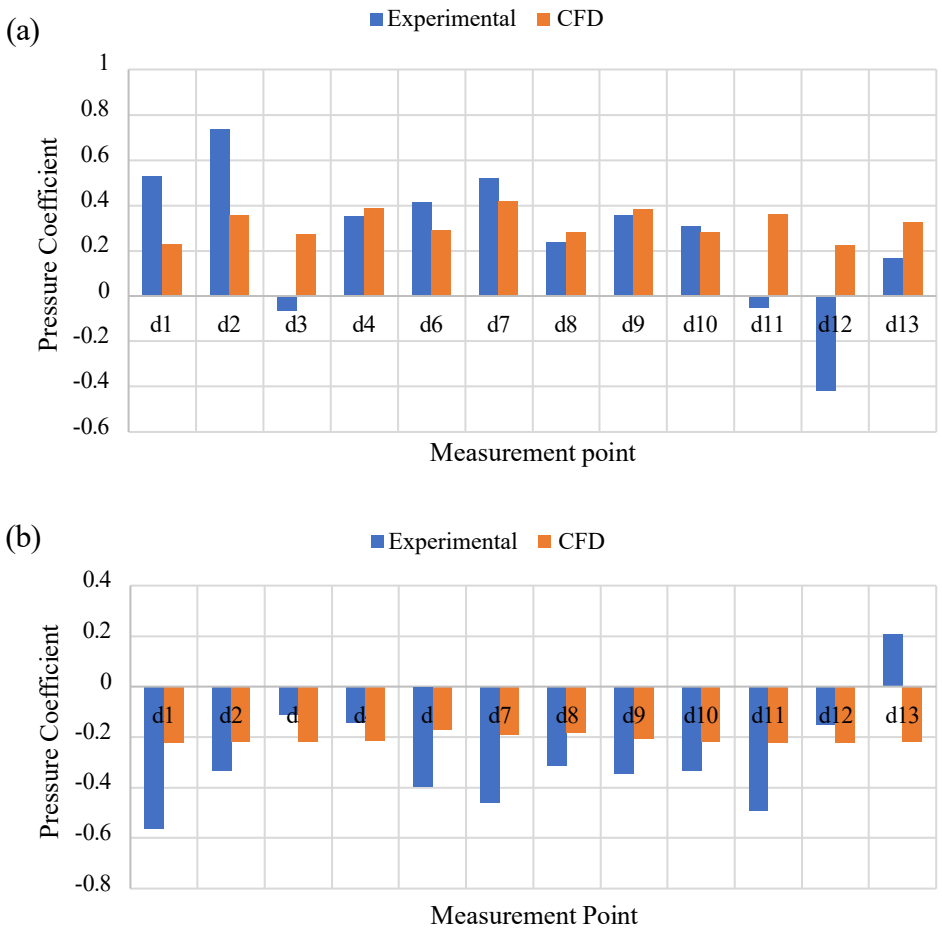


Figure 4.7 Comparison of Experimental and CFD Cp on the DSF Outer Skin for (a) 0 and (b) 180 degrees

The average Cp of the 12 pressure tap locations on the DSF outer skin calculated from the CFD model is 0.31, and -0.21 for wind angles of 0 and 180 degrees, respectively. Compared to the experimental data, these results produce an error of 23% for 0 degrees, and 27% for 180 degrees which are both relatively good compared to some of the Cp values obtained from the average of the whole DSF outer skin façade. Out of the two analyses, this is likely to provide better validation as not only are the errors reasonable, but the distribution of Cp across the 12 measurement points in the CFD model is like the experimental data for different wind angles.

To ensure that the CFD model, now validated by the experimental Cp data, does not have any inherent issues related to mesh, a grid independence test is performed in the following section.

4.3.2 Grid Independence Tests

The purpose of conducting grid independence tests of meshes used in computational fluid dynamics is to prove that the results of the simulation are independent of the mesh number and is a best-practice first step in experimentally verifying computational models [185],[186]. The grid independence tests in this research comprises developing three different meshes of approximately 1, 4 and 8 million for the 1:50 scale model geometries. The purpose is to show that a change in mesh number should not significantly affect the results, which in this case is the pressure coefficient values across all facades.

It should be noted that the grid independence tests here are most applicable to the small-scale geometry, and these mesh numbers will be adapted for the full-scale model accordingly. Figure 4.8 displays the difference in pressure coefficients across all facades under coarse, medium, and fine meshes for DSF outer skin.

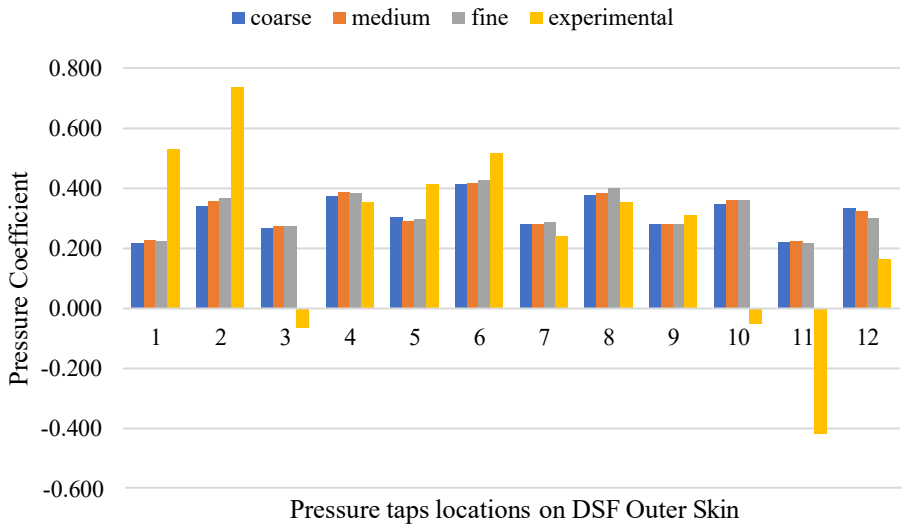


Figure 4.8 Grid Independence Results for DSF Outer Skin

Despite the change in mesh number, the calculated pressure coefficients remain similar and generally align with the experimentally derived pressure coefficients. On average, the error between the computational models and the experimental data is between 22 and 24% from a coarse mesh to fine mesh. This indicates not only a mesh independence, but also a reasonable error. Some of this error is likely due to higher fluctuations occurring experimentally than what would occur in computational fluid dynamics once stabilised, and this could be cause by a range of things such as loose pressure taps connections, or high turbulence in the wind tunnel that is not possible to replicate in the model.

As previously mentioned in the methodology, a medium mesh was chosen to be applied to the results as it offered good accuracy without compromising computational resource with modelling a higher count elemental model, such as the fine mesh. The next step in building a verified computational model which involves fluid dynamics is to apply different turbulence models.

4.3.3 Turbulence Model Sensitivity Analysis

As the computational studies are focussed on the fluid dynamics of air in and around the warehouse, a range of turbulence models should be applied to find a best match. The chosen models to assess this are variations of k-epsilon including standard, Renormalization Group (RNG), and realizable as they are the most suitable for a controlled, small domain such as the wind tunnel test section, and should be able to handle turbulent fluctuations appropriately [184-186].The preliminary model was modelled with k-epsilon standard, so this will be compared against RNG and Realizable for a medium mesh number to see if the error between the computational model and experimental data can decrease any further and obtain a better match. Figure 4.9 shows the result of this study.

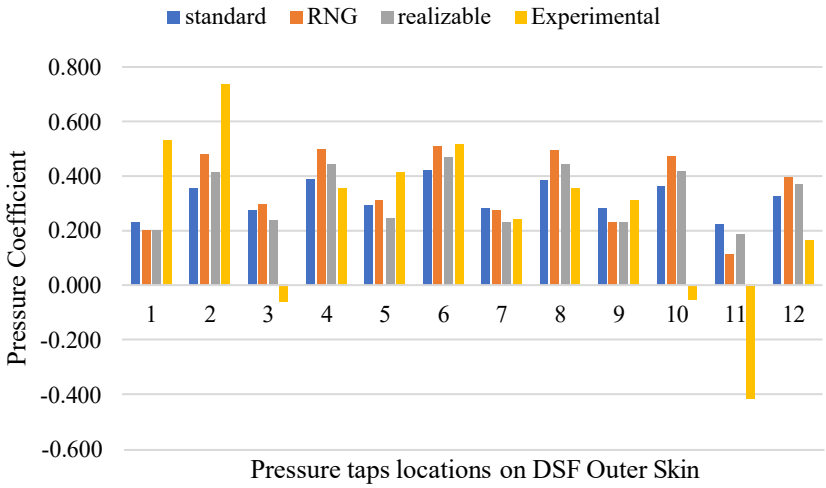


Figure 4.9 Sensitivity Analysis of Turbulence Models

Generally, the different turbulence models of k-epsilon standard, RNG and realizable show consistent predictions across most of the measurement points suggesting stability of the model from a turbulence perspective. There are some discrepancies with the experimental results for pressure coefficients however, these are the same points (3, 10 and 11) from the previous section that showed increasing mesh quality would not improve this and is probably unique to the experiment, and unable to be captured by CFD.

In terms of the error between the experimentally derived pressure coefficients and the different turbulence models, k-epsilon standard yielded an average error across all measurement points of 23%, RNG obtained 38% and realizable had 25%. This suggests that the best turbulence model for matching the computational model with the experimental data is k-epsilon standard, and so this will continue to be applied to the small-scale models within the wind tunnel test section.

The following section concludes the sensitivity analyses by examining the wind shear exponent used in wind profile calculations as the wind tunnel employed semi-urban to urban blocks and roughness, and a best fit needs to be determined to ensure validity of the CFD model.

4.3.4 Semi-Urban Wind Profile Coefficient

As the results of the computational model rely on the user-defined wind profiles, calculating the correct semi-urban to urban boundary layer to reflect the wind tunnel set-up requires looking at a range of typical wind shear exponent values that represent urban or rural environments. Following the information provided in Section 3.1.2 (i) of the methodology on typical values for different environments, this study looks at 0.16, 0.18, 0.20 and 0.22 which covers open to urban terrain. Figure 4.10 shows the wind profiles for a fan speed of 5m/s with changing coefficients reflecting open to urban terrain.

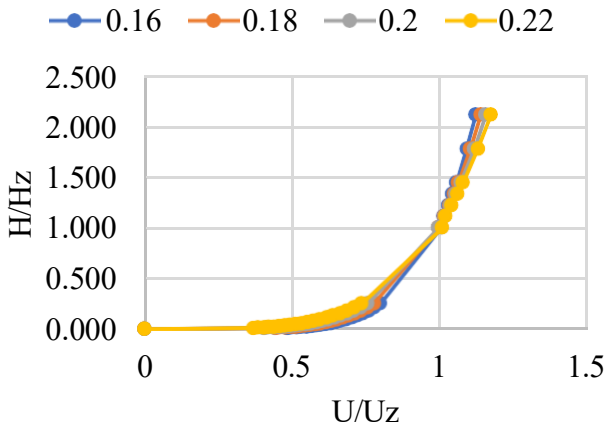


Figure 4.10 Wind Profiles with Different Wind Shear Exponents

Whilst there might not be much of a difference between these four wind profiles visually, even a slight change in the steepness can change the development of airflow and pressure around the building. For example, a higher wind shear exponent creates a steeper increase in wind speed over height and this impacts both static and dynamic pressures, and therefore pressure coefficient. Table 4.3 shows the average pressure coefficient obtained across the 12 measurement points on the DSF outer skin for four different CFD models employing wind profiles calculated with wind shear exponents in the range 0.16-0.22.

Table 4.3 Error between CFD and Experimental Data for Different Wind Shear Exponents

	α=0.16	α=0.18	α=0.20	α=0.22
Average Cp	*0.19*	*0.27*	*0.22*	*0.24*
Error with Exp Data (%)	*25*	*23*	*13*	*7.8*

The blocks and roughness fins in the wind tunnel test represented a semi-urban environment and a wind shear exponent of 0.18 was first applied to reflect this as an estimate, however the best match comes from a higher value of 0.22 at 8%. This result could be explained by the wind blockage ratio of the 1:50 scale model of the DSF warehouse and how the model itself might contribute to increased turbulence in the wind tunnel test section. This is illustrated by Figure 4.11 which shows the position of the 1:50 DSF within the cross-sectional area of the wind tunnel.

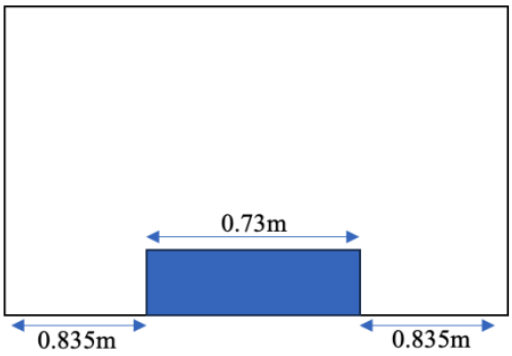


Figure 4.11 Visual of Model Wind Blockage

Whilst the scale model satisfies wind blockage requirements at less than 4% and a height less than the halfway mark of the test section, due to its large width, even at scale the model comprises 30% of the wind tunnel test section width, meaning it has less space between itself and the walls. This completely changes the aerodynamics around the building compared to if it was a model with a tall but thin aspect ratio. With this consideration in mind, this final version of the model will be used moving forward into the computational modelling of the full- scale DSF warehouse in the next section.

As an additional effort to validate the CFD method used in this thesis to assess wind performance, a separate analysis took place in Appendix Section A.3.3 where wind tunnel data of a scaled model of the Silsoe cube was used to validate a CFD model built in the same manner. The reason for this is non-existent literature of aerodynamic wind tunnel testing of warehouses.

4.4 Computational Modelling of a Full-scale DSF Warehouse

Following the validation of the experimental model which is 1:50 small scale version of the case study warehouse, it is imperative to examine the airflow and pressure variations at full- scale to reflect a realistic scenario. This part of the chapter marks the first stage of building the final computational model of a double skin façade retrofit for storage and distribution warehouses, confined to wind-driven ventilation performance only. The first sub- section looks at a dynamic similarity test to ensure that the validated lab-scale model is scaled-up appropriately. Then, the seasonal wind performance of the DSF warehouse is evaluated and pressure coefficients are obtained for the DSF outer and inner skins. The final sections include identification of the neutral pressure height (NPH), and an assessment of the cross-ventilation capacity of the DSF warehouse in terms of delivering outdoor air ventilation and promoting airflow around the large space.

4.4.1 Dynamic Similarity Test

The first step in proving dynamic similarity would be to develop a wind profile for the full- scale model that would ensure a Reynolds number is produced that matches the previous lab- scale model. However, this is unrealistic, and the following calculations demonstrate why.

Starting with a calculation for Reynolds number at 1:50 scale and using the equation for Re back in Chapter 3, Section 3.2, the density of air is 1.225kg/m^3, the viscosity of air is 1.81x10^{-5}, the wind tunnel speed is 5m/s, and the length characteristic is 0.22m, representing the height of the model:

Equation 4.1 Small Scale Model Reynolds Number

$$Re_{smallscale} = \frac{1.225 \cdot 5 \cdot 0.22}{1.81 \cdot 10^{-5}} = 74{,}000$$

If the objective was to ensure the full-scale model matched the lab-scale Reynolds number exactly, this would mean the wind velocity would have to be as small as 0.10m/s which is not realistic. The advantage of using an atmospheric boundary layer wind tunnel is that it can simulate realistic wind profiles, rather than exact matches of Re. As a result, the verification included here will be between the flow characteristics, including velocity distributions and turbulence, achieved at both small- and full-scale when applying the same wind profile that the wind tunnel produced.

Figure 4.12 shows the velocity vector contours for the (a) 1:50 lab-scale model and (b) full-scale model under the same wind profile.

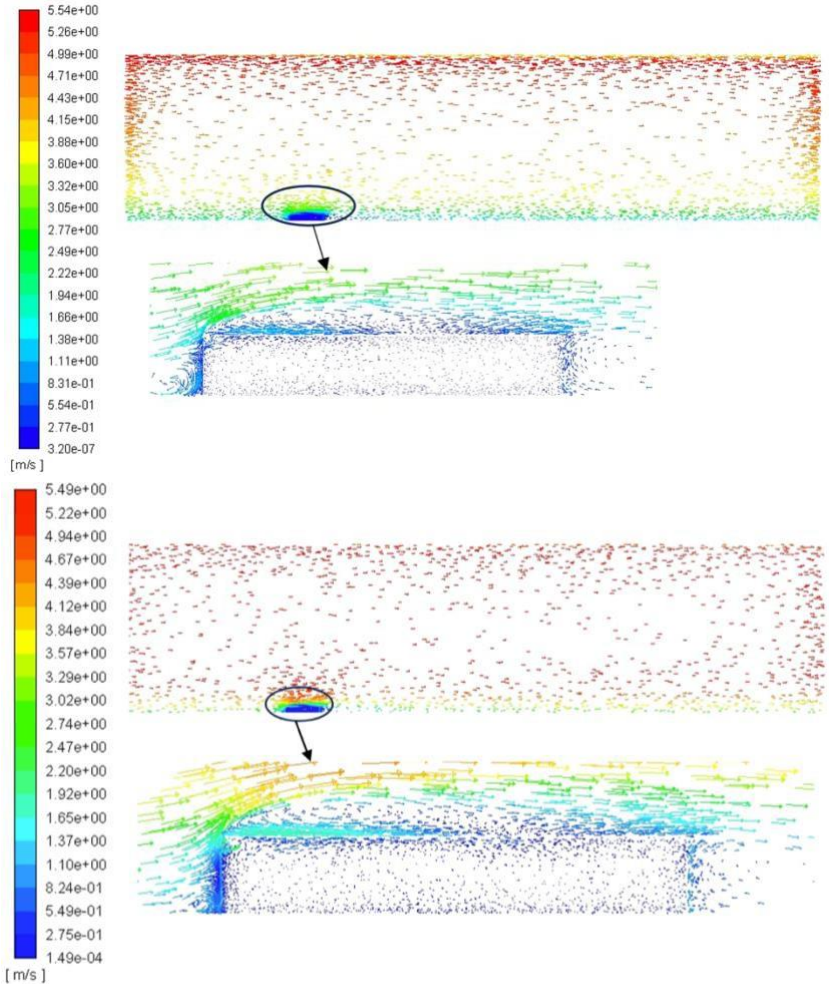


Figure 4.12 Velocity vector contours for (a) 1:50 and (b) full-scale models

The comparison of velocity magnitude and airflow distribution between the small-scale model in Figure 4.12 (a) and the full-scale model in (b) shows that there are many similarities. For example, the domain snapshot shows that the wind speed is lower around building height whether it is 0.23m or 11.8m tall implying that the wind profile was correctly scaled up. Almost identical flow separation occurs at the roof of the warehouse where lower, stagnant velocities at the double skin façade promote air to accelerate over the roof, represented by the darker blue arrows to green to yellow. At the back of the model, there is a similar level of recirculation occurring at both scales. Whilst these aerodynamic results give confidence that the full-scale modelling is accurate by the experimentally validated small-scale model, the pressure distribution should also be examined. Figure 4.13 shows the pressure contours for the (a) 1:50 lab-scale model and (b) full-scale model under the same wind profile.

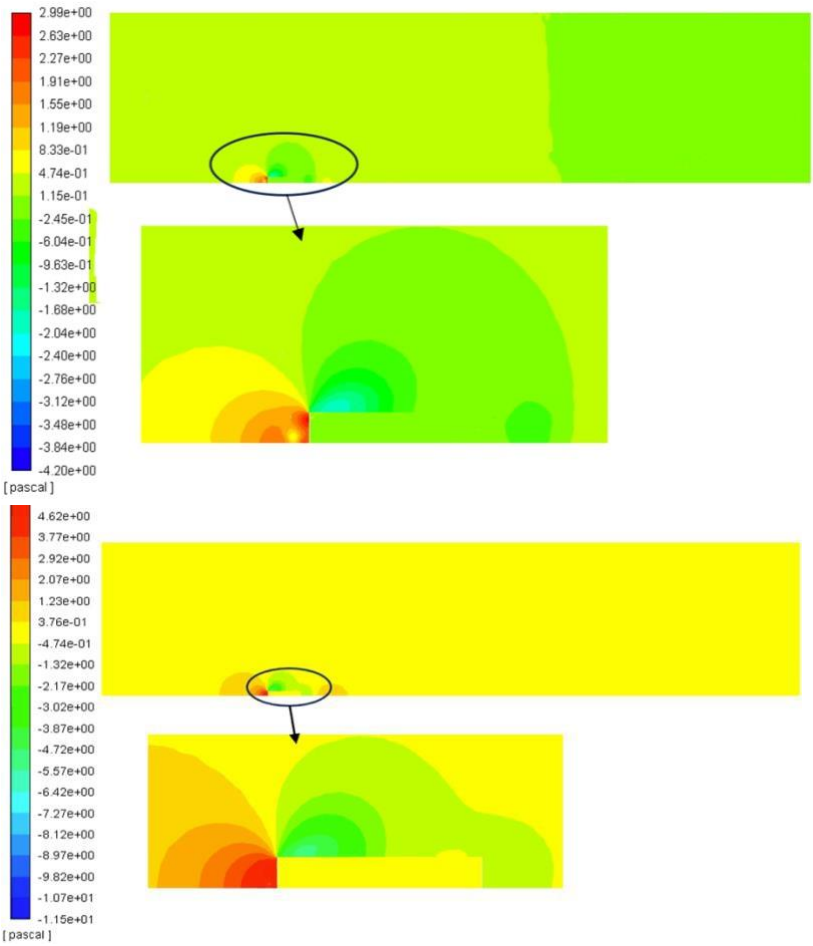


Figure 4.13 Static Pressure Contours for (a) 1:50 and (b) Full-Scale Models

Primarily, there is a difference in magnitude as a smaller model will experience lower static pressures compared to a full-scale model, even for the same wind profile. For both models, there is higher pressure at the DSF outer and front facades, and negative pressure over the roof and towards the back of the warehouse. Both domains show a similar distribution of pressure up to and after the no-slip condition at the sharp edge of the roof of the warehouse. The purpose of this study is not to get a perfect match, but to show that there is similarity at different scales, further exemplified by the pressure coefficient results in Table 4.4.

Table 4.4 Error between Cp for small-scale and full-scale dynamic similarity test

	Small Scale Cp	Full Scale Cp	% difference
DSF Outer	0.19	0.27	39
DSF Inner/Front	0.20	0.20	1
Back	-0.03	-0.04	60

Now that there is a level in confidence in the scaling up of the DSF warehouse and domain, the seasonal wind performance can be assessed at full-scale in the following section.

4.4.2 Seasonal Wind Performance of the DSF Warehouse

As a key objective of the research in this thesis is to assess the seasonal performance of the DSF retrofit for the warehouse, the next step is to simulate the full-scale warehouse with wind profiles derived from historical weather data for winter, summer, and intermediate scenarios. The wind profile is set to 0 degrees and only considers the predominant wind direction in the chosen climate, Nottingham, UK.

i. Wind Profile Calculations

Whilst the experimental validation of the small-scale model used the wind profiles calculated from the atmospheric boundary layer wind tunnel; the full-scale models use real-world data from the East Midlands Airport weather station from the case study climate. The average wind speed for the coldest month in winter, warmest month in summer and spring and autumn were chosen as the reference velocities for an annual period. As the computational domain has a height of five times the warehouse height, the height of the wind profiles was made to match this at 60m. A wind shear exponent of 0.22 reflecting an urban environment was applied to reflect industrial lots and the best match determined in the sensitivity analyses as part of the experimental verification of the small-scale computation model. Figure 4.14 shows the wind profile which is the same for all seasons.

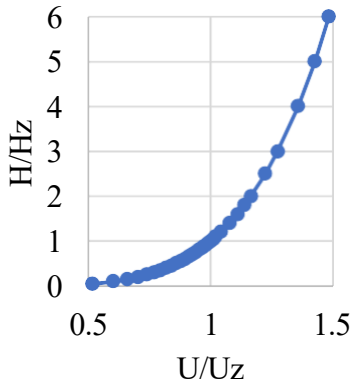


Figure 4.14 Wind Profile for Full-Scale Models (a=0.22)

The wind velocity data used to build the wind profiles which were imported to the computational models are in the Appendix, Section A.3.5. The reference wind speeds at reference height range from 3-8m/s, and as an annual average this is 5.83m/s which is slightly higher than what was tested in the ABL wind tunnel, from which the models in this section are built upon. The next sections look at pressure and velocity data extracted from the CFD models.

ii. *Pressure Coefficients on Double Skin Façade Outer and Inner skins*

Average pressure coefficients for the whole façade for a wind angle of 0 degrees were obtained for the DSF outer skin, and inner skin (depicted in Figure 4.15) and are detailed in Table 4.5. The data for the DSF outer and inner skin will be used in analytical pressure drop calculations later in Section 4.5 of this chapter.

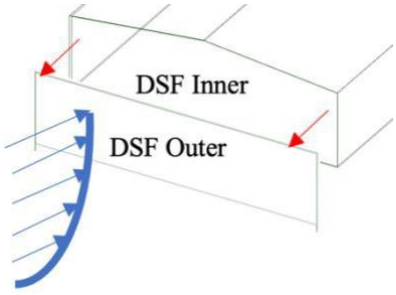


Figure 4.15 Schematic of windward DSF facades

Table 4.5 has the average pressure coefficients for the DSF outer and inner skin for the four seasonal models. A changing wind profile is not going to change the pressure coefficient of the DSF outer and inner skin significantly, but it is still worthwhile to examine any minor differences and find an average which can be used moving forward. These average Cp values for the DSF outer and inner skin will be used later in Section 4.5 to analytically calculate wind-driven flow rates within the cavity.

Table 4.5 Pressure Coefficients for DSF Outer and Inner Skins in Different Seasons

Pressure Coefficient	DSF outer	DSF inner
CFD January	0.27	0.23
CFD April	0.26	0.23
CFD July	0.27	0.24
CFD October	0.26	0.23
Average:	0.27	0.23

iii. *Velocity Profiles in the Double Skin Façade Cavity*

As a double skin façade is a cavity-based ventilation technology, it is essential to understand the distribution of airflow vertically and horizontally as the inlet is usually at the bottom, and the outlet is at the top but over a large span of 36m. To obtain a more accurate understanding of airflow and velocity within the DSF cavity, ten vertical measurement points were made at three different points as shown in Figure 4.16 below.

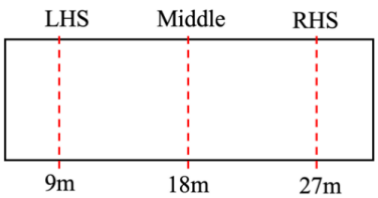


Figure 4.16 Schematic of Vertical Data Collection Points Across DSF Cavity Length

To facilitate this measurement, a rake of 10 points was taken at these three positions at a cavity depth of 0.1m (the middle) to capture how airflow distribution might change at the edges compared to the centre. Exact location coordinates are provided in Table A.15 in the Appendix. Figure 4.17 shows the vertical air velocity profiles for LHS, middle, and RHS measurements in (a) January (7.22m/s), (b) April (4.72m/s), (c), July (7.78m/s) and (d) October (3.6m/s).

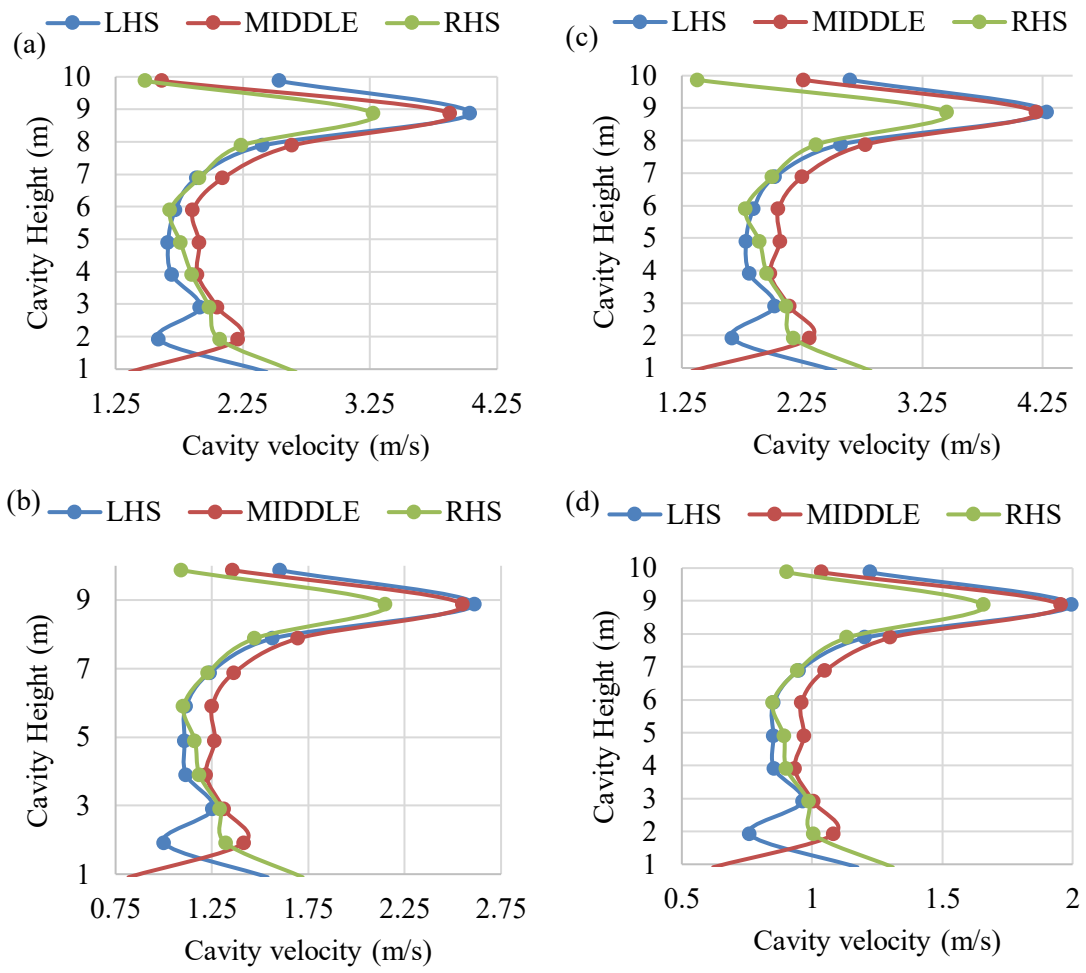


Figure 4.17 DSF Velocity Profiles for (a) January (7.22m/s), (b) April (4.72m/s), (c), July (7.78m/s) and (d) October (3.6m/s).

Whilst there is not much change in the evolution of the cavity air velocity over each season representing a wind speed range between 3.6-7.78m/s, there is a consistency in how the air velocity changes with height at the LHS, middle, and RHS positions. This indicates that when the DSF is windward and perpendicular to the upstream wind flow, the middle of the cavity will always experience the lowest air velocity whilst the LHS and RHS will experience higher magnitudes. There is a doubling of air velocity near the top of the cavity which is likely caused by the top being sealed off, therefore promoting recirculation and the increased turbulence from this can cause an increase in air velocity. Given that the warehouse model in this study has three

ventilation openings towards the top of the DSF cavity, around the positions of the LHS, middle, and RHS measurements, it is valuable to know that the inlet velocity across the width of the cavity is not uniform. The air velocity entering these openings through the cavity does not necessarily correlate to how well the internal space is ventilated so the next section looks at the impact of Neutral Pressure Height (NPH).

4.4.3 Neutral Pressure Height (NPH) in Wind-only Conditions

A Neutral Pressure Height (NPH) in wind-only conditions is influenced by variations in wind velocity and pressure coefficient with height, creating a pressure distribution of both positive and negative pressure zones on the same (windward) façade. When applying a double skin façade to this windward façade, it amplifies the pressure differential driving airflow through the openings by creating an additional differential across the cavity and openings to the warehouse space, potentially altering the NPH. Additionally, outlet openings on the leeward façade further promote airflow from positive to negative pressure zones. This can lead to improved air circulation through the building and influence the overall pressure profiles on opposing facades. By determining the neutral pressure height in wind-only conditions, an understanding of how the external wind pressures impact the internal pressure distribution in the warehouse with the double skin façade is developed. Table A.9 in the Appendix has the readings whilst Table A.14 has the coordinate locations of the external pressure data taken upstream of the model, and internal pressure data taken in the centre of the warehouse with the DSF, respectively as shown in Figure 4.18. The three inlet and outlet openings are addressed in the next Section 4.4.4.

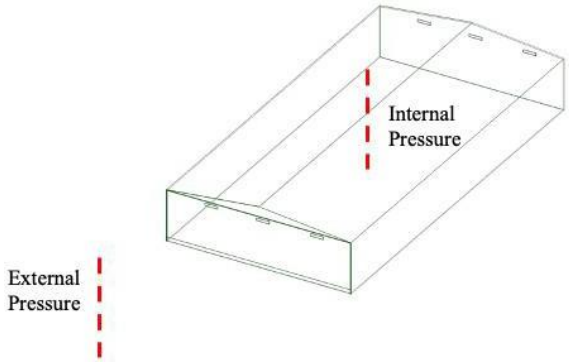


Figure 4.18 Position of External and Internal Pressure Measurements

The results from this study are shown in Table 4.6 and in Figure 4.19 where the intersection of external and internal pressure indicates the neutral pressure height for (a) January, (b) April, (c) July, and (d) October. There is not any kind of distinct relationship between the wind speed at building height and neutral pressure height, however the NPH remains around 4-4.75m which is less than half the building height at 11m.

Table 4.6 Neutral Pressure Heights for Different Seasons

Season	Wind Speed at Building Height (m/s)	Neutral Pressure Height (m)
January	7.22	4.00
April	4.72	4.40
July	7.78	4.40
October	3.60	4.75

Figure 4.19 shows how these NPH heights were obtained by identifying where the external and internal pressures intersect across the height of the warehouse with a double skin façade.

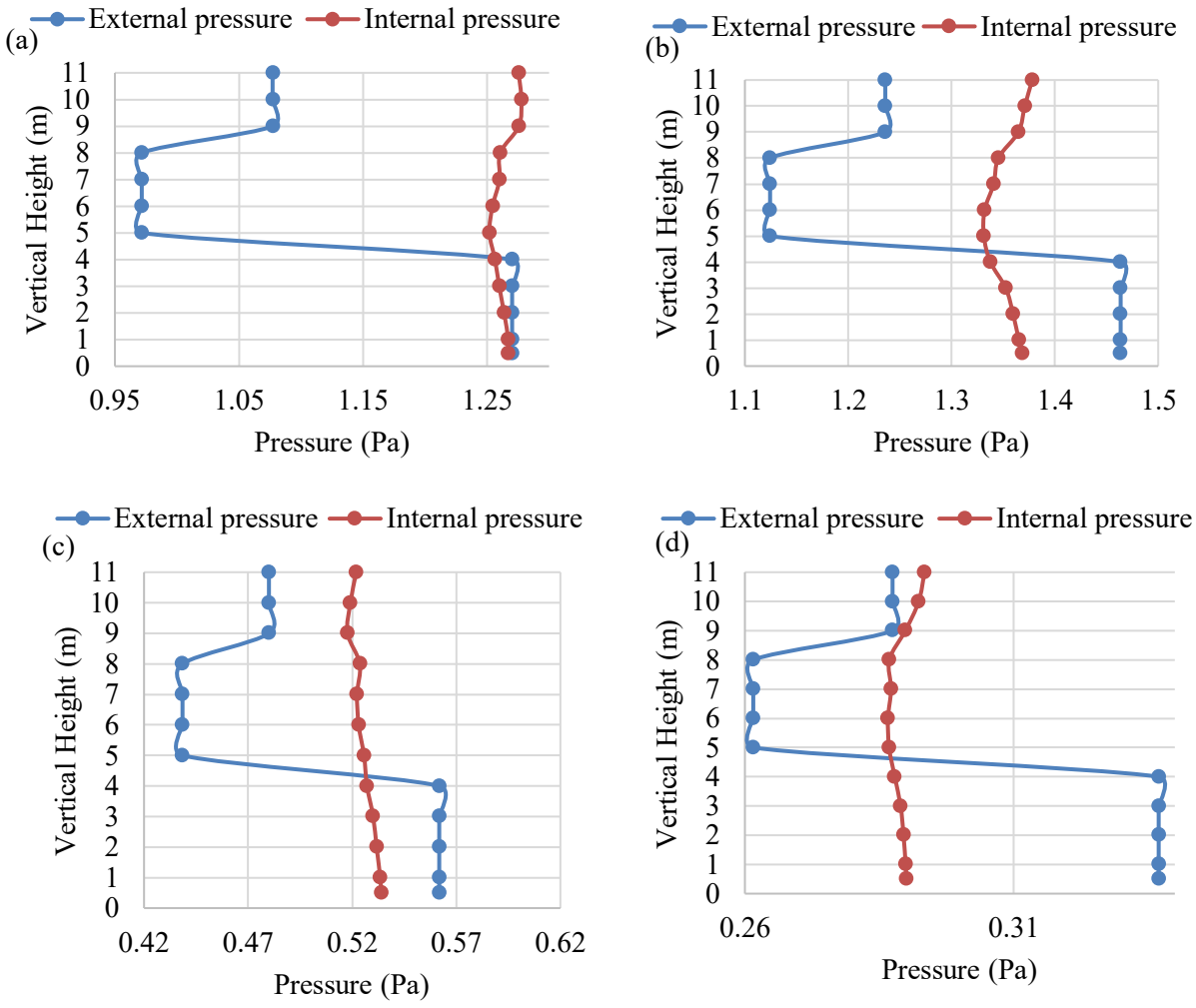


Figure 4.19 Vertical External and Internal Pressures for (a) January, (b) April, (c) July and (d) October

The external pressure remains lower than the internal pressure below the NPH range of 4-4.75m depending on the season, whereas the internal pressure exceeds the external pressure above the NPH. This is in line with what is expected, and typically inlet openings should not be above the NPH as it will experience air flowing out, but with a DSF attached to the façade where the inlet openings are, this does not apply. The pressure differential created in the DSF cavity can be enough to overcome outward flow through the inlet when at a position above the NPH. As the outlet openings on the back façade are also at 9m, they still follow the rule that encourages airflow out where the internal pressure is greater than the external. As this chapter deals with

wind-only scenarios, these results do not consider the primary driving force of a DSF system which is the stack effect and how this might counteract outward flow through inlet openings. The next section is an assessment of the wind-driven ventilation capacity of the DSF in terms of delivering outdoor air not only into the building but also at lower occupied levels.

4.4.4 Outdoor Air Ventilation Assessment

To best evaluate the performance of the double skin façade as a ventilation device, outdoor air data was collected from the CFD models for the warehouse alone, the warehouse with a fully open DSF inlet, and the warehouse with different percentages of closure at the DSF inlet. Nine measurement points were taken at the three inlet openings, and three outlet openings on the warehouse model so that the outdoor air entering and leaving the space could be quantified under the different DSF inlet opening scenarios. The coordinates for these are in Tables A.11 and A.12 in Appendix.

Based on the understanding that a fully closed DSF will generate more heat, and a fully open DSF will generate the least, the DSF inlet area has percentage closures to reflect each season as introduced in Figure 1.8, Chapter 1. For the coldest month of January, the DSF inlet will be closed 75%, April and October will be closed 50%, and the hottest month of July will be closed 25%. In terms of geometry adaptations for the closure, a solid, horizontal solid of 3mm thickness extending from the DSF outer skin was applied to simulate closed louvre grilles. Figure 4.20 below shows the differences in levels of outdoor air entering the inlet openings for the warehouse with and without the DSF.

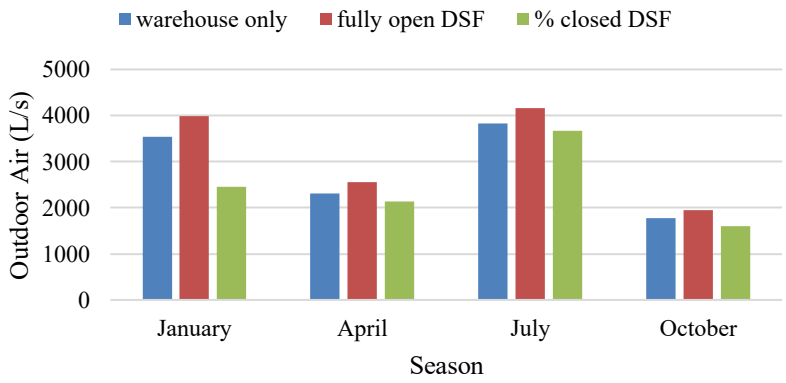


Figure 4.20 Outdoor Air Rates for the Warehouse, Fully Open DSF and Different Openings per Season

The openings on the warehouse, which were added to the scale model used in the wind tunnel to facilitate cross-ventilation, have an area of 1.25m^2 each totalling 3.75m^2 on both the

windward and leeward facades and have not been modelled with any complex geometry reflective of louvre grilles and is a simplification of this model and will yield higher outdoor air flow rates as a result.

Adding these cross-ventilation openings to the case-study warehouse which did not have any pre-existing ventilation openings results in an outdoor air delivery of 1700 and 3500L/s for a wind speed range of 3.6-7.78m/s. The fully open DSF inlet in all seasons but summer show an increase in outdoor air flow rates, and this is likely due to Bernoulli's principle whereby the DSF cavity represents a duct where air is flowing from a larger area (outside domain) to a smaller area (DSF inlet). The continuity equation dictates that the air speed should increase as a result. Proving that a DSF can have this impact, and that it follows typical duct or pipe theory helps to validate the analytical tool in the Section 4.5 which is built upon Bernoulli's principle and treating the DSF as a ventilation duct. Furthermore, if the DSF performs in this way, as an optimisation it should include a level of ventilation control as the figure above demonstrates this is an effective way to reduce the outdoor air flow rates. Implementing inlet closures can reduce ventilation by 37-49% in winter, spring, and autumn, however it further exacerbates the Bernoulli effect in summer, increasing ventilation by 88%. This is the end of the analysis of the DSF inlet openings in this chapter, however it is revisited in the next chapter experimentally, and then fully examined in the last chapter of results as part of a comprehensive optimisation stage.

To fully appreciate the ventilation capability of a DSF retrofit for warehouses, the level of ventilation at the occupancy height should be assessed, and not just what enters at the ventilation inlets. In this case, the openings are at a height of 9m whereas the occupant level can be assumed at a height of 2m where packing and loading is occurring at ground-level. Figure 4.21 represents the difference in height between the ventilation openings and where occupants are likely to be and visualises why it is important to get data at both heights.

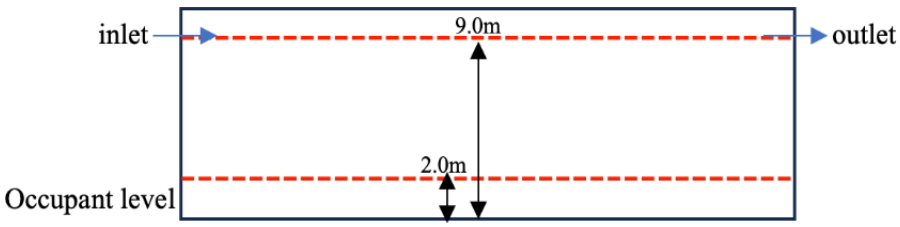


Figure 4.21 Schematic of Inlet Opening Height versus Occupant Level

A new set of nine measurement points (coordinates in Table A.13 in the Appendix) across the floor area at a height of 2.0m were applied to obtain air velocity data. Whilst this cannot be directly translated to outdoor air flow rates, it gives an indication of how the magnitude of airflow changes across the height of the internal warehouse space. Tables 4.7 and 4.8 show the percentage reduction in ventilation from the inlet to occupant level for the warehouse only, and DSF warehouse where the inlet is fully open, respectively.

Table 4.7 Average velocity at inlet and occupant heights for warehouse only

	Average velocity (m/s) at 9.0m (inlet)	Average velocity (m/s) at 2.0m (occupant level)	Ventilation reduction (%)
January	2.8	0.16	94
April	1.8	0.10	95
July	3.1	0.15	95
October	1.4	0.08	94

Table 4.8 Average velocity at inlet and occupant heights for fully open DSF

	Average velocity (m/s) at 9.0m (inlet)	Average velocity (m/s) at 2.0m (occupant level)	Ventilation reduction (%)
January	3.2	0.15	95
April	2.0	0.11	95
July	3.3	0.14	96
October	1.6	0.06	96

These results show that the ventilation of the space is reduced on average by 95% for a height difference of 7.0m. Whilst this is significant reduction, to understand what the air velocities represent, they should be converted into air changes per hour and compared to the standard for warehouses which is 2-3ACH [198]. The warehouse only and DSF warehouse yield annual averages of 40ACH and 37ACH (calculations in Appendix Section A.3.8 using Equations A.8 and A.9), which is thirteen- fold standard requirements. As this is not a final or optimised configuration of the DSF warehouse, results like this are to be expected as an initial starting point for developing the understanding of how it performs from a ventilation perspective. What this analysis does show is that warehouses are capable of cross-ventilation and that adding a double skin façade to this large space building type needs comprehensive airflow analysis to optimise its configuration.

The next section looks at how to analytically derive the mass flow rate within the full-scale DSF cavity in a wind-only scenario as this can be used to predict ventilation performance.

4.5 Ventilation Performance of a Full-scale DSF (Wind-only)

The ventilation capacity of a full-scale DSF in a wind-only scenario is determined by finding the external and internal wind pressures acting on the double skin façade to calculate the volumetric flow rates which can be converted in litres of outdoor air per second.

4.5.1 Treating the DSF as a Ventilation Duct

The adapted equation for wind pressure to incorporate pressure coefficients of the outer and inner skins of the DSF is below where the velocity is an average of the top and bottom of cavity obtained from the computational model.

Equation 4.2 Wind Pressure for a Double Skin Façade

$$p_{wind} = \frac{1}{2}\rho v_{cavity}^2 (Cp_{outer} - Cp_{inner})$$

Then, the volumetric flow rate, and outdoor air can be calculated from the following equations adapted for a double skin façade where the cross-sectional area is based on the cavity depth, d, and width of the outer skin, W which are 0.2m, and 36m, respectively.

Equation 4.3 Volumetric Flow Rate for a Double Skin Façade (Wind-Only)

$$Q_{dsfwind} = d \cdot W \cdot \sqrt{\frac{2\Delta p_{wind}}{\rho}}$$

Equation 4.4 Outdoor Air (Wind-Only)

$$Fresh\ air = Q_{dsfwind} \cdot 1000$$

Table 4.9 Outdoor Air Delivered from the DSF in Different Seasons

	v_{cavity} (m/s)	Cp_{outer}	Cp_{inner}	Δp_{wind} (Pa)	$Q_{dsfwind}$ (m^3/s)	$Fresh\ air$ (Ls/)
Winter	1.9	0.27	0.23	0.07	2.5	2500
Spring	1.4	0.27	0.23	0.04	1.8	1800
Autumn	2.1	0.27	0.24	0.08	2.7	2700
Summer	1.1	0.27	0.23	0.02	1.4	1400

These analytical results show that the DSF can provide 1400-2700L/s of outdoor air for a range of wind speeds at building height of 3.6-7.78m/s. This is thirteen-fold that required for occupant ventilation alone, not considering passive cooling in summer or destratification. This section concludes the results for the chapter on the wind-driven ventilation performance of a DSF warehouse. Example calculations of this process are in Appendix Section A.3.9.

4.6 Chapter Summary

This chapter explored the wind-driven ventilation performance of a double skin façade warehouse through original wind tunnel testing for validation of computational models capable of assessing aerodynamic evaluations, outdoor air assessments and more of a full-scale model.

4.6.1 Main Findings

In the wind tunnel test, the DSF outer skin performed as expected with a changing sign from positive to negative differential pressure under a 0- and 180-degrees wind angle, respectively. The roof panels, sloped at 6 degrees in opposite directions, responded with opposite signs of differential pressure when either was exposed to a windward or leeward direction under 90 and 270 degrees, respectively. This was followed by a good similarity between CFD and experimental data for the DSF outer skin when windward when comparing façade averages of Cp resulting in a low error of 3.4%, but less so when leeward producing 75%. To improve the comparison, the 12 pressure tap locations on the DSF outer skin were compared with the DSF model and this yielded an error of 23% when windward, and 27% when leeward. A series of analyses were conducted to find the best model set-up for validation and the results are a medium mesh from grid independence tests, k-epsilon standard from turbulence model comparison, and lastly a higher wind shear exponent of 0.22 reflecting a more urban environment. All these sensitivity analyses produced an error of 7.8% between CFD and the experimentally derived Cp for the DSF outer skin when windward, completing the validation.

As the validation of the CFD model was for a 1:50 scale model of the DSF warehouse, a dynamic similarity test was conducted when scaling up because despite it not being realistic to match Reynolds number in both cases, airflow and pressure distribution can be compared. A good agreement was found with the only difference between the magnitude of static pressure experienced by the 1:50 scale model versus the full-scale model even with the same wind profile. This is largely due to it having a smaller surface area. The full-scale CFD modelling determined the Cp for the DSF outer and inner skins with an average across the four seasons of 0.27 and 0.23, respectively. An analysis of vertical evolution of cavity velocity saw that for a range of wind speeds 3-8 m/s, the cavity velocity remained relative stable in magnitude until reaching a height of 9m where it is either entering the warehouse space or open to the ambient. As the model has 3 openings of the same area on the windward and leeward sides of to promote cross-ventilation, the NPH was determined at a height of 4-4.75m for all seasons which is higher than typical buildings that will have smaller storey levels.

In terms of ventilation performance, a fully open DSF could deliver outdoor air levels higher than the warehouse with ventilation openings, except in summer when the cavity air is exhausted out the top to avoid overheating and provide façade cooling. Certain configurations of the DSF inlet area openings illustrated a level of control over the magnitude of outdoor air delivery which is important as the chosen climate conditions yielded values north of 1000L/s. Internally, the magnitude of air velocity drops significantly by 94-96% from the height of the opening at 9m to occupancy level for both the warehouse with openings, and then the DSF warehouse. However, these values are still too high at 40 (warehouse) and 37ACH (DSF warehouse), both around thirteen-fold the requirements of the case study warehouse. The Bernoulli-adapted analytical tool calculated that the DSF can deliver 1400-2700L/s all year round, highlighting its potential as a ventilation technology.

4.6.2 Limitations and Future work

If time and resources allowed it, there could be some improvements made to the chosen methodologies. For example, a pressure transducer with a smaller range might be more applicable, and the tests could be repeated for higher wind speeds for the sake of improved reliability of data, but not necessarily a closer match to the chosen climate. Possible future work could look to procure small enough hot-wire anemometers to measure the air velocity in the openings of the 1:50 scale DSF warehouse to obtain a different set of validation data.

4.6.3 Closing Remarks

Overall, this chapter has highlighted that double skin facades for warehouses are understudied in terms of ventilation performance as a natural ventilation strategy. Additionally, there is little literature available for warehouse pressure coefficient data, so this chapter contributes to that gap. Extensive CFD modelling and the Bernoulli-adapted analytical tool have led to valuable insights into how the DSF warehouse performs for a four-season temperate climate, such as Nottingham UK for a range of realistic wind speeds experienced annually. Now that the wind-only component of ventilation has been explored, the next step is to look at how the DSF warehouse performs under a buoyancy-only scenario.

Chapter 5

Buoyancy-Driven Ventilation and Thermal Performance of a Double-Skin Façade Warehouse

5.1 Introduction

The primary mechanism of a double skin façade is the stack effect which depends on the height of the air column and temperature difference across the column's enclosure. Storage and distribution warehouses offer a unique real estate in terms of tall height of structure but without requirement for a high percentage of glazing. The stack effect is more effective in temperate climates such as the UK as there is typically a temperature differential across the façade of a building in winter, summer, and intermediate seasons. What is understood thus far about cavity-based ventilation solutions, such as a DSF, is the inverse relationship between possible heat recovery and air flow rate. Ultimately, in a buoyancy-only scenario, the airflow rate in the cavity impacts the convective heat transfer coefficient at the internal layers of the outer and inner skins, but there has not been a standardised attempt to quantify this impact.

This chapter builds upon the previous chapter 4 where the DSF was treated as a "ventilation duct" by combining it with a "thermal wall retrofit" which involves determining dynamic u- values as well as the magnitude of heat gain or removal to and from the cavity. Figure 5.1 demonstrates how the assessment of fluid dynamics moves from only the direction of the air flow in ventilation to then considering the horizontal energy balance occurring across the outer environment, cavity, and internal space. It also introduces the flexible opening concept which may influence performance. The maximum closure of the inlet is the depth of the cavity at 0.2m so 25%, 50% and 75% represent the 0.05m, 0.10m and 0.15m variable inlet closure lengths across the cavity depth from outer skin to inner skin and vice versa.

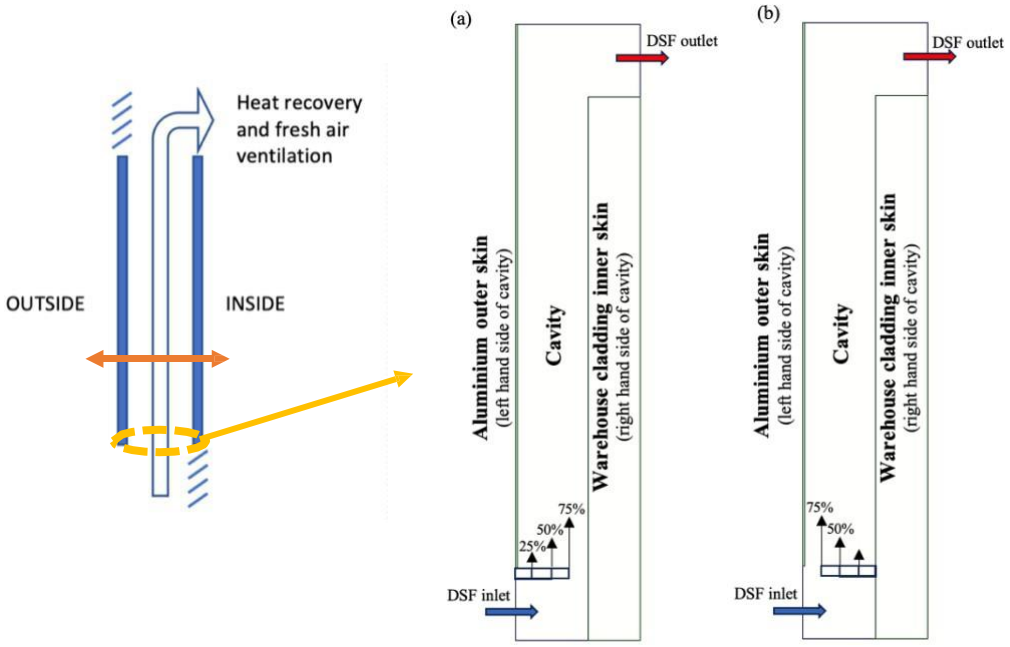


Figure 5.1 Schematic of (a) LHS and (b) RHS flexible openings in the double skin facade

Therefore, the aim of this chapter is to assess the ventilation and thermal performance of a small-scale prototype of the DSF retrofit for a warehouse considering buoyancy-only conditions. This is to look at the stack effect in isolation and understand the thermal conductance of the material composition. The objectives required to achieve this include:

- Conduct a thermal experiment of a small-scale section of a DSF retrofit comprising an aluminium outer layer and case-study warehouse cladding as the inner layer
- Test the concept of the seasonal-adaptive openings for the DSF cavity by percentage of "openness"
- Examine velocity and temperature profiles within the DSF cavity under different seasonal scenarios and determine dynamic U-values under different seasonal scenarios
- Use the validated computational model to investigate whether the full-scale double skin façade retrofit performs well thermally as either a buffer or source of pre-heating and as well as providing outdoor air ventilation

The novelty of this chapter is that it focusses on applying a buoyancy-only scenario in a computational model of an opaque double skin façade application for storage and distribution warehouses, verified by experimentally derived cavity data. The key research gaps include utilising a climate chamber and computational modelling to conduct thermal and ventilation analyses of the double skin façade in UK seasonal conditions. Other lesser studied areas that this study touches on include conducting outdoor air ventilation analyses, obtaining best-fit polynomials to represent cavity thermal and airflow performance and testing a range of external design temperatures.

5.2 Experimental Results

The experiment for examining the DSF retrofit for storage and distribution warehouses under a buoyancy-only scenario involved using an environmental chamber with the details of set-up described in the methodology Section 3.3. This comprised simulated solar irradiance tests to measure the heat flux from lamps, and thermal testing of the prototype in winter, summer, and intermediate external temperature conditions against a constant internal lab temperature of 18^{o}C. These tests produced measurements of velocity, temperature and heat flux variables which are used to calculate dynamic U-values. The importance of dynamic U-values in a DSF system is that they provide a more realistic metric of thermal performance under varying conditions such as seasonal temperature, and solar fluctuations. Optimisation of the proposed DSF looked at differing inlet opening sizes of the DSF cavity whilst the cavity width remained static at 0.2m.

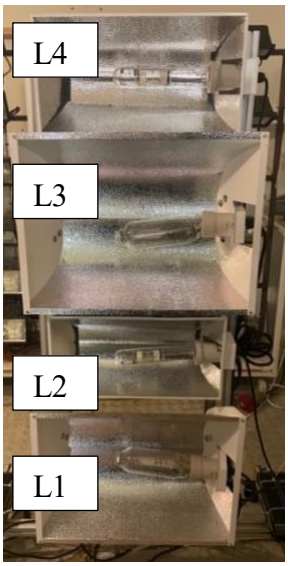
5.2.1 Simulated Solar Irradiance Tests

In Section 3.1.2 (ii), Chapter 3, a constant vertical solar irradiance value of 300W/m^2 for south-facing facades in the case study UK climate, applicable to all seasons, was derived from an analysis of historical data over five years. The point of this was to obtain a statistically likely solar scenario all-year round. Additionally, this analysis tackled the misconception that solar-assisted technologies such as double skin facades are rendered ineffective in "less sunny" climates. For example, whilst there may be a lower number of sunny days in the winter of a UK climate, it achieves the highest value of vertical irradiance and almost two-fold that achieved in the summer [164]. Furthermore, the intermediate seasons of spring and autumn show good levels of vertical irradiance on a south oriented façade and will experience more consistently "sunny" days compared to winter.

i. *Tests of the Lamp Array for Simulating Solar Irradiance*

Prior to the experiment, a pyranometer was used to test the effectiveness of the available lamp array to deliver the proposed solar irradiance value of 300W/m^2. The lamp array comprised four individual lamps, with both constant and variable wattage ratings. Figure 5.2 (a) shows the lamp array with the individually labelled lamps for reference and (b) is the layout of the heat flux meter measurement points. Ten tests were completed with the lamp array at a 0.5m distance from the aluminium outer skin of the structure with results in Table 5.1.

(a)



(b)

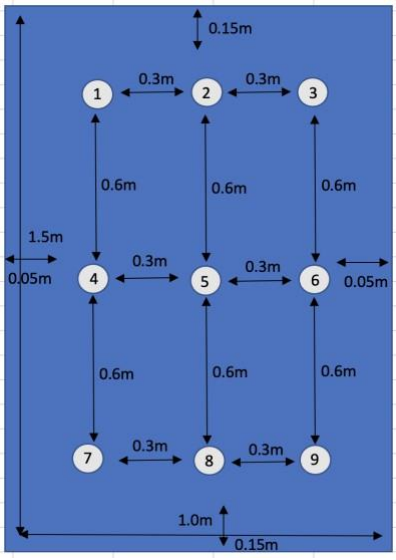


Figure 5.2 (a) Experimental lamp array and (b) Heat flux measurement locations

Table 5.1 Lighting Array Combinations and Resulting Heat Flux Values

Test	Lighting array combination	Average heat flux (W/m^2)
1	L1 250W	28.91
2	L1 & L3 250W	60.47
3	L2 400W	47.85
4	L2 & L4 400W	116.75
5	L1 & L3 250W and L2 & L4 400W	173.57
6	L1, L2, L3, L4 400W	214.35
7	L1 650W	74.04
8	L1 & L3 650W	168.65
9	L1 & L3 650W and L2 & L4 400W	290.29
10	L1 & L3 max boost, L2 & L4 400W	306.82

The combination of lamps which was able to produce the greatest average irradiance, and that closest to the propose simulated solar irradiance was Test 10. Whilst there is a limitation in that the lamp array cannot achieve higher irradiance levels observed in a UK climate, it is still applicable to the study. Figure 5.3 shows the distribution of irradiance in W/m^2 across the measurement points on the aluminium outer façade. The purpose of this is to show that using the average irradiance falling on the surface is a simplification of the set-up.

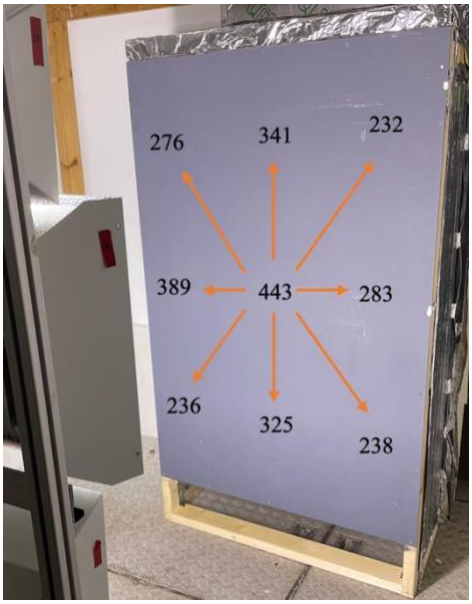


Figure 5.3 Distribution of irradiance on experimental DSF prototype (not-to-scale)

The irregular distribution across the whole surface can lead to unequal heating in the cavity where the greatest flux occurs central to the cavity. As the different lamps in the array available had different power ratings, this is to be expected but could be avoided in future tests by implementing uniform lamps. Following the testing of the lamp array to ensure it can deliver $300W/m^2$, the next section looks at the results obtained in the climate chamber experiment of the prototype double skin façade.

5.2.2 Cavity Velocity and Temperature Profiles

A common way to assess the performance of a double skin façade in existing literature is to evaluate the velocity and temperature profiles in the cavity ([55], [56], [70], [74] and more). In this experiment, velocity and temperature were measured at the centre of the cavity (0.1m) level with the internal opening to the lab (1.5m).

i. *Velocity Profiles*

The cavity velocity was measured at the top of the inner cladding skin, at a height of 1.5m and a 50% depth of the cavity. Figure 5.4 shows the average air velocity at the outlet of the DSF cavity for each configuration of the DSF inlet opening for winter, summer, and intermediate seasons scenarios reflecting the changing external design temperature of -4°C, 10°C and 25°C.

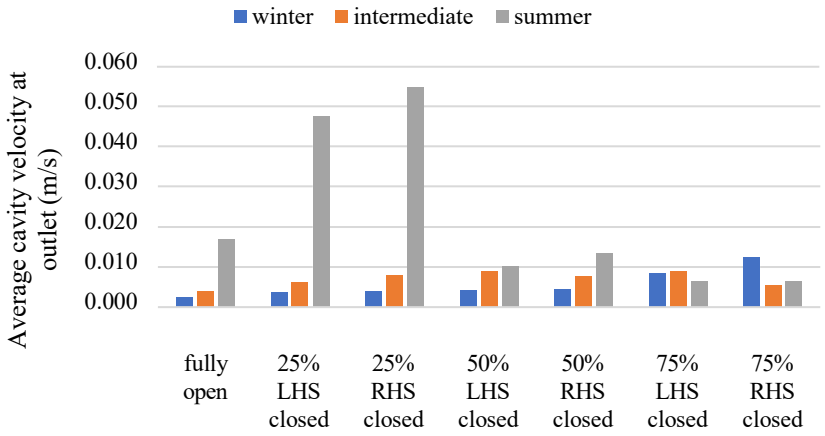


Figure 5.4 Average cavity velocity for different DSF inlet configurations and seasons

Generally, the velocity magnitude is low across all seasons ranging from 0.0018m/s to 0.03m/s generated only by the buoyancy heating within the cavity, therefore expected in the absence of simulated wind. As to whether a full-scale DSF could deliver outdoor air requirements in a buoyancy-only condition, this will be investigated in later sections. The highest cavity air velocity occurs in summer when the DSF inlet area is closed by 25% on the RHS (from the inner skin), followed by a closure of 25% from the outer skin. This is likely due to the closure being small enough to cause an obstruction but not significantly reduce the volume of air being drawn through the cavity. The inverse occurs when the opening is closed by 75% in both directions, at which point the closure is enough to decrease the airflow rate. Winter experiences the highest cavity velocity when the DSF cavity inlet is almost closed and this is because it has the strongest buoyancy force compared to other seasons, which will increase the velocity. The intermediate season has less conclusive trends. Table 5.2 shows the relationship of a fully open to almost closed DSF inlet area opening on cavity velocities.

Table 5.2 Impact of DSF Inlet Area on Cavity Velocity

Season	Fully open	75% front end closed	75% back end closed
Winter	0.003	0.008	0.011
Intermediate	0.006	0.009	0.007
Summer	0.031	0.007	0.006

For winter, the cavity air velocity increases by 170-270% when the cavity is closed 75% in either direction. From this, it can be inferred that there is a higher level of buoyancy-induced airflow and whilst this is good for outdoor air ventilation purposes, it could increase the heat loss at the warehouse façade which is not ideal in the heating seasons. The intermediate scenario sees the smallest change in cavity air velocity however it still increases like the winter test. In this case, there is an increase in air velocity by 17-50% dependent on the direction that the cavity is closed by 75%. Lastly, in summer conditions there is a 77-80% drop in airflow when the cavity is closed 75% in either direction. This shows that in these conditions if an increased airflow rate is required to encourage heat loss from the warehouse façade, then a fully open cavity is more appropriate. The outcome of this is that the seasonal-adaptive openings have less control over airflow rate when the temperature outside is 10°C.

ii. Temperature Profiles

The cavity temperature was measured at the top of the inner cladding skin, at a height of 1.5m and a 50% depth of the cavity. Figure 5.5 shows the relationship between external design temperature in each season and the cavity temperature at outlet height for a fully open DSF.

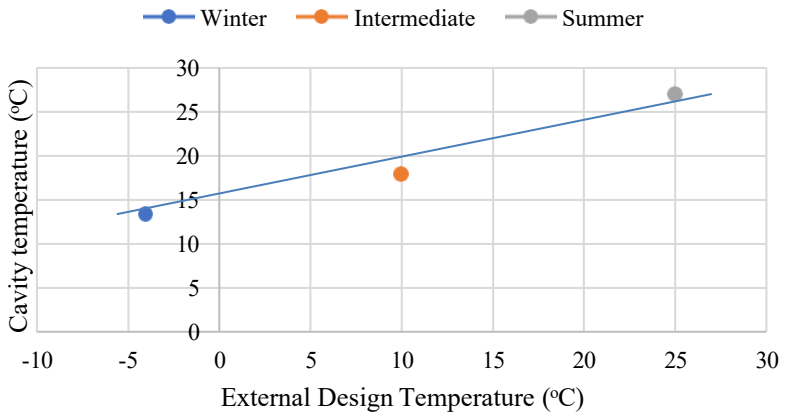


Figure 5.5 Relationship between external design temperature and DSF cavity temperature

As the external design temperature increases, the cavity temperature increases in an almost linear fashion, and this suggests there might be a way to predict DSF cavity temperature for a known solar irradiance value. Figure 5.6 shows the impact of different percentage openings of the DSF inlet area opening on cavity temperature at outlet height for winter, intermediate and summer seasons.

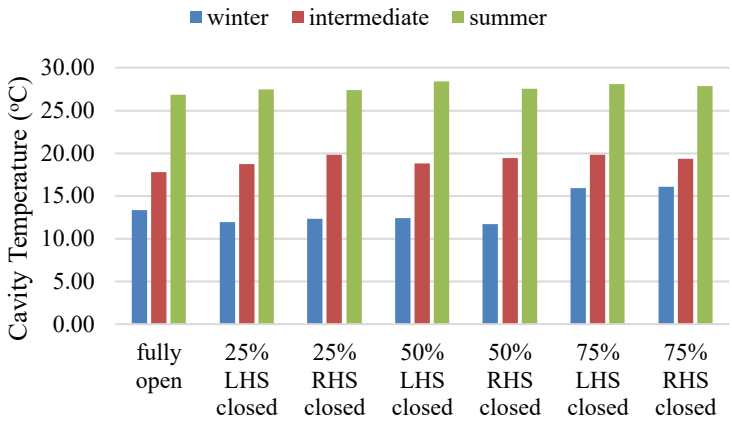


Figure 5.6 Average cavity temperature for different DSF inlet configurations and seasons

In winter, the 75% LHS and RHS closed openings yield the highest exhaust cavity temperatures between 16 and 17°C which is a 21°C increase, showing that a good level of pre-heating can be achieved. These openings also yield the highest exhaust cavity temperatures in summer which could cause overheating, and therefore it is better to use the lower percentage closures of the inlet opening. Regarding the intermediate season, the percentage openings are less conclusive as the 25% RHS opening yields the second highest exhaust temperature at just below 20°C whereas the 25% LHS opening achieves the lowest exhaust temperature at 18.6°C. These results show that where the openings are with respect to the inner and outer skins of the DSF can directly impact the thermal performance of the cavity. The seasonal-adaptive openings will be further explored computationally in the final chapter when the optimisation of the opaque double skin façade takes place.

5.2.3 Thermal Gradients

The height of the DSF cavity is constant at 1.5m throughout all the tests so the vertical temperature gradients for each season can be calculate using Equation 5.1.

Equation 5.1 Thermal gradient

$$\nabla T = \frac{\Delta T}{h}$$

Figure 5.7 shows the distribution of thermal gradients for each DSF inlet opening configuration across all seasons. The temperature gradient is the greatest across all openings for the winter season and is the highest when the cavity is 75% closed whilst it is the lowest for the summer when the cavity is 25% closed. The intermediate seasons sees a relatively constant temperature gradient across all openings. Referring to the previous Figure 5.6, these results are an inverse to reflect that the bigger the difference between external and internal design temperatures, the higher the thermal gradient across the DSF.

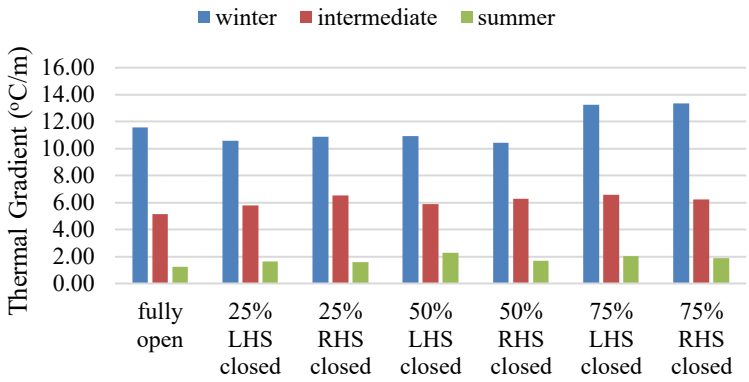


Figure 5.7 Thermal gradients for different DSF inlet configurations and seasons

The final section of the climate chamber experimental data is an error analysis to ensure that the measurement equipment obtained readings accurately which is important in this type of experiment where a variety of different equipment have been used.

5.2.4 Error Analysis

Error analysis in the form of fractional errors and standard deviation (where applicable) was carried out for the equipment hot-wire anemometers, PT-100s, a DataTaker, a Pyranometer, and heat flux meters used in the winter environmental chamber test with the fully open DSF.

i. *Fractional Errors*

Fractional errors, representative of the worst possible error, were calculated for the heat flux meters, PT-100 RTDs, and pyranometer as they had the relevant data available. Results are shown in Table 5.3.

Table 5.3 Fractional Errors for Climate Chamber Test Equipment

Equipment	Fractional error
Heat Fluxmeter OF1	3.20
Heat Fluxmeter OF2	0.15
Heat Fluxmeter IF1	2.56
Heat Fluxmeter IF2	0.78
PT-100 RTD TO1	1.16
PT-100 RTD TO8	0.90
PT-100 RTD CT8	0.66
PT-100 RTD CT7	0.66
PT-100 RTD TI2	2.01
PT-100 RTD TI1	0.93
Pyranometer	1.80

The range in these values from 0.15 to 3.20 show the limitations of compounded fractional error analysis for determining error with an overemphasis on absolute error. In this case, the absolute error is much smaller for the individual equipment compared to the DataTaker which also has an offset value. A much better way to analyse the accuracy of the data collected is to evaluate the standard deviation of readings and this is examined in the next section.

ii. *Standard Deviation Analysis*

Standard deviation was conducted with the built-in Microsoft Excel function. Table A.17 in the Appendix has the standard deviation values and description for each equipment and Figure 5.8 shows the error bar results for the (a) hot-wire anemometers, (b) heat flux meters, and (c) PT-100 RTDs.

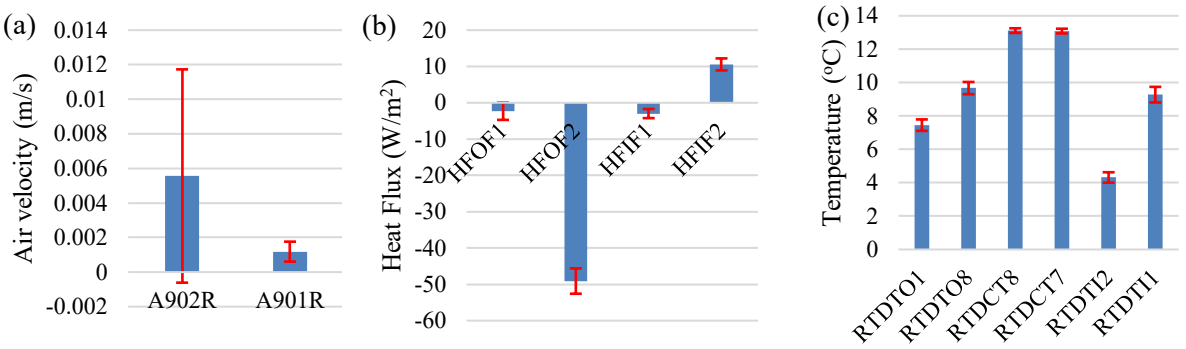


Figure 5.8 Standard deviation for (a) anemometers, (b) heat flux meters and (c) PT100 RTDs

Across all the measurements for air velocity, heat flux and temperature, the error bars are relatively small except for the hot-wire anemometer 902R which has a standard deviation like the actual reading of 0.0056m/s at 0.006. The reason for this is that the velocity transmitter for this anemometer has a maximum output of 5m/s, whereas the anemometer 901R has a maximum of 2.5m/s, and therefore there will be greater error at lower velocities.

5.3 Experimental Validation of Computational Model

The computational fluids dynamic model of the experimental prototype is 1:1 scale and is focused on the DSF only, not the internal warehouse space. The geometry is 3-dimensional, with a composition of solids representing the inner and outer skins and fluid volume representing air. The experimental verification starts with a preliminary validation of the CFD model against existing experimental data in the literature, followed by validation against the original experimental data obtained in the previous Section 5.2.2. This is followed by grid independence tests, and turbulence model sensitivity analyses to deliver a best match between the experimentally- and numerically derived cavity velocity and temperature profiles.

5.3.1 Preliminary Validation against Existing Literature

As a starting point for the validation of the computational model for the thermal modelling aspect of the proposed double skin façade for warehouses, the CFD model was initially validated against data which already exists in literature and is used by many other double skin façade researchers.

i. *Experimental Data from Existing Literature*

The experimental data comes from Mei et al. [199] as part of the proceedings for the Clima 2007 WellBeing Indoors conference and obtained air velocity and temperature values for an empty cavity with no blinds. Figure 5.9 shows an adaptation of the geometry taken to validate the model in this thesis.

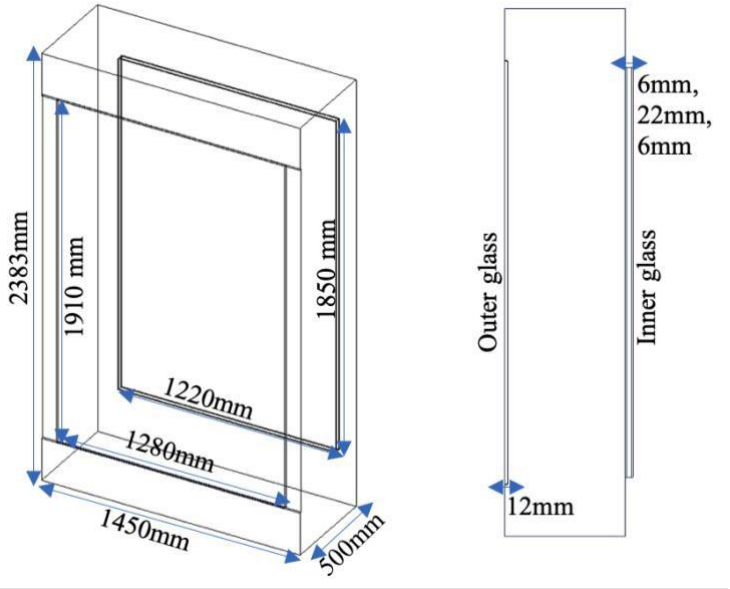


Figure 5.9 Adapted geometry for preliminary CFD validation from [199]

To simplify the model, the geometry does not include the original grilles as this is only a preliminary validation to provide a starting point for the validation of the computational model against original experimental data. In terms of meshing the geometry and the subsequent computational set-up in ANSYS Fluent, the method provided by Ahmadi et al. [200] was applied. Table A.18 in Appendix Section A.4.2 describes the model set-up and meshing properties. As a full grid sensitivity, turbulence model and boundary condition sensitivity analyses are conducted for the validation of the model with the original experimental data in the next section, it has been omitted here. Therefore, only one meshing scenario and boundary condition set-up has been considered where there is a pressure inlet and outlet at the DSF inlet and outlet, respectively and all walls except the glass layers are assumed to be adiabatic.

ii. *Results from Preliminary Validation*

Figures 5.10 (a) and (b) depict the comparison of the cavity air velocity and temperature readings obtained in CFD with that of Mei et al., respectively. Looking at both figures, the CFD models produce similar trends of air velocity and temperature across the depth of the double skin façade cavity.

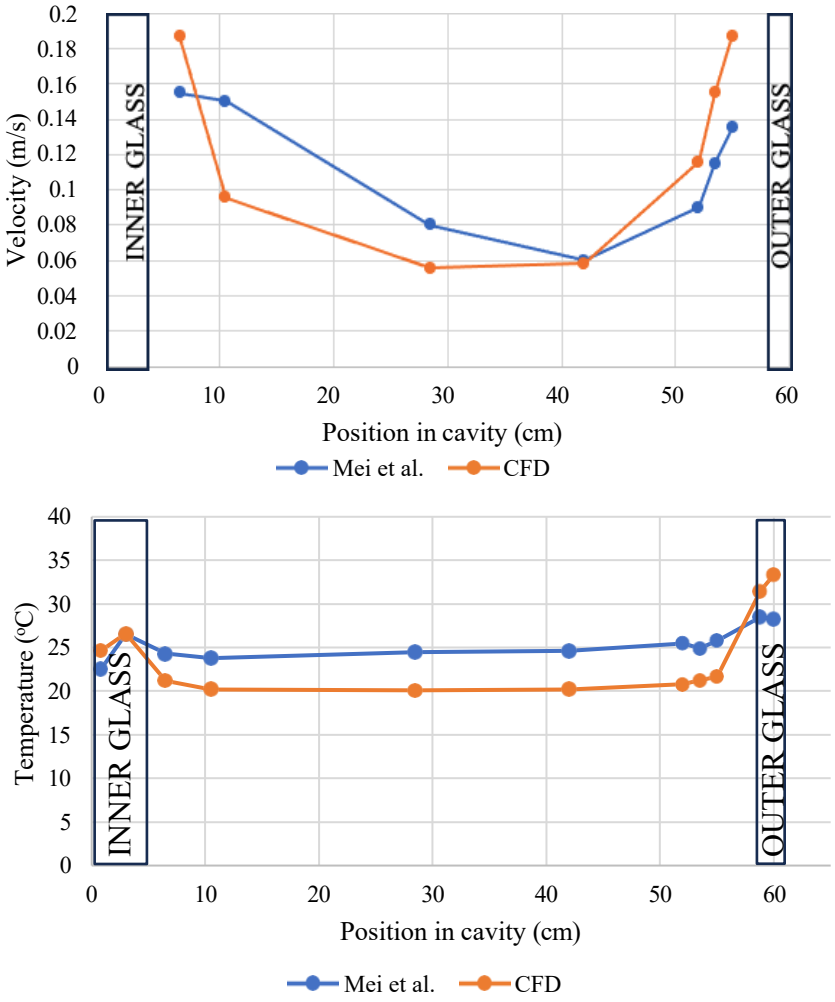


Figure 5.10 Horizontal Cross-Section Comparison of [189] to CFD model for (a) velocity and (b) temperature at a height of 1.1m from the top of the DSF inlet

Regarding the air velocity, the main discrepancy is in the readings closer to the inner glass where the experimental data seems to be higher. In terms of magnitude of error, the average is calculated at 27% where the distribution of error is greater towards the inner skin. A possible reason for this is that the CFD model excluded the grilles at the inlet and outlet, which can directly influence the airflow within the cavity. However, it still captures the expected relationship whereby closer to the solid surfaces, the air velocity increases whereas it is relatively even and lower towards the centre of the cavity. This performs like flow in pipes and makes physical sense in terms of predicted fluid dynamics.

The cavity and glass surface temperatures obtained in the CFD model shows many similarities to the experimental data such as the changes in temperature across the outer and inner layers of both the outer and inner glasses, and then a steady lower temperature across the cavity. The average error between the CFD model and experimental data was calculated as 16% with every measurement achieving an error less than 20%.

To further the understanding of phenomena occurring in a double skin façade cavity when exposed to simulated solar irradiance, Figure 5.11 (a), (b) and (c) show cross-section contours of the velocity, temperature, and velocity vectors in the cavity.

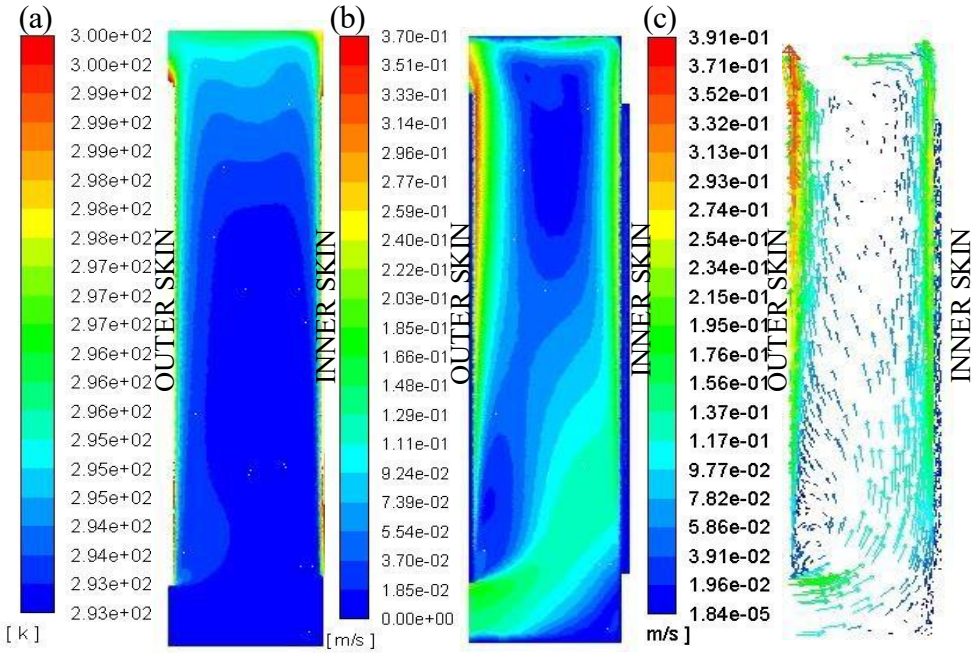


Figure 5.11 Contours of (a) temperature, (b) velocity, and (c) velocity vector

The temperature contour cross-section in Figure 5.11 (a) shows that most of the heating occurs towards the top of the cavity, changing quite significantly from the outdoor ambient temperature of 18ºC to around 25ºC. If the inlet to the cavity was smaller, or had the grilles been included in the geometry, this temperature would likely be achieved at a lower height. This is backed up by Figure 5.11 (b) which shows a strong airflow entering at the bottom of around 0.185m/s and following the inner skin side of the cavity until it reaches the top of the cavity and recirculates. It is widely understood that there is an inverse relationship between the magnitude of airflow into a DSF cavity, and the level of stack effect heating that can occur. The velocity vector contour in Figure 5.11 (c) is interesting as it shows a splitting of the airflow about a third of the way up the cavity where some of the flow attaches to the outer skin, whilst the majority sticks to the inner skin side. This is likely due to the position of the DSF outlet on the outer skin side at the top of the cavity as opposed to on the inner skin side, creating enough of a pressure differential to pull airflow back towards the outer skin.

Based on the analysis of the comparison of the initial thermal model of a double skin façade against widely reputable experimental data from literature, despite some simplification of the geometry and without extensive refinement, there is good agreement. Thus, it is with confidence that a similar meshing, and model set-up is used to compare the opaque ventilation façade developed in this thesis with the original experimental data in Section 5.3.2.

5.3.2 Validation against Original Experimental Data

Following the preliminary validation of the computational setup in the previous section, the CFD model now needs to be validated against the original experimental data for the prototype presented in the earlier Section 5.3.1. This involves computationally deriving the cavity temperature and velocity values at the same coordinates (in Table A.21 in Appendix A.4.4) the measurements were taken experimentally as shown in Figure 5.12.The LHS measurement line is 15cm from the left-side of the DSF cavity and the RHS is 5cm from the right, both are at a height of 1.5m and 0.1m depth into the cavity.

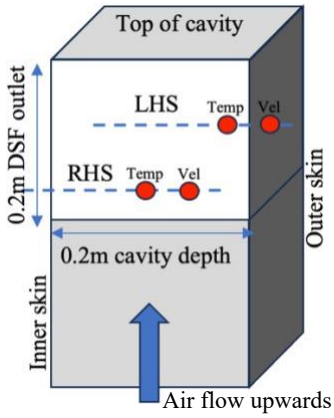


Figure 5.12 Location of experimental measurements of temperature and velocity

The results of the comparison of velocity and temperature measurements from the experiment against the initial CFD model is in Figure 5.13 (a) and (b) below.

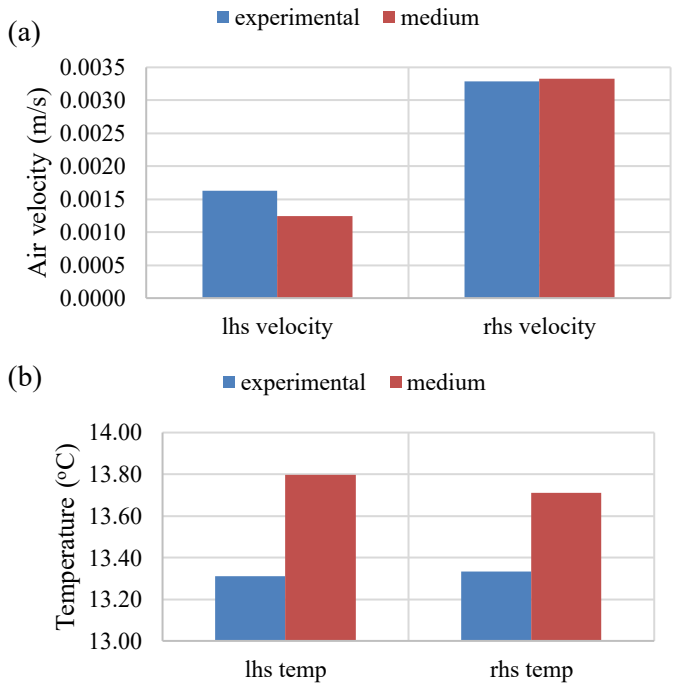


Figure 5.13 Comparison of original experimental data with CFD model for (a) velocity and (b) temperature

The error between the experimental data and CFD model for LHS and RHS velocity are 24% and -1%, respectively giving an average of 12%. There is good agreement between the CFD

model and experimental data not only in error magnitude but also trend whereby the RHS velocity is higher than the LHS velocity. The error between experimental data and CFD model for LHS and RHS temperature are -4 and -3%, respectively with an average of -3.5%. Visually, it looks like there is a higher discrepancy but the increments of the temperature on the y-axis are smaller compared to the velocity. Overall, these results are promising and show that for the model set-up and geometry build applied in ANSYS Fluent, the computational fluid dynamics model is validated against the original experimental data as well as the literature from Mei et al. in the previous section. A limitation here is the number of readings based on available and working equipment, and a maximum of 16 connections on the datalogger to cover all velocity, temperature and heat flux measurements in each test.

5.3.3 Grid Independence Analysis

The grid independence tests in this research comprises developing three different meshes of approximately 3, 5 and 8 million for the 1:1 model prototype of the opaque double skin facade. The purpose is to show that a change in mesh number should not significantly affect the results, for the cavity air velocity and temperature readings in winter conditions for a fully open DSF.

i. Results and Discussion

A rake of 10 points was taken at a height of 1.5m in the cavity to represent where the hot-wire anemometers and cavity RTDs were positioned. Whilst the experimental data only obtained two readings for the velocity and cavity temperature, 10 points have been extracted from CFD to visualise the evolution of these parameters across the 1 metre span of the double skin façade. Table 5.4 below shows the parameters of the different meshes which can indicate quality of the mesh. The average orthogonal quality for medium mesh is 0.85.

Table 5.4 Mesh Quality for CFD Model of DSF Prototype

Quality type	Mesh number	Max. Aspect Ratio	Min. Orthogonal Quality
Medium	3 million	23	0.0074
Fine	5 million	23	0.13
Finest	8 million	19	0.15

Figure 5.14 displays the difference in a) cavity velocity and (b) cavity temperature under medium, fine, and finest meshes with comparison to experimental data for the fully open winter scenario.

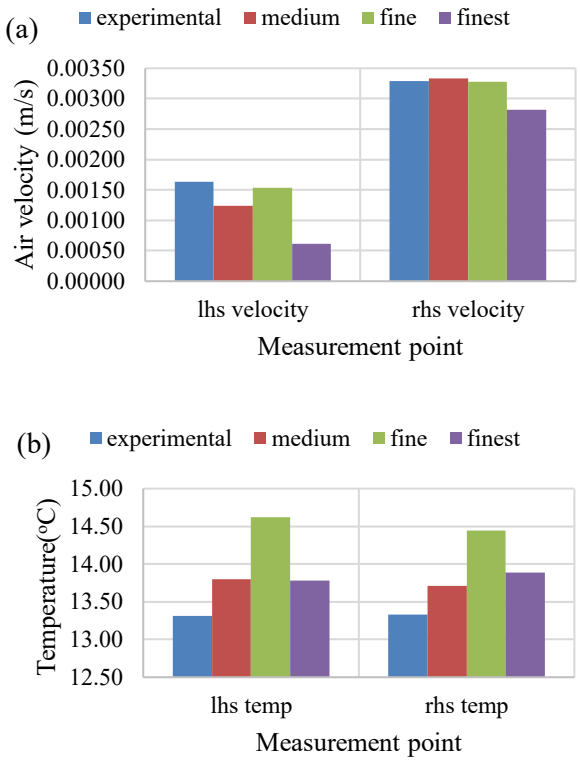


Figure 5.14 Grid sensitivity analysis of CFD model versus experimental data for (a) velocity and (b) temperature

Both figures show a general agreement between each model and the experimental data and despite some visual discrepancies, the magnitude of these is minimal. Figure 5.14 (a) shows the results of the grid sensitivity analysis for velocity measurements and as indicated, the medium and fine models produce best closeness with the values for the finest model being the lowest. There are many reasons behind this, but it is most worthwhile to point out that increased computational cost in terms of finer meshes does not always produce more accurate models, as the refinement is highly dependent on the requirements of the physics problem. Figure 5.14 (b) displays the results for the temperature readings and the main takeaway is that the computational model calculated higher values than the experiment. This is easily explained by boundary conditions, particularly in the model where adiabatic walls have been applied. The experimental prototype was insulated and sealed where these adiabatic boundaries are, however, these may not have been airtight enough to ensure no heat transfer from either side. Additionally, the laboratory side of the experiment was in use by other researchers using equipment or lighting so maintaining a constant room temperature of 18°C was difficult, whereas the computational model does not consider such variations.

Table 5.5 shows the average errors between each model and the experimental data for both velocity and temperature.

Table 5.5 Error Between Original Experimental Data and CFD Mesh Tests

	Error between medium and exp. Data (%)	Error between fine and exp. Data (%)	Error between finest and exp. Data (%)
Velocity	13	3	38
Temperature	3.5	9	4

Overall, in terms of the medium, fine, and finest meshes – there is relatively good agreement with the least difference being observed between the medium and finest meshes. As the simulations for this complex modelling takes multiple hours, computational resource is an important consideration and as a result, all the simulations moving forward use the medium mesh to ensure quality but without too high a computational expense. The next step in building a verified computational fluid dynamics model is to apply different turbulence models.

5.3.4 Turbulence Model Sensitivity

This step of the experimental validation of the computation model involves applying three different turbulence models, including k-epsilon standard enhanced wall treatment (EWT), K-epsilon RNG EWT and k-omega to determine which was the best fit to the experimental data. These were chosen based on similar CFD studies in DSF literature [73,75,83,90,116]. The data used to compare turbulence models is the velocity and temperature measurements in the DSF cavity.

i. *Results and Discussion*

Figure 5.15 displays the comparison of average cavity temperature and velocity readings for the different turbulence models.

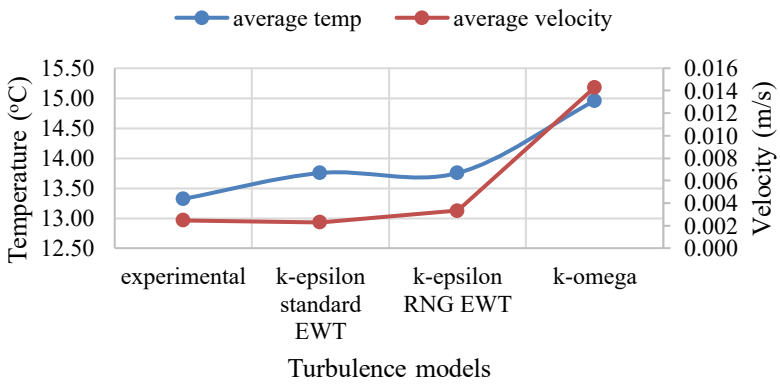


Figure 5.15 Turbulence model sensitivity analysis versus experimental data

The turbulence models that produce the most similar temperature and velocity values to the experimental data are k-epsilon standard and RNG enhanced wall treatment whilst k-omega shows much higher values. The average error between the k-epsilon models and the experimental data is the same at 13% for the air velocity, and 3.5% for the air temperature. Conversely, the k-

omega model experienced higher errors for the velocity at 510%, and 13% for the temperature. The primary reason for this is that k-omega was applied without enhanced wall treatment (EWT) as it is more associated with the k-epsilon models [201]. In computational modelling of double skin façade cavities, how the walls are treated is extremely important and if not done effectively will lead to inaccurate calculations of cavity air velocity, and temperature [202],[203]. As a result, the turbulence model sensitivity analysis has shown that the k-epsilon standard and RNG EWT models are most suitable for a closer match to the experimental data. Moving forward, the remainder of CFD results have been obtained using k- epsilon standard EWT.

5.3.5 Pre-Heating and Ventilation Analyses of DSF Prototype

Following the validation of the small-scale computational model, a more in-depth analysis of the pre-heating and ventilation capabilities of the DSF prototype can be conducted. A full- length vertical profile was not obtained in the experiment, but this can be derived from the validated computational model as well as more points at the DSF outlet and this is a key advantage of using CFD to model DSF performance. Figure 5.16 shows the position of measurement points for the (a) vertical cavity and (b) outlet which are used to collect the data in the following results , exact coordinates detailed in Appendix Tables A.22 and A.23.

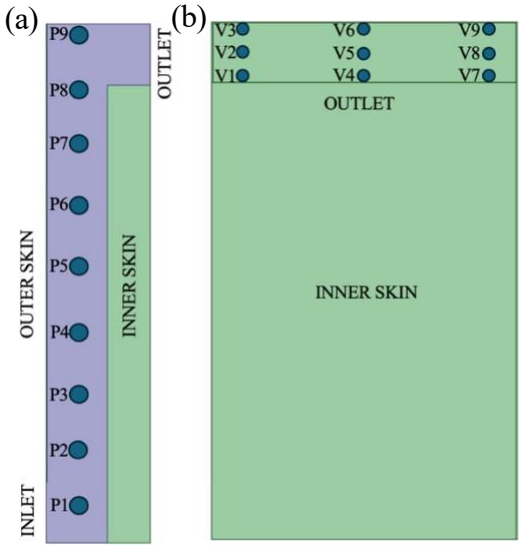


Figure 5.16 Diagram of CFD measurement points in (a) cavity and (b) outlet

i. Pre-Heating Capacity Investigation

The first step in this analysis is to evaluate the pre-heating capacity of the DSF prototype because of the stack effect induced heating. Figure 5.17 shows the evolution of temperature in the cavity with a best-fit polynomial when the external design temperature is (a) -4°C and (b) 10°C. It shows a steady increase in temperature across the height of the double skin façade from -4°C to 17.4°C, thus proving that the stack effect is present in the cavity. The polynomial best fit is of order 6 with an R^2 value of 1 (sextic polynomial) and represents the heating progression.

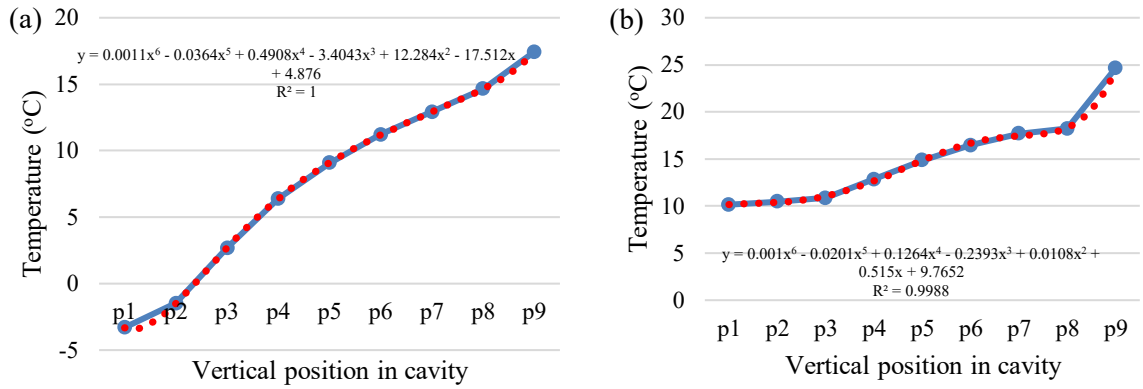


Figure 5.17 Vertical cavity temperature profiles for (a) winter and (b) intermediate seasons

When the DSF is exposed to an external design temperature of 10°C, the evolution of cavity heating changes to appear less steady, but nonetheless, still has a best fit polynomial of order 6 with an R^2 value of 0.9988. The reason behind the variations in cavity heating is due to the temperature differential decreasing as the external design temperature increases. This type of analysis can help with developing predictive models of the stack effect in DSF cavities. Table 5.6 details the pre-heating magnitude that can be achieved at the two external design temperatures tested in this study.

Table 5.6 Pre-Heating Capacity of DSF Prototype in Winter and Intermediate Seasons

External Design Temperature (°C)	Cavity Temp at height 1.7m (°C)	Pre-heating magnitude (°C)
-4	17.4	21.4
10	24.6	14.6

Evidently, the opaque double skin façade is capable of acceptable pre-heating requirements when exposed to an average solar irradiance of 300W/m^2 in winter external design temperatures in the range -4 to 10°C. As the case-study building that this has been developed for is warehouses which typically have an indoor design temperature of 16-18°C, this data shows that these conditions are met.

Figure 5.18 shows the evolution of temperature in the cavity on a contour taken at the mid-section of the double skin face for external design temperatures of (a) -4°C and (b) 10°C. The heating occurring within the cavity when exposed to -4°C (269K) outside is slow over the first 0.5m but then increases by 1-3K steadily as depicted in Figure 5.18 (a). The thermal gradient changes when the DSF is exposed to 10°C (283K) outside, taking longer to experience heating indicated by the larger plume of blue in Figure 5.18 (b).

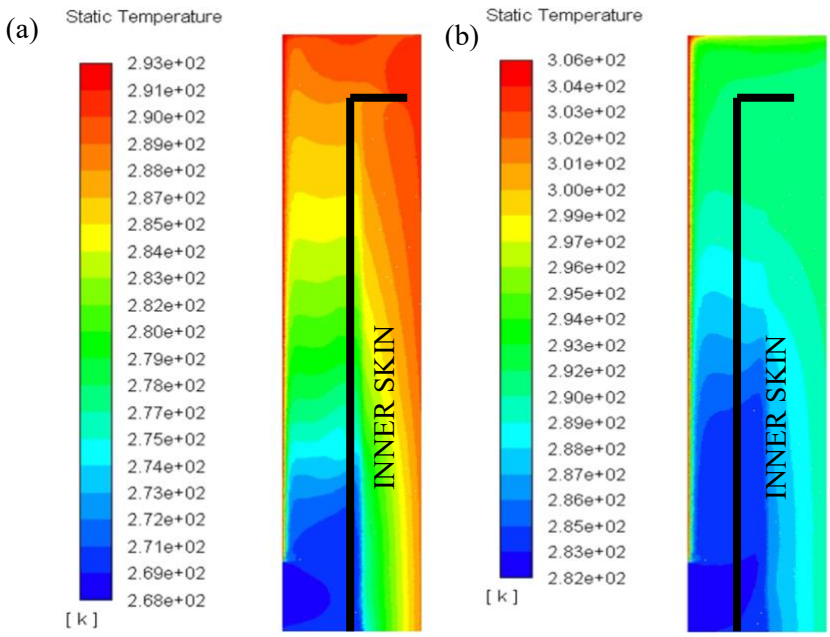


Figure 5.18 Vertical cavity temperature contours for (a) winter and (b) intermediate seasons

When exposed to cold outdoor air temperatures consistent with the UK climate, the DSF can achieve a peak temperature between 17 and 24°C. This range approaches or exceeds typical indoor design temperature requirements and therefore demonstrates the viability of the opaque double skin façade as a pre-heating technology.

ii. Buoyancy-Driven Airflow and Fresh-Air Ventilation Analyses

The second step in this analysis is to translate stack effect induced heating into buoyancy- driven ventilation. Figure 5.19 shows the evolution of velocity in the cavity with a best-fit polynomial when the external design temperature is (a) -4°C and (b) 10°C.

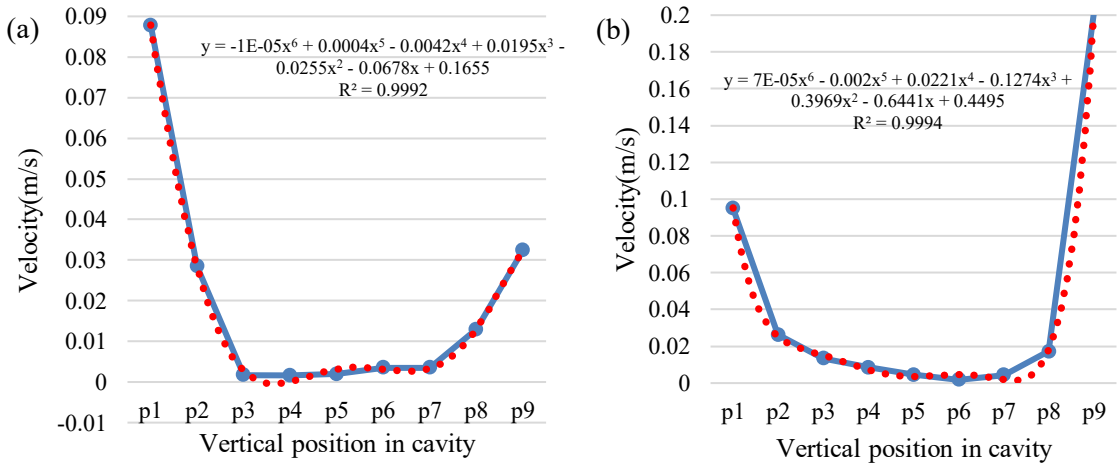


Figure 5.19 Vertical cavity velocity profiles for (a) winter and (b) intermediate seasons

Similarly to the vertical temperature profile, the vertical velocity distribution is best depicted by a 6th order polynomial for both external temperature conditions with R^2 values of 0.9992-0.9994. This exemplifies the complexity of a buoyancy-driven flow in a double skin façade whilst also proving the efficacy of utilising a methodology such as computational fluid dynamics as there is an increase in computational cost to solve this analytically. The main difference between these two figures is that the higher external temperature in (b) leads to a much higher air velocity reading at the top of the cavity, about five-fold compared to (a). The velocity near the inlet at P1 for both (a) and (b) is relatively similar at around 0.09m/s. The most notable takeaway is that regardless of external design temperature, the airflow will be minimal in the centre of the cavity, increasing at the boundaries.

Figure 5.20 shows the airflow distribution in the cavity on a contour taken at the mid-section of the double skin face for external design temperatures of (a) -4ºC and (b) 10ºC.

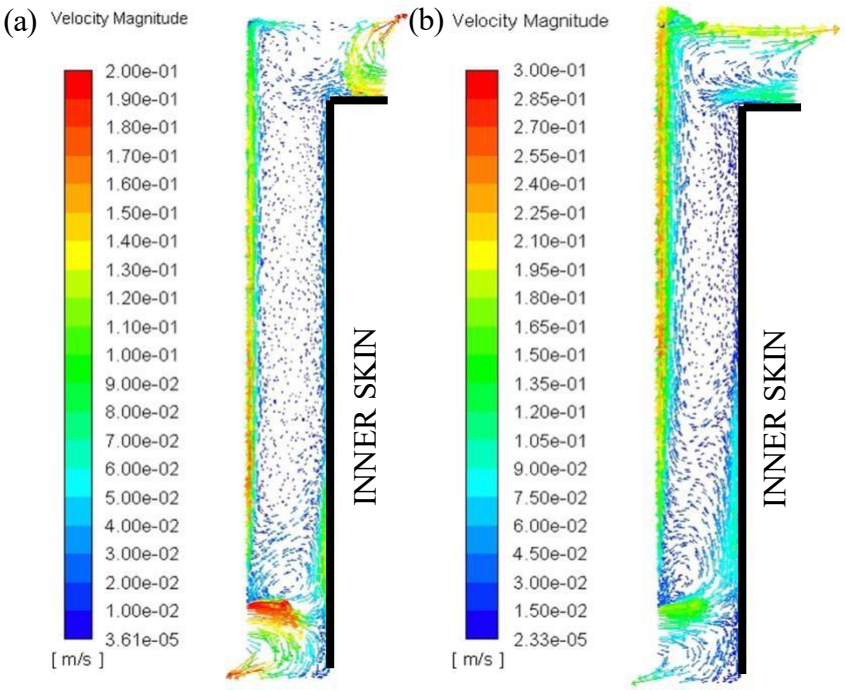


Figure 5.20 Vertical cavity velocity contours for (a) winter and (b) intermediate seasons

Both contours look relatively similar; however, the magnitude of the velocity is higher when the double skin façade is exposed to an external design temperature of 10ºC shown in (b). The recirculation seems to be stronger at the inlet and outlet in (a) compared to (b) where the inlet stream is stronger causing higher velocities close to the inner skin of the cladding. As there is an inverse relationship between airflow rate and the stack effect in terms of heating, the presence of higher velocities can negatively impact the level of pre-heating that can occur, even if it leads to higher ventilation rates. Additionally, the velocity profile shows that there can be minimal

airflow in the centre of the cavity whilst there is increased airflow at the outer and inner skins, and this is due to the greater temperature differential across these boundaries. The air velocity values obtained in this model are re-calculated as outdoor air flow rate using Equation 5.2 whilst Table 5.7 shows the results of these calculations.

Equation 5.2 Buoyancy-driven outdoor air from DSF

$$\text{Outdoor } air\ (L/s) = Air\ velocity\ (m/s)\ \cdot outlet\ area\ (m^2)\ \cdot 1000$$

Table 5.7 Ventilation Capacity of DSF Prototype in Winter and Intermediate Seasons

	External design temperature (°C)	
	-4	10
Average air velocity (m/s)	0.16	0.12
Outlet area (m^2)	0.20	0.20
Volumetric flow rate (m^3/s)	0.032	0.023
Outdoor air flow rate (L/s)	32	23

Due to a lack of standardised ventilation guidelines for storage and distribution warehouses in the UK, a typical value of 10-12L/s/person [8] is used for reference instead. Comparing this to the outdoor air flow rate values in the table above, the 1m-span prototype of the opaque double skin façade can deliver ventilation to 2-3 people. This is promising as a full-scale span of the case study warehouse is 36m and height 10m suggests that it will be able deliver an appropriate level of ventilation for higher occupancy levels. This is explored in depth in the following section.

5.4 Computational Modelling of a Full-Scale DSF (Buoyancy)

Following the validation of the experimental model which was a 1:1 scale of a 1.5 x 1m section of the DSF retrofit, it is imperative to examine the thermal conditions at full-scale to reflect a realistic scenario. This part of the chapter marks the second stage of building the final computational model of a double skin façade retrofit for storage and distribution warehouses, confined to buoyancy-only scenario. Under varying seasonal thermal conditions, the ventilation and thermal performance of the fully open DSF is assessed. Figure 5.21 shows the position of the 21 measurement points used to collect the data, details in Appendix Table A.24.

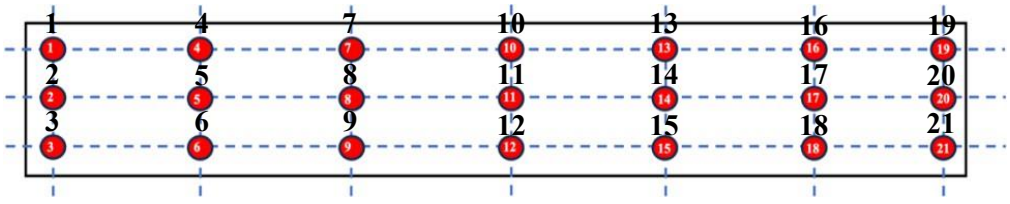


Figure 5.21 Position of 21 measurements points for full-scale DSF outlet

5.4.1 Cavity Velocity and Ventilation Performance

The ventilation performance of the DSF retrofit concerns whether there is a sufficient airflow rate to aid in heat recovery within the cavity and outdoor air to the indoor space adjacent to the DSF. By computationally determining the magnitude of air velocity at the top of the full-scale double skin façade cavity, the level of outdoor air ventilation delivered to an adjacent building can be estimated. It is important to note that to keep consistency with the validated model, the bottom inlet opening was extended across the entire façade resulting in a large area of 7.2m^2 and naturally, this will impact the airflow and ventilation rates compared to more realistic opening sizes which would not span across the whole length of the facade. This kind of optimisation of opening area is not explored in this chapter, but is later investigated in Chapter 7, Section 7.4.3.

Table 5.8 details the cavity velocity values obtained from ANSYS Fluent, and calculated ventilation flow rates.

Table 5.8 Ventilation Capacity of Full-Scale DSF Prototype in All Seasons

Season	External design temp (°C)	Cavity Velocity (m/s)	Area of inlet (m^2)	Flow rate (m^3/s)	Ventilation flow rate (L/s)
Winter	-4	0.15	7.2	1.0	1000
Intermediate	10	0.16	7.2	1.1	1100
Summer	25	0.86	7.2	6.2	6200

As the results only concern buoyancy-driven ventilation, it is expected that the outdoor air ventilation delivered would be relatively low compared to wind-driven conditions. This is particularly the case with the winter and intermediate external design temperatures of -4°C and 10°C yielding 1000L/s and 1100L/s, respectively. At the current building regulatory recommendations of 10-12L/s, the buoyancy-driven ventilation would fall short when external design temperatures are 10°C and below. Conversely, the summer external design temperature of 25°C resulted in an outdoor air supply that would satisfy 60 occupants.

The distribution of the air velocity across 21 measurement points at the cavity outlet, and therefore ventilation performance of the DSF, is shown in Figure 5.22 below. There is a similarity in airflow distribution between the winter and intermediate scenarios and this is likely due to the cavity reaching a similar temperature in both conditions, and it is these temperature fluctuations which drive these buoyancy forces and are explored in the next section.

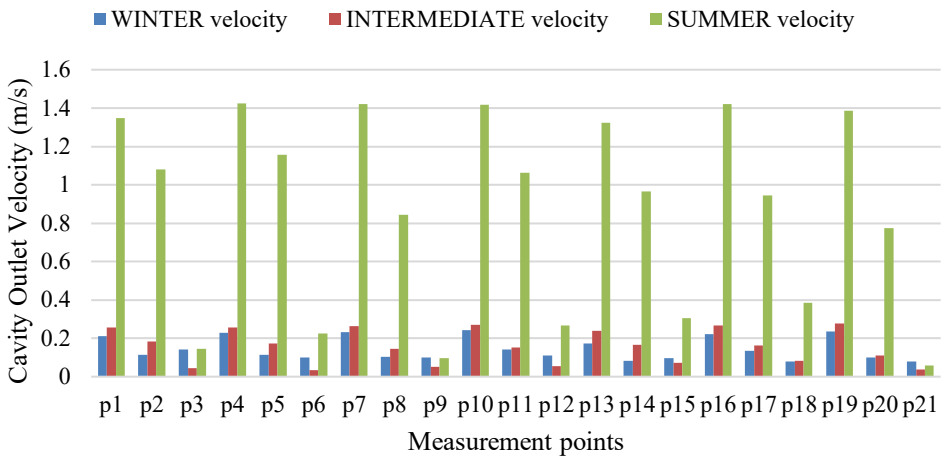


Figure 5.22 Velocity distribution at DSF outlet across 21 points for all seasons

To add, the summer condition experiences air velocity fluctuations from around 0.2 to 1.45m/s which is unsteady and inconsistent compared to the colder conditions. This demonstrates that moderate to cool temperatures below 10°C deliver a relatively consistent level of buoyancy-driven ventilation, whilst hotter external design conditions promote a more unstable ventilation performance.

Figure 5.23 shows the airflow patterns in the cavity for (a) winter, (b) intermediate, and (c) summer conditions with a focus on flow direction and magnitude at the top of the cavity taken at a midsection view of the 3D model.

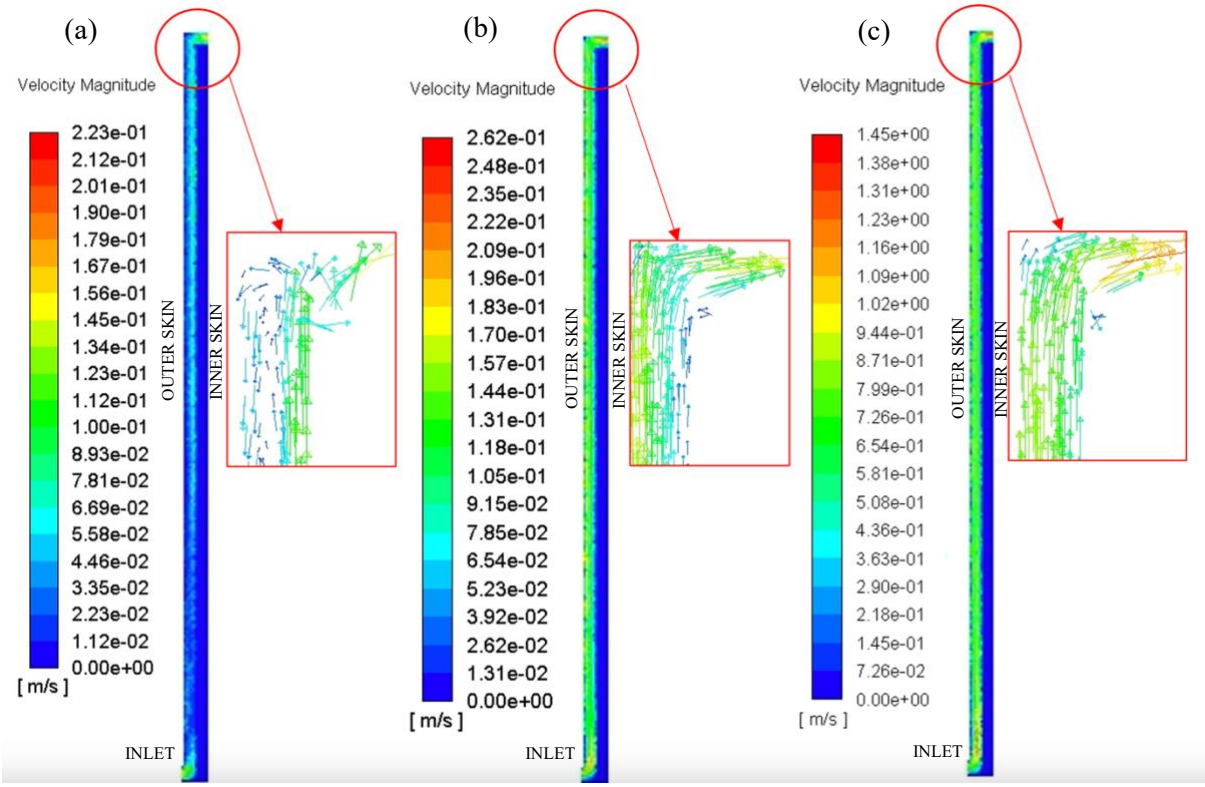


Figure 5.23 Velocity contours of full-scale DSF for (a) winter, (b) intermediate and (c) summer seasons

What is evident is that the coldest external design temperature of -4°C results in the lowest magnitude of velocity, however the average velocity measured at the outlet is only 0.012m/s lower than the intermediate scenario as demonstrated in the previous Table 5.9. Comparing the two velocity contours between (a) winter and (b) intermediate, there is still a significant difference in airflow patterns despite a similar average velocity at cavity outlet. For example, the winter contour shows recirculation of air at the top of the cavity with a stronger airflow closer to the inner skin of the cavity whereas the intermediate contour shows a strong flow without any recirculation. The average velocity calculated at the outlet in the summer scenario was greatest and six-fold the values obtained for winter and intermediate, however it has a similar airflow pattern to the intermediate scenario. Ultimately, this ventilation analysis has proven that the full-scale opaque aluminium double skin façade does experience buoyancy-driven ventilation in a range of external design temperatures with a constant solar heat flux of 300W/m^2. The next section explores this from a thermal performance perspective.

5.4.2 Cavity Temperature and Thermal Performance

The thermal performance of the DSF retrofit is the ability to reduce heat loss in winter and reduce overheating in cooling seasons by either ducting the pre-heated cavity air into the warehouse or exhausting it from the top of the DSF. By computationally determining the magnitude of air temperature at the top of the full-scale double skin façade cavity, the level of heat gain in the cavity can be estimated. Table 5.9 details the cavity temperature values obtained from the CFD model, and calculated levels of heating.

Table 5.9 Pre-Heating/Cooling Capacity of Full-Scale DSF Prototype in All Seasons

Season	External design temp (°C)	Cavity Temp (°C)	Cavity Heating, ΔT(°C)	Inside temp reached (°C)
Winter	-4	16	20	-1.5
Intermediate	10	17	7	0.90
Summer	25	24	-0.66	6.3

The key finding from the data in the table above is that in colder external design conditions, the cavity can deliver a high magnitude of pre-heating but also perform as a thermal buffer in the intermediate and warmer environmental temperatures when exposed to a solar vertical irradiance of 300W/m^2. There is an element of overheating in the summer scenario when comparing the cavity temperature to the internal design condition of 18°C, however generally in other building types, there is an expectation that indoor conditions are around 24°C [8]. Figure 5.24 shows the variation in air temperature at the cavity outlet for winter, intermediate and summer conditions across the 21 measurement points.

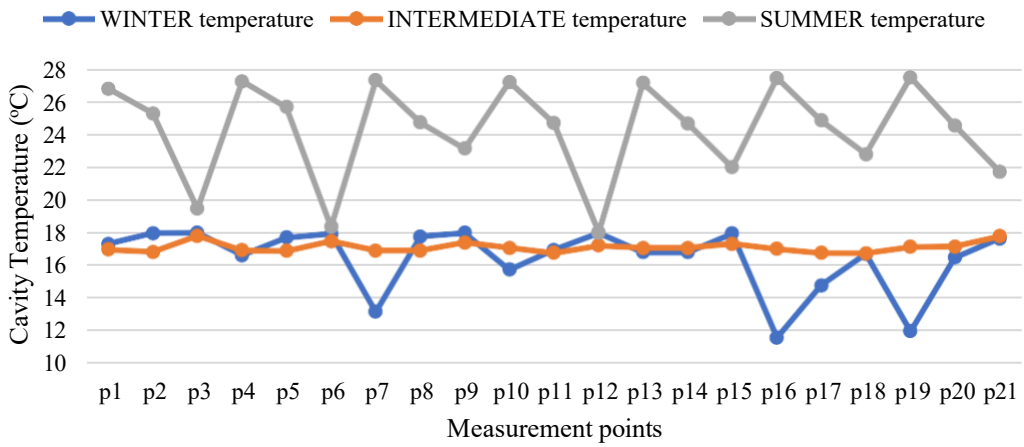


Figure 5.24 Temperature distribution across 21 measurement points at DSF outlet for all seasons

The summer scenario depicted by the grey line has the greatest variation in cavity temperature, and this is likely due to the buoyancy-driven air velocity magnitude shown in the previous section in Figure 5.22. The intermediate conditions have the least variation and shows the opaque double skin façade's ability to perform as a thermal buffer to reduce heat loss from the warehouse to the environment. Lastly, the winter external temperature does produce some variation in cavity temperature but does not peak above the temperatures achieved in an intermediate season. Given that the external temperature difference between winter and intermediate is 14°C, this is an interesting finding for colder-to-moderate climates. To gauge a better understanding of the DSF's thermal performance, Figure 5.25 shows the temperature distribution in the cavity for (a) winter, (b) intermediate, and (c) summer conditions taken at a midsection view of the 3D model.

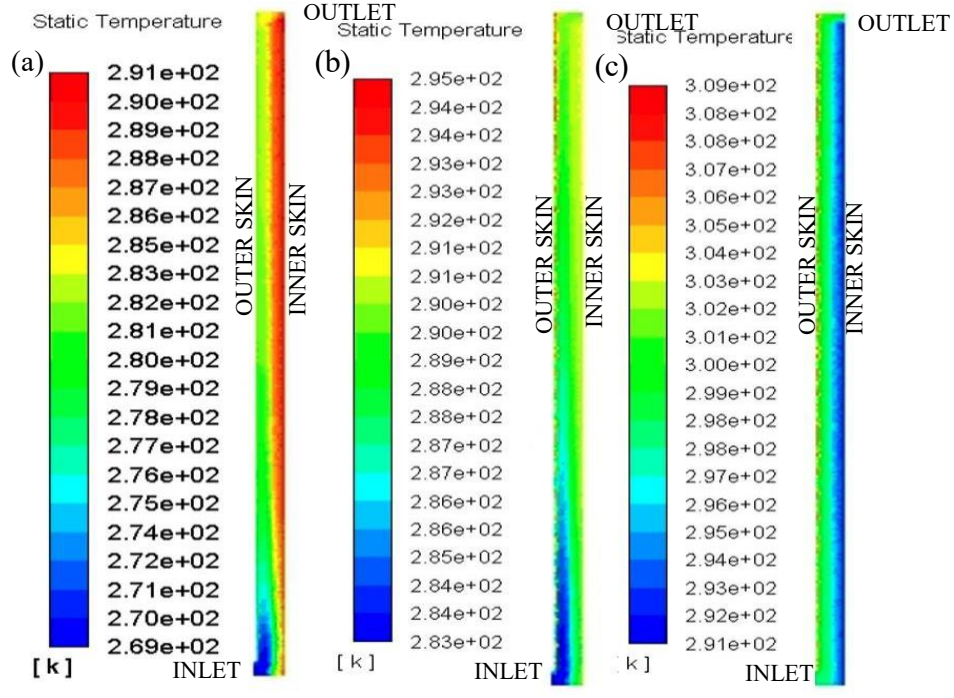


Figure 5.25 Temperature contours of full-scale DSF for (a) winter, (b) intermediate and (c) summer seasons

What is apparent from the temperature contours is that as the external design temperature increases, the outer skin and inner skin temperatures swap positions as the hottest surface. For example, in winter there is a strong red denoting the 22°C difference between internal and external temperatures whilst intermediate sees a balancing out of surface temperatures, and finally the dark blue in the summer conditions to represent that the internal space is cooler than the cavity. This highlights the importance of physically modelling the adjacent building space when analysing the performance of double skin facades as accurately portraying the thermal conditions at the outer and inner skins is essential for obtaining realistic thermal phenomena within the cavity. The next section of the chapter looks at how to quantify the ventilation and thermal performance of the DSF in terms of energy savings.

5.5 Energy Savings from a Full-Scale DSF (Buoyancy-Only)

Finding the energy savings that a full-scale DSF can achieve involves two steps. Firstly, by treating the DSF as a thermal duct and calculating the heat gain or removal as a function of mass flow rate (determined by buoyancy pressure drop), and secondly, by approximating new dynamic u-value for the DSF in different seasons and inlet configurations. Both metrics can help to understand how the DSF retrofit can reduce the energy consumption of the adjacent warehouse. Assumptions include a uniform vertical temperature gradient and no friction loss.

5.5.1 Treating the DSF as a Thermal Duct

Using the equations in Chapter 3, Section 3.3, the buoyancy-driven pressure and mass flow rate can be determined, and finally the heat gain or removal from the cavity. Details of an example calculation and the values required for this are in Appendix Section A.4.5 using the necessary details from Table 5.10.

Table 5.10 Values Required to Calculate DSF Energy Savings in All Seasons

	Winter	**Intermediate**	**Summer**
$\rho_{average}$ (kg/m^3)	1.259	1.229	1.198
g (m/s^2)	9.81	9.81	9.81
H_{cavity} (m)	9.8	9.8	9.8
$T_{cavitytop}$ (°C)	16	17	24
$T_{cavitybottom}$ (°C)	-4	10	25
A_{cavity} (m^2)	7.2	7.2	7.2
c_p (J/kg/°C)	1005	1006	1006

The cavity velocity can be determined in two ways: using the simplified analytical approach or applying the values from the CFD model from the previous section 5.3.1. The results of both are in Table 5.11 where the buoyancy pressure for winter, intermediate and summer seasons is 38Pa, -4.9Pa and 0.12Pa, respectively.

Table 5.11 Cavity Heat Gain, Velocity, Mass Flow and Volumetric Flow Rate (Analytical and CFD Values)

	V_{cavity} (m/s)		$\dot{m}$ (kg/s)		$Q_{flowrate}$ (m^3/s)		$Q_{heatgain}$ (kW)	
	Analytical	CFD	Analytical	CFD	Analytical	CFD	Analytical	CFD
Winter	7.7	0.15	70	1.3	56	1.0	1,400	27
Intermediate	2.8	0.16	25	1.4	20	1.1	179	9.9
Summer	0.46	0.86	3.9	7.4	3.3	6.2	-2.6	-4.9

Comparing the two sets of cavity velocity, the analytical calculation overestimates the winter and intermediate velocities by 53% and 18% compared to the validated CFD model whilst underestimating the cavity velocity in summer by 53%. The main reason for this level of discrepancy is that equation for cavity velocity is highly simplified, not considering viscous effects, drag, flow obstructions, turbulence complexities and more whereas the CFD model is more capable of solving this. The CFD derived heat gains show that for a range of external design temperatures of 10°C down to -4°C, it can generate between 9.9 and 27kW of heat, and in summer temperatures of 25°C provides cooling of 4.9kW, all under an average vertical solar irradiance of 300W/m^2. Overall, this tool helps not only to prove that the full-scale DSF is capable of heating and cooling but also provides a method quantify the magnitude of heat gain or removal in the cavity.

5.5.2 Treating the DSF as a New Wall

This section looks at how implementing the DSF as a retrofit changes the thermal properties of the existing façade. The values required to calculate the previous equations are laid out in Table 5.12 below:

Table 5.12 Values Required to Calculate DSF Retrofit Dynamic U-Value in All Seasons

	Winter	**Intermediate**	**Summer**
$U_{cladding}$	0.31	0.31	0.31
$d_{aluminium}$ (m)	0.003	0.003	0.003
$k_{aluminium}$ (W/mk)	235	235	235
$\rho_{cavityaverage}$ (kg/m^3)	1.259	1.229	1.198
$v_{cavityaverage}CFD$ (m/s)	0.145	0.157	0.860
L (m)	9.8	9.8	9.8
$\mu_{cavityaverage}$ (kg/ms)	1.750	1.784	1.820
$k_{cavityaverage}$ (W/mk)	0.02489	0.02542	0.02598

The results for Reynolds and Nusselt numbers, convective heat transfer coefficient (CHTC), and thermal resistances of the total and different DSF components required to calculate the new U-values are in Table 5.13.

Table 5.13 Reynolds, Nusselt, CHTC, Thermal Resistances and New U-Values for All Seasons

	Re	Nu	h (W/m^2K)	R_{cavity} (Km^2/W)	$R_{cladding}$ (Km^2/W)	$R_{aluminium}$ (Km^2/W)	R_{total} (Km^2/W)	$U_{dsfretrofit}$ (W/m^2K)
Winter	100000	204	0.52	1.9	3.22	0.00001	5.2	0.19
Intermediate	100000	210	0.55	1.8	3.22	0.00001	5.1	0.20
Summer	550000	790	2.1	0.48	3.22	0.00001	3.7	0.27

It is important to note that the energy savings calculations at this stage are only reflective of average solar conditions of 300W/m^2. Whilst a temperature differential across the DSF and internal warehouse space is usually always present in the UK climate, these do not reflect all possible scenarios. The value of approximating a dynamic U-value with the fully open DSF inlet configuration as an example is to assess revised heating or cooling gains for the south- facing façade of the case study warehouse. The existing façade comprised a cladding of U-value 0.31W/m^{2}K, and in all seasons, the dynamic U-value with the DSF retrofit is lower and therefore improves the overall thermal performance of the façade by reducing heat loss, and heat gain. Figure 5.26 has the heat loss/gain values for winter, summer and intermediate seasons compared to the existing warehouse façade.



Figure 5.26 Comparison of heat loss through warehouse façade and DSF retrofit

In all seasons, the DSF has improved the thermal performance of the existing south-facing façade on the warehouse from a thermal conductance perspective. At a minimum, the application of the DSF alone will reduce the heating and cooling loads by 39% and 13%, respectively. This is before delivering any pre-heating or local cooling driven by the stack effect in the cavity. These results are based on dynamic u-values of 0.19, 0.20, and 0.27W/m^{2}K for winter, intermediate and summer conditions.

5.6 Chapter Summary

This chapter investigated the thermal performance of a prototype-scale of the "seasonal-adaptive" opaque double skin façade, designed specifically for storage and distribution warehouses. Various studies took place including climate chamber testing of the DSF under different thermal conditions to obtain cavity air temperature and velocity data for validation of computational models in addition to a preliminary validation against existing data in literature. Full-scale computational modelling of the DSF when applied case-study warehouse including in-depth analysis of cavity heating from the stack effect, and buoyancy-driven ventilation.

5.6.1 Main findings

The climate chamber experiment tested the buoyancy-driven ventilation and thermal performance of the 1.5m by 1.0m by 0.2m double skin façade prototype with an outer skin of 3mm aluminium, and 151mm warehouse cladding. Summer conditions with an external temperature of 25°C led to the highest cavity air velocity for a fully open, 25% and 50% LHS/RHS closed DSF inlet configuration, but the lowest for 75% LHS/RHS closed. The overall magnitude of cavity air velocity is low, below 0.06m/s at a peak and on average, less than 0.02m/s which is expected in buoyancy only conditions. For thermal performance, there is a linear relationship between an increase in external temperatures and the cavity temperature at the DSF outlet. In all DSF inlet configurations, the summer conditions yield the highest cavity temperature, followed by intermediate and winter conditions. However, in terms of the temperature gradients across the height of the cavity, winter has the best performance with a gradient in the range 8-13 in all DSF inlet configurations.

This chapter offered a dual approach to validation of the CFD models by comparing it against existing literature as well as the original climate chamber experimental data. The comparison with literature saw good agreement of cavity air velocity and temperature at 27% and 16%, respectively. It should be noted that the CFD model for this was simplified to not include the grilles in the DSF inlet and outlet and this is likely the root of some of the discrepancy. Overall, there was the same trend of increased temperature and therefore velocity at the fluid interfaces of the outer and inner skins with lower magnitudes in the central DSF cavity. When comparing the CFD model of the DSF prototype to the original experimental data, the LHS measurement of cavity air velocity resulted in an error of 24% whilst the RHS yielded only -1%. This could be due to less equal velocity distribution in the experimental set-up than can be achieved in CFD. The temperature readings were better however, resulting in -3% and -4% for LHS and RHS measurement points, respectively. The grid independence tests found a medium mesh is best, followed by turbulence models capable of enhanced wall treatment and full buoyancy effects.

The DSF prototype was then scaled up to match the 36m x 9m area of the case study warehouse façade to obtain realistic full-scale performance. The ventilation flow rates achieved are 1000L/s, 1100L/s and 6200L/s for a fully open DSF inlet configuration in winter, intermediate and summer seasons, respectively. The cavity heating for winter is 21°C, followed by 7.1°C in intermediate, and -0.66°C in summer, thus proving the DSF's ability to deliver pre-heating as

well as performing as a thermal buffer. The Bernoulli-adapted tool was compared to the CFD model and found to overestimate the level of heat generation in the DSF's cavity. Based on the CFD model-derived data, the DSF can achieve 27kW of heating in winter, 10kW in intermediate seasons and -5kW in summer. In terms of retrofit performance, the dynamic u- value is 0.19W/m^2K, 0.20 W/m^2K and 0.27 W/m^2K for winter, intermediate and summer seasons, all of which are lower than the original 0.31W/m^2K for the cladding on the case study warehouse, highlighting an improvement in thermal conductance.

5.6.2 Limitations and recommendations for future work

If time and resources allowed it, an improvement to the environmental chamber tests could include looking at a double-sided climate chamber where both sides can have controlled temperatures as opposed to just one side. Additionally, the computational modelling of average solar irradiance of 300W/m^2 was simplified by applying a heat generation value to the outer skin surface of the DSF however ANSYS Fluent has capabilities to do more complex radiation modelling which would be good to look at in the future. The most effective way to validate this DSF prototype would be to collect data from a pilot study of the double skin façade on a real warehouse, and this is a recommendation for future work in the conclusion of this thesis.

Other areas where this research could expand later include looking at a range solar irradiance values and other climates with a greater range of external and internal design temperatures. In terms of application, it could be applied to other building types with unobstructed vertical spaces such as airports, venue halls and datacentres.

5.6.3 Closing remarks

The climate chamber experiment of a 1.5 by 1m section of the DSF prototype for storage and distribution warehouses and subsequent computational modelling in this chapter has produced evidence that it works as a ventilation and passive heating and/or cooling strategy. Both the wind-only and buoyancy-only components of ventilation have now been investigated, but before looking at how the full-scale DSF warehouse performs in combined with and thermal conditions, the phenomenon of stratification within warehouse spaces is addressed in the next chapter.

Chapter 6

Stratification in Warehouses

6.1 Introduction

This chapter stands alone amongst the other results as it focusses solely on the case study warehouse, excluding the proposed double skin façade retrofit. The main objective of examining thermal stratification is it is a large research gap unique to warehouses due to high floor-to-ceiling heights largely unobstructed by typical storey levels seen in other buildings such as residential or offices. Additionally, thermal stratification is incorporated into the final CFD model of the DSF and warehouse in Chapter 7 in the form of internal heat gains.

Thermal stratification, or stratified air, is defined as the phenomenon that occurs when cool, dense air sinks while the warm, less dense air rises and is an issue in tall buildings where there is an accumulation of hot air in top floor or open ceiling zones [204]. Within warehouses, this has previously only been addressed with a mechanical solution known as destratification fans by various companies who report competitive energy savings of 20-50% [24], [205]. However, these savings will be offset against the electricity consumption of the fans which typically constitute 25% of a building's energy consumption [206]. Therefore, if the primary purpose of installing destratification fans is to increase indoor temperatures at working level, and reduce heat loss through the roof fabric, whilst there will be a reducing in heating bills, for heating- dominant climates such as the UK, the destratification fans will be needed for most of the year. As a result, it is imperative to understand how stratification occurs in spaces such as the case study warehouse in this thesis.

This research underscores the importance of Grashof number determination as a fundamental step towards understanding the impact of stratification in warehouses as tall structures where measuring temperature stratification in full-scale warehouses is not always possible as per accessibility or budget constraints. The novelty of this study is in two prongs: firstly, the method of conducting scale thermal studies of stratification in warehouse; and, secondly, the simulation of 100% capacity storage racking to resemble a typical storage and distribution warehouse. Overall, this chapter aims to start a discussion with the hope of later informing new regulatory frameworks for storage and distribution warehouses in the UK to consider the impact of stratification on energy consumption and internal environment conditions. The objectives required to achieve this include:

- Conduct a thermal experiment of a scaled case-study warehouse model with and without storage racking
- Determine Grashof's number and thermal gradients to indicate scale of buoyancy

phenomena for the small-scale case study warehouse

- Develop a computational model of stratification in warehouses, validated by the experimental data

6.2 Experimental Results

The 1:50 scale warehouse model from the wind tunnel experiment in Chapter 4 was re- purposed for a small-scale experimental investigation to determine the Grashof number, Gr, a fundamental parameter for assessing buoyancy-driven flows, within warehouse storage spaces. All the openings were sealed to create a closed internal space to avoid interactions with the wind tunnel environment. The experiment involved creating controlled stratification conditions within a scaled-down warehouse model using heat mats. Two scenarios were considered including an empty warehouse, and 100% capacity storage racking spanning the length of the model, as shown in Figure 6.1 below. Temperature gradients were measured at various heights, and airflow velocities were assessed in computational fluid dynamics to capture the stratified airflow patterns.

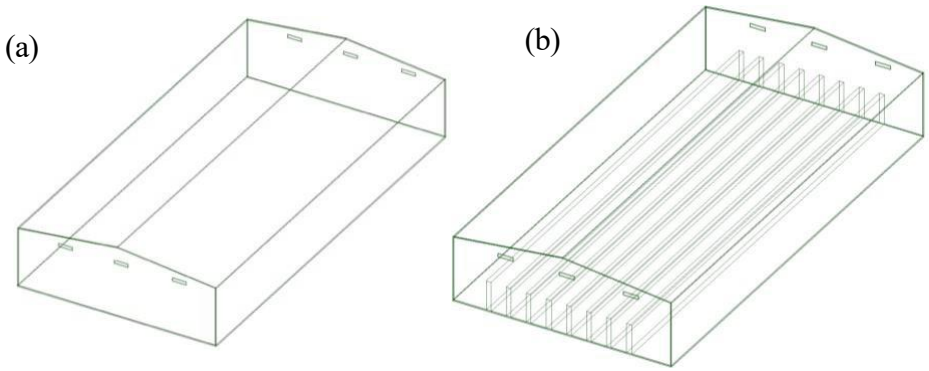


Figure 6.1 Cross-Ventilation Openings in the(a) Empty and (b) Storage Racking Scenarios in the Case Study Warehouse

For the small-scale stratification testing, the cross-ventilation openings were sealed to create an enclosed internal space for ideal heating, but these are re-introduced in Section 6.4.

6.2.1 Empty Warehouse (No DSF)

As stratification occurs in warehouses naturally, with or without a DSF retrofit, this section is only concerned with the empty case study warehouse at a 1:50 scale, repurposing the wind tunnel model. The conditions in the wind tunnel are described as “ambient” where the fan is off, and the average wind tunnel temperature was recorded at 19.2^{o}C as per the readings in Table A.27 in the Appendix. The heat mats are a simplification of casual heat gains within the indoor warehouse space and do not represent a realistic distribution of heat sources in a warehouse. Preliminary tests were completed to ensure the heat mats were working to the rated capacity.

i. Temperature Gradient

The first experiment with the 7W heat mat was conducted to demonstrate that taking measurements at different points in the warehouse could yield contrasting results. Three positions were measured, as detailed in Section 3.4.2 of the methodology chapter where Figure 3.13 shows a schematic of the measurement layout. Table 6.1 shows the temperature data collected for the three measurement points, '1/3 forwards', 'middle' and '1/3 backwards' in the empty warehouse model when the heat mat was turned on.

Table 6.1 Temperature Data for Three Different Measurement Points

Measurement point	Vertical height (m)	Temperature (°C)		
		1/3 forwards	Middle	1/3 backwards
1 Bottom	0.04	20.55	34.37	20.72
2	0.09	20.82	27.85	20.89
3	0.13	21.03	24.89	21.16
4	0.18	21.25	24.63	21.39
5 Top	0.20	21.99	24.55	21.89

As expected, the middle measurement produced a "flipped" scenario of hot to cooler temperatures as these were taken directly above the heat mat. This measurement has primarily been included to demonstrate the evolution of temperature distribution with a central heat source. Table 6.2 shows the temperature gradient for the measurements at "1/3 forwards" and "1/3 backwards" positions. Equation 5.1, Chapter 5 for thermal gradient is applied here.

Table 6.2 Temperature Gradients for 1:50 Scale Warehouse Model

	1/3 forwards	1/3 backwards	% difference between positions
ΔT(°C)	2.79	2.69	
H(m)	0.20	0.20	
∇T(°C/m)	13.95	13.45	4

The starting lab temperature, 19.2°C and end temperature at the tallest height of 0.2m in the warehouse are used. These temperature gradients are quite high and if applied with a linear scale factor to predict stratification for the full-scale model, it would yield unrealistic results. Figure 6.2 displays the temperature stratification measured by the "1/3 forwards" and "1/3 backwards" positions from the centre of the model.

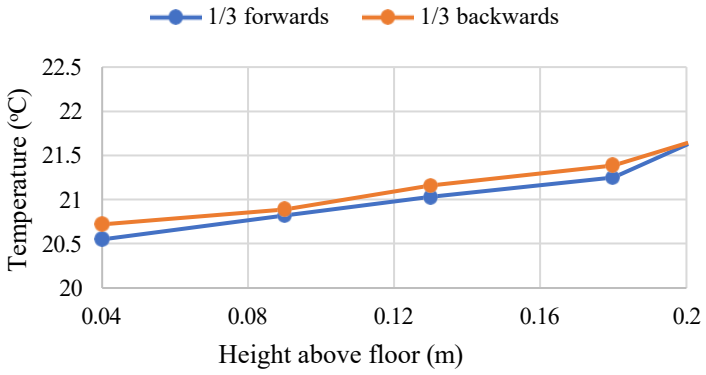


Figure 6.2 Vertical Temperature Distribution in 1:50 Scale Warehouse Model

There is little difference between the temperature measurements at positions 1/3 forwards and backwards, and therefore for the results in the next section, the data has been obtained from the 1/3 forwards position.

ii. Grashof Number

As the fluid motion is driven by density variations due to temperature differences. The Grashof number (Gr) is a nondimensional parameter which represents the ratio of buoyancy to viscous forces [207], described by Equation 6.1 below where g is the acceleration of gravity (m/s^2), β is the expansion coefficient of air (1/K), ΔT is the vertical temperature difference (K), L is the characteristic length (m) and μ is the viscosity of air (Ns/m^2).

Equation 6.1 Grashof Number

$$Gr = \frac{g\beta\Delta T L^3}{\mu^3}$$

As buoyancy reflects temperature differences in the air, the Gr number can be used in this case to confirm whether there is a high level of stratification in the small-scale model of the warehouse. Table 6.3 details the parameters required to calculate the Gr number.

Table 6.3 Parameters Required to Calculate Gr Number (7W heat mat)

Parameter	Experimental values
g (m/s^2)	9.81
β(1/^{o}C)	0.00343
ΔT(^{o}C)	2.79
L(m)	0.20
μ(m^2/s)	0.00001516
Grashof number:	3,209,262

For the experimental 1:50 scale model of the empty warehouse, the Grashof number was calculated to be 3.2 x10^6 which suggests that the buoyancy forces are much more significant than the viscous forces [207]. This value is a good indication of the level of stratification within the space. The results of this section prove the existence of high stratification levels in a small-scale model of the case-study storage and distribution warehouse. An average temperature gradient of 14 and a Grashof number of 3.2x10^6 reflect the magnitude of stratification within an empty space. For a more realistic insight, the next section looks at the same test but for the model with polystyrene blocks to simulate storage racking that is typical in a storage warehouse.

6.2.2 Warehouse with Storage Racking (No DSF)

An adaptation of stratification studies is to add structures to replicate 100% capacity storage racking as the primary purpose of storage and distribution warehouses is the picking and packing of goods. These tall racking, separated by aisles, could influence the thermal performance of the building as well as the airflow distribution in the context of air entering from open loading bay doors or specially designed ventilation inlets. The details of the storage racking sizing guidelines that have been applied in these studies are in Section 3.4.2 of the methodology chapter as well as Figure 3.13 which shows the schematic of measurements, and Table 3.7 has the dimensions of the polystyrene blocks used to simulate storage racking.

i. *Temperature Gradient*

Table 6.4 shows the temperature data collected at the 1/3 forwards position for both the empty warehouse and storage racking model set ups. For these tests, a 20W heat mat was used.

Table 6.4 Temperature Data for Different Measurement Points (20W heat mat)

Measurement point	Vertical height (m)	Temperature (°C)	
		20W Empty	20W Storage Racking
1 - bottom	0.04	21.19	22.97
2	0.09	21.58	23.00
3	0.13	21.96	23.11
4	0.18	22.20	23.59
5 - top	0.20	22.49	23.50

The first notable difference between the two models is that the storage racking model had a higher starting temperature value at measurement point 1, 1.8°C higher than the empty model. This is likely due to the polystyrene storage racking promoting an accumulation of heat towards the floor of the model. These results exemplify why stratification tests of storage and distribution warehouses should include storage racking, whether at small or full-scale. Figure 6.3 shows the temperature distribution across the vertical temperature measurement points for both the empty and storage racking warehouse models.

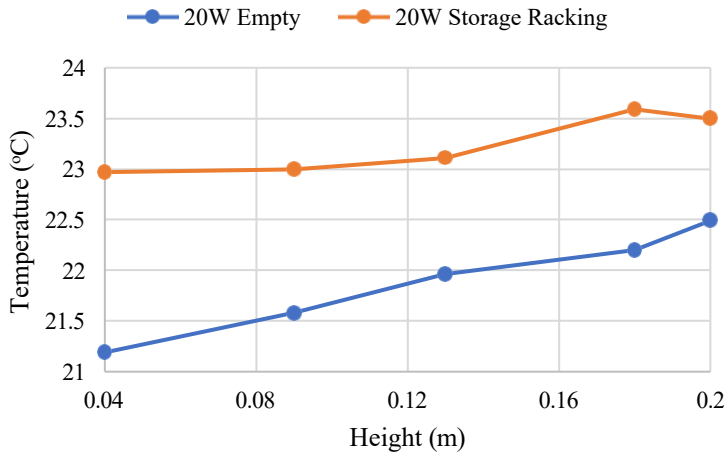


Figure 6.3 Vertical Temperature Distribution in 1:50 Scale Warehouse Model With and Without Storage Racking

The empty warehouse has a much steeper temperature gradient compared to the model with storage racking which implies that there is a quicker temperature change across the height of warehouse. The storage racking test shows that it helps to reduce the level of stratification, however it leads to warmer temperatures at floor level which may cause discomfort in summer seasons. Table 6.5 shows the percentage difference in temperature gradients for these models. A 23% increase in temperature gradient between the empty and storage racking warehouse models quantitively shows how important it is to model this building type correctly, as not doing so will lead to significant inaccuracies in the simulation of airflow and thermal phenomena within the space. The next section looks at a dimensionless number used to predict the onset of natural convection.

Table 6.5 Temperature Gradients for 1:50 Scale Warehouse Model With and Without Storage Racking

	20W Empty	20W Storage Racking	% difference between positions
ΔT(°C)	3.29	4.30	
H(m)	0.20	0.20	
∇T(°C/m)	16.45	21.50	23

ii. Grashof Number

Equation 6.1 in Chapter 6.2.1 was used again to calculate the Grashof number for the small-scale model with storage racking with the required parameters in Table 6.6. The Grashof number for the small-scale empty model in this test was calculated as 3.8×10^6 and the model with storage racking was 5.0×10^6.

Table 6.6 Parameters Required to Calculate Gr Number (20W Heat Mat)

Parameter	20W Empty	20W Storage Racking
g	9.81	9.81
β	0.00343	0.00343
ΔT	3.29	4.30
L	0.20	0.20
μ	0.00001516	0.00001516
Grashof number:	3,800,000	5,000,000

These values both indicate the presence of high levels of buoyancy forces, and therefore stratification. As the Gr number is proportional to the change in temperature, the model with the higher vertical temperature difference resulted in the greater value of Gr. These values will be used in the later Section 6.4.1 to highlight the challenges in analytically predicting stratification compared to full-scale modelling in CFD. The results of this section highlight the importance of including storage racking in thermal modelling of storage and distribution warehouses. For example, the temperature gradient and Grashof number of the model with storage racking was less than half of that of the empty model.

6.2.3 Error Analysis

Error analysis including fractional error and standard deviation analysis was carried out for the PT-100 RTDs and a DataTaker used in the stratification tests.

i. *Fractional Error*

The fractional error ranges from 25-42% dependent on which measured value it is evaluated against where a higher temperature yields lower error. As the fractional error represents the maximum possible error, most of this comes from the datalogger as the PT-100 RTDs used to measure temperature have an accuracy of 0.15°C.

ii. *Standard Deviation*

There are five vertical temperature readings in the stratification tests, so the standard deviation of the raw readings for each of these was calculated for 3600 recordings. Figure 6.4 shows the results for the 7W heat mat test at a distance from the heat source. The standard deviation ranges from 0.03 to 0.47, and the average is 0.24. The first reading at point 1 represents the PT-100 RTD position closest to the floor which could explain the larger error bar as there is likely to be more variation, and the smallest error bar occurs at measurement point 5 which is the highest vertical measurement taken. The remaining points 2-4 represent the middling heights where vertical temperature readings were taken. They also follow a similar trend whereby as the height where the temperature is measured increases, the error bar reduces. This is likely due to greater stability of temperature distribution the further away from the heat source.

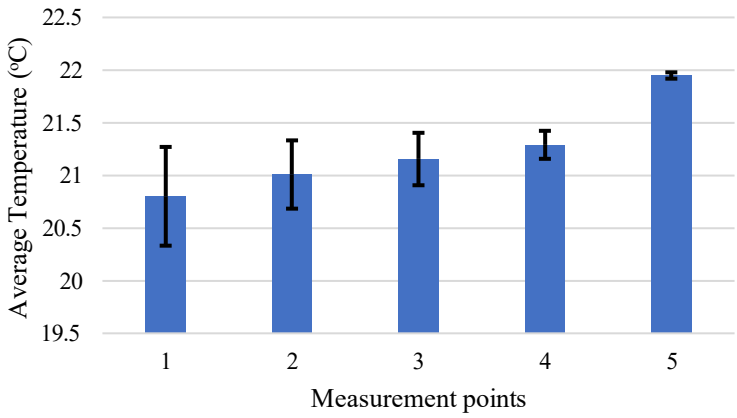


Figure 6.4 Standard deviation analysis of PT-100 RTDs in stratification tests

Overall, the error analysis outcome provides confidence that the temperature readings are reliable and can be used to validate the computational model in the next section.

6.3 Validation of Computational Model

The computational fluids dynamic model of the 1:50 small scale warehouse does not include the DSF retrofit as it is focusing purely on the stratification that arises due to the unique structure. The geometry is 3-dimensional, with a composition of solids representing the MDF shell of the warehouse model and fluid volume representing air. The main boundary conditions are a pressure inlet and outlet, heat source, and adiabatic walls. The same mesh obtained through grid independence analyses in chapter 4 are applied here as the model has not changed, except for excluding the double skin façade and the computational domain as only the fluid volume within the warehouse model is evaluated.

6.3.1 Small-Scale Empty Warehouse Model

This section takes the experimental readings for the 20W heat mat test at a forwards distance from the heat source and compares them to the values obtained in ANSYS fluent as shown in Figure 6.5. The average error between the experimental and numerically derived temperatures for the forwards measurement points for the 20W heat mat test is 2%. As well as visually producing a close match (especially at a height of 0.2m), this reasonable magnitude of error is a good indication that using a boundary condition on the ground floor of the building space is an effective way to model stratification.

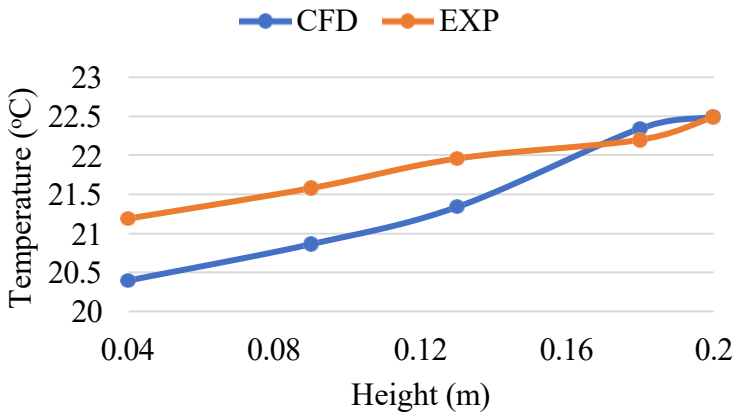


Figure 6.5 Comparison of Experimental to CFD Temperature Data in 1:50 Scale Empty Warehouse

The temperature values obtained in the CFD model produce a slightly steeper gradient, and this is likely due to discrepancies between assumptions in the model and the experimental set- up. To qualitatively demonstrate the impact that a ground-floor heat source can have in a warehouse space, Figure 6.6 below shows the (a) contours of temperature and (b) velocity vectors for the 20W heat mat test. These contours were taken at a mid-section view of the model.

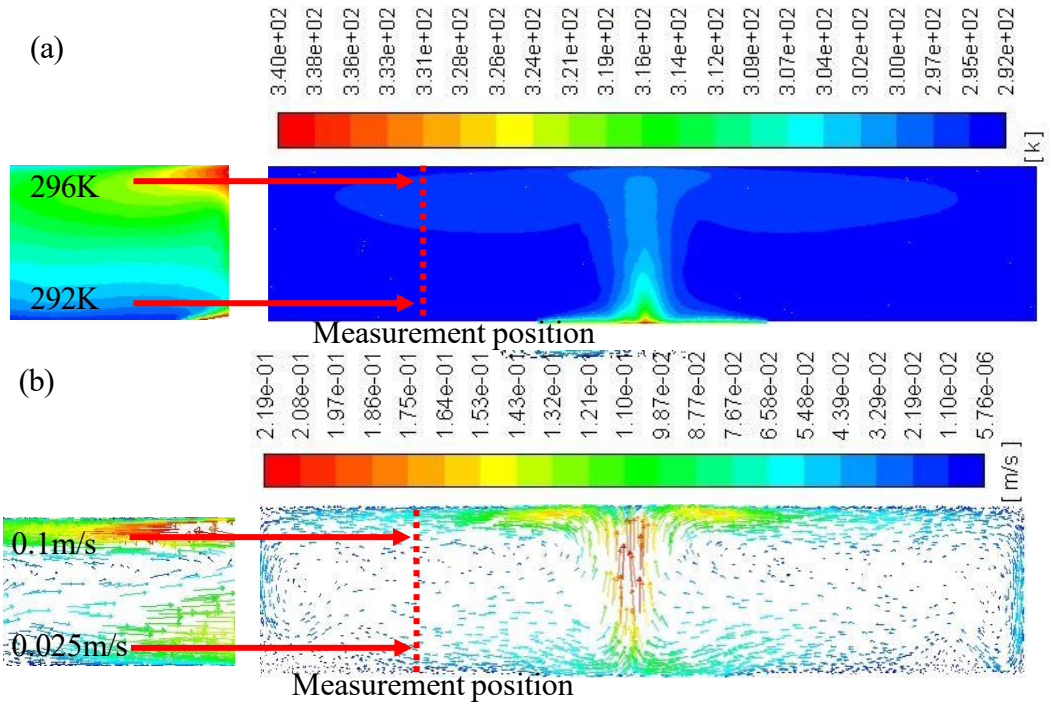


Figure 6.6 Contours of (a) Temperature and (b) Velocity Vectors of 1:50 Scale Empty Warehouse

The temperature contour in Figure 6.6 (a) shows that at a central position directly above the heat source representative of the heat mat, the temperature is highest closest to the ground and decreases with height, denoted by a red colour changing to dark blue. At a distance to either side of this central position, there is the reverse taking place whereby the temperature is ambient and increases slightly towards the top of the model. Similarly, in Figure 6.6 (b), the air velocity is reflective of these changes across the length of the model respective of the heat mat's position. It also shows how the different temperature gradients influence air flow and distribution. For example, there is a stronger air velocity directly above the heat mat and upon meeting the ceiling, encourages airflow across the ceiling height and down the sides of the model. Both these contours demonstrate how the presence of stratification impacts the fluid dynamics within a warehouse space.

6.3.2 Small-Scale Warehouse Model with Storage Racking

The results in this section build upon that of the previous section by comparing the experimental data for the small-scale warehouse with storage racking to the computational fluid dynamics model, as shown in Figure 6.7 below. There is visually a greater difference between the experimental and computational data for this version of the warehouse with storage racking, and this is to be expected as the complexity of the geometry has increased significantly and will affect the thermal phenomena occurring within the space.

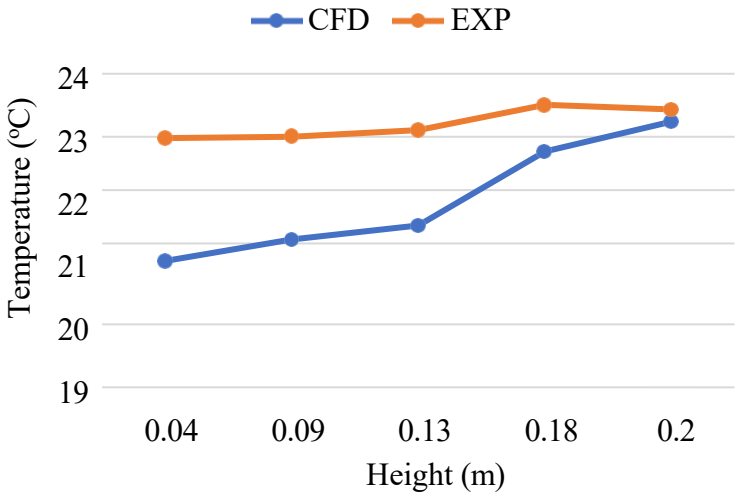


Figure 6.7 Comparison of Experimental to CFD Temperature Data in 1:50 Scale Warehouse with Storage Racking

The average of the errors between each point is 6% and there is a similar trend of temperature increase from vertical heights 0.04m to 0.09m, but the measurements from the CFD model produce a steeper gradient from this point. To highlight how the internal fluid dynamics change with the presence of storage racking in a warehouse space, temperature and velocity vector contours have been taken at the mid-section of the model to capture this across the length of the warehouse. Figure 6.8 displays the impact of storage racking on (a) the internal warehouse temperature, and (b) the internal air velocity.

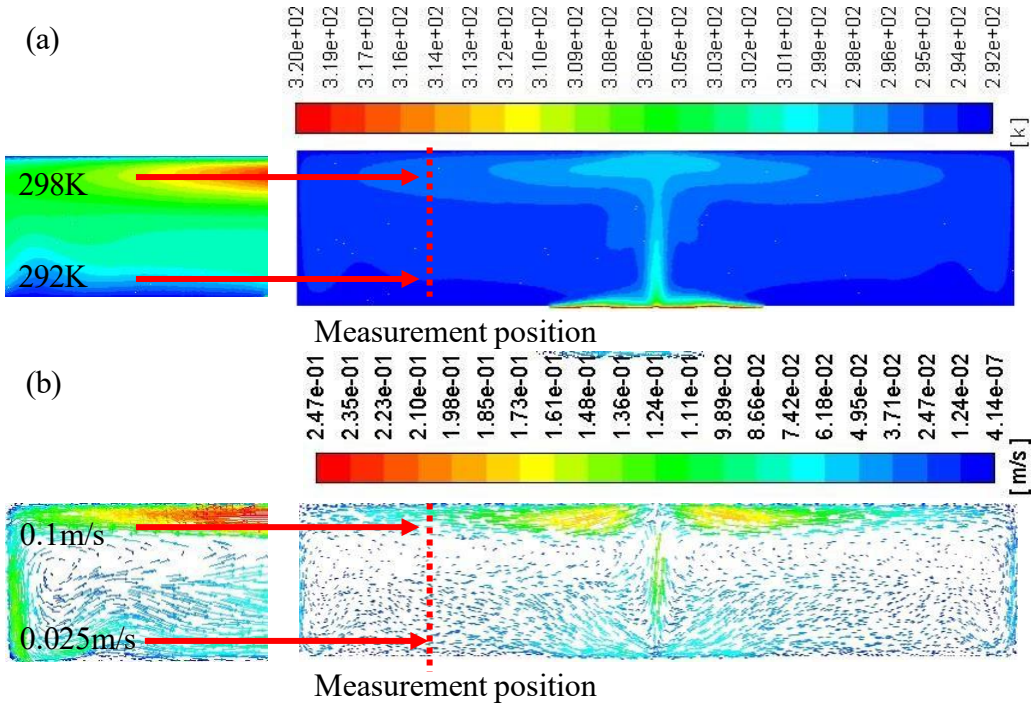


Figure 6.8 Contours of (a) Temperature and (b) Velocity Vectors of 1:50 Scale Warehouse with Storage Racking

Compared to Figure 6.6 in the previous section for an empty warehouse, the main differences

are that there is a higher magnitude of temperature towards the ceiling of the model, and a slightly higher air velocity as a result. The presence of storage racking running across the heat mat is the primary cause of this, reducing the rate of heat dissipation from the heat mat, and contributing to the effects of stratification across the height of the warehouse.

The warehouse model with storage racking has a higher temperature at the maximum vertical position of 24°C which is just over 1 degree more than what was achieved in the empty model. The key takeaway is that the presence of stored goods at height impacts internal stratification but with the consideration that this is a simplification of heat gains in an actual warehouse where the position of heat source, accumulation and distribution of heat gain will be entirely different and bespoke to the specific internal conditions of the warehouse. This is a limitation of publicly available internal warehouse data in research.

6.4 Stratification Modelling of Full-Scale Warehouse

To better understand stratification in warehouses in realistic conditions, thermal analyses of a full-scale version the case study warehouse is needed, starting with a short comparison of estimated and actual Grashof number at full-scale from the 1:50 scale model. The geometry includes the cross-ventilation openings shown in Figure 6.1 to simulate their impact on stratification, for both an empty warehouse and with storage racking. Following CIBSE AM10 guidelines for naturally ventilated buildings, a minimum cooling load of 40W/m^2 [12] (including solar and casual heat gains) is applied to the floor area.

6.4.1 Challenges with Thermal Scaling

One of the difficulties with using a small-scale test of stratification to validate a CFD model is the thermal scaling to a full-scale model. For example, taking the temperature change across the 1:50 scale model height from the previous section, and scaling up dimensionally, the Grashof number at full-scale can be estimated at 4.8x10^{11}. However, when taking the small- scale CFD model and scaling up dimensionally, this yields a much smaller Grashof number at full-scale of 4.5x10^9. The most probable reason for this is that the impact of the heat source's flux of 170W/m^2 is much higher in the 1:50 scale model compared to that in the full-scale model. However, the temperature contour of the midsection of the full-scale warehouse in Figure 6.9 below indicates that thermal stratification does take place, but at a lower magnitude.

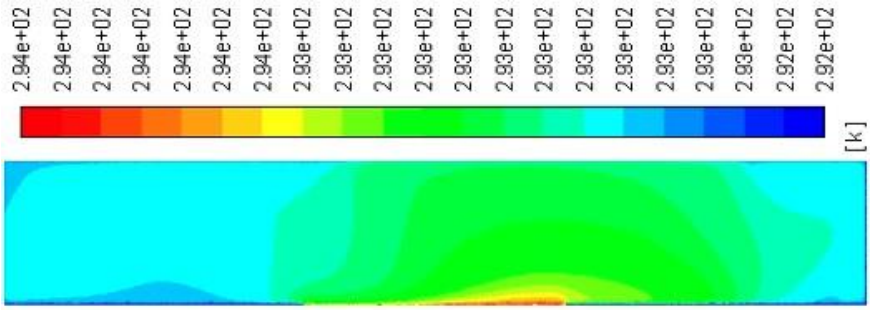


Figure 6.9 Temperature Mid-Section Contour of Full-Scale Warehouse (20W Heat Mat)

6.4.2 Empty versus Storage Racking

The warehouse with and without storage racking was initially modelled with an internal temperature of 18ºC in line with the previous chapter's experimentally validated thermal set-up. Figure 6.10 shows the vertical temperature profiles for the warehouse (a) with and (b) without storage racking.

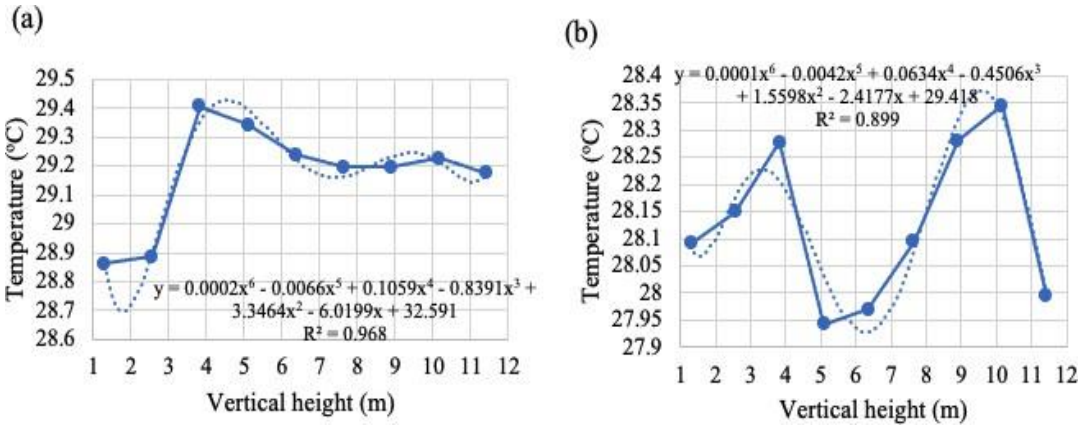


Figure 6.10 Vertical Temperature Profiles for (a) Empty and (b) Storage Racking Full-Scale Warehouse Models

Figure 6.10 (a) shows that at lower heights below 4m, there is a steeper gradient which represents rising warm air followed by a transition downwards to flatter gradient at a height in the approximate range of 7.5-9m. This is the height where the neutral plane exists as the temperature profiles becomes more stable. A polynomial can be approximated to identify a numerical index representative of temperature increase but those created here are likely overfitted to fit the inconclusive trends even if the R^2 value is close to 1. However, the higher order polynomial of 6 is in line with CIBSE AM10 which states that a value of 7 represents the bulk of the temperature increase occurring at higher levels, implying stratification [12]. Figure 6.10 (b) shows a much more complex stratification pattern caused by the presence of several aisles of storage racking spanning the length of the warehouse. Like the empty warehouse, the air is heating up below a height of 4m, and then drops, although more significantly before rising again before reaching a

peak at 10m. As the curve does not level out noticeably, it is hard to identify where the neutral plane exists which presents an issue for ventilation design. There is no literature on this for warehouses with storage racking, and these results show the motive for including such complex structures in ventilation studies.

As the presence of stratification is directly related to vertical changes in air density, promoting buoyancy forces to drive air movement, it is important to assess the pressure and air velocity within the space. Figure 6.11 shows a mid-plane snapshot of pressure at the centre of the warehouse which is (a) empty and (b) with storage racking. The main difference in static pressure across the height of the warehouse is that the model with storage racking experiences a smaller pressure distribution of -2.7 to 0.92Pa compared to the empty model with -3.7 to 1Pa. The 23% reduction in pressure distribution is likely caused by the obstruction to airflow that the storage racking aisles present, and the surface area of physical obstruction will lead to more turbulence, higher drag and friction losses.

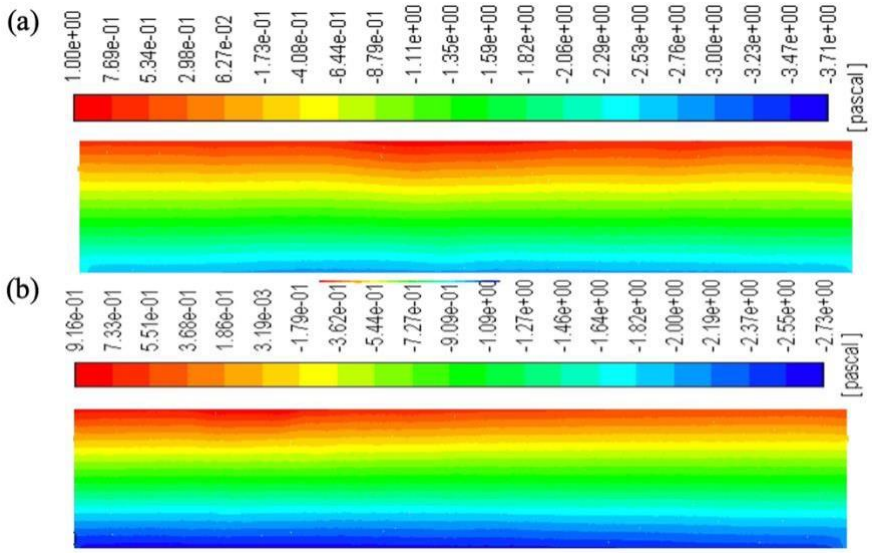


Figure 6.11 Pressure Contours for (a) Empty and (b) Storage Racking Full-Scale Warehouse Models

These phenomena can produce uneven airflow, creating areas with too high or low air velocities, and this can impact the delivery of outdoor air ventilation, indoor air quality and thermal comfort. The next set of figures look at how the presence of storage racking influences the air velocity in the warehouse.

Figure 6.12 shows a mid-plane snapshot of air velocity at the centre of the warehouse which is (a) empty and (b) with storage racking. As expected, the air velocity is higher in the central space for the storage racking simulation as the aisles between the racking will accelerate airflow.

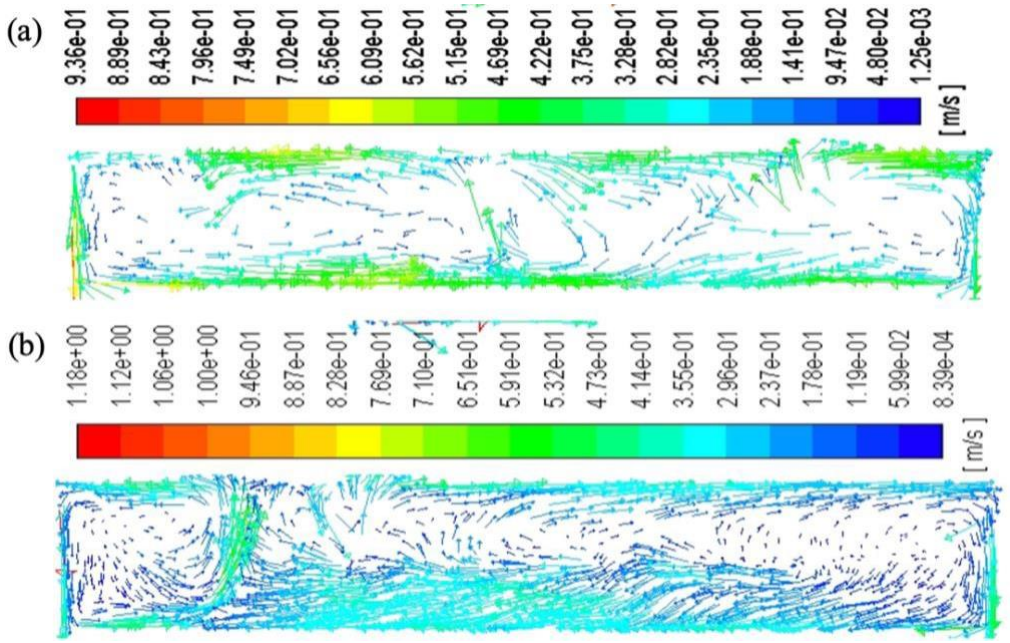


Figure 6.12 Velocity Vector Contours for (a) Empty and (b) Storage Racking Full-Scale Warehouse Models

In terms of circulation, Figure 6.11 (a) shows that above the band of light blue representing air velocity in between storage racking, there is recirculation of air above the height of this whereas the empty warehouse has an airflow pattern promoting air circulation at lower heights. In both cases, the air "sticks" to the ceiling and walls with some flow separation occurring to deliver outdoor air throughout the space. Table 6.7 shows the magnitude of velocity at different heights in the space for both models to quantify the impact of obstruction from the storage racking on internal airflow. The presence of storage racking increases velocity at all heights and therefore is an important considering in ventilation modelling of warehouses.

Table 6.7 Air velocity at Different Heights for An Empty Warehouse and With Storage Racking

Height (m)	Air velocity-Empty (m/s)	Air velocity-Storage Racking (m/s)
0.2 (near ground)	0.25	0.30
2.0 (occupant level)	0.26	0.33
4.5 (storage racking)	0.12	0.25
9 (vent openings)	0.21	0.22

Thermal comfort guidelines such as ASHRAE Standard 55 suggest that indoor air velocity should typically be below 0.2m/s [208]. Based on the values at occupant level, these results are higher by 0.06m/s and 0.13m/s for the empty warehouse and with storage racking, respectively. This evidences that internal environments of warehouses need evaluating in isolation, without energy efficiency measures such as the DSF proposed in this thesis, as so little is understood about these parameters that matter in other building types.

6.5 Chapter Summary

This chapter provides an in-depth overview of how to approach predicting stratification within warehouse spaces. This included conducting small-scale thermal tests of a 1:50 warehouse with and without storage racking to obtain thermal gradients for validation of a computational model, analysis of Grashof number at scale, and computationally modelling stratification in the full-scale case study warehouse with cross-ventilation openings.

6.5.1 Main Findings

For a fully sealed empty warehouse model of 1:50 scale, the difference in thermal gradients between two measurement points either side of the 7W heat mat (179W/m^2) was 4%, indicating a level of symmetry in the space heating. The value of thermal gradient was an average of 14, showing a high level of stratification and further exemplified by a Grashof number of 3.2x10^6. For the comparison between the scale model with and without storage racking exposed to a 20W heat (170W/m^2), the model with storage racking had a temperature 1.78^{o}C higher at a height of 0.20m than the empty model and a thermal gradient difference of 23%. The empty scale warehouse achieved a Grashof number of 3.9x10^6 compared to 5x10^6 for the storage racking model. These results highlight the importance of considering significant obstructions in internal warehouse spaces.

The validation of the CFD models led to an average error of 2% for the empty model, increasing to 6% for the model with storage racking. Both showed similar temperature evolution and therefore a good agreement. Prior to the full-scale modelling of the warehouse with cross-ventilation openings, the case study warehouse was sealed and had a scaled-up flux of 170W/m^2 applied to see if the prediction of Grashof number from the small-scale model was accurate. The predicted Grashof number of 4.8x10^{11} is significantly larger than the actual Grashof number of 4.5x10^9 which highlights the challenges of scaling thermal phenomena.

The full-scale warehouse with cross-ventilation openings had a constant 18^{o}C set to the internal walls, and 40W/m^2 applied to the floor area to normalise heat gains. The empty model has a higher temperature increase between the heights of 3-4m and then stabilises whereas the storage racking model instead sees a temperature drop between 4-5m before increasing again. The vertical pressure distribution in the empty warehouse is large at -3.7Pa to 1Pa compared to 0.92Pa in the presence of storage racking which also has double the velocity difference between ground and ceiling. This study was limited in comparison to previous chapters, but the research

here shows an insight into why modelling an empty space for a warehouse drastically oversimplifies the complex thermal and airflow phenomena occurring.

6.5.2 Limitations and Future Work

The main limitation of conducting a small-scale laboratory test of stratification in a building is the thermal scale effect as the small-scale model may have geometrical differences to the real building as it is a simplified version. Even the slightest difference can influence how the air stratifies, and this is further exemplified by the assumption that casual heat gains (the heat source in this scenario) is normalised against the floor area of the building. Additionally, the 1:50 scale model is made from MDF as it was re-purposed from the wind tunnel test in Chapter 4, and therefore the thermal properties of the building envelope are not reflective of the real building materials.

Whilst this study found that the presence of storage racking does affect internal stratification, its effect might be different in actual warehouses where the source of heat gains will be varied. Regarding future work, the most valuable data to collect is from a real warehouse to understand how the internal structures in the form of storage racking, and changing internal operations influence the fluid dynamics within the space and therefore the vertical stratification. Alongside full-scale testing, a more advanced computational model could be developed to couple the temperature data from the internal warehouse space to help predict when stratification is most likely to occur.

6.5.3 Closing Remarks

As the magnitude of thermal stratification occurring in warehouses is unique to their structural heights, and a singular thermal zone usually unobstructed by typical storey levels, the results in this chapter offer a contribution to the understanding of the complex thermal and fluid interactions across the height. The following, and final chapter takes the findings of all previous results to present a combined ventilation, thermal and energy performance assessment of a DSF warehouse.

Chapter 7

Combined Wind- and Buoyancy-Driven Ventilation, Thermal and Energy Performance of a Double-Skin Façade Warehouse

7.1 Introduction

Double skin facades are popular in building technology research, but the extensive literature review from Chapter 2 highlighted that there is presently no standardised way of assessing the viability of a double skin façade system from a technical, economic, and environmental perspective. This in part is since most current research focuses on the DSF as a standalone building technology, rather than developing it as a retrofit directly integrated with a chosen building type. This led to the theory behind the research in this thesis: 'A building-first approach to designing double-skin facades'. By measuring the performance of a DSF as a function of the building to which it is applied, this conclusion of this thesis offers a new standardised approach to assess both the ventilation and thermal performance of a DSF retrofit when applied to large-space buildings such as storage and distribution warehouses.

This chapter combines the results of the three previous chapters to produce a final computational model and energy analysis tool of a double-skin façade retrofit for storage and distribution warehouses. The analytical tool is used to assess the heat gain/removal in the cavity as a function of combined wind and buoyancy pressure drops, and these values are then normalised against typical seasonal sun hours to determine annual performance. Finally, a simplified feasibility study including electricity savings and carbon reductions, embodied energy and initial investment cost and payback period are conducted to evaluate the commercial viability of the DSF retrofit for storage and distribution warehouses.

The aim of this chapter is to deliver a cohesive ventilation, thermal and energy analysis of a seasonal-adaptive double-skin façade retrofit for large-space storage and distribution warehouses in the UK. The objectives required to achieve this include:

- Validate cross-ventilation in the warehouse with an analytical method
- Combine the experimentally validated wind-only and buoyancy-only CFD models to create a final model capable of assessing ventilation and thermal performance of the DSF warehouse
- Combine the analytical components from previous chapters to produce the final heat gain/removal performance tool and examine energy performance
- Complete an embodied energy analysis and payback period for the DSF retrofit

7.2 Analytical Validation of Cross-Ventilation in Warehouses

In absence of ventilation data from a real warehouse to compare against, ventilation flow rates for combined wind and buoyancy-driven cross-ventilation for the case-study warehouse only (without the DSF) were calculated analytically, utilising a method from literature [209]. These analytical values are then used to validate a computational fluid dynamics model of the case-study warehouse for winter, summer and intermediate seasons. The purpose of this is to provide a reliable model set-up for the final DSF warehouse model. Prior to this, a sensitivity analysis of inlet opening area was conducted to find an optimal level of outdoor air as detailed in Appendix A.6.1. Solar gains have been excluded from this stage of the CFD model development as the primary focus is on buoyancy-driven ventilation arising from a temperature differential across the indoor and outdoor environment, and the local wind conditions for wind-driven ventilation.

7.2.1 Cross-Ventilation and Climate scenario

Figure 7.1 shows the simplified layout of the case study warehouse with level inlet and openings at a height, z, of 9m reflecting the height of openings of the wind tunnel model but at full-scale. The inlet and outlet openings are on the windward and leeward sides of the building, respectively.

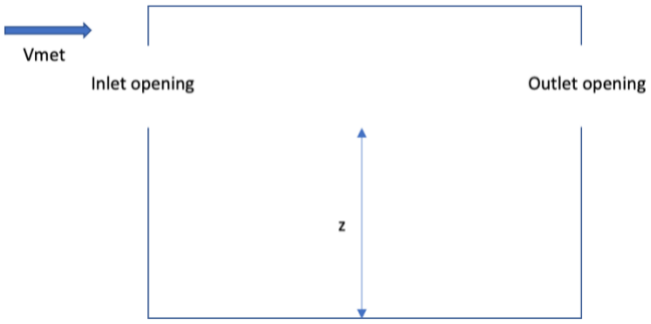


Figure 7.1 Diagram of Cross-Ventilation Scenario

The ratio of the warehouse length to width is 2:1, and it is considered a low-rise building in a semi-urban environment using the pressure coefficient of the windward façade obtained in the atmospheric boundary layer experiment back in Chapter 4. The assumption made here is that the pressure coefficient of the leeward façade is the same magnitude of the experimentally derived windward façade but negative. There are limitations to this in the context of turbulence and fluctuating wind conditions, however the ABL wind tunnel results in Chapter 4 showed that the flow pattern around the warehouse was relatively symmetrical. Table 7.1 has the local climate details which are required in the following calculations where the velocity at height was determined using Equation 3.1 in Chapter 3.

Table 7.1 Coldest Month Meteorological Scenario

Season	External design temp (°C)	Height of opening(m)	Reference Height(m)	Wind shear exponent	Reference Velocity(m/s)	Velocity at height (m/s)
Winter	-4	9	10	0.22	7.22	7.05

7.2.2 Analytical Results

The purpose of this section is to obtain a volumetric flow rate which can be compared against the computational model. This is found by calculating the pressure difference across the inlet and outlet, wind velocity pressure, buoyancy pressure, and the combined wind and buoyancy pressure drop.

i. Pressure Difference Across Inlet and Outlet

The pressure difference across inlet and outlet, P_0, was calculated for level height of the inlet and outlet openings in each season using the following equation which is modified to reflect the two openings with same magnitude of pressure coefficient. The results are below in Table 7.2.

Equation 7.1 Pressure Difference Across Inlet and Outlet

$$\Delta P_0 = 0.5 \cdot \rho \cdot U^2 \cdot (2 \cdot (Cp_{windward} - Cp_{leeward}))$$

Table 7.2 *Pressure Difference Across Inlet and Outlet*

Season	Air density	*Windward Pressure coefficient	*Leeward pressure coefficient	Velocity at height (m/s)	Pressure difference (Pa)
January	1.311	0.6	-0.35	7.05	62
*taken from Table 4.A1.4, CIBSE Guide A [8]					

ii. Wind Velocity Pressure

Equation 7.2 for wind velocity pressure was used to obtain the results in Table 7.3.

Equation 7.2 Wind Velocity Pressure

$$P_{wind} = 0.5\rho U^2 C_p$$

Table 7.3 Wind Velocity Pressure

Opening	Density (kg/m^3)	Site Velocity (m/s)	Pressure coefficient	Wind pressure (Pa)
inlet	1.311	7.05	0.6	20
outlet	1.311	7.05	-0.35	-11

iii. Buoyancy Pressure

Prior to calculating the buoyancy pressures, the change in density is required. For this, an indoor temperature of 18°C is used, based on a BSRIA rule of thumb for light work in an industrial building in both winter and summer [32]. Both equations 7.3 and 7.4 for buoyancy pressure were used to obtain the results in Table 7.4.

Equation 7.3 Density Changes in Buoyancy Pressures

$$\Delta\rho = \frac{\rho\Delta T}{T_E + 273}$$

Equation 7.4 Buoyancy Pressure

$$P_{buoyancy} = \Delta\rho g z_A$$

Table 7.4 Buoyancy Pressure Results

Season	External temp (°C)	Internal Temp (°C)	Temperature difference (°C)	Density (kg/m^3)	Density change(kg/m^3)	Gravity (m/s^2)	Height (m)	Buoyancy pressure (Pa)
January	-4	18	22	1.311	0.107	9.81	9	9.5

iv. Combined Pressure Drops and Volumetric Flow Rate

Equation 7.5 for the combined wind and buoyancy pressure drop, and Equation 7.6 for volumetric flow rate were used to obtain the results in Table 7.5. A standard discharge coefficient value of 0.65 along with an opening (free) area size of 1.25m^2 were applied.

Equation 7.5 Combined Wind and Buoyancy Pressure for Cross-Ventilation

$$\Delta P_A = P_0 - \Delta\rho g z_A + 0.5\rho U^2 C_p$$

Equation 7.6 Volume Flow Rate for Cross-Ventilation (no DSF)

$$Q = C_d A \sqrt{\frac{2\Delta P_A}{\rho}}$$

Table 7.5 Combined Pressure Drops and Volumetric Flow Rate for Cross-Ventilation

Season	Discharge coefficient	Opening area (m^2)	Combined pressure (Pa)	Air density (kg/m^3)	Volumetric flow rate (m^3/s)
January	0.65	1.25	72	1.311	8.5

The calculated volumetric flow rate is 8.5m^3/s and this value will be used to compare with and validate the computational fluid dynamics model of the cross-ventilation scenario in the warehouse.

7.2.3 Validation of Computational Model

The model set-up includes a velocity inlet which has a wind profile matching that in the analytical method, the external domain temperature of -4°C, and the internal walls are set to 18°C with a pressure outlet at the domain exit. Nine measurement points were taken at the inlet opening to obtain air velocity values which can then be converted into volumetric flow rates for comparison against the analytical values. Figure 7.2 shows the main boundary conditions of the CFD model, and the location of measurement points at the windward and leeward openings. Exact coordinates of these are in Appendix Tables A.39 and A.40.

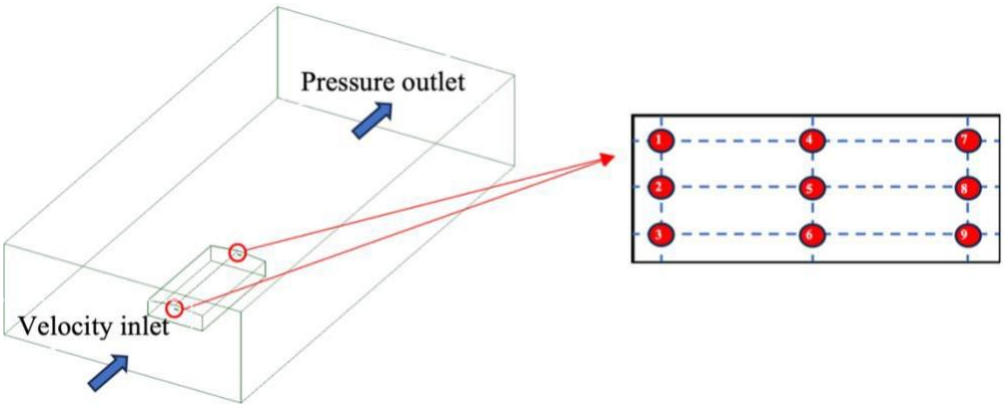


Figure 7.2 Location of Nine Measurement Points in CFD Cross-Ventilation Model

As the inlet and outlet velocities are taken past their respective openings, the volumetric flow rate calculation is simplified, already accounting for discharge coefficient and is found from Equation 7.7. Table 7.6 details the results and comparison between the analytical and CFD models.

Equation 7.7 Volumetric Flow rate from CFD Model

$$Q_{flowrate} = A_{opening} \cdot V_{opening}$$

Table 7.6 Comparison of Volumetric Flow Rate for Analytical and CFD Models

	Analytical model	CFD model
Volume flow rate (m^3/s)	5.3	4.1

The error between volumetric flow rate across the analytical and computation models is 23%, and the difference between inlet and outlet flow rates is 16%. The similarity in the inlet and outlet flow rates indicate that the CFD model is set up correctly and conserves mass. The higher flow rate achieved by the analytical model can be explained by limitations such as assumption of uniform flow, not accounting for turbulence, and geometry simplification. As the wind and buoyancy aspects of the computational model have already been validated experimentally individually, and there is an acceptable agreement between the analytical model of cross-ventilation in the warehouse, this satisfies the validity of the final model in simulating cross-ventilation under combined wind and buoyancy conditions.

Figures 7.3 shows the (a) velocity vector and (b) temperature contours obtained from the computational model and illustrate the level of cross-ventilation achieved in the warehouse. The flow pattern in Figure 7.3 (a) shows that a cross-ventilation scenario is occurring where high-speed air velocity of around 6m/s enters the windward opening, promoting air circulation along the lower levels of the warehouse across to the leeward outlet.

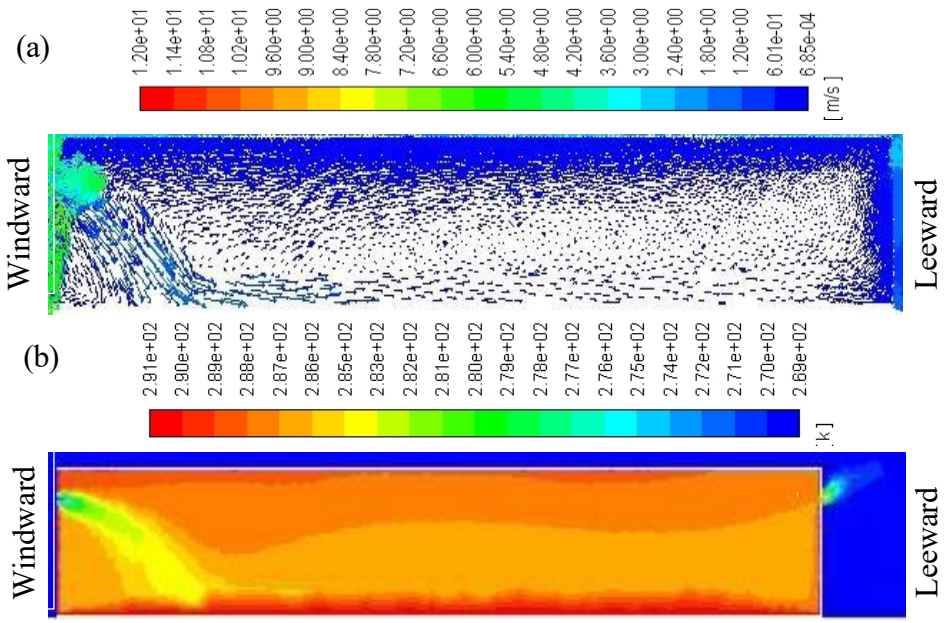


Figure 7.3 Contours of (a) Velocity Vector and (b) Temperature for the Cross-Ventilated Warehouse

Despite the inlet opening having a height of 9m, the flow is forced to lower levels which indicates that the density differentials are being handled properly as the inlet airflow is at a temperature of 269K compared to the internal temperature of 291K. This is confirmed by Figure 7.3 (b) which shows the temperature distribution at the mid-section of the warehouse. Without the DSF, the colder, external air is cooling the internal design temperature to a range of 287K-285K, and the heavier denser air is pushed towards the ground floor, whilst the hotter, less dense air rises to the top of the warehouse roof. This shows the presence of buoyancy which is the other driving force of ventilation in this space and falls in line with the findings regarding stratification in Chapter 6.

Overall, despite the analytical validation method not being as rigorous and comprehensive as real warehouse data in validating the full-scale computational model of the warehouse due to certain assumptions and simplifications, it adds confidence that the CFD model correctly handles wind-driven and buoyancy-driven ventilation when modelled together. This last step of CFD validation has provided the model and set-up for full-scale DSF warehouse in the following sections.

7.3 Wind and Buoyancy Modelling of a DSF Warehouse

This section looks simulating the full-scale DSF warehouse in combined wind and thermal conditions and is a combination of the individually validated wind and buoyancy models from

previous chapters. The assumptions are that no personnel or loading bay doors open in the geometry, and the internal walls are set to the internal design temperature of 18°C. The only openings are the ventilation openings included as part of the cross-ventilation scenario and the DSF retrofit, validated by the wind model in Chapter 4. Figure 7.4 shows a diagram of the warehouse with DSF operations for (a) heating and (b) cooling as well as the positions of three measurements rakes (LHS, middle, RHS) across the span of the facade.

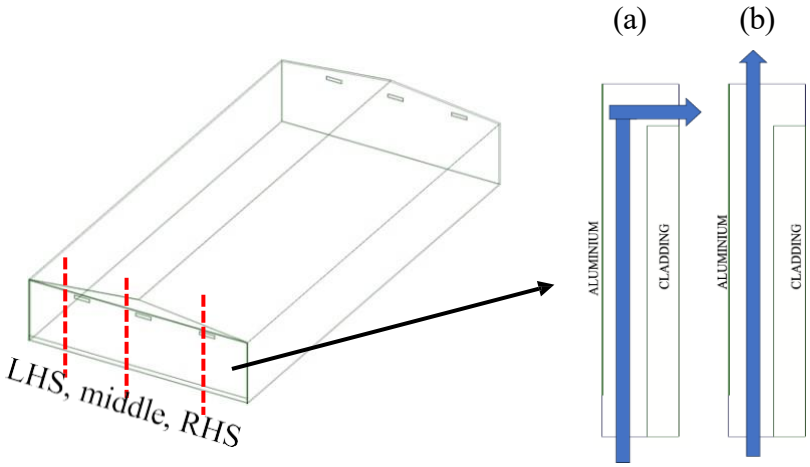


Figure 7.4 DSF Warehouse Measurement Point Locations with (a) Heating and (b) Cooling Configurations

The data collected from the models is from rakes at three different positions in the DSF cavity as shown the above figure, and the coordinates of these points are in Table A.15 in Appendix Section A.3.7.

7.3.1 Thermal Performance of a Fully Open DSF Warehouse

The thermal performance of a full-scale DSF warehouse is evaluated using the same method in Chapter 5 by determining cavity temperature profiles as well as average cavity outlet temperatures under realistic seasonal scenarios using real meteorological data. In this case, the temperature distribution is evaluated for both the length and height of the DSF cavity. As optimisation occurs in the next section, the configuration of the DSF inlet area looked at here is fully open only.

i. *Temperature Distribution Across the Length and Height of the DSF*

Figure 7.5 shows the vertical cavity profiles of temperature for (a) winter, (b) spring, (c) summer, and (d) autumn for three different measurement positions across the length of the cavity.

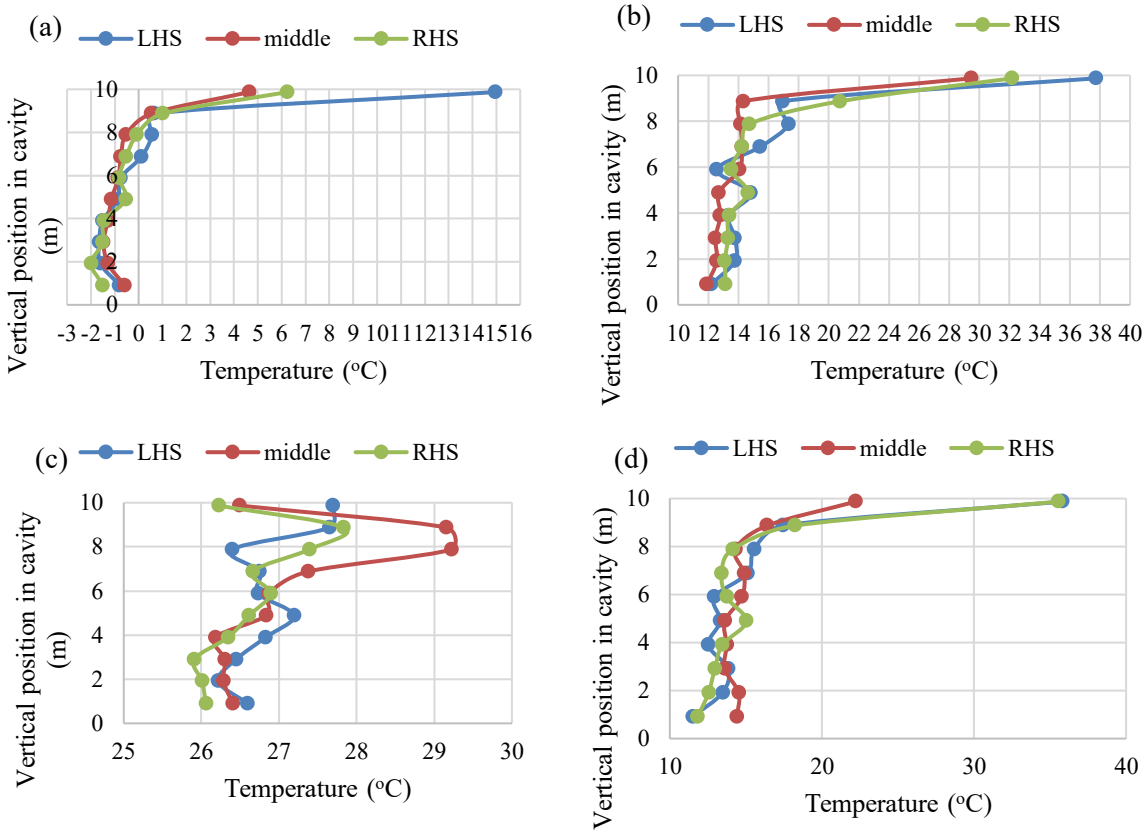


Figure 7.5 DSF Vertical Cavity Profiles of Temperature for (a) Winter, (b) Spring, (c) Summer, and (d) Autumn

When the DSF is in heating operation during Winter, Spring and Autumn, the cavity temperature is generally higher on the LHS side of the DSF cavity, followed by the RHS, and then the middle. The temperature distribution across the length of the DSF cavity is especially important when dealing with large-span buildings such as warehouses as it is wrong to assume that heating will be uniform when exposed to a local environment.

For example, the temperature variation at a cavity height of 9.87m for the typical heating seasons of winter through autumn are 10.31°C, 8.27°C, and 13.61°C for winter, spring and autumn respectively. The general heating trend is similar from DSF inlet to a height of around 8m, and then heating capacity increases significantly. This differs to the cooling operation of the DSF in the summer season whereby the overall magnitude of heating in the cavity due to the stack effect is much smaller and expelled out the top of the cavity rather than into the internal warehouse space. The temperature variation at 9.87m across the length of the DSF in summer is only 1.20°C, and whilst there is a similar trend to the heating operation with the LHS being the warmest, it is then the middle location followed by the RHS.

To visually interpret the impact of the stack effect on cavity pre-heating throughout the year in a

temperate climate such as the UK, Figure 7.6 shows the temperature contours of a side-profile of the DSF in (a) winter, (b) spring, (c) summer and (d) autumn.

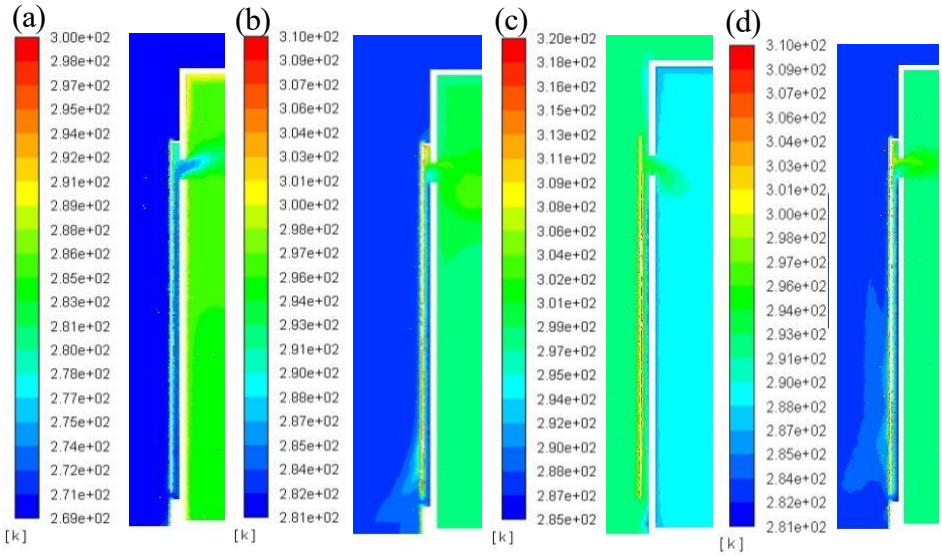


Figure 7.6 Temperature Contours of the DSF Cavity for (a) Winter, (b) Spring, (c) Summer, and (d) Autumn

The case study warehouse was modelled with a constant temperature of 18°C on the internal walls, in all seasons, to reflect the upper end of design guidelines of thermal comfort in warehouses and to reflect how the DSF might work to offset the demand of an existing HVAC system. In winter (a), spring (b) and autumn (d), there is a strong temperature differential across the DSF represented by the dark blue outside, and bright green internally. The DSF does not significantly alter the internal temperature in the intermediate seasons depicted by a constant colour gradient at the top of the DSF cavity into the warehouse space, however the winter scenario shows that the DSF is cooling the internal space. If this were to operate as a pre- heating system, the DSF might be ducted to an air-handling unit to supply this level of heating which can be topped up by the mechanical system, reducing the overall energy consumption to meet the demand. This is discussed further in the next section where the minimum acceptable internal temperature is queried as warehouses in the UK are largely unconditioned and do not deliver 18°C of space heating. The DSF in cooling operation for the summer season in Figure 7.6 (c) does show a small amount of heating denoted by the green entering the blue internal space, however it does cool down the outer skin of the DSF, in red, by expelling most of this heat out the top of the cavity.

ii. Does the DSF Satisfy Internal Thermal Requirements of the Warehouse?

Table 7.7 shows the average level of heating that occurs at a height of 9.87m in the DSF cavity whether in heating or cooling operation for the four seasons.

Table 7.7 Cavity Temperature at Height of Inlet to Warehouse

Season and mode	External design temp (°C)	Temp at 9.87m (°C)	Pre-heating in DSF cavity (°C)
Winter (heating)	-4	8.6	12.62
Spring (heating)	10	33.1	23.13
Summer (cooling)	25	26.80	1.80
Autumn (heating)	10	31.20	21.20

With the storage and distribution classification of warehouses, the primary concern is delivering the lowest level of heating that provides frost protection of water sprinkler systems, rather than the usual higher thermal comfort standards seen in offices or retail spaces. This value is a minimum of 4°C for the UK according to fire regulations [210]. Even though the case study warehouse has been modelled as incorporating internal design temperatures in line with thermal comfort of warehouse workers, at a baseline standard, the DSF can deliver temperatures higher than the minimum required for anti-frost of sprinkler systems when exposed to average vertical solar irradiance of 300W/m^2 seen commonly in all four seasons.

The DSF in winter, when exposed a local wind and thermal environment, meets the requirements of the anti-frost protection, and can provide 70% of the heating required to reach an internal design temperature of 18°C. In Spring and Autumn, the DSF not only exceeds the anti-frost level but also surpasses the 18°C internal temperature thermal comfort requirement by around 20%. Lastly, the DSF in Summer shows it serves as a thermal buffer by keeping heating within the cavity less than 2°C, and by allowing for increased airflow at the south- facing façade in warmer temperatures, an increased convective heat transfer provides an element of local cooling which can help to preserve the goods and environment within the warehouse. It is important to note that these results for the fully open configuration of the opaque aluminium double skin façade only, and not the final and optimised configuration for each season. The next section looks at the ventilation that the full-scale DSF can provide to the warehouse in combined wind and thermal conditions.

7.3.2 Ventilation Performance of a Full-Scale DSF Warehouse

The ventilation performance of a full-scale DSF warehouse is evaluated by determining cavity velocity profiles as well as average cavity outlet velocity under realistic seasonal scenarios using real meteorological data. This data, like the previous section, was also collected for a fully open DSF configuration only. The airflow distribution across the length and height of the DSF cavity both quantitively, and qualitatively is assessed in this section, as well as the pressure coefficients of every façade within the warehouse building envelope which are compared to CIBSE guidelines.

i. *Airflow Distribution Across the Length and Height of the DSF Cavity*

Figure 7.7 shows the vertical cavity profiles of air velocity for (a) winter, (b) spring, (c) summer, and (d) autumn for three different cavity positions, titled LHS, middle, and RHS.

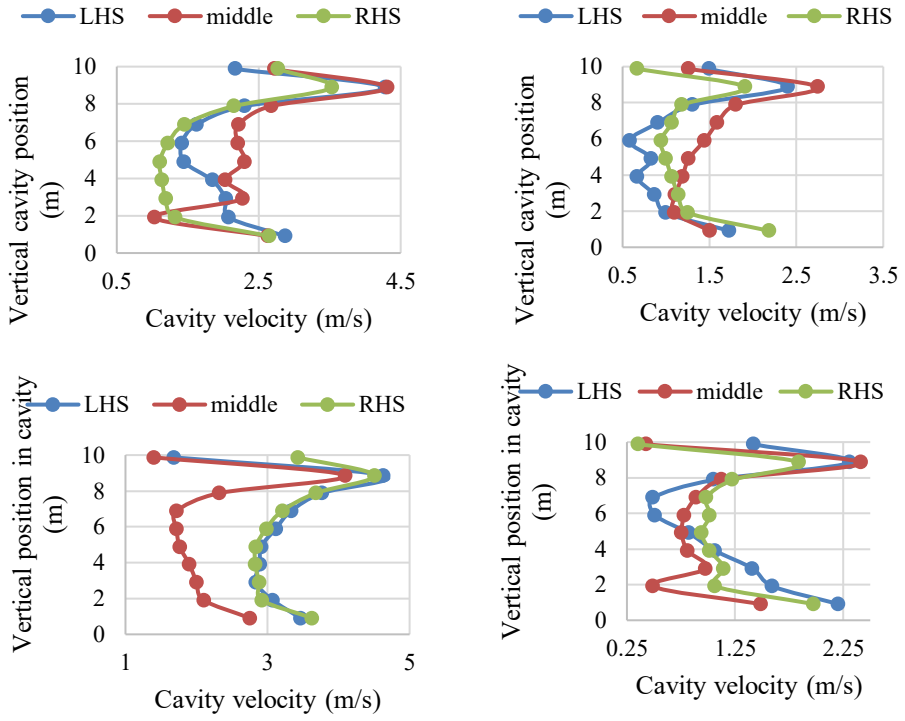


Figure 7.7 DSF Vertical Cavity Profiles of Velocity for (a) Winter, (b) Spring, (c) Summer, and (d) Autumn

In all four seasons, the air velocity in the cavity peaks at around 9m, and then reduces and this is due to the presence of the inlet opening to the warehouse at this height, with the end of the DSF cavity being closer to 10m. Figure 7.7 (c) shows the results for the open-top DSF cavity in cooling mode for summer and shows that the general relationship between height and velocity is almost parabolic between 0 and 9m. This suggests recirculation or complex flow and shows that air enters at a higher speed at the bottom inlet but then perhaps slows due to friction losses or resistance, before accelerating again towards the height of the inlet into the warehouse or outlet at the top of the cavity. The other seasons in (a), (b), and (d) have less refined curves due to increased complexity of flow that would occur within a closed-top cavity. The LHS and RHS measurements in all seasons show a greater similarity of velocity evolution compared to the middle position.

Figure 7.8 shows the velocity vector contours of a side-profile of the DSF in (a) winter, (b) spring, (c) summer, and (d) autumn to capture how airflow moves through the DSF cavity where the dashed line represents the DSF outer skin and interface at the environment.

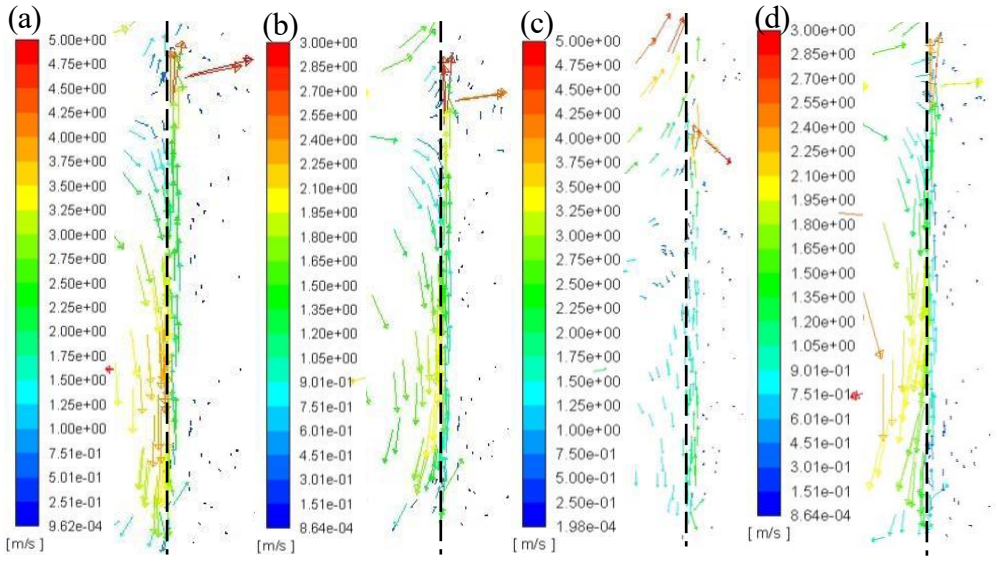


Figure 7.8 Velocity Vector Contours of the DSF Cavity for (a) Winter, (b) Spring, (c) Summer, and (d) Autumn

In all seasons, air enters at the bottom where the DSF inlet is and flows upwards through the vertical cavity as depicted by the arrows on the right-hand side of the dashed line whilst the external wind experiences flow separation towards the top of the DSF cavity and promotes recirculation outside the DSF. The next section looks at taking the average cavity velocity across these three positions at the inlet height of 9.0m to determine whether there is sufficient flow for outdoor air ventilation or even cooling.

ii. Does the DSF Satisfy Ventilation Requirements of the Warehouse?

The baseline scenario that the results in Table 7.8 have been prepared for are that the DSF cavity inlet is fully open, and all three warehouse inlet openings are also fully open and designed with no grilles. As a result, these values are the maximum possible level of outdoor air that can be delivered for the specified reference wind speed at building height.

Table 7.8 Outdoor Air Delivery at Height of Inlet to Warehouse

Season and mode	Wind speed at building height (m/s)	Velocity at 9.87m (m/s)	Total Area of 3 inlets (m^2)	Volumetric flow rate (m^3/s)	Outdoor air (L/s)
Winter (heating)	7.22	4.04	3.75	15.15	15000
Spring (heating)	4.72	2.35	3.75	8.81	8800
Summer (cooling)	7.78	4.41	3.75	16.54	17000
Autumn (heating)	3.60	2.19	3.75	8.21	8200

The constraints of this study are taking the upper limit of generic ventilation standards in the UK of 12L/s/person for maximum wind speeds in winter and summer, average wind speeds in spring and autumn, a fully open DSF cavity inlet and three fully open inlets of 2m x 0.5m dimensions. The outcome is the DSF can deliver enough outdoor air to satisfy between 680 and 1350 people which is 2-3 times the requirement of the occupancy in the case study warehouse. As a result,

this is too high, and would lead to issues with thermal comfort, therefore highlighting the need for optimisation – not only of the opening to the DSF cavity, but also how the DSF works in tandem with the ventilation inlets on the warehouse façade. This will be explored later in Section 7.3.

Considering the magnitude of ventilation delivered from cross-ventilation openings, or the DSF, it should be discussed at this point if the existing infiltration rate alone is sufficient to deliver the occupancy ventilation requirements due to the sheer size of warehouse volumes. Referencing Table 3.1 in Chapter 3, the number of occupants for the case study warehouse volume of 25920m^3 is estimated at 25 people with an infiltration rate of 0.4ACH. This translates to 288L/s delivered from infiltration which would almost satisfy the total occupancy ventilation requirements of 300L/s. However, as illustrated in Chapters 5 and 6, the purpose of ventilation in warehouses is not confined to delivering outdoor air for occupancy ventilation. Other needs for ventilation include natural destratification, cooling and the recirculation of air in a space that is likely to experience a lack of mixing across height. Further, in the broader context of airtightness the validity of the infiltration rate of 0.4ACH from CIBSE for modern warehouses is debatable. For example, the UK regulations Part L state new non-dwelling buildings should achieve an air permeability of 8.0$m^3/h/m^2$ at 50Pa, but there is industry reporting of modern warehouses achieving values as low as 0.33$m^3/h/m^2$ at 50Pa[13],[24]. Therefore, it is still uncertain whether a warehouse occupancy ventilation need can be met by infiltration alone, especially if they are extremely airtight.

iii. Pressure Coefficient Data for Double Skin Facades

Figure 7.9 shows a schematic of the other facades and how they are labelled for this analysis.

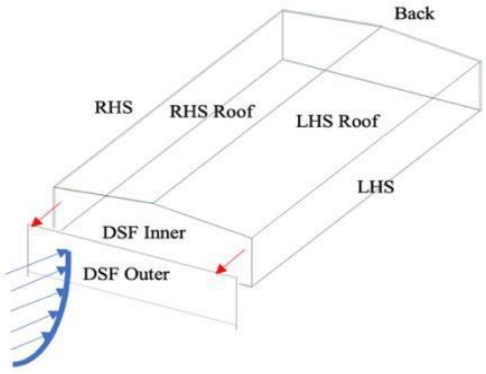


Figure 7.9 Wind Direction with Labelled Facades of DSF and Warehouse

The case study warehouse used in this thesis has an aspect ratio of length-to-width of 2:1 so the pressure coefficient (Cp) data, except for the DSF inner skin, which is internal pressure, can be

compared to the values provided by CIBSE Guide A Table 4.A1.4 [8]. Table 7.9 shows the results of the pressure coefficients for the different facades exposed to different wind speeds in the various seasons along with CIBSE's data for an exposed, sheltered or highly sheltered environment.

Table 7.9 Comparison of Cp with CIBSE Data [8]

Pressure Coefficient	DSF outer	DSF inner	LHS	RHS	Back	LHS Roof	RHS Roof
CFD January (7.22m/s)	0.61	0.59	-0.14	-0.14	-0.14	-0.16	-0.16
CFD April (4.72m/s)	0.26	0.29	-0.25	-0.25	-0.22	-0.01	-0.01
CFD July (7.78m/s)	0.33	0.18	-0.07	-0.07	-0.07	-0.07	-0.07
CFD October (3.6m/s)	0.22	0.26	-0.26	-0.26	-0.24	-0.01	-0.01
CIBSE exposed	0.60	N/A	-0.50	-0.50	-0.35	-0.80	-0.80
CIBSE sheltered	0.40	N/A	-0.35	-0.35	-0.30	-0.60	-0.60
CIBSE highly sheltered	0.18	N/A	-0.20	-0.20	-0.20	-0.41	-0.41

The reference wind speeds for January and July were taken as maximum values recorded in the meteorological period in 2023 whereas the average wind speeds were applied for the intermediate seasons of April, and October. There is a general trend of the outer and inner skins of the DSF being positive throughout the seasons and taking an average would place a similarity with the CIBSE sheltered Cp for the windward façade. The other facades are generally negative April through to October for wind speeds of 4.72m/s, 7.78m/s and 3.60m/s, respectively but are all positive in January at a wind speed of 7.22m/s. This is unexpected but can be explained by flow theory where perhaps this wind speed falls within the critical speed range for reattachment causing the flow to reattach temporarily or partially compare to the much lower and slightly higher wind speeds where the flow might be more stable and fully separated, producing negative pressures. These findings highlight the importance of obtaining real pressure coefficient data from a full-scale DSF on a warehouse. The next section aims to incorporate a level of refinement into the DSF warehouse by considering the optimisation of the seasonal-adaptive openings and warehouse inlet openings.

7.4 Optimisation of the Seasonal-Adaptive and Inlet openings

The key technical novelty of the DSF retrofit is the seasonal-adaptive openings in the cavity, introduced in Figure 1.8 in Chapter 1. This section looks at the optimisation of these different types of openings for winter, summer and intermediate seasons for the DSF warehouse to find the best performing openings. The previous sections have shown that having a fully open cavity does not always best serve the thermal or ventilation demands of the warehouse, so it is essential to incorporate some level of control. The following sub-sections include an overview of the relationship between airflow rate and temperature in the DSF cavity, and average values for all tested configurations of the DSF with suggestions of which is optimal for the different seasons. It goes a step further to suggest which inlet opening on the inner skin side of the DSF (warehouse

façade) should be used in conjunction with the DSF inlet configurations, denoted in Figure 7.10 to use as a key for the results in this section.

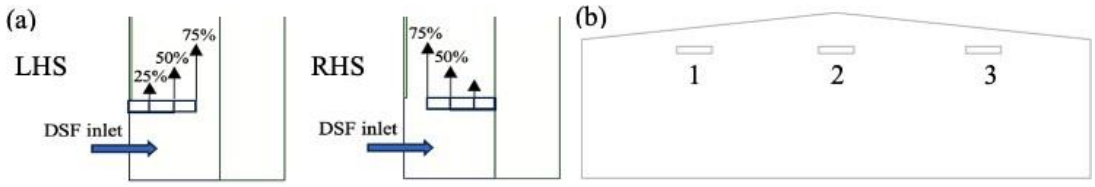


Figure 7.10 Key for (a) DSF Inlet Configurations and (b) Warehouse Inlet Openings

7.4.1 The Inverse Relationship Between Airflow Rate and Heating

An analysis of different opening configurations in the DSF cavity for the four seasons resulted in a reoccurring relationship between the air velocity and temperature. Figure 7.11 shows the plots of velocity against temperature for (a) winter, (b) spring, (c) summer and (d) autumn where each point represents a different DSF inlet configuration (labelled).

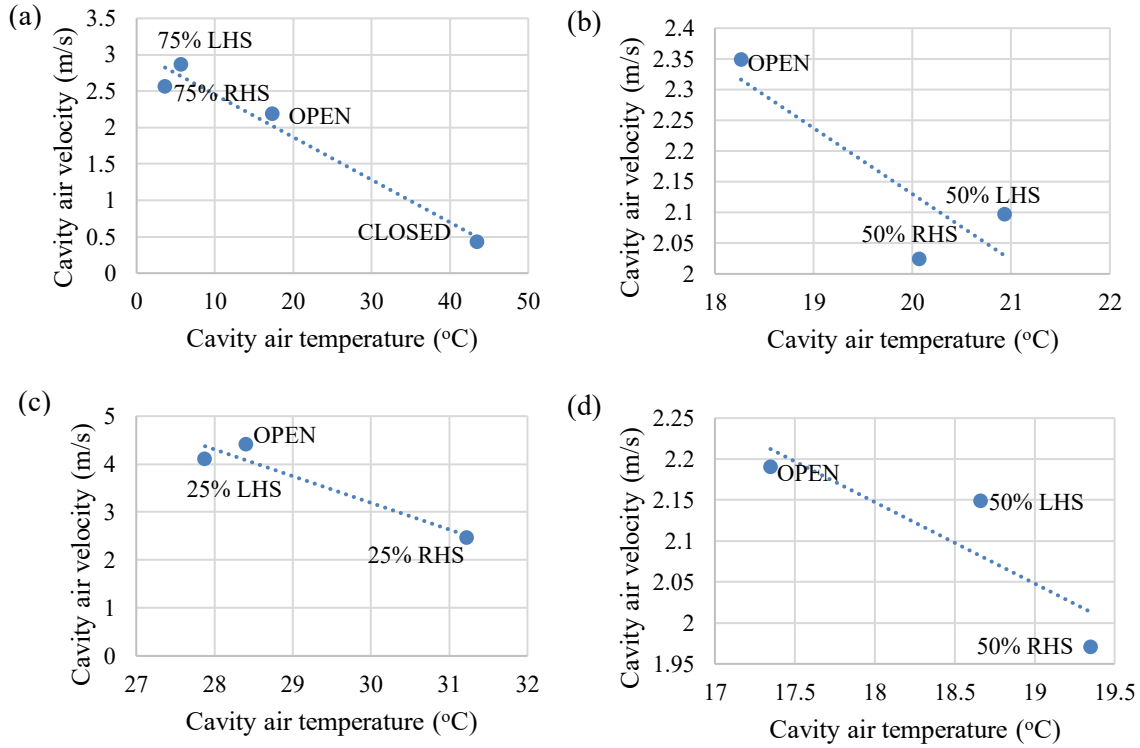


Figure 7.11 Relationship between Airflow Rate and Heating for (a) Winter, (b)Spring, (c) Summer, and (d) Autumn

The gradient of each of these trendlines indicates how sensitive the temperature in the cavity is to the air velocity whereby the steepest occurs in Figure 7.11 (c) with a gradient of -0.5569. This is the results for a fully open, 25% LHS and 25% RHS closed cavity in the summer cooling mode with an open-top cavity. The lowest gradient occurs in winter in Figure 7.11 (a) with a value of -0.06, followed by Autumn with -0.10, and then Spring with -0.11. The overall range of gradient is quite high at 0.50 which proves that different configurations in different seasons lead to varying

results and analysis should be done to determine the optimal performance. In terms of optimisation, the steeper gradient in summer is in line with expecting that a higher airflow is effective at reducing heating, and therefore a fully open cavity is most applicable. Conversely, in winter the best configuration for maximum heating capacity is a closed cavity. The Spring and Autumn seasons produced very similar gradients of less than 7.5% difference and showed that whether higher airflow or more heating is required, it can be configured in such a way to suit either demands. This type of gradient analysis could be used to develop predictive models or control algorithms in future work.

7.4.2 Airflow and Temperature Distribution Within The Cavity

Figure 7.12 shows the airflow and temperature distribution across the cavity for different DSF inlet configurations in (a) winter, (b) spring, (c) summer, and (d) autumn.

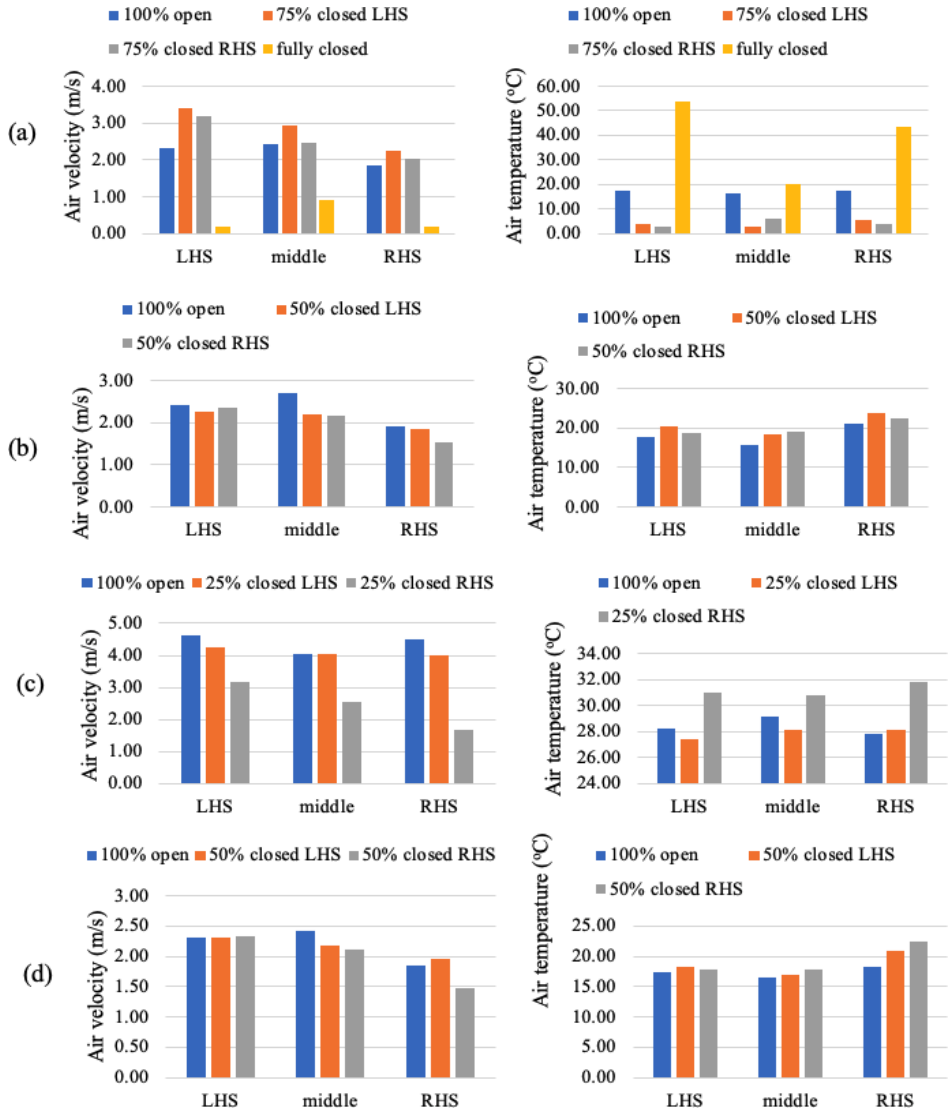


Figure 7.12 Average Velocity and Temperature for Different Openings in (a) Winter,(b) Spring, (c) Summer, and (d) Autumn

The figure can be used to balance the ventilation/cooling and heating needs and identify which opening configuration of the DSF inlet best serves the different demands throughout the year. For example, Figure 7.12 (a) shows that the inverse relationship between airflow rate and heating capacity is most prevalent in winter conditions for all DSF configurations, but especially when it is fully closed where the cavity velocity is low at 0.20-0.90m/s and the cavity temperature is highest at 16-17^{o}C. The intermediate seasons of spring and autumn in Figure 7.12 (b) and (d) have similar results and indicate that the RHS of the cavity yields the lowest air velocity compared to the middle and LHS positions. This is important when it comes to placing ventilation inlets from the DSF cavity to the adjacent warehouse. In terms of the opening percentage of the DSF inlet, these results indicate that closing the inlet closer to the inner skin of the DSF, or the warehouse, leads to lower cavity velocities across all seasons. This suggests that there is value in seasonal-adaptive openings that work to "control" convective heat transfer rates at either the outer skin or inner skin side of a double skin façade cavity. As the position of the measurements were taken in line with the position of the three inlet openings to the warehouse (depicted in Figure 7.10 (b) at the start of this section), the optimal opening placement can be determined. Table 7.10 shows the results based on the data above.

Table 7.10 Optimal DSF Heat Mode and Inlet Opening

Season	Primary demand	Optimal DSF Inlet Configuration	Optimal Warehouse Inlet Configuration
Winter	Heating	Fully closed	RHS only
Spring	Heating/cooling	100% or 50% open	RHS for heating, middle for cooling
Summer	Cooling	Fully open	Middle, or all
Autumn	Heating/Cooling	100% or 50% open	RHS for heating, middle for cooling

What this indicates is that the three inlet openings on the warehouse are appropriate, and either one, all or none can be open dependent on the demands of the warehouse and the external environmental conditions. Whilst this section has shown the importance of having control over the depth the cavity, the next section looks at how the length of the DSF inlet opening spanning the entire facade and overall area can impact ventilation requirements.

7.4.3 Using the Continuity Equation to Optimise the DSF Inlet Dimensions

The original cross-sectional area of the DSF is 36m x 0.2m led to oversized ventilation rates in previous sections which could cause issues in the internal space, therefore an optimisation of the DSF inlet area is required to best serve the warehouse's outdoor air (and cooling) needs. This involves using the continuity equation as there are two sets of openings involved, the DSF inlet and the warehouse inlet openings.

Equation 7.8 Continuity Equation

$$Q = A_1 \cdot V_1 = A_2 \cdot V_2$$

In Equation 7.8, Q is the minimum require volumetric flow rate in the space, A_1 is the optimised area of the DSF inlet, V_1 is the known air velocity at DSF inlet, A_2 is the area of the warehouse inlet and V_2 is the velocity of air at the warehouse inlet. Following the 2021 update to Part F of building regulations [11] which states that for non-dwelling buildings the ventilation rate is 10L/s/person or 1L/s/m^2, where the largest should be applied, the minimum volumetric flow rate can be determined knowing that the warehouse has a floor area of 2592 m^2 (36m x 72m):

Equation 7.9 Calculated Volumetric Flow Rate

$$Q = \frac{(Floor\ area\ \cdot 1L/s)}{1000} = \frac{(2592\ \cdot 1L/s)}{1000} = 2.59\,m^3/s$$

Now, the velocity required at the warehouse inlet can be calculated where there are three openings of 1.25m^2 area each:

Equation 7.10 Calculated Air Velocity at Inlet Opening to Warehouse

$$V_2 = \frac{Q}{A_2} = \frac{2.59}{3.75} = 0.69m/s$$

Finally, the area of the DSF inlet to meet these minimum ventilation requirements can be determined for each season with the results in Table 7.11.

Table 7.11 Optimised Area of Inlet Opening to Warehouse

Season	Velocity at inlet (m/s)	Optimised area (m^2)	Dimensions (m x m)
Winter	2.72	0.95	4.76 x 0.2
Spring	1.81	1.43	7.16 x 0.2
Summer	3.28	0.79	3.95 x 0.2
Autumn	1.89	1.37	6.85 x 0.2

These results show that, on average, for sufficient DSF inlet velocities between 1.81-3.28m/s, the actual inlet opening area required can span less than 20% of the original length of the DSF at 36m. As the velocity range does not include no wind conditions, this does not mean that these are the optimised DSF inlet openings for all wind speeds and can only be used for these specific meteorological scenarios. For example, a much lower air velocity of 0.5m/s would require an area of 5.18m^2 and at a fixed cavity depth of 0.2m , this requires a length of just under 26m which is over 70% of the original length of the DSF façade.

To conclude, this analysis has shown that for a cavity depth of 0.2m, it is possible that a large portion of the full-scale length is open to deliver the minimum outdoor air requirements. If the DSF was applied to a real warehouse as a pilot study, future work could investigate how to facilitate these different inlet opening areas depending on external wind speeds. The next section looks at the combined wind and buoyancy analytical tool for determining heat gain and removal of the DSF.

7.5 Combined Wind and Buoyancy Analytical Tool

The combined wind and buoyancy pressure driving the airflow in the DSF is calculated from Equation 7.12, and the results for this are in Table 7.12 with supplementary data in Appendix A.6.4. To obtain more realistic values, a friction loss should be applied using the Haaland and Darcy-Welsbach equations back in Chapter 3 (Equation 3.5) and the calculations for these are also in Appendix Tables A.45 and A.46.

Equation 7.11 Combined Wind and Buoyancy Pressure for DSF

$$\Delta P_{total} = \frac{1}{2}\rho v^2 (Cp_{outer} - Cp_{inner}) + \rho g H \left(\frac{1}{T_{out}} - \frac{1}{T_{in}}\right)$$

Table 7.12 Combined Pressure for all DSF Seasonal Configurations

DSF Inlet Opening		Pwind (Pa)	Pbuoyancy (Pa)	Ptotal (Pa)	Friction (Pa)	Pfinal (Pa)
Fully open	Winter	0.10	41	40.78	2.04	38.74
	Spring	-0.06	-7.6	-7.64	0.76	-8.39
	Summer	0.96	-0.28	0.67	2.51	-1.84
	Autumn	-0.09	-7.4	-7.46	0.73	-8.19
25% LHS closed	Summer	0.50	-0.83	-0.34	1.94	-2.28
25% RHS closed		1.14	-0.84	0.30	0.65	-0.35
50% LHS closed	Spring	-1.01	-5.67	-6.68	0.31	-6.99
	Autumn	-1.21	-5.04	-6.24	0.30	-6.55
50% RHS closed	Spring	-0.74	-5.44	-6.18	0.47	-6.66
	Autumn	-0.82	-5.24	-6.07	0.32	-6.38
75% LHS closed	Winter	1.35	47.35	48.70	0.69	48.00
75% RHS closed		1.55	58.42	59.97	0.73	59.24
Fully closed	Winter		30.35	30.35	0.04	30.30

These results show that the dominant driving force within the DSF cavity in all seasons and all inlet opening configurations is buoyancy, as indicated by a higher magnitude compared to wind pressure. The buoyancy pressure ranges from -7.6Pa to 58Pa whereas the wind pressure ranges from -1.2Pa to 1.5Pa. This is expected given that the presence of the DSF outer skin shields the DSF inlet and will considerably reduce the volume of airflow entering with the same surface area that is exposed to solar irradiance.

The change in sign to negative for most of the opening configurations in all seasons except for fully open (winter), 75% LHS/RHS closed (winter), and fully closed (winter) shows a change in direction of flow. Having flow exit at the inlet can be beneficial to avoid overheating in the cavity in summer or warm conditions and shows that for external ambient temperatures between 10°C and 25°C, pre-heating in the cavity is lower compared to more extreme temperatures of -4°C. However, there is still a presence of airflow which can be useful for ventilation and cooling by increasing the convective heat transfer rate at the warehouse façade. To translate these pressure drops to estimates of heat gain/removal in kW and a metric of energy performance, the volumetric flow rate and mass flow rate are calculated the same way as before in Chapters 4, Section 4.5 and 5, Section 5.5. Finally, the heat gain/removal can be approximated in Table 7.13.

Table 7.13 Heat Gain/Removal for all DSF Seasonal Configurations

DSF Inlet Opening		Vol. flow rate (m^3/s)	Mass flow rate (kg/s)	Heat (kW)
Fully open	Winter	36.72	46.23	586
	Spring	17.29	21.26	495
	Summer	8.20	9.83	18
	Autumn	17.09	21.00	448
25% LHS closed	Summer	9.13	10.94	32
25% RHS closed	Summer	3.57	4.27	27
50% LHS closed	Spring	15.78	19.40	213
	Autumn	15.28	18.77	164
50% RHS closed	Spring	15.41	18.93	192
	Autumn	15.08	18.53	174
75% LHS closed	Winter	7.97	263.94	2569
75% RHS closed	Winter	9.84	263.71	2022
Fully closed	Winter	6.52	203.51	9703

Some of the heat gain/removal values are very high, particularly in winter conditions when the DSF inlet is either 75% or fully closed reaching up to 9700kW. Whilst peak performance is expected in a closed cavity operation an ideal thermal buffer, these values are exaggerated largely due to the sheer size of the DSF outer skin area of $324m^2$. Hence, these results show that smaller working areas of the DSF could be sufficient to deliver pre-heating in colder conditions. The lowest values of heat gain occur in the summer conditions for a fully open or 25% closed cavity with a range of 18-32kW, but again these are significant quantities and so having the cavity open at the top to exhaust this heat to avoid overheating and promote surface cooling at the inner warehouse façade is achievable. Future work could propose a solution for heat recovery when the DSF is in an exhaust configuration so waste heat from warmer conditions can be recycled in cooler months.

7.5.1 Using CFD-derived Values to Calculation Heat Gain/Removal Directly

These values are not to compare with those obtained earlier as they are taken for a height of 9.87m rather than 9m where the air enters the warehouse. However, there are similar trends such

as the relationship between magnitude of heating and air velocity in the cavity. The purpose of this section is to show that heat gain/removal can be calculated in CFD directly as a quicker, perhaps more accurate tool based on its assumptions. For example, the velocity and pressure fields are calculated together and as a result account for friction loss through the cavity. It also considers spatial variation whereas the analytical tool cannot, assuming instead a uniform distribution of velocity and temperature across the cavity. Figure 7.13 shows the CFD-derived values of heat gain and removal across all seasons for the various DSF inlet configurations where Appendix Section A.6.5 has the other values required to calculate this.

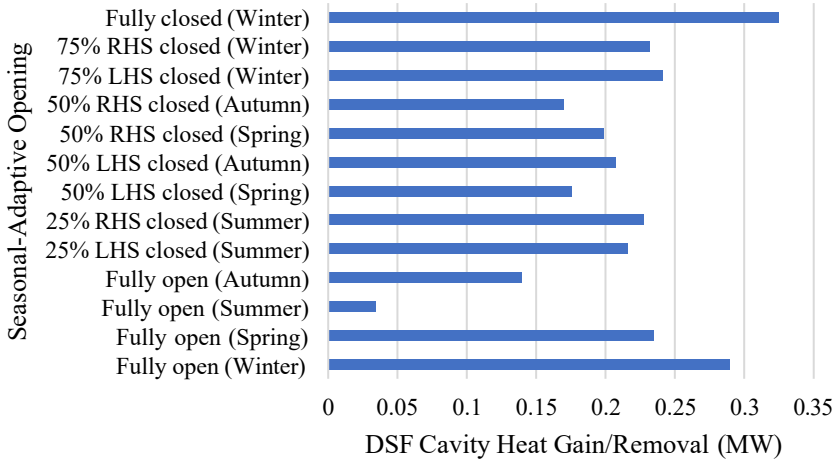


Figure 7.13 Magnitude of Heat Gain/Removal in DSF Cavity for different Seasonal-Adaptive Openings

For the winter season, the opaque aluminium double skin façade can achieve 0.23-0.32 MW of heating; for the spring, summer and autumn seasons, it can achieve 0.18-0.24MW, 0.03-0.23MW, and 0.14-0.21MW, respectively. These results indicate substantial energy savings if the DSF is applied as a pre-heating technology and indicates how an increased convective heat transfer at the warehouse façade can exhaust these levels of heat gain out the top of the cavity in summer conditions. Now that the ventilation, thermal and energy performance of the proposed double skin façade for warehouses has been examined, the last Section 7.6 explores how heat gain/removal values can be translated into an energy consumption metric.

7.6 Energy Performance Assessment of a DSF Warehouse

The energy performance assessment of the opaque aluminium double skin façade (DSF) retrofit for storage and distribution warehouses includes the evaluation of the energy, financial and carbon savings, in comparison to the estimated cost of the case study warehouse. This is to better illustrate how it could work as an energy efficient retrofit.

7.6.1 Energy Benchmarks for the Case Study Warehouse

The case-study building, climate information, and industry benchmarks detailed in Appendix Section A.6.2 are used to calculate the heating and cooling loads of the base-case warehouse. Also included are estimations of the electricity/gas cost and carbon emissions associated with the heating and cooling loads. Table 7.14 details a summary of the heating and cooling loads, and associated cost and carbon impact for the case-study warehouse.

Table 7.14 Case Study Warehouse Consumption, Energy and Carbon Emissions

Plant mode	Load (kW)	Electricity and gas total cost[1](£)	Carbon emissions[2] (kgCo2)
Heating	224	17,498	127,687
Cooling	57		
[1]BSRIA rule of thumb £7/m^2 (combined electricity and gas) [211] [2]BSRIA rule of thumb 49.8kgCO_2 per metre squared (combined electricity and fossil thermal) [211]			

7.6.2 Normalised Annual Energy and Carbon Savings of the DSF

To translate the energy savings of the DSF in Section 7.5, the heat gain/removal rates in kW should be converted to kWh and this requires working out equivalent sun hours for the four seasons in a year. Then, the energy, financial and carbon savings can be determined in as shown in Table 7.15 where the most recent price of electricity for non-domestic consumers is 32.17 pence per kWh [212], and carbon emissions of electricity is 0.207kgCO_2e per kWh [213] .

Table 7.15 Annual Energy, Financial and Carbon savings of DSF Retrofit

Season	DSF configuration	Heat gain/removal (kW)	Annual sun hours (h)	energy savings (kWh)	Financial savings (£)	Carbon reduction (kgCO2)
winter	fully open	586	179	104894	33744.40	21713
	75% LHS closed	2569	179	459851	147934.07	95189
	75% RHS closed	2022	179	361938	116435.45	74921
	fully closed	9703	179	1736837	558740.46	359525
spring	fully open	495	469	232155	74684.26	48056
	50% LHS closed	213	469	99897	32136.86	20678
	50% RHS closed	192	469	90048	28968.44	18639
summer	fully open	18	523	9414	3028.48	1948
	25% LHS closed	32	523	16736	5383.97	3464
	25% RHS closed	27	523	14121	4542.73	2923
autumn	fully open	448	282	126336	40642.29	26151
	50% LHS closed	164	282	46248	14877.98	9573
	50% RHS closed	174	282	49068	15785.18	10157

The main assumptions are the DSF is operating under a constant annual average of 300W/m^2, so these results do not reflect low-sun or no sun periods, and conversely higher sun periods; the external design temperatures for winter and summer represent an extreme and those for autumn and spring are an average. It is possible to apply this tool to different conditions, and future work could be to expand the application to other climates and large-space building types where an opaque seasonal-adaptive DSF might be appropriate. As these results are for the maximum surface area available for the DSF at 324m^2 (most of the south-facing façade of the case study

warehouse), the values reflect this and show that even a much smaller DSF may be sufficient to deliver the energy requirements of the case study warehouse in Table 7.14. The purpose of proportioning the annual energy savings across the four seasons, rather than the typical heating and cooling periods, is to demonstrate that intermediate seasons are being overlooked for energy savings potential, exemplified by Figure 7.14 which focusses on the fully open DSF configuration only.

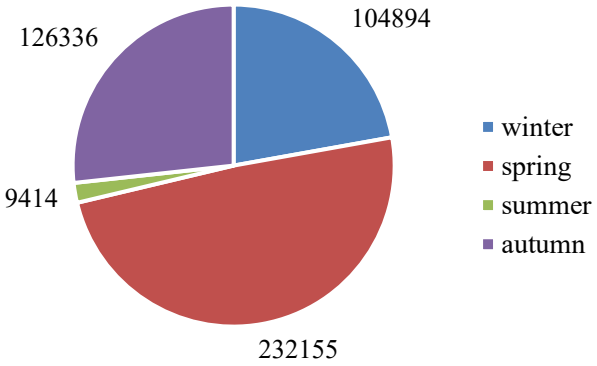


Figure 7.14 Annual Energy Savings from the Fully Open Double Skin Façade (kWh)

According to these results, under these representative conditions of the UK climate in an annual period, the operation of the fully open DSF in intermediate seasons contributes to 76% of the total energy savings. This is important in the light of the impact of climate change on seasonal changes. For example, the average number of days of frost (0ºC or below) is now 17% lower, and the growing season for crops and plants (5ºC or above) is a month longer compared to historical seasons [214], [215], indicating warmer or longer "intermediate" seasons.

To determine the feasibility of applying an opaque seasonal-adaptive DSF to a real warehouse, the next section covers a simplified analysis of the added embodied energy as a retrofit, and the payback period.

7.6.3 Embodied Energy and Payback Period

An important aspect of any building retrofit is to understand the added embodied energy to the existing building, and the payback period both of which are addressed in this section. The UK Green Building Council defines embodied carbon as the 'emissions associated with materials and construction processes throughout the whole lifecycle of a building or infrastructure'[216]. For this thesis, the constraints are that only the carbon cost of the raw materials are considered to give a simplified estimate, as detailed in Table 7.16 below. The primary raw materials related to the façade retrofit include aluminium for the outer skin of the double skin façade, stainless steel

for the purlins and side rails support structure, and fasteners, weatherproof sealant used to seal joints and seams between panels and weather membrane to protect against moisture.

Table 7.16 Typical Carbon Costs of DSF Materials

Construction component	Material	Carbon Cost	Amount (kg)	Calculated Carbon ($kgCO_2e$)
Outer facade	Aluminium	6.8$kgCO_2e$/kg [217]	2620	17,816
Purlins and rails	Stainless steel	6.15$kgCO_2e$/kg [218]	613.44	3,773
Weatherproof sealant	Silicone/Mastic	11.3CO_2e/kg [219]	1.736	20
Weather membrane	Polymer-bitumen roll-fed sheet	150kg CO_2e per tonne [220]	66.24kg	106
Outer façade coating	Slate Grey Paint RAL 7015	5 litres =13.58$kgCO_2e$ [221]	25 litres	68
			Total:	21,783

Comparing the embodied energy of the proposed DSF retrofit of 21,783$kgCO_2$ to that of the operational energy of the case study warehouse at 127,687$kgCO_2$, and that the fully open DSF configuration can annually save 21,713$kgCO_2$ and 1,948$kgCO_2$ in winter and summer, respectively, it is reasonable to suggest that its embodied carbon is negligible in terms of energy expense.

The initial investment has been costed based on the materials, labour and equipment required to install the DSF retrofit. Some assumptions have been made for simplification; these include: the four key materials are aluminium, steel, silicone sealant and HDPE membrane; transportation involves the fuel cost of the lorries to deliver materials; labour includes man- hours for the build, and the equipment includes large machinery such as a crane to lift materials, and cherry pickers for assembling at height. Table 7.17 has the details and the total cost in Great British Pounds. Table A.50 in the Appendix was used to find the final cost values.

Table 7.17 Cost Breakdown of Proposed DSF Retrofit

	Cost (£)
Materials Total: £9569.34	
Aluminium	£4236.58
Galvanised Steel Purlins	£3,402.00
Cleats/Bolts	96 cleats(£912.00), 384 bolts (4 x £10.80= £43.20) Total: £955.20
Sealant	£259.53
Membrane	£149.73
Paint	£566
Transportation Total:	
Site delivery	Fuel (£162.77)
Labour	
Manual	3 people, 150m^2 per day = 2 days' work at £300 per person per day = £1800
Equipment	
Crane	£420 per day so total = £840
Cherry pickers	£385 per day = £770
Total:	£13,141.51

The initial investment of the DSF retrofit is estimated to be £13,141.51 within the constraints and simplifications applied here. Most of the cost is due to the scale of the retrofit, and therefore

the amount of material and resource required to install it. Compared to average warehouse construction cost at £918 per m^2, this is approximately 1% of an estimated £2.4 million construction cost of the case study warehouse [222]. Combining the normalised annual energy savings values from Table 7.15 for the fully open DSF configuration in winter (£33,744.40) and summer (£3,028.48) gives a total of £36,772.88. The payback period is calculated using Equation 7.12 below:

Equation 7.12 Payback Period

$$Payback\ period = \frac{initial\ investment}{annual\ savings}$$

Applying the respective values for initial investment and annual savings leads to a payback period of 0.35 years or roughly 4 months which is indicative of promising retrofit potential. However, this number is resultant of the exaggerated level of energy savings due to the assumption that the DSF spans the entire façade. Additionally, it does not consider fluctuating hourly performance and the most effective means of achieving a realistic payback period is to conduct a pilot study of the proposed DSF retrofit on a real warehouse of similar scale.

7.7 Chapter Summary

This results chapter covered an analytical validation of cross-ventilation in warehouses, wind and buoyancy modelling of a DSF warehouse, optimisation of flexible openings at the DSF inlet, and a comprehensive energy performance assessment of the DSF warehouse. The purpose of this chapter was to finalise the new energy analysis tool for assessing the ventilation and thermal performance of a double skin façade retrofit for warehouses as well as highlighting the economic viability of the building technology.

7.7.1 Main Findings

The first section in this chapter evaluated whether cross-ventilation was possible in a warehouse, and analytical calculations using real meteorological data were conducted to validate a computational model of the full-scale warehouse. An error of 23% between the analytical and computational model was obtained which is likely due to the implicit simplifications of the empirical equations versus the Reynolds-Averaged Navier Stokes derived velocity, pressure and density values in CFD. A 16% difference between inlet and outlet openings offers confidence in the CFD model for calculating cross-ventilation.

The thermal performance of a fully open DSF warehouses was assessed in terms of temperature

distribution across the cavity, stack effect and pre-heating. The key results show that the fluid layer closest to the outer skin will always have the highest temperature value in all seasons as it is directly exposed to solar irradiance, followed by the fluid layer at the inner skin as it benefits from the internal design temperature of 18°C as well as cavity heating. The magnitude of pre-heating levels is 12.6°C, 23.1°C, and 21.20°C for a winter temperature of -4°C, and spring and autumn temperature of 10°C, respectively. This is significant considering the current building regulations regarding internal temperatures for warehouses are confined to a minimum of 4°C as per fire safety standards. If applying the thermal comfort internal temperature of 18°C, the DSF can provide 70% of this in winter, and exceed it by 20% in spring and autumn. The DSF in summer produces only a small amount of cavity heating at 1.80°C, with a horizontal temperature distribution of 1.20°C both of which indicate it can perform as a thermal buffer and exhausting the heat out the top of the cavity is an effective way to avoid overheating.

The ventilation performance of the fully open DSF warehouse was also explored and the primary findings conclude that for a starting inlet opening on the warehouse façade or inner skin of the DSF of total area 3.75m^3, it can deliver a range of 8210-16540L/s. This can satisfy ventilation requirements for 680-1530 occupants which is 2-3 times the occupancy of the case study warehouse. Pressure coefficients were obtained for the DSF outer and inner skins for different seasons for use in the energy savings calculations, and in all cases, the pressure coefficient of the inner skin is lower, indicating a pressure drop across the cavity. The DSF inlet area started at 36m x 0.2m to reflect the whole span of the façade, however applying the continuity equation to ensure ventilation requirements were met (and not oversized) suggested the area could be reduced to 4.76 x 0.2m, 7.16 x 0.2m, 3.95m x 0.2m, and 6.85 x 0.2m for winter, spring, summer and autumn, respectively.

An optimisation of the seasonal-adaptive DSF inlet openings was conducted to show the inverse relationship between airflow rate and pre-heating in the cavity, and how different percentage of inlet closures could provide a level of control over this. It was found that the best performing combination of DSF inlet and warehouse is fully closed and opening 3 for winter; 50% or fully open and opening 3 for heating and opening 2 for cooling in spring and autumn; and, fully open for with opening 2 or all openings 1-3 for summer.

Lastly, an assessment of the DSF's energy and economic feasibility found that the large surface area of 360m^2 can produce extremely high monetary, electricity, and carbon savings, and as a result suggest a payback period of less than a year. The initial investment of the DSF retrofit is

less than 2% the estimated cost of the construction of the case study warehouse, further indicating its potential as a building retrofit.

7.7.2 Limitations and Future Work

There are a few different methodologies applied in this chapter that have some form of limitation or assumption incorporated to make it feasible within the scope of the research conducted in this thesis. Whilst the research objectives are met, there are other directions that the different studies could go in.

The main limitations of using analytical calculations to validate a computational fluid dynamics model of cross-ventilation in a warehouse space is the inherent simplifications within the analytical equations. These include assumptions of uniform flow, simplification of building geometry, inability to fully capture turbulence and complex flow phenomena and more. Due to time and budget constraints, it remained sufficient to provide a level of validation to the full- scale CFD model. However, future work could include taking a small-scale model in a wind tunnel and measuring air velocity at cross-ventilation inlet and outlets or implementing velocity sensors at different points within a real warehouse to assess airflow distribution.

As before in chapters 4,5, and 6, the primary limitation of the computational models is the use of steady state modelling compared to transient, among other aspects such as altered geometry, meshing method and set-up.

7.7.3 Closing Remarks

Overall, this chapter has proven that within the constraints and assumptions made within this thesis, the seasonal-adaptive double skin façade has high potential as a low-energy retrofit for warehouses. This was determined by analytically and computationally assessing the ventilation, thermal and energy performance (and feasibility) under combined wind and thermal conditions likely to arise on an annual basis in a temperate UK climate. The research objectives delivered in this chapter come together to highlight the potential of double skin facades and how they are under-utilised as an energy efficiency measure, and ventilation building technology for warehouses.

Chapter 8

Conclusions

The UK's built environment is rapidly evolving, reflected by the huge growth in warehouse construction in response to the modern e-commerce demand. Until now, there has been little understanding of the fluid dynamics, thermal phenomena and energy consumption (including passive solutions such as double skin facades) of warehouses. This research addresses this by proving the viability of a "seasonal-adaptive" opaque double skin façade as a building retrofit for storage and distributions warehouses in the UK to deliver pre-heating, cooling/buffering and ventilation. Additionally, it advances the building physics modelling of warehouses through the novel validated computational fluid dynamics tool for assessing the ventilation, thermal and energy performance of the proposed DSF for warehouses.

8.1 Summary of Key Findings

The key findings in this thesis are outlined to match the order of the objectives detailed in Chapter 1, Section 1.5. The first objective of developing an experimental and computational methodology is achieved through a systematic meta-analysis of the existing literature on double skin facades in the 21st century using an adapted PRISMA method. It highlighted gaps in the application of DSFs for warehouses, the development of an opaque DSF with a coated aluminium outer skin and warehouse cladding inner skin, and an assessment of "seasonal-adaptive" DSF cavity inlet openings. This led to a clear multi-methodology design of incorporating empirical data collection and CFD simulation to build the validated CFD tool capable of assessing the ventilation, thermal and energy performance of the DSF through an adjacent Bernoulli-adapted tool.

Chapter 4 contains results related to the second objective of experimentally testing the DSF under wind-only conditions in a successful wind tunnel test of a case study warehouse. It demonstrated the DSF's ability to facilitate natural ventilation in the case study warehouse in wind-only conditions. Expected pressure variations on the DSF outer skin were replicated in the CFD model, and further improvements led to a final error of 7.8%. The full-scale seasonal modelling showed stable vertical cavity profiles up to 9m where flow either enters the warehouse or is exhausted to the environment. The warehouse had three 1.25m^2 openings which with the application of the DSF can support cross-ventilation, maintaining a neutral pressure height of 4-4.75m. The fully open DSF provided 1440-2496L/s annually, achieving thirteen times the required occupancy ventilation rate, but with the caveat that ventilation sizing for warehouses should be less occupancy-driven, and more redistribution and mixing-focussed. These findings show the effectiveness of using small-scale wind tunnel data to validate full scale application of double skin facades in large-space warehouses as part of the assessment of its performance.

The findings in Chapter 5 also stem from the second objective but in this case the DSF is experimentally tested under buoyancy-only conditions as a working prototype in a climate chamber. It proved the technical viability of the seasonal-adaptive opaque DSF as a pre-heating, ventilation, and thermal buffering/cooling system in a buoyancy-only conditions typical in the UK. A summer outdoor temperature of 25^{o}C and a fully open DSF inlet saw the highest cavity temperatures but the greatest vertical temperature gradient (8-13^{o}C/m) occurred in winter. In all cases, cavity air velocity remained below 0.06m/s due to the absence of wind. Validation against literature achieved errors of 27% and 16% for velocity and temperature, reducing to 12% and 3.5% against the climate chamber data. When scaled to full warehouse dimensions, the DSF delivered buoyancy-driven ventilation rates of up to 6192L/s (summer) and maximum heating of 27kW (winter) whilst reducing the warehouse façade's U-value to 0.19-0.27W/m^{2}K. The importance here is that thermally testing the DSF with realistic material properties is as crucial to the development of the validated computational tool as testing the DSF on a case study warehouse, at scale.

The penultimate results chapter addresses the third objective of thermal scale testing for stratification in warehouses using as simple a method as heat mats and a scale model. It highlighted the complexity of capturing thermal stratification in warehouses, addressing a key literature gap, and the challenges to thermal scaling of Grashof number using empirical versus computational methods. The 1:50 scale model of the warehouse (without the DSF) showed high levels of stratification with a vertical thermal gradient of 13.5^{o}C/m and a Grashof number of 3.2x10^{6}. Adding storage racking common in warehouses increased this gradient by 23%, producing a higher Grashof number of 5x10^{6}. When compared to the CFD models, low errors of 2% (empty) and 6% (storage racking) were obtained but revealed uncertainty in scaling Grashof numbers empirically, favouring CFD methods. Overall, this chapter suggests that computational methods based on Reynolds-Averaged-Navier-Stokes equations, such as CFD, might be better at accurately capturing complex phenomenon such as stratification and that internal spaces should be modelled as realistically as possible. Whilst this chapter is experimentally limited compared to Chapters 4 and 5, it produced enough temperature data to prove the presence of thermal stratification and validate an integral thermal modelling aspect of the CFD tool.

The final chapter reflects the last objective of integrating the three previous results chapters to deliver the new computational tool to assess the integrated ventilation, thermal and energy performance of a seasonal-adaptive double skin façade retrofit for warehouses in the UK. It

completed the validation of the CFD tool through empirical comparisons of cross-ventilation in the full-scale warehouse without the DSF leading to an error of 23% and mass conservation. With the application of the DSF under real seasonal wind conditions and annual average 300W/m^2 solar irradiance, significant pre-heating was achieved with cavity temperatures of 12.6^{o}C in winter (covering 70% of heating demand) and 21.2-23.1^{o}C in Spring and Autumn (exceeding internal temperatures by 20%), while in summer, overheating was minimized by exhausting heat. Ventilation analysis showed that a maximum DSF inlet opening area of 7.2m^2 is oversized delivering 8210-16,540L/s of outdoor air whilst smaller areas of 0.95-1.4m^2 could be sufficient for all seasons. Optimal configurations of DSF inlet opening percentages and warehouse inlets were identified but a simplified economic analysis demonstrated substantial energy, financial and carbon savings for all configurations across all seasons. These results, along with an estimated payback period of under a year with an initial investment cost of less than 2% of the case study warehouse's construction cost suggests real-world potential of the DSF. In conclusion, this chapter provided an integrated assessment of the DSF's technical feasibility and effectiveness as a low-energy solution for warehouses. The computational tool has shown that it can accurately predict DSF behaviour under different seasonal conditions, supporting its significance in the application of DSF for large-space buildings such as warehouses which require careful and expert design.

8.2 Contribution to Knowledge and Research Impact

This research makes significant contributions to low-energy solutions for warehouses in the UK. The development of the seasonal-adaptive opaque DSF and CFD tool specifically for warehouses addresses the gap in natural ventilation assessment and passive alternatives to traditional HVAC, space heaters and destratification fans in warehouses. The research impact associated with these developments is original experimental validation at each stage of computational model development unlike much of the existing DSF literature which relies on reused experimental data, thus enhancing the rigor of the CFD tool. Additionally, the use of a Bernoulli-adapted analytical tool provides a standardised method for evaluating DSF energy performance.

Another area that this research has made advancements in is the regulatory and design guidelines for warehouses. This includes suggestions for how to design cross-ventilation strategies in large spaces, and improvements to existing energy efficiency and natural destratification design guidelines in warehouses. The studies conducted in this thesis prove that cross-ventilation can take place in large-space warehouses with an aspect ratio of length to width of 2:1 when openings

are placed on the opposite facades. This could inform new changes to design guidelines such as CIBSE Guide AM10: Natural Ventilation following proper testing in real warehouses. Equally, CIBSE Guide A currently indicates internal thermal comfort temperatures of 18°C for warehouses, but UK warehouses are traditionally "ambient" meaning that the temperature could be higher or lower at different points in the year. A lack of availability of this type of internal temperature data is why 18°C was applied for the case study warehouse in this thesis.

8.3 Future Research and Closing Remarks

The three main areas where this research could be built upon are aspects of the computational modelling, building application and climate as well as pilot study. A dynamic transient modelling approach could improve upon the steady-state method, especially for analysing stack effect and buoyancy in changing environmental conditions. Further to this, the CFD tool could be adapted for other large-space buildings such as airports, malls, cinemas and other retail spaces where vertical space is unobstructed by typical storey levels and likely to experience similar airflow behaviour. Similarly, the feasibility of DSFs for warehouses could be explored in extreme hot or cold climates. However, a pilot study of the DSF on a real warehouse under real-world conditions across all seasons in a temperate climate, such as the UK, would be the most impactful next step to understand its potential as a low-energy building technology.

This thesis has explored research-led innovation in double skin facades for warehouses, addressing the long-overlooked fluid dynamics and thermal phenomena in these uniquely large spaces. With the UK warehouse sector expanding to 700 million square feet, energy efficiency and ventilation and thermal regulations or design guidelines have failed to modernise. By developing the new computational fluid dynamics tool, this thesis has demonstrated the viability of the seasonal-adaptive opaque double skin facade for warehouses. These findings provide the foundation for driving industry-wide change and advancing the future of low-energy warehousing solutions and internal space assessment methodology.

References

[1] IBM, “Building energy analytics for cooling and heating is helping to fight climate change,” 2020. [Online]. Available: https://www.ibm.com/blogs/ibm-anz/building-energy-analytics-for-cooling-and-heating-is-helping-to-fight-climate-change/. [Accessed July 2021].

[2] United Kingdom Warehouse Association (UKWA), “New report reveals major growth and seismic changes in UK warehousing sector,” UKWA, 2021. [Online]. Available: https://www.ukwa.org.uk/market-intel/new-report-reveals-major-growth-and-seismic-changes-in-uk-warehousing-sector/. [Accessed July 2022].

[3] United Kingdom Warehouse Association (UKWA), “https://www.ukwa.org.uk/wp-content/uploads/2021/05/Savills-UKWA-A4-8pp-Report-Interactive3.pdf,” UKWA, 2021.

[4] CIBSE, “CIBSE Guide B - Heating, Ventilating, Air-Conditioning and Refrigeration,” CIBSE, 2020.

[5] OVO Energy, “Average electricity usage in the UK: how many kWh does your home use?,” 18 March 2021. [Online]. Available: https://www.ovoenergy.com/guides/energy-guides/how-much-electricity-does-a-home-use. [Accessed July 2022].

[6] Savills, “The size and make-up of the UK warehousing sector – 2021,” 28 June 2021. [Online]. Available: https://www.savills.co.uk/research_articles/229130/315446-0#:~:text=The%20trend%20for%20larger%20warehouse,increased%20from%2011m%20to%2014m.. [Accessed July 2022].

[7] Financial Times, “Britain could run out of warehouse space within a year,” 24 October 2021. [Online]. Available: https://www.ft.com/content/c1e7b270-c6c6-4904-90a2-57f3e6ef963c. [Accessed July 2022].

[8] CIBSE, “CIBSE Guide A: Environmental Design,” CIBSE, 2006.

[9] European Centre for Disease Prevention and Control, “Heating, ventilation and air-conditioning systems in the context of Covid-19: first update,” 11 November 2020. [Online]. Available: https://www.ecdc.europa.eu/en/publications-data/heating-ventilation-air-conditioning-systems-covid-19. [Accessed July 2022].

[10] EMG - Transmission Group, “COVID-19 Risk by Occupation and Workplace,” UK GOV, 2021.

[11] UK GOV, “Ventilation:Approved Document F,” UK GOV, 2010.

[12] CIBSE, “CIBSE Approved Manual 10 Natural Ventilation in Non-domestic Buildings,” CIBSE, 2005.

[13] UK GOV, “Conservation of Fuel and Power: Approved Document L, Volume 2”, UK GOV, 2023.

[14] National Association of Rooflight Manufacturers (NARM), "Recommended Good Practice For Daylighting in Metal Clad Buildings", MCRMA, 2004.

[15] National Renewable Energy Laboratory (NREL), "U.S. Solar Photovoltaic System and Energy Storage Cost Benchmarks, With Minimum Sustainable Price Analysis Q1, 2022", U.S Department of Energy, 2022.

[16] International Renewable Energy Agency (IRENA), "End-of-life Management: Solar Photovoltaic Panels", IRENA, 2016.

[17] EnergyPlus , "EngineeringReference," U.S. Department of Energy, 29 March 2022. [Online]. Available: https://bigladdersoftware.com/epx/docs/8-2/engineering-reference/outside-surface-heat-balance.html. [Accessed July 2022].

[18] International Energy Agency, "Ventilated Double Skin Facades: Classification & Illustration of facade concepts," Air Infiltration and Ventilation Centre (AIVC), Brussels, 2005.

[19] TATA Steel, "Unglazed Transpired Solar Collector (uTSC)," 2022. [Online]. Available:https://www.tatasteeleurope.com/construction/products/renewables/active-solar-air-heating/unglazed-transpired-solar-collector. [Accessed July 2022].

[20] S. A. Kalogirou, "Building integration of solar renewable energy systems towards zero or nearly zero energy buildings," *International Journal of Low-Carbon Technologies,* vol. 10, no. 4, pp. 379-385, 2013.

[21] Concrete Construction, "SUSTAINABLE CONSTRUCTION WITH CONCRETE: TROMBE WALLS," 26 March 2007. [Online]. Available: https://www.concreteconstruction.net/projects/residential/sustainable-construction-with-concrete-trombe-walls_o. [Accessed July 2022].

[22] International Association of Certified Home Inspectors, "Trombe Walls," 2022. [Online]. Available: https://www.nachi.org/trombe-walls.htm. [Accessed July 2022].

[23] ArchDaily, "How do Double-Skin Facades Work?," 20 August 2019. [Online]. Available: https://www.archdaily.com/922897/how-do-double-skin-facades-work. [Accessed July 2022].

[24] CA Group, "Solarwall," 2022. [Online]. Available: https://www.cagroup.co.uk/renewables-product-page. [Accessed July 2022].

[25] Modern Building Services, "Solar energy becomes another 'brick' in the wall," 12 January 2010. [Online]. Available: https://modbs.co.uk/news/fullstory.php/aid/7391/_65279%3BSolar_energy_becomes_another_____91brick_92_in_the_wall.html. [Accessed July 2022].

[26] Modern Building Services, "Exploiting solar energy halves heating costs," 16 June 2007. [Online]. Available:

https://modbs.co.uk/news/fullstory.php/aid/3459/Exploiting_solar_energy_ _halves_heating_costs.html. [Accessed July 2022].

[27] W. Li, *Numerical and Experimental Study of Thermal Stratification in Large Warehouses,* 2016.

[28] British Standards, "BS 5925:1991 Code of practice for ventilation principles and designing for natural ventilation," British Standards, 1991.

[29] UK GOV, "Energy consumption in new domestic buildings 2015 – 2017 (England and Wales)," 19 December 2019. [Online]. Available: https://assets.publishing.service.gov.uk/government/uploads/system/uploads/attachment_data/file/853067/energy-consumption-new-domestic-buildings-2015-2017-england-wales.pdf. [Accessed July 2022].

[30] BRE, "BRE Digest 210 Principles of natural ventilation," BRE, 1982.

[31] D. a. S. M. Etheridge, Building Ventilation - Theory and Measurement, Chichester: John Wiley & Sons, 1996.

[32] BSRIA, "The Illustrated Guide to Ventilation," BSRIA, 2009.

[33] M. Baeli, Residential Retrofit: 20 Case Studies, RIBA publishing, 2013.

[34] Ellen Macarthur Foundation, n.d. *What is the Circular Economy?*. [Online] Available at: https://www.ellenmacarthurfoundation.org/circular-economy/what-is-the-circular-economy [Accessed 1 July 2021].

[35] Allouhi, A. et al., 2015. Energy consumption and efficiency in buildings: current status and future trends. *Journal of Cleaner Production,* Volume 109, pp. 118-130.

[36] Perez-Lombard, L., Oritz, J. & Pout, C., 2008. A review on buildings energy consumption information. *Energy and Buildings,* 40(3), pp. 394-398.

[37] IEA (2022), *Buildings*, IEA, Paris https://www.iea.org/reports/buildings, License: CC BY 4.0

[38] Cao, X., Dai, X. & Liu, J., 2016. Building energy-consumption status worldwide and the state-of-the-art technologies for zero-energy buildings during the past decade. *Energy and Buildings,* Volume 128, pp. 198-213.

[39] IEA, 2020. *Building Envelopes,* Paris: IEA.

[40] Lucon, O. et al., 2014. *Buildings. In: Climate Change 2014: Mitigation of Climate Change. Contribution of Working Group III to the Fifth Assessment Report of the Intergovernmental Panel on Climate Change,* s.l.: Cambridge University Press.

[41] (IBM) Vishwanath, D. A., 2020. *Building Energy Analytics for Cooling and Heating is helping to fight climate change.* [Online] Available at: https://www.ibm.com/blogs/ibm-anz/building-energy-analytics-for-cooling-and-heating-is-helping-to-fight-climate-change/ [Accessed 1 July 2021].

[42] European Centre for Disease Prevention and Control, 2020. *Heating, Ventilation and air-conditioning systems in the context of COVID-19: first update,* s.l.: European Centre for Disease Prevention and Control.

[43] International Well Building Institute, n.d. *Operable Windows.* [Online] Available at: https://standard.wellcertified.com/air/operable-windows [Accessed 1 July 2021].

[44] Department of Health and Social Care, 2020. *New film shows importance of ventilation to reduce spread of COVID-19,* London: Department of Health and Social Care.

[45] Scientific Advisory Group for Emergencies, 2020. *EMG: Role of ventilation in controlling SARS-CoV-2 transmission, 30 September 2020.* [Online] Available at: https://www.gov.uk/government/publications/emg-role-of-ventilation-in-controlling-sars-cov-2-transmission-30-september-2020 [Accessed 1 July 2021].

[46] Yu, J., Ouyang, Q., Zhu, Y., Shen, H., Cao, G., Cui, W. 2012, 'A comparison of the thermal adaptability of people accustomed to air-conditioned environments and naturally ventilated environments', *Indoor Air*, vol. 22, pp. 110-118

[47] Energy Efficiency Best Practice Programme (EEBPP) 1993, 'Energy Consumption guide 19', London: Energy Efficiency Office/HMSO

[48] Allard, F. 1998, 'Natural Ventilation in Buildings', London: James & James (Science Publisher) Ltd.

[49] BBRI, 2005. *Ventilated Double Skin Facades Classification & Illustration of facade concepts,* Brussels: International Energy Agency.

[50] Bonham, M. B., 2020. *Bioclimatic Double-Skin Facades.* First ed. Oxford, Ohio: Routledge, Taylor & Francis.

[51] Oesterle, E., Lieb, R.-D., Lutz, M. & Heusler, W., 2001. *Double Skin Facades – Integrated Planning.* Munich: Prestel Verlag.

[52] Vaglio, J., 2011. *Structural Response of Multistory Double Skin Facades,* Tampere: Glass Performance Days.

[53] Chan, A., Chow, T., Fong, K. & Lin, Z., 2009. Investigation on energy performance of double skin façade in Hong Kong. *Energy and Buildings,* November, 41(11), pp. 1135-1142.

[54] Ching, F. D., 2014. *Building Construction Illustrated.* Hoboken, New Jersey: John Wiley & Sons.

[55] Jankovic, Aleksandar, and Francesco Goia. "Impact of Double Skin Facade Constructional Features on Heat Transfer and Fluid Dynamic Behaviour." *Building and environment* 196 (2021): 107796. Web.

[56] Su, Z., Li, X. & Xue, F., 2017. Double-skin façade optimization design for different climate zones in China. *Solar Energy,* October, Volume 155, pp. 281-290.

[57] Gelesz, A. et al., 2020. Characteristics that matter in a climate façade: A sensitivity analysis with building energy simulation tools. *Energy and Buildings,* December, Volume 229, p. 110467.

[58] Aleksandrowicz, O. & Yezioro, A., 2018. Mechanically ventilated double-skin facade in a hot and humid climate: summer monitoring in an office tower in Tel Aviv. *Architectural Science Review,* March, 61(3), pp. 171-188.

[59] Larsen, F. S., Rengifo, L. & Filippin, C., 2015. Double skin glazed façades in sunny Mediterranean climates. *Energy and Buildings,* September, Volume 102, pp. 18-31.

[60] Xu, L. & Ojima, T., 2007. Field experiments on natural energy utilization in a residential house with a double skin façade system. *Building and Environment,* May, Volume 42, pp. 2014-2023.

[61] Andelkovic, S. A., Gvozdenac-Urosevic, B., Kljajic, M. & Ignjatovic, G. M., 2015. Experimental research of the thermal characteristics of a multi-storey

naturally ventilated double skin façade. *Energy and Buildings,* January, Volume 86, pp. 766-781.

[62] Kim, G.-H., Kwon, H.-M. & Yang, J.-H., 2018. Ventilation Rate and Thermal Environment Properties of Double Skin Façade Considering Wind Profile and Direction. *Journal of Asian Architecture and Building Engineering,* October, 16(3), pp. 675-682.

[63] Hu, G., Hassanli, S., Kwok, K. & Tse, K., 2017. Wind-induced responses of a tall building with a double-skin façade system. *Journal of Wind Engineering and Industrial Aerodynamics,* September, Volume 168, pp. 91-100.

[64] Saroglou, T., Theodosiou, T., Givoni, b. & Meir, A. I., 2020. Studies on the optimum double-skin curtain wall design for high-rise buildings in the Mediterranean climate. *Energy and Buildings,* February, Volume 208, p. 109641.

[65] Yoon, B. Y., Seo, B., Koh, B. B. & Cho, S., 2019. Performance analysis of a double-skin façade system installed at different floor levels of high-rise apartment building. *Journal of Building Engineering,* November, Volume 26, p. 100900.

[66] Ballestini, G., De Carli, M., Masiero, N. & Tombola, G., 2005. Possibilities and limitations of natural ventilation in restored industrial archaeology buildings with a double-skin façade in Mediterranean climates. *Building and Environment,* 40(7), pp. 983-995.

[67] Slavkovic, B. P., 2017. Application of the double skin façade in rehabilitation of the industrial buildings in Serbia. *Thermal Science,* 21(6B), pp. 2945-2955.

[68] Gratia, E. & De Herde, A., 2004. Is day natural ventilation still possible in office buildings with a double-skin façade?. *Building and Environment,* April, 39(4), pp. 399-409.

[69] Inan, T. & Basaran, T., 2019. Experimental and numerical investigation of forced convection in a double skin façade by using nodal network approach for Istanbul. *Solar Energy,* May, Volume 183, pp. 441-452.

[70] Gratia, E. & De Herde, A., 2007. Greenhouse effect in double-skin facade. *Energy and Buildings,* 39(2), pp. 199-211.

[71] Chou, S., Chua, K. & Ho, J., 2009. A study on the effects of double skin façades on the energy management in buildings. *Energy Conversion and Management,* September, 50(9), pp. 2275-2281.

[72] Vatavalis, P. & Bikas, D., 2017. Thermal Performance Investigation in Cooling Season for a Corner Double Skin Façade with Rotating Glass Louvres. *Procedia Environmental Services,* Volume 38, pp. 86-93.

[73] Sanchez, E., Rolando, A., Sant, R. & Ayuso, L., 2016. Influence of natural ventilation due to buoyancy and heat transfer in the energy efficiency of a double skin facade building. *Energy for Sustainable Development,* August, Volume 33, pp. 139-148.

[74] Alberto, A., Ramos, N. M. & Almeida, R. M., 2017. Parametric study of double-skin facades performance in mild climate countries. *Journal of Building Engineering,* July, Volume 12, pp. 87-98.

[75] Dama, A. & Angeli, D., 2016. Wind and buoyancy driven natural ventilation in double skin façades. *International Journal of Ventilation,* September, 15(3-4), pp. 288-301.

[76] Andelkovic, A. S., Mujan, I. & Dakic, S., 2016. Experimental validation of a EnergyPlus model: Application of a multi-storey naturally ventilated double skin façade. *Energy and Buildings,* April, Volume 118, pp. 27-36.

[77] Perez-Grande, I., Meseguer, J. & Alonso, G., 2005. Influence of glass properties on the performance of double-glazed facades. *Applied Thermal Engineering,* December, 25(17-18), pp. 3163-3175.

[78] Gavan, V., Woloszyn, M., Kuznik, F. & Roux, J.-J., 2010. Experimental study of a mechanically ventilated double-skin façade with venetian sun-shading device: A full-scale investigation in controlled environment. *Solar Energy,* February, 84(2), pp. 183-195.

[79] Wang, Y., Chen, Y. & Zhou, J., 2016. Dynamic modeling of the ventilated double skin façade in hot summer and cold winter zone in China. *Building and Environment,* September, Volume 106, pp. 365-377.

[80] Mingotti, N., Chenvidyakarn, T. & Woods., A. W., 2011. The fluid mechanics of the natural ventilation of a narrow-cavity double-skin facade. *Building and Environment,* April, 46(4), pp. 807-823.

[81] Gratia, E. & De Herde, A., 2007. The most efficient position of shading devices in a double-skin facade. *Energy and Buildings,* March, 39(3), pp. 364-373.

[82] Wong, P., Prasad, D. & Behnia, M., 2008. A new type of double-skin façade configuration for the hot and humid climate. *Energy and Buildings,* 40(10), pp. 1941-1945.

[83] Shen, C. & Li, X., 2016. Thermal performance of double skin façade with built-in pipes utilizing evaporative cooling water in cooling season. *Solar Energy,* November, Volume 137, pp. 55-65.

[84] Pomponi, F., Piroozfar, P. A. & Farr, E. R., 2016. An Investigation into GHG and non-GHG Impacts of Double Skin Façades in Office Refurbishments. *Journal of Industrial Ecology,* April, 20(2), pp. 234-248.

[85] Hay, R. & Ostertage, C. P., 2018. Life cycle assessment (LCA) of double-skin façade (DSF) system with fiber-reinforced concrete for sustainable and energy-efficient buildings in the tropics. *Building and Environment,* September, Volume 142, pp. 327-341.

[86] Hassanli, Sina et al. "Potential Application of Double Skin Façade Incorporating Aerodynamic Modifications for Wind Energy Harvesting." *Journal of wind engineering and industrial aerodynamics* 174 (2018): 269–280. Web.

[87] Wang, Y., Chen, Y. & Li, C., 2020. Energy performance and applicability of naturally ventilated double skin façade with Venetian blinds in Yangtze River Area. *Sustainable Cities and Society,* October, Volume 61, p. 102348.

[88] Nasrollahi, Nazanin, and Majid Salehi., 2015 "Performance Enhancement of Double Skin Facades in Hot and Dry Climates Using Wind Parameters." Renewable energy 83: 1–12. Web.

[89] Balocco, C., 2002. A simple model to study ventilated facades energy performance. *Energy and Buildings,* June, 34(5), pp. 469-475.

[90] Kim, D. D., 2020. Computational fluid dynamics assessment for the thermal performance of double-skin façades in office buildings under hot climatic condition. *CIBSE Building Services Engineering Research and Technology,* August, 42(1), pp. 45-61.

[91] Wang, Y., Chen, Y. & Li, C., 2019. Airflow modeling based on zonal method for natural ventilated double skin façade with Venetian blinds. *Energy and Buildings,* May, Volume 191, pp. 211-223.

[92] Iken, O. et al., 2019. Thermal and energy performance investigation of a smart double skin facade integrating vanadium dioxide through CFD simulations. *Energy Conversion and Management,* September, Volume 195, pp. 650-671.

[93] Wen, Y., Guo, Q., Xiao, P.-a. & Ming, T., 2017. The Impact of Opening Sizing on the Airflow Distribution of Double-skin Facade. *Procedia Engineering,* Volume 205, pp. 4111-4116.

[94] Tao, Y. et al., 2021. Ventilation performance of a naturally ventilated double-skin façade in buildings. *Renewable Energy,* April, Volume 167, pp. 184-198.

[95] Radhi, H., Sharples, S. & Fikiry, F., 2013. Will multi-facade systems reduce cooling energy in fully glazed buildings? A scoping study of UAE buildings. *Energy and Buildings,* January, Volume 56, pp. 179-188.

[96] Lee, J., Mohamed, H. & Chang, J. D., 2016. Elsevier Procedia Engineering Volume 145, 2016, Pages 892-899 Procedia Engineering The Effect of Positions of Vertical Glass Fins inside a Double Skin Façade Air Cavity as Acoustical Barriers and Ventilation Potentials. *Procedia Engineering,* Volume 145, pp. 892-899.

[97] Guardo, A. et al., 2009. A CFD approach to evaluate the influence of construction and operation parameters on the performance of Active Transparent Façades in Mediterranean climates. *Energy and Buildings,* May, 41(5), pp. 534-542.

[98] Kimouche, N. et al., 2017. Effect of inclination angle of the adiabatic wall in asymmetrically heated channel on natural convection: Application to double-skin façade design. *Journal of Building Engineering,* July, Volume 12, pp. 171-177.

[99] Ding, W., Hasemi, Y. & Yamada, T., 2005. Natural ventilation performance of a double-skin façade with a solar chimney. *Energy and Buildings,* April, 37(4), pp. 411-418.

[100] Tao, Y. et al., 2021. Naturally ventilated double-skin façade with adjustable louvers, Solar Energy, Volume 225, 2021, Pages 33-43, ISSN 0038-092X, https://doi.org/10.1016/j.solener.2021.07.013.

[101] Tao, Y. et al., 2022. Solar-assisted naturally ventilated double skin façade for buildings: Room impacts and indoor air quality, Building and Environment, Volume 216, 2022, 109002, ISSN 0360-1323, https://doi.org/10.1016/j.buildenv.2022.109002.

[102] Yoon, N. et al., 2022. Dynamic compartmentalization of double-skin façade for an office building with single-sided ventilation, Building and Environment, Volume 208, 2022, 108624,ISSN 0360-1323,https://doi.org/10.1016/j.buildenv.2021.108624.

[103] Hamza, N., 2008. Double versus single skin facades in hot arid areas. *Energy and Buildings,* 40(3), pp. 240-248.

[104] Chan, A., Chow, T., Fong, K. & Lin, Z., 2009. Investigation on energy performance of double skin façade in Hong Kong. *Energy and Buildings,* November, 41(11), pp. 1135-1142.

[105] Hoseggen, R., Wachenfeldt, B. & Hanssen, S., 2008. Building simulation as an assisting tool in decision making: Case study: With or without a double-skin façade?. *Energy and Buildings,* 40(5), pp. 821-827.

[106] Barbosa, S. & Alberto, K. C., 2019. Effect of the double skin façade material on the thermal performance of the educational building in tropical climate. *Architectural Science Review,* March, 62(3), pp. 206-215.

[107] Barbosa, S. & Ip, K., 2016. Predicted thermal acceptance in naturally ventilated office buildings with double skin façades under Brazilian climates. *Journal of Building Engineering,* September, Volume 7, pp. 92-102.

[108] Blanco, J. M. et al., 2016. Energy assessment and optimization of perforated metal sheet double skin façades through Design Builder; A case study in Spain. *Energy and Buildings,* January, Volume 111, pp. 326-336.

[109] Srisamranrungruang, T. & Hiyama, K., 2020. Balancing of natural ventilation, daylight, thermal effect for a building with double-skin perforated facade (DSPF). *Energy and Buildings,* March, Volume 210, p. 109765.

[110] Souza, L., Souza, H. & Rodrigues, E., 2018. Experimental and numerical analysis of a naturally ventilated double-skin façade. *Energy and Buildings,* April, Volume 165, pp. 328-339.

[111] Safer, Nassim, Monika Woloszyn, and Jean Jacques Roux, 2005. "Three-Dimensional Simulation with a CFD Tool of the Airflow Phenomena in Single Floor Double-Skin Facade Equipped with a Venetian Blind." Solar energy 79.2: 193–203. Web.

[112] Hanby, VI et al., 2008 "Nodal Network and CFD Simulation of Airflow and Heat Transfer in Double Skin Facades with Blinds." Building services engineering research & technology 29.1: 45–59. Web.

[113] Fallahi, A., Haghihat, F. & Elsadi, H., 2010. Energy performance assessment of double-skin façade with thermal mass. *Energy and Buildings,* September, 42(9), pp. 1499-1509.

[114] Kuznik, F. et al., 2011. Numerical modelling of combined heat transfers in a double skin façade – Full-scale laboratory experiment validation. *Applied Thermal Engineering,* October, 31(14-15), pp. 3043-3054.

[115] Pourshab, N., Tehrani, M. D., Toghraie, D. & Rostami, S., 2020. Application of double glazed façades with horizontal and vertical louvers to increase natural air flow in office buildings. *Energy,* June, Volume 200, p. 117486.

[116] Luo, Y. et al., 2017. A comparative study on thermal performance evaluation of a new double skin façade system integrated with photovoltaic blinds. *Applied Energy,* August, Volume 199, pp. 281-293.

[117] Luo, Y. et al., 2018. Experimental study and performance evaluation of a PV-blind embedded double skin façade in winter season. *Energy,* December, 165(Part B), pp. 326-342.

[118] Li, Y., Darkwa, J., Kokogiannakis & Su, W., 2019. Phase change material blind system for double skin façade integration: System development and thermal performance evaluation. *Applied Energy,* October, Volume 252, p. 113376.

[119] Li, Yilin et al. "Effect of Design Parameters on Thermal Performance of Integrated Phase Change Material Blind System for Double Skin Façade Buildings." *International journal of low carbon technologies* 14.2 (2019): 286–293. Web.

[120] Stec, W., van Passen, A. & Maziarz, A., 2005. Modelling the double skin façade with plants. *Energy and Buildings,* May, 37(5), pp. 419-427.

[121] Park, C.-S.et al., 2004. Calibration of a lumped simulation model for double-skin façade systems. *Energy and Buildings,* November, 36(11), pp. 1117-1130.

[122] Park, C.-S.et al., 2004. Real-time optimization of a double-skin façade based on lumped modeling and occupant preference. *Building and Environment,* August, 39(8), pp. 939-948.

[123] Hong, T. et al., 2013. Assessment of Seasonal Energy Efficiency Strategies of a Double Skin Facade in a Monsoon Climate Region. *energies,* 6(9), pp. 4352-4376.

[124] Yoon, Y. B., Seo, B., Koh, B. B. & Cho, S., 2020. Heating energy savings potential from retrofitting old apartments with an advanced double-skin façade system in cold climate. *Frontiers in Energy,* March, Volume 14, pp. 224-240.

[125] Stec, W. & van Passen, A., 2005. Symbiosis of the double skin façade with the HVAC system. *Energy and Buildings,* May, 37(5), pp. 461-469.

[126] Bueno, B., Street, M., Pflug, T. & Braesch, C., 2017. A co-simulation modelling approach for the assessment of a ventilated double-skin complex fenestration system coupled with a compact fan-coil unit. *Energy and Buildings,* September, Volume 151, pp. 18-27.

[127] Radmard, H. et al., 2020. Examining a numerical model validity for performance evaluation of a prototype solar oriented Double skin Façade: Estimating the technical potential for energy saving. *Solar Energy,* November, Volume 211, pp. 799-809.

[128] Seo, B., Beom, Y. & Jung, H. M. S. C., 2019. Application of Artificial Neural Network for the Optimum Control of HVAC Systems in Double-Skinned Office Buildings. *Energies,* 12(24), p. 4754.

[129] Peng, J. et al., 2016. Developing a method and simulation model for evaluating the overall energy performance of a ventilated semi-transparent photovoltaic double-skin facade. *Progress in Photovoltaics,* June, 24(6), pp. 781-799.

[130] Peng, J. et al., 2016. Numerical investigation of the energy saving potential of a semi-transparent photovoltaic double-skin facade in a cool-summer Mediterranean climate. *Applied Energy,* March, Volume 165, pp. 345-356.

[131] Preet, S. et al., 2020. Performance evaluation of photovoltaic double-skin facade with forced ventilation in the composite climate. *Journal of Building Engineering,* November, Volume 32, p. 101733.

[132] Ioannidis, Z., Buonomano, A., Athienitis, A. & Stathopoulos, T., 2017. Modeling of double skin façades integrating photovoltaic panels and automated roller shades: Analysis of the thermal and electrical performance. *Energy and Buildings,* November, Volume 154, pp. 618-632.

[133] Wang, M. et al., 2017. Comparison of energy performance between PV double skin facades and PV insulating glass units. *Applied Energy,* May, Volume 194, pp. 148-160.

[134] Zhu, L. et al., 2020. Comprehensive analysis of heat transfer of double-skin facades integrated high concentration photovoltaic (CPV-DSF). *Renewable Energy,* December, Volume 161, pp. 635-649.

[135] Lee, C.-s., Lee, H., Choi, M. & Yoon, J., 2019. Design optimization and experimental evaluation of photovoltaic double skin facade. *Energy and Buildings,* November, Volume 202, p. 109314.

[136] Elarga, H. et al., 2016. Thermal and electrical performance of an integrated PV-PCM system in double skin façades: A numerical study. *Solar Energy,* October, Volume 136, pp. 112-124.

[137] Yang, S. et al., 2020. Performance assessment of BIPV/T double-skin façade for various climate zones in Australia: Effects on energy consumption. *Solar Energy,* March, Volume 199, pp. 377-399.

[138] Shakouri, M. et al., 2022. Multi-objective 4E analysis for a building integrated photovoltaic thermal double skin Façade system, Solar Energy, Volume 233, 2022, Pages 408-420, ISSN 0038-092X, https://doi.org/10.1016/j.solener.2022.01.036.

[139] Sotelo-Salas, C., Escobar-del Pozo, C. & Esparza-Lopez, C. J., 2021. Thermal assessment of spray evaporative cooling in opaque double skin facade for cooling load reduction in hot arid climate. *Journal of Building Engineering,* June, Volume 38, p. 102156.

[140] Yan, S. et al., 2019. A method to describe the thermal property of pipe-embedded double-skin façade: Equivalent glass window. *Energy and Buildings,* July, Volume 195, pp. 33-44.

[141] Shen, C. & Li, X., 2016. Thermal performance of double skin façade with built-in pipes utilizing evaporative cooling water in cooling season. *Solar Energy,* November, Volume 137, pp. 55-65.

[142] Bielek, B., Klem, J. & Macak, M., 2019. Physical Cavity of a Double Skin Facade as a Source of Pre-Heated Air in the Winter Season for the Heat Recovery Unit of a Facade. *Slovak Journal of Engineering,* December, 27(4), pp. 7-10.

[143] Sung, U.-J. & Kim, S.-H., 2019. A Study on the Improvement of Double-Skin Facade Operation for Reducing Heating Load in Winter. *sustainability,* November, 11(22), p. 6238.

[144] Hou, K., Li, S. & Wang, H., 2020. Simulation and experimental verification of energy saving effect of passive preheating natural ventilation double skin façade. *Energy Exploration & Exploitation,* September, 39(1), p. 2021.

[145] Ioannidis, Z., Rounis, E.-D., Athienitis, A. & Stathopoulos, T., 2020. Double skin façade integrating semi-transparent photovoltaics: Experimental study on forced convection and heat recovery. *Applied Energy,* November, Volume 278, p. 115647.

[146] Alibaba, Halil Z., and Mesut B. Ozdeniz (2016). "Energy Performance and Thermal Comfort of Double-Skin and Single-Skin Facades in Warm-Climate Offices." Journal of Asian architecture and building engineering 15.3 (2016): 635–642. Web.

[147] Li, H., Zhong, K. & Zhai, Z. (., 2020. A new double-skin façade system integrated with TiO2 plates for decomposing BTEX. *Building and Environment,* August, Volume 180, p. 107037.

[148] Yahiaoui, A., 2020. Modeling and Control of Hybrid Ventilation in a Building With Double Skin Façade. *IEEE,* September, Volume 8, pp. 184172-184186.

[149] Kilaire, A, and M Stacey. "Design of a Prefabricated Passive and Active Double Skin Façade System for UK Offices." *Journal of Building Engineering* 12 (2017): 161–170. Web.

[150] Chow, C. L., 2013 “Full-Scale Burning Tests on Double-Skin Façade Fires.” *Fire and materials* 37.1 (2013): 17–34. Web.

[151] Chow, Cheuk Lun. “Spread of Smoke and Heat Along Narrow Air Cavity in Double-Skin Façade Fires.” Thermal science 18.2 (2014): 405–416. Web.

[152] Chow, C. L., S. S. Li, and D. X. Huang. “Apron Design for Protecting Double-Skin Façade Fires.” Fire and materials 39.3 (2015): 189–206. Web.

[153] Ghadamian, H. et al., 2012. Analytical solution for energy modeling of double skin façades building. *Energy and Buildings,* July, Volume 50, pp. 158-165.

[154] Valentin, D. et al., 2013. Assessment of the Economic and Environmental Impact of Double Glazed Facade Ventilation Systems in Mediterranean Climates. *Energies,* 6(10), pp. 5069-5087.

[155] Zomorodian, Z. S. & Tahsildoost, M., 2018. Energy and carbon analysis of double skin façades in the hot and dry climate. *Journal of Cleaner Production,* October, 197(1), pp. 85-96.

[156] Pomponi, F. & D'Amico, B., 2017. Holistic study of a timber double skin façade: Whole life carbon emissions and structural optimisation. *Building and Environment,* November, Volume 124, pp. 42-56.

[157] Lucchino, E. et al., 2021. Modelling double skin façades (DSFs) in whole-building energy simulation tools: Validation and inter-software comparison of a mechanically ventilated single-story DSF, Building and Environment, Volume 199, 2021, 107906, ISSN 0360-1323, https://doi.org/10.1016/j.buildenv.2021.107906.

[158] Office for National Statistics, “The rise of the UK warehouse and the “golden logistics triangle”,” 11 April 2022. [Online]. Available: https://www.gov.uk/government/statistics/the-rise-of-the-uk-warehouse-and-the-golden-logistics-triangle. [Accessed July 2022].

[159] Network Space, “Woodhouse Link, Woodhouse Mill, Sheffield,” 2022. [Online]. Available: http://www.networkspace.co.uk/services/development/woodhouse-link/. [Accessed July 2022].

[160] MEON, “Floor markings and your facility,” 2 March 19. [Online]. Available: https://meonuk.com/blogs/news/floor-markings-and-your-facility. [Accessed July 2022].

[161] C. a. E. M. Boonyaputthipong, “Stack Effect Ventilation in Different Climates,” *Journal of Building, Energy and Environment,* vol. 1, 2018.

[162] Iowa State University, “Iowa Environmental Mesonet,” 2022. [Online]. Available: https://mesonet.agron.iastate.edu/. [Accessed July 2022].

[163] ASHRAE, “ASHRAE Handbook of Fundamentals 2001,” ASHRAE, 2001.

[164] Solcast, 2024. Global solar irradiance data and PV system power output data. URL https://solcast.com/

[165] D. W. Etheridge, “Ventilation measurements at model scale in a turbulent flow,” *Building and Environment,* vol. 14, no. 1, pp. 53-64, 1979.

[166] D. W. Etheridge, Building Ventilation - Theory and Measurement, Chichester: John Wiley & Sons, 1996.

[167] AIVC, “Wind Pressure Coefficient,” 2022. [Online]. Available: https://www.aivc.org/keywords/wind-pressure-coefficient. [Accessed July 2022].

[168] British Standards, “BS6399 Annex A,” 2017.

[169] J. Holmes, “Wind Loading of Structures,” 2004.
[170] Sofotasiou, P., “Aerodynamic optimisation of sports stadiums towards wind comfort”, 2017.
[171] Simiu, E., and Scanlan, R. H., “Wind effects on structures: fundamentals and applications to design”, Wiley, 1996.
[172] Anderson, J.D. (2010) “Fundamentals of Aerodynamics”. McGraw-Hill Education
[173] Schlichting, H. & Gersten, K. (2016) “Boundary-Layer Theory”. Springer.
[174] Incropera, Frank P., and David P. DeWitt. 1990. *Introduction to Heat Transfer*. Second edition. New York: Wiley.
[175] Aguilar-Santana, Jorge Luis, Mariana Velasco-Carrasco, and Saffa Riffat. “Thermal Transmittance (U-Value) Evaluation of Innovative Window Technologies.” *Future cities and environment* 6.1 (2020): n. pag. Web.
[176] Euroclad Group. (n.d.) Elite 55. https://www.eurocladgroup.com/gb/en/products/wall-solutions/wall-systems/elite-55/
[177] M. Wood and L. Phil. M and Jesch, “Transparent insulation technology: a technical note,” *International Journal of Ambient Energy,* vol. 14, no. 3, pp. 117-122, 1993.
[178] A. M. Qahtan, “Thermal performance of a double-skin façade exposed to direct solar radiation in the tropical climate of Malaysia: A case study,” *Case Studies in Thermal Engineering,* vol. 14, no. 100419, 2019.
[179] J. Darkwa and Y. a. C. D. Li, “Heat transfer and air movement behaviour in a double-skin façade,” in *Centre for Sustainable Energy Technologies (CEST)*, Ningbo, 2019.
[180] Holman, J.P. (2009) Heat Transfer. 10th Edition, McGraw-Hill, New York.
[181] Mecalux. (n.d.) Conventional Pallet Racking. https://www.mecalux.co.uk/pallet-racking/conventional-pallet-racking
[182] Taylor, J.R. (1997) An Introduction to Error Analysis: The Study of Uncertainties in Physical Measurements. 2nd Edition, University Science Books, Sausalito.
[183] Dieck, R.H. (2007) Measurement Uncertainty: Methods and Applications. ISA.
[184] Devore, Jay L. 1995. *Probability and Statistics for Engineering and the Sciences*. 4th ed. Belmont: Duxbury Press.
[185] Roache, P. J. 1997, ‘Quantification of Uncertainty in Computational Fluid Dynamics. Annual Review of Fluid Mechanics’, Vol. 29, pp. 123-160
[186] Roache, P. J. 1998, ‘Verification and Validation in Computational Science and Engineering’, New Mexico: Hermosa Publishers
[187] H. Versteeg, W. Malalasekera 2007, An Introduction to Computational Fluid Dynamics: The Finite Volume Method - ISBN 10: 0131274988 - ISBN 13: 9780131274983 - Prentice Hall
[188] John Anderson 1995, Computational Fluid Dynamics McGraw-Hill Education; UK ed. edition (ISBN: 9780071132107)
[189] Ferziger, J.H. and Perić, M. 2002, Computational Methods for Fluid Dynamics, Springer Verlag, Berlin Heidelberg New York, 3rd edition.
[190] Richards, P.J. and Hoxey, R.P. 1993, ‘Appropriate boundary conditions for computational wind engineering models using the k-ε turbulence model’, *Journal of Wind Engineering and Industrial Aerodynamics*, Vol. 46 & 47, pp. 145-153

[191] Mochida, A., Tominaga, Y., Murakami, S., Yoshie, R., Ishihara, T. and R. Ooka 2002, “Comparison of various k- models and DSM to flow around a high rise building - report of AIJ cooperative project for CFD prediction of wind environment”, Wind & Structures, Vol. 5, No. 2-4, pp. 227-244

[192] Franke, Jörg, Antti Hellsten, Heinke Schlünzen, Bertrand Carissimo, David Grawe, István Goricsán, Zbyňek Jaňour and Ari Karppinen. “BEST PRACTICE GUIDELINE FOR THE CFD SIMULATION OF FLOWS IN THE URBAN ENVIRONMENT.” (2007).

[193] Whitaker,S. Introduction to Fluid Mechanics. Prentice-Hall; 1968.

[194] Turner JS. *Buoyancy Effects in Fluids*. Cambridge University Press; 1973.

[195] The Engineering Toolbox. (n.d). https://www.engineeringtoolbox.com/

[196] Anderson, D., Tannehill, J.C., Pletcher, R.H., Munipalli, R., & Shankar, V. (2020). Computational Fluid Mechanics and Heat Transfer (4th ed.). CRC Press. https://doi.org/10.1201/9781351124027

[197] Modest, F. M. (2013). Radiative Heat Transfer. Academic Press; 2013.

[198] ASHRAE. (2003) Ventilation for Acceptable Indoor Air Quality.

[199] Mei, L. et al. 2007. The influence of blinds on temperatures and air flows within ventilated double-skin facades. Conference article. University of Salford.

[200] Ahmadi, Javad et al. “Evaluating the Different Boundary Conditions to Simulate Airflow and Heat Transfer in Double-Skin Facade.” *Building simulation* 15.5 (2022): 799–815. Web.

[201] Wilcox, D. C.. 2006. “Turbulence Modelling for CFD, Volume 1”. Third edition. DCW Industries.

[202] Hanjalić K, Launder BE. A Reynolds stress model of turbulence and its application to thin shear flows. *Journal of Fluid Mechanics*. 1972;52(4):609-638. doi:10.1017/S002211207200268X

[203] Pope, S. B. (2000). *Turbulent Flows*. Cambridge: Cambridge University Press.

[204] AirFixture, “What is Stratified Air?,” 2022. [Online]. Available: https://airfixture.com/glossary/stratified-air. [Accessed July 2022].

[205] Airius, “What is destratification?,” 2022. [Online]. Available: https://www.airius.co.uk/all-resources/what-is-destratification/#:~:text=Destratification%20systems%20optimise%20heating%20by,systems%20evenly%20within%20the%20space.. [Accessed July 2022].

[206] Department of Energy, United States of America, “Quadrennial Technology Review: An Assessment of Energy Technologies and Research Opportunities,” DoE, USA, 2015.

[207] Shires, G. L. (2011). *Grashof Number*. Thermopedia. https://www.thermopedia.com/content/824/

[208] American Society of Heating, Refrigerating and Air-Conditioning Engineers (ASHRAE). (2020). *ANSI/ASHRAE Standard 55-2020: Thermal Environmental Conditions for Human Occupancy*. ASHRAE.

[209] M. Sohail, “An Attempt to Design a Naturally Ventilated Tower in Subtropical Climate of the Developing Country; Pakistan,” *Environmental and Climate Technologies,* vol. 21, pp. 47-67, 2017.

[210] Fire Protection Association. (2004). *RC38: Recommendations for frost protection measures for sprinklers*. Fire Protection Association.

[211] BSRIA. 2011 “Rules of Thumb. Guidelines for building services.” 5th edition.

[212] Department for Energy Security & Net Zero, U.K. Gov. 2024. “Price of fuels purchased by non-domestic consumers in the U.K.” Table 3.4.1.

[213] UK Government. "Government Conversion Factors for Company Reporting of Greenhouse Gas Emissions." *GOV.UK*, 8 July 2024, https://www.gov.uk/government/collections/government-conversion-factors-for-company-reporting.

[214] McSweeney, Robert. "England’s Growing Season Now Almost a Month Longer, Says Met Office." *Carbon Brief*, 23 March 2016, https://www.carbonbrief.org/englands-growing-season-now-almost-a-month-longer-says-met-office.

[215] Met Office. (2024). *Temperature extremes and records most affected by UK’s changing climate*. Met Office. https://www.metoffice.gov.uk/about-us/news-and-media/media-centre/weather-and-climate-news/2024/temperature-extremes-and-records-most-affected-by-uks-changing-climate

[216] UK Green Building Council. (n,d). Operational and Embodied Carbon Explainer Guide. UK GBC. https://ukgbc.org/wp-content/uploads/2023/02/operational-and-embodied-carbon-1.pdf

[217] European Aluminium. A Low Carbon Footprint. European Aluminium. https://european-aluminium.eu/projets/a-low-carbon-footprint/

[218] Carbon Cloud. Stainless Steel. Climate Hub. https://apps.carboncloud.com/climatehub/product-reports/id/1773163665238

[219] Saevarsdottir, G., Magnusson, T., Kvande, H. (2021). Reducing the Carbon Footprint: Primary Production of Aluminium and Silicon with Changing Energy Systems. Journal of Sustainable Metallurgy.

[220] Kelsey, C. (2018) Carbon Footprint advantages of HDPE Geomembranes. Geosynthetica. https://www.geosynthetica.com/carbon-footprint-hdpe-geomembranes-aug2018/

[221] Miller, S., Niessen, L., Heap, G. (2016) Rediscover Paint – Investigating Methods for the Expansion of Paint Reuse in Ireland. Environmental Protection Agency.

[222] CheckATrade. (2022) Cost to Build A Warehouse. https://www.checkatrade.com/blog/cost-guides/cost-build-warehouse/

Appendix

This appendix contains data to support the main text such as contextual warehouse benchmark calculations, vertical solar irradiance calculations, and data collection and calculations for wind-only, buoyancy-only, stratification and combined wind and buoyancy stages of the computational fluid dynamics model and tool build.

A.1 Contextual Warehouse Benchmark Calculations

To supplement the main text information provided in Chapter 1 regarding the gap in building regulation and design guidelines for warehouses in the UK, the following sections detail supporting calculations to discussions within the introduction of this thesis.

A.1.1 Minimum Ventilation Guidelines Analysis

The introduction explores the lack of clarity in building regulation for minimum ventilation requirements when it comes to large-space buildings such as warehouses. Below are the calculations that arrive to the values spoken about in the main text. The purpose of providing a comparison of ventilation requirements using outdoor air per person and air changes per hour is to highlight when these standards are applied to a large volume space with low occupancy, such as a warehouse, they will yield contrasting results. In the introduction of this thesis, a hypothetical scenario is explored for 20 workers in a 10,000m^3 warehouse space. Per CIBSE recommendations of 10L/s/person of outdoor air, the following ventilation requirement based on occupancy can be calculated for the hypothetical scenario:

$$Total\ outdoor\ air\ required = 20\ x\ 10\ L/s/person = 200\ L/s \qquad \text{(Equation A.1)}$$

Then, to see how this minimum outdoor air requirement translates to air changes per hour, the following is calculated:

$$Flow\ rate = \frac{200\ L/s}{1000} = 0.2\ m^3/s \qquad \text{(Equation A.2)}$$

$$ACH\ equivalent = \frac{3600 \cdot q}{volume} = \frac{3600 \cdot 0.2}{10{,}000} = 0.072ACH \qquad \text{(Equation A.3)}$$

In terms of whether a natural ventilation system is applicable to a building, according to CIBSE it should be able to deliver between 0.5 and 5ACH and therefore shows that the ventilation provided to satisfy occupancy would not satisfy these natural ventilation conditions. Taking both the lowest and highest value of 0.5ACH and 5ACH, the calculation can be reversed to find what occupancy equivalent is needed if designing outdoor air per person but also satisfying natural ventilation capacity. These results highlight why current British design guidelines need updating or clarity when it comes to unique spaces such as warehouses.

$$Occupancy\ equivalent = \left(\frac{ACH \cdot volume}{3600}\right) \cdot 1000 = \left(\frac{0.5 \cdot 10000}{3600}\right) \cdot 1000 = 139\ people \quad \text{(Equation A.4)}$$

$$Occupancy\ equivalent = \left(\frac{ACH \cdot volume}{3600}\right) \cdot 1000 = \left(\frac{5 \cdot 10000}{3600}\right) \cdot 1000 = 1389\ people \quad \text{(Equation A.5)}$$

A.1.2 Energy Consumption Benchmarks

The chosen case study warehouse did not have publicly available energy consumption data, so benchmarks had to be applied. The calculations below show what typical values of energy and carbon emissions a warehouse could use/emit. The CIBSE benchmark for warehouse electricity consumption is 50kWh/m^2/year, and the average sized warehouse in 2020 was 31,587m^2. Using these values, a rough estimate of annual energy consumption can be calculated:

$$Energy\ consumption = 50\ x\ 31{,}587 = 1.6Twh \quad \text{(Equation A.6)}$$

To provide a visual context of how large this quantity is, it can be compared to the annual electricity consumption for a UK home which is 3,940 kWh to find how many homes are equivalent to one warehouse's consumption:

$$Energy\ consumption\ equivalent = 1.6Twh\ /3{,}940kWh = 400\ homes \quad \text{(Equation A.7)}$$

A.2 Vertical Solar Irradiance Calculations

As the double skin façade is vertical, the global horizontal irradiance information from SolCast was converted to vertical irradiance. This was done utilising historical solar data recorded at solar noon from the years 2017-2021 for a representative month of each season in the UK. A highest and lowest value (above zero) was calculated so that an average for each season is

determined. The values for wall tilt angle and wall azimuth remain the same and the values for these are 90 degrees (1.57 radians), and 180 degrees (3.14 radians), respectively.

Table A.1 Vertical Solar Irradiance Data

		Vertical Irradiance (W/m2)		Sun elevation (degrees/radians)	Sun azimuth (degrees/radians)	Zenith (degrees/radians)
Winter	January 2021	Highest	744	15/0.26	176/3.07	75/1.31
		Lowest	17	18/0.31	177/3.09	72/1.26
	January 2020	Highest	725	14/0.24	176/3.07	76/1.33
		Lowest	4	16/0.28	175/3.05	74/1.29
	January 2019	Highest	767	18/0.31	177/3.09	72/1.26
		Lowest	99	19/0.33	177/3.09	71/1.24
	January 2018	Highest	697	19/0.33	177/3.09	71/1.24
		Lowest	32	14/0.24	175/3.05	76/1.33
	January 2017	Highest	743	18/0.31	177/3.09	72/1.26
		Lowest	59	15/0.26	175/3.05	75/1.31
Spring	April 2021	Highest	567	45/0.79	149/2.60	45/0.79
		Lowest	2	41/0.72	152/2.65	49/0.86
	April 2020	Highest	568	45/0/79	150/2.62	45/0.79
		Lowest	31	40/0/70	153/2.67	50/0.87
	April 2019	Highest	614	41/0.72	152/2.65	49/0.86
		Lowest	3	47/0.82	148/2.58	43/0.75
	April 2018	Highest	622	40/0.70	153/2.67	50/0.87
		Lowest	42	39/0.68	154/2.69	51/0.89
	April 2017	Highest	591	41/0.72	152/2.65	49/0.86
		Lowest	11	42/0.73	151/2.64	48/0.84
Summer	July 2021	Highest	394	55/0.96	147/2.57	35/0.61
		Lowest	1	54/0.94	148/2.58	36/0.63
	July 2020	Highest	418	55/0.96	146/2.55	35/0.61
		Lowest	5	53/0.93	148/2.58	37/0.65
	July 2019	Highest	388	56/0.98	145/2.53	34/0.59
		Lowest	3	53/0.93	148/2.58	37/0.65
	July 2018	Highest	416	56/0.98	145/2.53	34/0.59
		Lowest	10	54/0.94	147/2.57	36/0.63
	July 2017	Highest	398	56/0.98	145/2.53	34/0.59
		Lowest	2	53/0.93	148/2.58	37/0.65
Autumn	October 2021	Highest	741	26/0.45	169/2.95	64/1.12
		Lowest	56	33/0.58	169/2.95	57/0.99
	October 2020	Highest	363	24/0.42	169/2.95	66/1.15
		Lowest	10	28/0.49	169/2.95	62/1.08
	October 2019	Highest	746	33/0.58	169/2.95	57/0.99
		Lowest	55	28/0.49	169/2.95	62/1.08
	October 2018	Highest	728	31/0.54	169/2.95	59/1.03
		Lowest	20	34/0.59	169/2.95	56/0.98
	October 2017	Highest	744	23/0.40	169/2.95	67/1.17
		Lowest	6	24/0.42	169/2.95	66/1.15

A.3 Wind-Only Scenario Data Collection and Calculations

To support the main results in Chapter 4, the following sections have been included in this appendix and show either example calculations or measurement coordinates. The boundary conditions for both the small-scale and full-scale models include velocity inlet for the wind profile, default pressure outlet on the opposite side of the 5H, 5H, 15H domain based on a length of 72m. All warehouse surfaces are labelled.

A.3.1 Raw Data and Error analysis Examples

The table below takes the average of 5000 readings for each pressure tap point on each façade.

Table A.2 Differential Pressure Readings from ABL Wind Tunnel

Measurement points	DSF Outer skin		Back Facade		RHS Facade		LHS Facade		LHS Roof		RHS Roof	
	0°	180°	0°	180°	0°	180°	0°	180°	0°	180°	0°	180°
1	0.436	-1.702	-0.863	-0.771	-0.502	-0.485	-0.726	-0.394	-0.409	-0.737	-0.668	-0.158
2	1.132	-1.010	-0.513	-0.639	-0.543	-0.748	-0.709	-0.749	0.160	-0.463	-0.423	-0.081
3	-0.659	-0.333	-0.637	-0.745	-0.843	-0.436	-0.736	-0.556	-0.365	0.142	0.087	-0.745
4	0.190	-0.436	-0.888	-0.609	-0.495	-0.413	-0.815	-0.600	-0.543	0.055	-0.477	-1.000
5	0.426	-1.122	-0.684	-0.527	-0.522	-0.576	-0.882	-0.805	-0.512	-0.849	-0.463	-0.033
6	0.276	-1.392	-0.558	-0.667	-0.698	-0.612	-0.711	-0.424	0.342	-0.569	-0.621	0.072
7	0.191	-0.950	-0.800	-0.709	-0.773	-0.575	-0.656	-0.781	-0.474	0.010	0.066	-0.469
8	0.373	-1.041	-0.815	-0.600	-0.779	-0.535	-0.851	-0.837	-0.580	0.086	-0.476	-0.835
9	0.249	-1.006	-0.677	-0.847	-0.742	-0.559	-0.753	-0.711	-0.321	-0.840	-0.522	-0.050
10	-1.143	-1.485	-0.718	-0.521	-0.595	-0.663	-0.710	-0.574				
11	-1.207	-0.453	-0.753	-0.746	-0.654	-0.521	-0.729	-0.586				
12	-0.03	0.624	-0.778	-0.663	-0.802	-0.744	-1.057	-0.767				
13			-0.729	-0.632								
14			-0.669	-0.615								
Average	0.0195	-0.859	-0.720	-0.664	-0.662	-0.572	-0.779	-1.289	-0.300	-0.341	-0.389	-0.367

For standard deviation, the following results were obtained for the differential pressure readings for the DSF warehouse at a wind angle of 0 degrees, and these form the error bar graph in Figure 4.5 in Section 4.2.3.

Table A.3 Error Analysis of Differential Pressure Readings of the DSF Outer Skin

	Standard deviation (Pa)	Average differential pressure reading (Pa)	Maximum (Pa)	Minimum (Pa)
1	0.849	1.600	2.450	0.751
2	0.853	2.223	3.076	1.370
3	0.783	-0.191	0.593	-0.974
4	0.927	1.074	2.001	0.147
5	0.648	0.273	0.921	-0.376
6	0.650	0.179	0.829	-0.471
7	0.660	0.108	0.768	-0.552
8	0.668	0.213	0.881	-0.455
9	0.648	0.136	0.784	-0.512
10	0.650	0.125	0.775	-0.526
11	0.652	0.135	0.787	-0.517
12	0.651	0.138	0.789	-0.513
Average:	0.720	0.501	1.221	-0.219

A.3.2 Reference Pressure and Velocity Measurements

These values were taken off-centre to the airflow stream at the position of the pitot tube in the wind tunnel test section, 0.5m ahead of the scaled model and 0.38m from the viewing window. Both total and the difference in pressure across the pitot and static port were read from the pitot tube connected to a micromanometer. The results are in Tables A.4 and A.5 below.

Table A.4 Micromanometer Total Pressure Readings

	Micromanometer Total Pressure Reading (mmH_2O)							Pressure (Pa)
	1	2	3	4	5	6	Average	
1m/s	0.019	0.019	0.020	0.021	0.020	0.020	0.0198	0.19
2m/s	0.092	0.090	0.100	0.094	0.091	0.101	0.0947	0.93
3m/s	0.217	0.174	0.220	0.230	0.189	0.189	0.203	1.99
4m/s	0.337	0.316	0.407	0.367	0.376	0.330	0.336	3.49
5m/s	0.552	0.608	0.601	0.566	0.546	0.650	0.587	5.76

Table A.5 Micromanometer Pitot-Static Difference Pressure Readings

	Micromanometer Pitot-Static Difference Pressure Reading (mmH_2O)							Pressure (Pa)
	1	2	3	4	5	6	Average	
1m/s	0.003	0.003	0.006	0.002	0.001	0.000	0.0025	0.0245
2m/s	-0.020	-0.010	-0.021	-0.021	-0.016	-0.031	0.0198	0.194
3m/s	-0.173	-0.216	-0.206	-0.194	-0.196	-0.183	0.195	1.909
4m/s	-0.426	-0.468	-0.389	-0.439	-0.356	-0.462	0.423	4.15
5m/s	-0.482	-0.695	-0.575	-0.589	-0.477	-0.560	0.563	5.52

A.3.3 Silsoe Cube Validation

In the absence of relevant warehouse literature for Cp comparison, the study of the Silsoe Cube in an atmospheric boundary layer wind tunnel was used as a substitute to validate the CFD modelling process. The results of the study by [A-1] are in Figure A.1 whilst the CFD recreation is in Figure A.2 where (a) is for a wind angle of 90 degrees and (b) is 45 degrees.

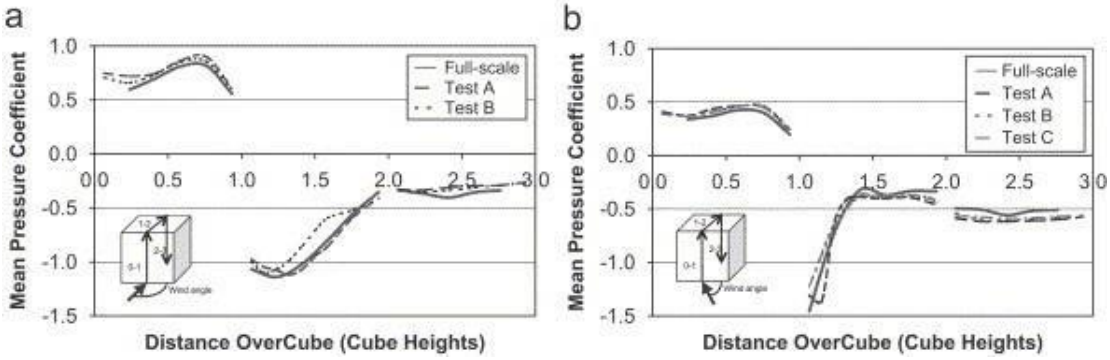


Figure A.1 Mean Pressure Coefficients of the 1:40 Scale Silsoe Cube for (a) 90 and (45) degrees

Simplifications include taking only an average pressure coefficient across the central line of each façade, rather than plotting each individual point as the primary objective was to achieve visual and magnitude similarity, rather than a best match.

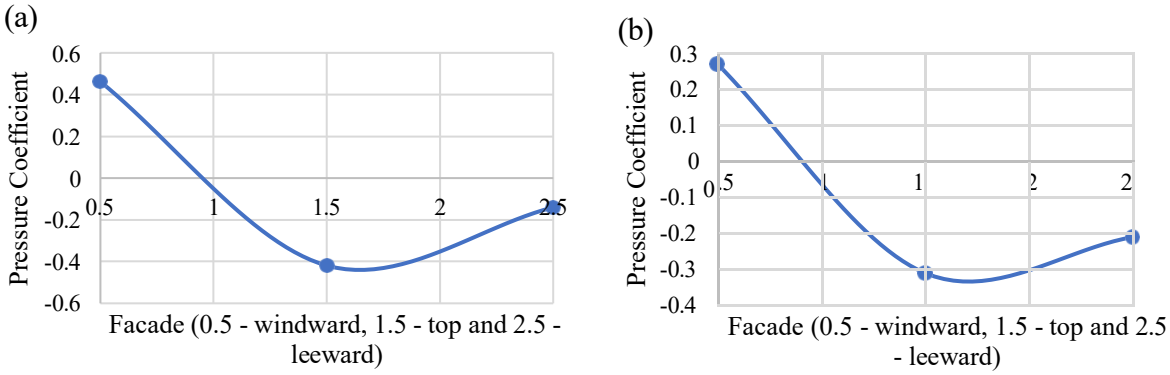


Figure A.2 CFD Recreation of the Mean Pressure Coefficients of the 1:40 Scale Silsoe Cube for (a) 90 and (45) degrees

Whilst not a perfect match, these results show that the Cp has an overall larger magnitude for the 90 degrees angle, and similar trend whilst the 45 degrees produced a smaller magnitude. Overall, they show that the main-text CFD model is correctly modelling wind and pressure.

A.3.4 Lab-Scale Wind Profiles

The preliminary wind profile used in the computational model was calculated using the data below whereby the maximum height was halfway up the test section where maximum velocity typically occurs. The wind shear exponent starts at 0.18 which is halfway between an urban and open country terrain to indicate a semi-urban environment. It also includes non- dimensional height and velocity terms which are used to normalize the wind profile so it can be compared against other conditions. This same method was used to calculate further wind profiles in Chapters 4 and 7.

Table A.4 Wind Tunnel Velocity Profile

Height (m)	Reference velocity (m/s)	Reference height (m)	Velocity (m/s)	Wind shear exponent	U/Uref	H/Href
0	5	0.9	0.000	0.18	0.000	0.000
0.01	5	0.9	2.224	0.18	0.011	0.445
0.012	5	0.9	2.299	0.18	0.013	0.460
0.015	5	0.9	2.393	0.18	0.017	0.479
0.018	5	0.9	2.473	0.18	0.020	0.495
0.022	5	0.9	2.564	0.18	0.024	0.513
0.026	5	0.9	2.642	0.18	0.029	0.528
0.031	5	0.9	2.727	0.18	0.034	0.545
0.037	5	0.9	2.815	0.18	0.041	0.563
0.044	5	0.9	2.904	0.18	0.049	0.581
0.052	5	0.9	2.993	0.18	0.058	0.599
0.062	5	0.9	3.089	0.18	0.069	0.618
0.073	5	0.9	3.181	0.18	0.081	0.636
0.086	5	0.9	3.277	0.18	0.096	0.655
0.102	5	0.9	3.379	0.18	0.113	0.676
0.12	5	0.9	3.479	0.18	0.133	0.696
0.141	5	0.9	3.582	0.18	0.157	0.716
0.165	5	0.9	3.684	0.18	0.183	0.737
0.194	5	0.9	3.793	0.18	0.216	0.759
0.227	5	0.9	3.902	0.18	0.252	0.780
0.9	5	0.9	5.000	0.18	1.000	1.000
1	5	0.9	5.096	0.18	1.111	1.019
1.1	5	0.9	5.184	0.18	1.222	1.037
1.2	5	0.9	5.266	0.18	1.333	1.053
1.3	5	0.9	5.342	0.18	1.444	1.068
1.6	5	0.9	5.546	0.18	1.778	1.109
1.9	5	0.9	5.720	0.18	2.111	1.144

A.3.5 Full-Scale Wind Profiles

The full-scale wind profiles refer to real meteorological wind data obtained for the chosen case study climate of Nottingham for each season with representative months of January, April, July and October. A range of wind shear exponents have been applied from 0.16 to 0.22. These four wind profiles were used to create user-defined wind profile files which were imported into the CFD model and applied at the velocity inlet boundary condition.

Table A.5 Full-scale Velocity Profile for Winter

WINTER - JANUARY - COLDEST DAY						
H	U_ref	H_ref	U (0.18)	U(0.20)	U(0.16)	U (0.22)
0.5	7.22	10	4.211	3.97	4.47	3.74
1	7.22	10	4.770	4.56	5.00	4.35
1.5	7.22	10	5.131	4.94	5.33	4.76
2	7.22	10	5.404	5.23	5.58	5.07
2.5	7.22	10	5.626	5.47	5.78	5.32
3	7.22	10	5.813	5.67	5.95	5.54
3.5	7.22	10	5.977	5.85	6.10	5.73
4	7.22	10	6.122	6.01	6.24	5.90
4.5	7.22	10	6.253	6.15	6.35	6.06
5	7.22	10	6.373	6.29	6.46	6.20
5.5	7.22	10	6.483	6.41	6.56	6.33
6	7.22	10	6.586	6.52	6.65	6.45
6.5	7.22	10	6.681	6.62	6.74	6.57
7	7.22	10	6.771	6.72	6.82	6.68
7.5	7.22	10	6.856	6.82	6.90	6.78
8	7.22	10	6.936	6.90	6.97	6.87
8.5	7.22	10	7.012	6.99	7.03	6.97
9	7.22	10	7.084	7.07	7.10	7.05
9.5	7.22	10	7.154	7.15	7.16	7.14
10	7.22	10	7.220	7.22	7.22	7.22
10.5	7.22	10	7.284	7.29	7.28	7.30
11	7.22	10	7.345	7.36	7.33	7.37
12	7.22	10	7.461	7.49	7.43	7.52
14	7.22	10	7.671	7.72	7.62	7.77
16	7.22	10	7.857	7.93	7.78	8.01
18	7.22	10	8.026	8.12	7.93	8.22
20	7.22	10	8.179	8.29	8.07	8.41
25	7.22	10	8.515	8.67	8.36	8.83
30	7.22	10	8.799	8.99	8.61	9.19
40	7.22	10	9.266	9.53	9.01	9.79
50	7.22	10	9.646	9.96	9.34	10.29
60	7.22	10	9.968	10.33	9.62	10.71

Table A.6 Full-scale Velocity Profile for Summer

SUMMER - JULY- HOTTEST DAY						
H	U_ref	H_ref	U (0.18)	U(0.20)	U(0.16)	U (0.22)
0.5	7.78	10	4.537	4.27	4.82	4.02
1	7.78	10	5.140	4.91	5.38	4.69
1.5	7.78	10	5.529	5.32	5.74	5.13
2	7.78	10	5.823	5.64	6.01	5.46
2.5	7.78	10	6.062	5.90	6.23	5.73
3	7.78	10	6.264	6.12	6.42	5.97
3.5	7.78	10	6.440	6.31	6.58	6.18
4	7.78	10	6.597	6.48	6.72	6.36
4.5	7.78	10	6.738	6.63	6.85	6.53
5	7.78	10	6.867	6.77	6.96	6.68
5.5	7.78	10	6.986	6.90	7.07	6.82
6	7.78	10	7.097	7.02	7.17	6.95
6.5	7.78	10	7.200	7.14	7.26	7.08
7	7.78	10	7.296	7.24	7.35	7.19
7.5	7.78	10	7.387	7.35	7.43	7.30
8	7.78	10	7.474	7.44	7.51	7.41
8.5	7.78	10	7.556	7.53	7.58	7.51
9	7.78	10	7.634	7.62	7.65	7.60
9.5	7.78	10	7.708	7.70	7.72	7.69
10	7.78	10	7.780	7.78	7.78	7.78
10.5	7.78	10	7.849	7.86	7.84	7.86
11	7.78	10	7.915	7.93	7.90	7.94
12	7.78	10	8.040	8.07	8.01	8.10

14	7.78	10	8.266	8.32	8.21	8.38
16	7.78	10	8.467	8.55	8.39	8.63
18	7.78	10	8.648	8.75	8.55	8.85
20	7.78	10	8.814	8.94	8.69	9.06
25	7.78	10	9.175	9.34	9.01	9.52
30	7.78	10	9.481	9.69	9.28	9.91
40	7.78	10	9.985	10.27	9.71	10.55
50	7.78	10	10.394	10.73	10.07	11.09
60	7.78	10	10.741	11.13	10.36	11.54

Table A.7 Full-scale Velocity Profile for April (Intermediate)

APRIL - AVERAGE						
H	U_ref	H_ref	U (0.18)	U(0.20)	U(0.16)	U (0.22)
0.5	4.72	10	2.753	2.59	2.92	2.44
1	4.72	10	3.118	2.98	3.27	2.84
1.5	4.72	10	3.355	3.23	3.48	3.11
2	4.72	10	3.533	3.42	3.65	3.31
2.5	4.72	10	3.678	3.58	3.78	3.48
3	4.72	10	3.800	3.71	3.89	3.62
3.5	4.72	10	3.907	3.83	3.99	3.75
4	4.72	10	4.002	3.93	4.08	3.86
4.5	4.72	10	4.088	4.02	4.15	3.96
5	4.72	10	4.166	4.11	4.22	4.05
5.5	4.72	10	4.238	4.19	4.29	4.14
6	4.72	10	4.305	4.26	4.35	4.22
6.5	4.72	10	4.368	4.33	4.41	4.29
7	4.72	10	4.426	4.40	4.46	4.36
7.5	4.72	10	4.482	4.46	4.51	4.43
8	4.72	10	4.534	4.51	4.55	4.49
8.5	4.72	10	4.584	4.57	4.60	4.55
9	4.72	10	4.631	4.62	4.64	4.61
9.5	4.72	10	4.677	4.67	4.68	4.67
10	4.72	10	4.720	4.72	4.72	4.72
10.5	4.72	10	4.762	4.77	4.76	4.77
11	4.72	10	4.802	4.81	4.79	4.82
12	4.72	10	4.877	4.90	4.86	4.91
14	4.72	10	5.015	5.05	4.98	5.08
16	4.72	10	5.137	5.19	5.09	5.23
18	4.72	10	5.247	5.31	5.19	5.37
20	4.72	10	5.347	5.42	5.27	5.50
25	4.72	10	5.566	5.67	5.47	5.77
30	4.72	10	5.752	5.88	5.63	6.01
40	4.72	10	6.058	6.23	5.89	6.40
50	4.72	10	6.306	6.51	6.11	6.73
60	4.72	10	6.516	6.75	6.29	7.00

Table A.8 Full-scale Velocity Profile for October (Intermediate)

OCTOBER - AVERAGE						
H	U_ref	H_ref	U (0.18)	U(0.20)	U(0.16)	U (0.22)
0.5	3.6	10	2.100	1.98	2.23	1.86
1	3.6	10	2.378	2.27	2.49	2.17
1.5	3.6	10	2.559	2.46	2.66	2.37
2	3.6	10	2.695	2.61	2.78	2.53
2.5	3.6	10	2.805	2.73	2.88	2.65
3	3.6	10	2.899	2.83	2.97	2.76
3.5	3.6	10	2.980	2.92	3.04	2.86
4	3.6	10	3.053	3.00	3.11	2.94
4.5	3.6	10	3.118	3.07	3.17	3.02
5	3.6	10	3.178	3.13	3.22	3.09
5.5	3.6	10	3.233	3.19	3.27	3.16
6	3.6	10	3.284	3.25	3.32	3.22
6.5	3.6	10	3.331	3.30	3.36	3.27

7	3.6	10	3.376	3.35	3.40	3.33
7.5	3.6	10	3.418	3.40	3.44	3.38
8	3.6	10	3.458	3.44	3.47	3.43
8.5	3.6	10	3.496	3.48	3.51	3.47
9	3.6	10	3.532	3.52	3.54	3.52
9.5	3.6	10	3.567	3.56	3.57	3.56
10	3.6	10	3.600	3.60	3.60	3.60
10.5	3.6	10	3.632	3.64	3.63	3.64
11	3.6	10	3.662	3.67	3.66	3.68
12	3.6	10	3.720	3.73	3.71	3.75
14	3.6	10	3.825	3.85	3.80	3.88
16	3.6	10	3.918	3.95	3.88	3.99
18	3.6	10	4.002	4.05	3.95	4.10
20	3.6	10	4.078	4.14	4.02	4.19
25	3.6	10	4.246	4.32	4.17	4.40
30	3.6	10	4.387	4.48	4.29	4.58
40	3.6	10	4.620	4.75	4.49	4.88
50	3.6	10	4.810	4.97	4.66	5.13
60	3.6	10	4.970	5.15	4.80	5.34

A.3.6 Neutral Pressure Height Readings

The supplementary data for the neutral pressure height analysis is provided in the tables below for the DSF warehouse in each season.

Table A.9 External and Internal Pressure Readings for all Seasons

	January (winter)		April (spring)		July (summer)		October (Autumn)	
Vertical Height (m)	External pressure (Pa)	Internal pressure (Pa)	External pressure (Pa)	Internal pressure (Pa)	External pressure (Pa)	Internal pressure (Pa)	External pressure (Pa)	Internal pressure (Pa)
0.5	1.270	1.267	0.562	0.534	1.464	1.368	0.337	0.290
1	1.270	1.267	0.562	0.533	1.464	1.365	0.337	0.290
2	1.270	1.264	0.562	0.532	1.464	1.360	0.337	0.290
3	1.270	1.260	0.562	0.530	1.464	1.352	0.337	0.289
4	1.270	1.256	0.562	0.527	1.464	1.338	0.337	0.288
5	0.972	1.252	0.438	0.526	1.124	1.331	0.262	0.287
6	0.972	1.254	0.438	0.523	1.124	1.332	0.262	0.287
7	0.972	1.260	0.438	0.522	1.124	1.341	0.262	0.287
8	0.972	1.261	0.438	0.524	1.124	1.345	0.262	0.287
9	1.077	1.276	0.480	0.518	1.236	1.365	0.287	0.290
10	1.077	1.278	0.480	0.519	1.236	1.371	0.287	0.292
11	1.077	1.275	0.480	0.523	1.236	1.378	0.287	0.293

A.3.7 Measurement Coordinates

The table below details the CFD coordinates relative to each pressure tap location on the DSF outer skin, roof, LHS and RHS sides and front and back facades, at 1:50 lab scale and full scale.

Table A.10 CFD Coordinate Positions of Pressure Tap Locations (1:50 and Full-Scale)

Scanivalve point	Tap no.	1:50 Lab Scale			Full-scale		
		X	Y	Z	X_50	Y_50	Z_50
1	RP6	-0.365	0.1	0.27	-18.25	5	13.5
2	RP17	-0.365	0.175	-0.451	-18.25	8.75	-22.55
3	RP15/16	-0.365	0.1	-0.271	-18.25	5	-13.55
4	RP10	-0.365	0.025	0.09	-18.25	1.25	4.5

5	RP4	-0.365	0.025	0.45	-18.25	1.25	22.5
6	RP14	-0.365	0.175	-0.271	-18.25	8.75	-13.55
7	RP8	-0.365	0.175	0.09	-18.25	8.75	4.5
8	RP19	-0.365	0.025	-0.451	-18.25	1.25	-22.55
9	RP20	-0.365	0.1	-0.6	-18.25	5	-30
10	RP2	-0.365	0.175	0.45	-18.25	8.75	22.5
11	RP1	-0.365	0.1	0.63	-18.25	5	31.5
43	RP12	-0.365	0.1	-0.09	-18.25	5	-4.5
12	BP3	-0.346	0.025	-0.7025	-17.3	1.25	-35.125
13	BP13	-0.136	0.105	-0.7025	-6.8	5.25	-35.125
14	BP25	0.074	0.025	-0.7025	3.7	1.25	-35.125
15	BP30	0.179	0.105	-0.7025	8.95	5.25	-35.125
16	BP19	-0.031	0.105	-0.7025	-1.55	5.25	-35.125
17	BP35	0.269	0.105	-0.7025	13.45	5.25	-35.125
18	BP9	-0.241	0.025	-0.7025	-12.05	1.25	-35.125
19	BP31	0.179	0.025	-0.7025	8.95	1.25	-35.125
20	BP14	-0.136	0.025	-0.7025	-6.8	1.25	-35.125
21	BP20	-0.031	0.025	-0.7025	-1.55	1.25	-35.125
22	BP2	-0.346	0.105	-0.7025	-17.3	5.25	-35.125
23	BP36	0.269	0.025	-0.7025	13.45	1.25	-35.125
24	BP8	-0.241	0.105	-0.7025	-12.05	5.25	-35.125
25	BP24	0.074	0.105	-0.7025	3.7	5.25	-35.125
26	FP18	0.02	0.105	0.7025	1	5.25	35.125
27	FP16	0.072	0.025	0.7025	3.6	1.25	35.125
28	FP24	-0.084	0.105	0.7025	-4.2	5.25	35.125
29	FP33	-0.24	0.025	0.7025	-12	1.25	35.125
30	FP2	0.333	0.105	0.7025	16.65	5.25	35.125
31	FP22	-0.026	0.025	0.7025	-1.3	1.25	35.125
32	FP13	0.124	0.105	0.7025	6.2	5.25	35.125
33	FP29	-0.188	0.105	0.7025	-9.4	5.25	35.125
34	FP5	0.28	0.025	0.7025	14	1.25	35.125
35	FP7	0.228	0.105	0.7025	11.4	5.25	35.125
36	FP27	-0.136	0.025	0.7025	-6.8	1.25	35.125
37	FP11	0.176	0.025	0.7025	8.8	1.25	35.125
38	LP10	0.365	0.025	0.09	18.25	1.25	4.5
39	LP8	0.365	0.175	0.09	18.25	8.75	4.5
40	LP6	0.365	0.1	0.27	18.25	5	13.5
41	LP1	0.365	0.1	0.63	18.25	5	31.5
42	LP14	0.365	0.175	-0.27	18.25	8.75	-13.5
44	LP4	0.365	0.025	0.45	18.25	1.25	22.5
45	LP16	0.365	0.025	-0.27	18.25	1.25	-13.5
46	LP17	0.365	0.175	-0.45	18.25	8.75	-22.5
47	LP2	0.365	0.175	0.45	18.25	8.75	22.5
48	LP12	0.365	0.1	-0.09	18.25	5	-4.5
49	LP19	0.365	0.025	-0.45	18.25	1.25	-22.5
50	LP20	0.365	0.1	-0.595	18.25	5	-29.75
51	D1	-0.299	0.1	0.725	-14.95	5	36.25
52	D2	-0.246	0.175	0.725	-12.3	8.75	36.25
56	D3	-0.193	0.1	0.725	-9.65	5	36.25
54	D4	-0.14	0.175	0.725	-7	8.75	36.25
55	D6	-0.034	0.1	0.725	-1.7	5	36.25
53	D7	0.019	0.175	0.725	0.95	8.75	36.25
57	D8	0.072	0.1	0.725	3.6	5	36.25
58	D9	0.125	0.175	0.725	6.25	8.75	36.25
59	D10	0.178	0.1	0.725	8.9	5	36.25
60	D11	0.231	0.175	0.725	11.55	8.75	36.25
61	D12	0.283	0.1	0.725	14.15	5	36.25
62	D13	0.336	0.175	0.725	16.8	8.75	36.25
49	TP13	-0.18	0.22	-0.2	-9	11	-10
50	TP12	-0.28	0.21	-0.33	-14	10.5	-16.5
51	TP15	-0.28	0.21	0.02	-14	10.5	1
52	TP10	-0.18	0.22	-0.55	-9	11	-27.5
53	TP11	-0.09	0.23	-0.33	-4.5	11.5	-16.5
54	TP14	-0.09	0.23	0.02	-4.5	11.5	1

55	TP18	-0.28	0.21	0.37	-14	10.5	18.5
56	TP16	-0.18	0.22	0.15	-9	11	7.5
57	TP17	-0.09	0.23	0.37	-4.5	11.5	18.5
1	TP5	0.09	0.23	0.02	4.5	11.5	1
2	TP9	0.28	0.21	-0.33	14	10.5	-16.5
3	TP7	0.18	0.22	-0.15	9	11	-7.5
4	TP2	0.09	0.23	0.37	4.5	11.5	18.5
5	TP6	0.28	0.21	0.02	14	10.5	1
6	TP8	0.09	0.23	-0.33	4.5	11.5	-16.5
7	TP1	0.18	0.22	0.55	9	11	27.5
8	TP4	0.18	0.22	0.2	9	11	10
9	TP3	0.28	0.21	0.37	14	10.5	18.5

The coordinates for measurements taken at each inlet on the front façade, each outlet on the back façade of the warehouse, occupant level points and external and internal pressure to collect ventilation data are in the tables A.11-A.14 below.

Table A.11 CFD Coordinate Positions of Full-Scale Warehouse Inlet Openings Readings

	Inlet 1 (LHS)				Inlet 2 (middle)				Inlet 3 (RHS)			
		x	y	z		x	y	z		x	y	z
bottom	i1p1	-11.27	9.15	35.13	I2p1	-1.2	9.15	35.13	I3p1	9.75	9.15	35.13
middle	i1p2	-11.27	9.35	35.13	I2p2	-1.2	9.35	35.13	I3p2	9.75	9.35	35.13
top	i1p3	-11.27	9.55	35.13	I2p3	-1.2	9.55	35.13	I3p3	9.75	9.55	35.13
bottom	i1p4	-10.15	9.15	35.13	I2p4	0.2	9.15	35.13	I3p4	10.95	9.15	35.13
middle	i1p5	-10.15	9.35	35.13	I2p5	0.2	9.35	35.13	I3p5	10.95	9.35	35.13
top	i1p6	-10.15	9.55	35.13	I2p6	0.2	9.55	35.13	I3p6	10.95	9.55	35.13
bottom	i1p7	-8.9	9.15	35.13	I2p7	1.6	9.15	35.13	I3p7	12.15	9.15	35.13
middle	i1p8	-8.9	9.35	35.13	I2p8	1.6	9.35	35.13	I3p8	12.15	9.35	35.13
top	i1p9	-8.9	9.55	35.13	I2p9	1.6	9.55	35.13	I3p9	12.15	9.55	35.13

Table A.12 CFD Coordinate Positions of Full-Scale Warehouse Outlet Openings Readings

	Outlet 3 (LHS)				Outlet 2 (middle)				Outlet 1 (RHS)			
		x	y	z		x	y	z		x	y	z
bottom	o1p1	9.75	9.15	-35.13	o2p1	-1.2	9.15	-35.13	o3p1	-11.27	9.15	-35.13
middle	o1p2	9.75	9.35	-35.13	o2p2	-1.2	9.35	-35.13	o3p2	-11.27	9.35	-35.13
top	o1p3	9.75	9.55	-35.13	o2p3	-1.2	9.55	-35.13	o3p3	-11.27	9.55	-35.13
bottom	o1p4	10.95	9.15	-35.13	o2p4	0.2	9.15	-35.13	o3p4	-10.15	9.15	-35.13
middle	o1p5	10.95	9.35	-35.13	o2p5	0.2	9.35	-35.13	o3p5	-10.15	9.35	-35.13
top	o1p6	10.95	9.55	-35.13	o2p6	0.2	9.55	-35.13	o3p6	-10.15	9.55	-35.13
bottom	o1p7	12.15	9.15	-35.13	o2p7	1.6	9.15	-35.13	o3p7	-8.9	9.15	-35.13
middle	o1p8	12.15	9.35	-35.13	o2p8	1.6	9.35	-35.13	o3p8	-8.9	9.35	-35.13
top	o1p9	12.15	9.55	-35.13	o2p9	1.6	9.55	-35.13	o3p9	-8.9	9.55	-35.13

Table A.13 CFD Coordinate Positions of Full-Scale Warehouse Occupant Level Readings

	x	y	z
ocp1	-11.45	2	28
ocp2	-11.45	2	0
ocp3	-11.45	2	-28
ocp4	0	2	28
ocp5	0	2	0
ocp6	0	2	-28
ocp7	11.45	2	28
ocp8	11.45	2	0
ocp9	11.45	2	-28

Table A.14 CFD Coordinate Positions of Full-Scale Warehouse External and Internal Pressure Readings

External pressure points				Internal pressure points			
	X	Y	Z		X	Y	Z
EP1	0	0.5	180	IP1	0	0.5	0
EP2	0	1	180	IP2	0	1	0
EP3	0	2	180	IP3	0	2	0
EP4	0	3	180	IP4	0	3	0
EP5	0	4	180	IP5	0	4	0
EP6	0	5	180	IP6	0	5	0
EP7	0	6	180	IP7	0	6	0
EP8	0	7	180	IP8	0	7	0
EP9	0	8	180	IP9	0	8	0
EP10	0	9	180	IP10	0	9	0
EP11	0	10	180	IP11	0	10	0
EP12	0	11	180	IP12	0	11	0

Table A.15 CFD Coordinate Positions of Full-Scale DSF Width Positions

	LHS Opening		Middle Opening		RHS Opening	
X	8	8	18	18	28	28
Y	9.87	0.91	9.87	0.91	9.87	0.91
Z	0.1	0.1	0.1	0.1	0.1	0.1

A.3.8 Air Changes Per Hour at Occupant Level

$$ACH_{warehouse} = \frac{(0.123 \cdot 2520) \cdot 3600}{27720} = 40 \quad \text{(Equation A.8)}$$

$$ACH_{dsfwarehouse} = \frac{(0.115 \cdot 2520) \cdot 3600}{27720} = 37 \quad \text{(Equation A.9)}$$

A.3.9 Performance Tool Example

An example calculation for the wind-only analytical part of the performance tool for a DSF warehouse has been included here as reference. The data applied is for the winter conditions whereby the full-scale wind profile applied to the CFD model is detailed in A.2.3. Using Equation A.8 for wind pressure, the following is calculated for winter where air density is 1.225 kg/m^3, cavity air velocity is 1.880m/s, and outer and inner pressure coefficients are 0.268 and 234, respectively:

$$P_{wind} = \frac{1}{2} \cdot 1.225 \cdot 1.880^2 \cdot (0.268 - 0.234) = 0.074Pa \quad \text{(Equation A.10)}$$

Then, Equations A.9 and A.10 for wind-only volumetric flow rate, and outdoor air are calculated using the above wind pressure where the cavity depth is 0.2m and cavity width is 36m:

$$Q_{wind} = 0.2 \cdot 36 \cdot \sqrt{\frac{2 \cdot 0.074}{1.225}} = 2.5\, m^3/s \quad \text{(Equation A.11)}$$

$$Fresh\ air_{wind} = 2.5\, m^3/s \cdot 1000 = 2500\, L/s \quad \text{(Equation A.12)}$$

A.4 Buoyancy-Only Scenario Data Collection and Calculations

To support the main results in Chapter 5, the following sections have been included in this appendix and show either example calculations or measurement coordinates.

A.4.1 Raw Experimental Data and Error Analysis

Table A.16 Average Temperature and Velocity Readings from the Climate Chamber

	Cavity temperature (°C)			Cavity velocity (m/s)		
	Winter	Intermediate	Summer	Winter	Intermediate	Summer
Fully open	13.32	17.75	26.85	0.0025	0.0038	0.0168
25% front	11.91	18.71	27.44	0.0037	0.0061	0.0475
50% front	12.42	18.82	28.42	0.0042	0.0089	0.0102
75% front	15.89	19.84	28.05	0.0085	0.0090	0.0063
25% back	12.34	19.82	27.35	0.004	0.008	0.0549
50% back	11.67	19.44	27.52	0.0043	0.0076	0.0133
75% back	16.04	19.34	27.82	0.0125	0.0099	0.0065

Table A.17 Standard Deviation of Equipment used in Climate Chamber Experiment

Equipment	Standard deviation
Anemometer type-902R (A902R)	0.006
Anemometer type-901R (A901R)	0.001
Heat Fluxmeter on Outer Skin -External (OF1)	2.375
Heat Fluxmeter on Outer Skin – Internal (OF2)	3.489
Heat Fluxmeter on Inner Skin - External (IF1)	1.261
Heat Fluxmeter on Inner Skin – Internal (IF2)	1.652
PT-100 type Resistive Temperature Detector on Outer Skin (RTD TO1)	0.344
PT-100 type Resistive Temperature Detector on Outer Skin (RTD TO8)	0.367
PT-100 type Resistive Temperature Detector in Cavity (RTD CT8)	0.139
PT-100 type Resistive Temperature Detector in Cavity (RTD CT7)	0.141
PT-100 type Resistive Temperature Detector on Inner Skin (RTD TI2)	0.312
PT-100 type Resistive Temperature Detector on Inner Skin (RTD TI1)	0.467
Pyranometer	1.80

A.4.2 Mei. et. al. Model and Set-Up

As part of the preliminary validation of the buoyancy-only CFD model, an initial model was recreated to reflect the experimental set-up from Mei. et al. and the details of how this was achieved in ANSYS Fluent are below.

Table A.18 CFD Model Set-up for Validation against Literature

General	Pressure-based solver Absolute velocity formulation Steady time Gravity ON -9.81
Models	Energy ON Viscous – Standard k-e, Enhanced Wall function (pressure gradient and thermal effects); full buoyancy effects
Materials	**Air:** 1.2047kg/m3 (Boussinesq density); 1006.1 j/kgK (specific heat); 0.0255 w/mk (thermal conductivity); 1.8205e-05 kg/ms (viscosity); 0.00341 (thermal expansion coefficient) **Aluminium:** 2719 kg/m3 (density); 871j/kgk (specific heat); 202.4 w/mk (thermal conductivity) **Outer and inner glass:** 2500kg/m3 (density); 840j/kgk (specific heat); 1.7w/mk (thermal conductivity)

Cell zone conditions	**Air:** 0.159w/m3 (energy source term) **Outer glass:** 29,976.74w/m3 (energy source term) **Inner glass layer 1 and 2:** 4,445 w/m3 (energy source term) **Inner glass cavity:** no energy source term **Operating conditions:** Boussinesq temperature, 293.15K; Boussinesq density, 1.2047 kg/m3
Boundary conditions	**Outer glass:** convection; 25w/m2k (heat transfer coefficient); 293.15K (free stream temperature) **Inner glass:** convection; 7.7w/m2k (heat transfer coefficient); 293.15K (free stream temperature) **Pressure inlet:** 293.15K (total temperature) **Pressure outlet:** 300K, default (backflow total temperature)
Methods	**Pressure-velocity coupling scheme:** SIMPLE **Gradient:** least squares cell based **Pressure:** body force weighted **Momentum, Turbulent Kinetic Energy, Turbulent Dissipation Rate, and Energy:** Second order upwind
Iterations	4000
Inflation	First Layer Height: 0.00021m Maximum Layers: 20 Growth Rate: 1.2
Body Sizing	0.009m
Face Sizing	0.01m
No. of Elements	2,925,524
Min. Orthogonal Quality	0.198
Max. Aspect Ratio	13.31

A.4.3 Material Properties and Boundary Conditions of Opaque Aluminium DSF

The tables below have information required for the CFD model set-up of the aluminium DSF.

Table A.19 Material Properties of Opaque Aluminium DSF for all Seasons

Material	Density (kg/m^3)	Specific Heat (J/kgK)	Thermal Conductivity (W/mK)	Viscosity (kg/ms)	Thermal expansion coefficient (1/K)
Aluminium	2719	871	202.4		
Cavity Air (Winter)	1.259 (Boussinesq)	1005	0.02489	1.75e-05	0.00341
Cavity air (Intermediate)	1.229 (Boussinesq)	1006	0.02542	1.784e-05	0.00341
Cavity Air (Summer)	1.198 (Boussinesq)	1006	0.02598	1.82e-05	0.00341
Warehouse Cladding	132	711	0.286		

Table A.20 Boundary Conditions of Opaque Aluminium DSF for all Seasons

Boundary Condition	
Pressure Inlet	269.15K (Winter);
Pressure Outlet	Default in all cases
Aluminium Outer	Convection, HTC: 25W/m^{2}K and respective external temp
Aluminium Inner	Coupled
Warehouse Cladding Outer	Convection, HTC: 7.7W/m^{2}K and internal 291.15K (18^{o}C)
Warehouse Cladding Inner	Coupled
Air	Heat source – 100,000W/m^3

A.4.4 Measurement Coordinates

The CFD coordinates for experimental validation, and the CFD rake coordinates for the DSF prototype are in A.21 and A.22.

Table A.21 CFD Coordinates for Validation against Climate Chamber

	LHS of Cavity	RHS of Cavity
X	0.15	0.95
Y	1.25	1.25
Z	-0.1	-0.1

Table A.22 CFD Rake Coordinates for Vertical Profile in DSF Cavity

Start		End	
X	-1.5	X	0.2
Y	0.55	Y	0.55
z	-0.1	Z	-0.1

Tables A.23 and A.24 details the outlet measurement coordinates for the DSF prototype and full-scale.

Table A.23 CFD Coordinates for DSF Prototype Outlet

VENTILATION OUTLET MEASUREMENT POINTS

	X	Y	Z
V1	0.9	1.325	-0.33
V2	0.9	1.4	-0.33
V3	0.9	1.475	-0.33
V4	0.5	1.325	-0.33
V5	0.5	1.4	-0.33
V6	0.5	1.475	-0.33
V7	0.1	1.325	-0.33
V8	0.1	1.4	-0.33
V9	0.1	1.475	-0.33

Table A.24 CFD Coordinates of Full-Scale DSF Outlet

Point	X	Y	Z
1	35.85	9.75	-0.34
2	35.85	9.70	-0.34
3	35.85	9.65	-0.34
4	29.95	9.75	-0.34
5	29.95	9.70	-0.34
6	29.95	9.65	-0.34
7	24.05	9.75	-0.34
8	24.05	9.70	-0.34
9	24.05	9.65	-0.34
10	18.15	9.75	-0.34
11	18.15	9.70	-0.34
12	18.15	9.65	-0.34
13	12.25	9.75	-0.34
14	12.25	9.70	-0.34
15	12.25	9.65	-0.34
16	6.35	9.75	-0.34
17	6.35	9.70	-0.34
18	6.35	9.65	-0.34
19	0.45	9.75	-0.34
20	0.45	9.70	-0.34
21	0.45	9.65	-0.34

A.4.5 Performance Tool Calculations

The tables below show each step of the calculations for pressure buoyancy, mass flow rate and heat gain removal for the different seasons using CFD-derived top cavity temperatures.

Table A.25 Pressure Buoyancy Calculations

	Pbuoyancy (pa)	Average density (kg/m^3)	G (m/s^2)	Cavity height (m)	Tcavitytop (°C)	Tcavitybottom (°C)
winter	37.61	1.259	9.81	9.8	16.47	-4
intermediate	-4.91	1.229	9.81	9.8	17.1	10
summer	0.12	1.198	9.81	9.8	24.34	25

Table A.26 Mass Flow Rate Calculations

	Cavity Velocity (m/s)	Cavity Area (m^2)	Qflowrate (m^3/s)	Average Density (kg/m^3)	Mass Flow Rate (kg/s)
winter	7.73	7.2	55.65	1.259	70.07
intermediate	2.83	7.2	20.34	1.229	25.00
summer	0.46	7.2	3.29	1.198	3.94

Table A.27 Heat Gain/Removal Calculations

	M (kg/s)	Cp (J/kg°C)	Tcavitytop (°C)	Tcavitybottom (°C)	Qheat (W)	Qheat (kW)
winter	70.07	1005	16.47	-4	1441408	1441
intermediate	25.00	1006	17.1	10	178581	179
summer	3.94	1006	24.34	25	-2615	-3

A.5 Stratification Data Collection and Calculations

To support the main results in Chapter 6, the following sections have been included in this appendix and show either example calculations or measurement coordinates. The boundary conditions of the 1:50 model include a flux of 178W/m^2 and 170W/m^2 for the central heat mat, a lab temp of 19.2°C for the remaining floor area and adiabatic on all the walls. At full-scale, this changes to a flux of 40W/m^2 across the whole floor area, and cross-ventilation openings with a pressure inlet and outlet.

A.5.1 Raw Experimental Data and Error Analysis

The table below details the raw temperature readings for the lab, and three positions within the 1:50 scale warehouse model when the 7W heat mat is turned on, along with averages. The purpose of this is to show that the middle position 3 is not a good indicator of stratified temperature as being directly above the heat source will have the inverse relationship with height, and therefore readings from either position 2 or 4 should be used.

Table A.27 Stratification Heat Mat Tests Temperature Readings

Vertical position	Thermocouple	Lab temp (ºC)	7W Heat Mat		
			Position 2 temp (ºC)	Position 3 temp (ºC)	Position 4 temp (ºC)
Bottom	TO1	19.20	20.55	34.37	20.72
	CT8	19.16	20.82	27.85	20.89
	TI2	19.19	21.03	24.89	21.16
	CT7	19.17	21.25	24.63	21.39
Top	TO8	19.29	21.99	24.55	21.89
	Average:	19.20	21.13	27.26	21.21

Readings were taken at position 4 for a 20W heat mat with and without the polystyrene "storage racking" rows. The results are provided in the table below.

Table A.28 Stratification Heat Mat Tests Temperature Readings(With Storage Racking)

	Empty model	Storage racking
1	21.19	22.97
2	21.58	23.00
3	21.96	23.11
4	22.20	23.59
5	22.49	23.50

A.5.2 Measurement Coordinates

Tables A.29 and A.30 shows the CFD coordinates for measurements taken in the stratification modelling of the small- and full- scale models.

Table A.29 Small-scale CFD Stratification Coordinates

1:50 Scale Model			
START		END	
X	0	Xo	0
Y	0	Yo	0.20
Z	0.33	Zo	0.33

Table A.30 Full-scale CFD Stratification Coordinates

Full Scale Model			
START		END	
X	0	Xo	0
Y	0	Yo	10
Z	16.5	Zo	16.5

A.6 Combined Wind and Buoyance Data Collection and Calculation

To support the main results in Chapter 7, the following sections have been included in this appendix and show either example calculations or measurement coordinates. The material properties from Chapter 5 and boundary conditions from Chapters 4, 5 and 6 have been combined for the final model. This includes thermal properties for the DSF and warehouse, a computational domain of 5H, 5H, and 15H with a velocity inlet and default pressure outlet.

A.6.1 Warehouse Openings Sensitivity Analysis

The final design of three openings of dimensions 2.5m x 0.5m and 1.25m^2 each was the result of a sensitivity analysis of opening areas in winter and summer conditions, as shown in Table A.31 and A.32. The idea is that not all the openings are always required but span the length of the warehouse façade where the double skin façade is attached to give a variety of options for an inlet point.

Table A.31 Winter Results for Warehouse Inlet Openings Analysis

Winter						
Q (L/s)	Q (m^3/s)	z (m)	Cd	A(m^2)	delta PA (Pa)	Rho (kg/m^3)
1263	1.26	9	0.65	0.34	19.59	1.2
2525	2.53	9	0.65	0.68	19.59	1.2
3787	3.79	9	0.65	1.02	19.58	1.2
5049	5.05	9	0.65	1.36	19.57	1.2
6311	6.31	9	0.65	1.7	19.57	1.2
7572	7.57	9	0.65	2.04	19.56	1.2
8832	8.83	9	0.65	2.38	19.56	1.2
10093	10.09	9	0.65	2.72	19.55	1.2
11353	11.35	9	0.65	3.06	19.55	1.2
12612	12.61	9	0.65	3.4	19.54	1.2

Table A.32 Summer Results for Warehouse Inlet Openings Analysis

Summer						
Q (L/s)	Q (m^3/s)	z (m)	Cd	A (m^2)	delta PA (Pa)	Rho (kg/m^3)
477	0.48	8.99	0.65	0.34	2.79	1.2
953	0.95	8.98	0.65	0.68	2.79	1.2
1430	1.43	8.97	0.65	1.02	2.79	1.2
1907	1.91	8.96	0.65	1.36	2.79	1.2
2383	2.38	8.95	0.65	1.7	2.79	1.2
2860	2.86	8.94	0.65	2.04	2.79	1.2
3338	3.34	8.93	0.65	2.38	2.79	1.2
3815	3.81	8.92	0.65	2.72	2.79	1.2
4292	4.29	8.91	0.65	3.06	2.79	1.2
4769	4.77	8.9	0.65	3.4	2.79	1.2

A.6.2 Case Study Warehouse Energy Consumption and Carbon Emissions

Based on the data provided in the methodology chapter, the following benchmark heating and cooling loads were calculated for the case study warehouses.

Table A.33 Fabric heat loss calculations

Fabric type	U value[1]	Area (m^2)	Outdoor temp[2]	Indoor temp[3]	Fabric loss (kW)
Walls	0.26	2035.15	-4	19	12.2
Pitched Roof	0.16	2564.13	-4	19	9.4
Floor	0.18	2564.13	-4	19	10.6
Rooflights	2.2	256.41	-4	19	13.0
Loading bay/level access doors	1.3	85.4	-4	19	2.6
Personnel doors	1.6	11.34	-4	19	0.4

[1]U-values obtained from Table 4.3 of Approved Document L1(a)
[2,3]BSRIA rule of thumb

Table A.34 Ventilation loss calculations

Ventilation requirements and infiltration	
Infiltration (ACH)	0.4
Outdoor air requirements (L/s)	768
Outdoor air requirements (ACH)	0.11
Minimum NV system requirements (ACH)	0.5
Combined outdoor air and infiltration (ACH)	0.51
Combined max. NV system and infiltration (ACH)	0.90
Volume of building (m^3)	25,466

Table A.35 Heating loads

Heating Load	
Total Fabric loss (kW)	48.2
Ventilation loss (option 1)	99.6
Ventilation loss (option 2)	175.7
Heating load (option 1) (kW)	147.8
Heating load (option 2) (kW)	223.9

These two heating loads are compared with a benchmark for industrial buildings provided by BSRIA rule of thumb of 80W/m^2 [33] to determine which is more reliable, and to highlight why ventilation regulations of warehouses influence energy demand projections. When using the ventilation loss based off minimum outdoor air requirements per area from ASHRAE, the heating load for this warehouse is just over 100kW less than using the benchmark value for this warehouse to achieve 205kW. However, the difference in heating load value when setting the ventilation requirements to the minimum ACH of a natural ventilation system, is much smaller as it overestimates by 19kW. This analysis presents the difficulty of obtaining reliable heating load estimations if there is no consistent ventilation standard for warehouse, either in UK or international building regulations.

Table A.36 Casual heat gains calculations

Casual heat gains and occupancy	
Occupancy (no. of people)	37
Sensible heat gain (kW)	2.7
Latent heat gain (kW)	2.2
Lighting load (kW)	17.9
Equipment load (kW)	5.5

Table A.37 Solar gains calculations

Wall type	Solar Gain (kW)
Roof	14.6
North	1.6
South	3.7
East	2.7
West	6.1

Table A.38 Cooling load

Cooling Load	
Total casual heat gains (kW)	28.3
Total solar heat gains (kW)	28.7
Cooling load (kW)	57

A.6.3 Measurement Coordinates

The CFD coordinate locations for the analytical validation of cross-ventilation in the full-scale warehouse are in the tables below.

Table A.39 CFD Coordinates of Inlet Measurement Points (Analytical Validation)

inlet points									
	p1	p2	p3	p4	p5	p6	p7	p8	p9
x	17.65	17.65	17.65	18.8	18.8	18.8	19.95	19.95	19.95
y	9.05	9.25	9.45	9.05	9.25	9.45	9.05	9.25	9.45
z	-0.15	-0.15	-0.15	-0.15	-0.15	-0.15	-0.15	-0.15	-0.15

Table A.40 CFD Coordinates of Outlet Measurement Points (Analytical Validation)

outlet points									
	p1	p2	p3	p4	p5	p6	p7	p8	p9
x	19.95	19.95	19.95	18.8	18.8	18.8	17.65	17.65	17.65
y	9.05	9.25	9.45	9.05	9.25	9.45	9.05	9.25	9.45
z	-71.84	-71.84	-71.84	-71.84	-71.84	-71.84	-71.84	-71.84	-71.84

The coordinate locations for measurements at the three inlets on the front façade of the warehouse, and the rake positions in the DSF cavity are in the tables below.

Table A.41 CFD Coordinates of Inlet Measurement Points (Final Model)

	inlet 1 (LHS)				inlet 2 (middle)				inlet 3 (RHS)			
		x	y	z		x	y	z		x	y	z
top	i1p1	7.47	9.46	-0.15	I2p1	17.57	9.46	-0.15	I3p1	28.07	9.46	-0.15
middle	i1p2	7.47	9.26	-0.15	I2p2	17.57	9.26	-0.15	I3p2	28.07	9.26	-0.15
bottom	i1p3	7.47	9.06	-0.15	I2p3	17.57	9.06	-0.15	I3p3	28.07	9.06	-0.15
top	i1p4	8.63	9.46	-0.15	I2p4	18.73	9.46	-0.15	I3p4	29.23	9.46	-0.15
middle	i1p5	8.63	9.26	-0.15	I2p5	18.73	9.26	-0.15	I3p5	29.23	9.26	-0.15
bottom	i1p6	8.63	9.06	-0.15	I2p6	18.73	9.06	-0.15	I3p6	29.23	9.06	-0.15
top	i1p7	9.87	9.46	-0.15	I2p7	19.97	9.46	-0.15	I3p7	30.47	9.46	-0.15
middle	i1p8	9.87	9.26	-0.15	I2p8	19.97	9.26	-0.15	I3p8	30.47	9.26	-0.15
bottom	i1p9	9.87	9.06	-0.15	I2p9	19.97	9.06	-0.15	I3p9	30.47	9.06	-0.15

Table A.42 CFD Rake Coordinates for Three Positions in DSF Cavity (Final Model)

	LHS		MIDDLE		RHS	
X	8	8	18	18	28	28
Y	9.87	0.91	9.87	0.91	9.87	0.91
Z	0.1	0.1	0.1	0.1	0.1	0.1

A.6.4 Performance Tool Calculations

The following tables A.43-A.47 show each step of the final analytical tool.

Table A.43 Environmental Data Required for Heat Gain/Removal Calculations

	Ext. temp(°C)	Average density (kg/m^3)	Ext. density (kg/m^3)	Average specific heat capacity (J/kgK)	Dynamic viscosity(kg/ms)
winter	-4	1.259	1.311	1005	0.0000175
spring	10	1.229	1.246	1006	0.00001784
summer	25	1.198	1.184	1006	0.0000182
autumn	10	1.229	1.246	1006	0.00001784

Table A.44 Wind and Buoyancy Pressure Drop Calculations for all Seasons and DSF Configurations

DSF Inlet Opening		Temp at top of cavity(°C)	Cp outer	Cp inner	velocity at DSF inlet (m/s)	Cd	A(m2)	Pwind (Pa)	Pbuoyancy (Pa)
Fully open	Winter	8.62	0.61	0.59	2.72	0.65	7.2	0.0968	40.68
	Spring	33.13	0.26	0.29	1.81	0.65	7.2	-0.0611	-7.58
	Summer	26.8	0.33	0.18	3.28	0.65	7.2	0.9553	-0.28
	Autumn	31.2	0.22	0.26	1.89	0.65	7.2	-0.0893	-7.37
25% LHS closed	Summer	27.88	0.33	0.28	4.10	0.65	5.4	0.4973	-0.83
25% RHS closed		31.23	0.33	0.01	2.46	0.65	5.4	1.1430	-0.84
50% LHS closed	Spring	20.93	0.26	0.63	2.10	0.65	3.6	-1.014	-5.67
	Autumn	18.66	0.22	0.64	2.15	0.65	3.6	-1.2072	-5.04
50% RHS closed	Spring	20.07	0.26	0.55	2.02	0.65	3.6	-0.7396	-5.44
	Autumn	19.35	0.22	0.56	1.97	0.65	3.6	-0.8221	-5.24
75% LHS closed	Winter	5.68	0.61	0.36	2.87	0.65	1.8	1.3468	47.35
75% RHS closed		3.63	0.61	0.25	2.56	0.65	1.8	1.5475	58.42
Fully closed	Winter	43.44	0.61	-0.12	0.43	0.65	0		30.35

Table A.45 Reynolds and Friction Factor Calculations for all Seasons and DSF Configurations

		L of DSF (m)	Dh of cavity	Average density (kg/m^3)	Average velocity (m/s)	Reynolds	Surface roughness of Aluminium	Haaland	Friction factor
Fully open	Winter	9	0.398	1.259	3.38	96660	0.00005	8.93	0.0125
	Spring	9	0.398	1.229	2.08	57009	0.00005	8.93	0.0125
	Summer	9	0.398	1.198	3.84	100650	0.00005	8.93	0.0125
	Autumn	9	0.398	1.229	2.04	55945	0.00005	8.93	0.0125
25% LHS closed	Summer	9	0.398	1.198	3.38	88544	0.00005	8.93	0.0125
25% RHS closed		9	0.398	1.198	1.95	52105	0.00005	8.93	0.0125
50% LHS closed	Spring	9	0.398	1.229	1.33	36394	0.00005	8.93	0.0125
	Autumn	9	0.398	1.229	1.32	36159	0.00005	8.93	0.0125
50% RHS closed	Spring	9	0.398	1.229	1.65	45197	0.00005	8.93	0.0125
	Autumn	9	0.398	1.229	1.34	36809	0.00005	8.93	0.0125
75% LHS closed	Winter	9	0.398	1.259	1.97	56258	0.00005	8.93	0.0125
75% RHS closed		9	0.398	1.259	2.02	57939	0.00005	8.93	0.0125
Fully closed	Winter	9	0.398	1.259	0.50	14182	0.00005	8.93	0.0125

Table A.46 Wetted Perimeter Calculations for all Seasons and DSF Configurations

DSF Configuration		Velocity at inlet (m/s)	Velocity at top (m/s)	Average velocity in cavity (m/s)	Aflow (m^2)	W(m)	H (m)	Pwetted (m)
Fully open	Winter	2.72	4.04	3.38	7.2	0.2	36	72.4
	Spring	1.81	2.35	2.08	7.2	0.2	36	72.4
	Summer	3.28	4.41	3.84	7.2	0.2	36	72.4
	Autumn	1.89	2.19	2.04	7.2	0.2	36	72.4
25% LHS closed	Summer	2.66	4.10	3.38	7.2	0.2	36	72.4
25% RHS closed		1.43	2.47	1.95	7.2	0.2	36	72.4
50% LHS closed	Spring	0.56	2.10	1.33	7.2	0.2	36	72.4
	Autumn	0.49	2.15	1.32	7.2	0.2	36	72.4
50% RHS closed	Spring	1.28	2.02	1.65	7.2	0.2	36	72.4
	Autumn	0.72	1.97	1.34	7.2	0.2	36	72.4
75% LHS closed	Winter	1.06	2.87	1.97	7.2	0.2	36	72.4
75% RHS closed		1.49	2.56	2.02	7.2	0.2	36	72.4
Fully closed	Winter	0.56	0.43	0.50	7.2	0.2	36	72.4

Table A.47 Friction Loss, Final Pressure Drop and Heat Gain/Removal Calculations

Ptotal (Pa)	Pfriction (Pa)	Pfinal (Pa)	Pfinal pos.(Pa)	Vol flow rate (m^3/s)	Mass flow rate (kg/s)	Heat gain/removal (W)	Heat (kW)
40.78	2.04	38.74	38.74	36.72	46.22	586270	586
-7.64	0.75	-8.39	8.39	17.29	21.25	494570	495
0.67	2.51	-1.84	1.84	8.20	9.83	17796	18
-7.46	0.73	-8.19	8.19	17.08	21.00	447806	448
-0.34	1.94	-2.28	2.28	9.13	10.94	31687	32
0.30	0.65	-0.35	0.35	3.57	4.27	26767	27
-6.68	0.31	-6.99	6.99	15.78	19.40	213367	213
-6.24	0.30	-6.55	6.55	15.28	18.77	163571	164
-6.18	0.47	-6.66	6.66	15.40	18.93	191785	192
-6.06	0.31	-6.38	6.38	15.08	18.53	174287	174
48.69	0.69	48.00	48.00	7.97	263.94	2568614	2569
59.97	0.73	59.24	59.24	9.84	263.71	2021792	2022
30.35	0.04	30.30	30.30	6.52	203.51	9702775	9703

A.6.5 CFD-Derived Values of Heat Gain and Removal in the DSF

The tables A.48 and A.49 in this section describe the values obtained from CFD to calculate the heat gain/removal in the DSF directly.

Table A.48 CFD-Derived Density and Velocity to Calculate Mass Flow Rate

DSF Inlet Configurations and Seasons		Average density (kg/m^3)	Average velocity (m/s)	DSF Area (m^2)	Volumetric Flow Rate (m^3/s)	Mass Flow Rate (kg/s)
Fully open	Winter	1.259	2.502	7.2	18.01	22.68
	Spring	1.229	1.142	7.2	8.22	10.10
	Summer	1.198	2.170	7.2	15.62	18.71
	Autumn	1.229	0.739	7.2	5.32	6.54

25% LHS closed	Summer	1.198	2.270	7.2	16.34	19.58
25% RHS closed		1.198	1.907	7.2	13.73	16.45
50% LHS closed	Spring	1.229	0.792	7.2	5.70	7.01
	Autumn	1.229	0.997	7.2	7.18	8.82
50% RHS closed	Spring	1.229	0.883	7.2	6.36	7.81
	Autumn	1.229	0.836	7.2	6.02	7.40
75% LHS closed	Winter	1.259	1.766	7.2	12.71	16.01
75% RHS closed		1.259	1.521	7.2	10.95	13.79
Fully closed	Winter	1.259	0.529	7.2	3.81	4.80

Table A.49 CFD-Derived Outlet Temperature to Calculate Heat Gain/Removal

DSF Inlet Configurations and Seasons		Average Outlet Temp (°C)	Inlet Temp (°C)	Specific Heat (J/kg°C)	Qheat (kW)
Fully open	Winter	8.71	-4	1005	290
	Spring	33.13	10	1006	235
	Summer	26.80	25	1006	34
	Autumn	31.20	10	1006	139
25% LHS closed	Summer	35.96	25	1006	216
25% RHS closed		38.75	25	1006	228
50% LHS closed	Spring	34.96	10	1006	176
	Autumn	33.38	10	1006	207
50% RHS closed	Spring	35.26	10	1006	198
	Autumn	32.79	10	1006	170
75% LHS closed	Winter	11.01	-4	1005	241
75% RHS closed		12.73	-4	1005	232
Fully closed	Winter	63.33	-4	1005	325

A.6.6 Embodied Energy and Investment Cost of the DSF

Below is some supplementary data to support the short economic and environmental analyses of the opaque aluminium double skin façade in the main text.

Table A.50 Cost, Carbon and Weight of DSF Materials

Material	Monetary Cost	Carbon cost (CO2e/kg)	Weight (kg)	Size (m^2 or m^3)
Aluminium	£1783.75/tonne [A-2]	14.3	8.19	288m^2
Stainless Steel	£436.22/tonne [A-3]	0.39 CO_2e per ton		
Weatherproof Sealant (silicone)	£2.99/m Tube of 310ml covers 12.4m of a gap with depth and width of 5mm (7 tubes) [A-4]	11.3CO_2e/kg Si	N/A	(8 x 36m) x 2 = 88m perimeter
Weather Membrane (HDPE)	£51.99 per 100m^2 [A-5]	High density polyethene 1.60kgCO_2/kg polyethene	23kg per 100m^2 so 66.24kg	288m^2
Paint (Slate Grey RAL 7015)	12m^2 per litre , £22.64 per litre [A-6]	A 5-litre gallon of paint may result in 13.58 kg CO_2e	N/A	25 litres

- Weight of aluminium for 3mm x 1000mm x 1000mm is 8.19kg. So 1m^2 of aluminium weighs 8.19kg so 290m2 of aluminium weighs. 8.19kg x 290m2 = 2375.1kg = 2.38

tonnes. Assumption is that the aluminium comes in panels of 1m by 8m which is 36 sheets.

- Euroliner of length 13.5m-13.6m, width of 2.45m-2.5m, height 2.45m – 2.7m, max payload 25 tonnes – 9.5 miles per gallon of fuel. 210 miles from Dover to Nottingham so this is 210/9.5 = 23 gallons of fuel. UK price is 675.88 pence per gallon which is £6.76 per gallon so £155.48 for the whole journey. One gallon of diesel fuel emits 10180 grams of CO2 and driving one mile on average emits 404 grams of CO_2. So, 23 gallons emits 235 kgCO_2.
- Purlins fixed back to structural hot rolled steel frame of the building using cleats by welding or bolted. The cold rolled purlins are bolted to the cleats using M16 bolts.

A.7 Appendix References

A-1 Richards. P. J., Hoxey. R. P., Connell B.D., Lander, D.P. (2007) Wind-tunnel Modelling of the Silsoe Cube. Journal of Wind Engineering and Industrial Aerodynamics. 95; 1384-1399.

A-2 London Metal Exchange. Aluminium. (n,d) https://www.lme.com/en/metals/non-ferrous/lme-aluminium#Summary

A-3 MEPS International. (n,d) World Stainless Steel Prices. https://mepsinternational.com/gb/en/products/world-stainless-steel-prices

A-4 UK Sealants. (n,d) Soudal Aquafix All Weather Sealant. https://www.uksealants.co.uk/soudal-aquafix-all-weather

A-5 Newton Waterproofing. High-density Polyethylene (HDPE). https://www.newtonwaterproofing.co.uk/high-density-polyethylene-hdpe/

A-6 Thorndown Paints. (n,d) RAL 7015 Slate Grey. https://thorndown.co.uk/product/ral-7015-slate-grey-wood-paint/